Spring 5-19-2017

Microwave-Assisted Topochemical Manipulation of Layered Oxide Perovskites: From Inorganic Layered Oxides to Inorganic-Organic Hybrid Perovskites and Functionalized Metal-Oxide Nanosheets

Sara Akbarian-Tefaghi
University of New Orleans, sakbaria@uno.edu

Microwave-Assisted Topochemical Manipulation of Layered Oxide Perovskites: From Inorganic Layered Oxides to Inorganic-Organic Hybrid Perovskites and Functionalized Metal-Oxide Nanosheets

A Dissertation

Submitted to the Graduate Faculty of the
University of New Orleans
in partial fulfillment of the
requirements for the degree of

Doctor of Philosophy
in
Chemistry
Materials

by

Sara Akbarian-Tefaghi

B.Sc., Polymer Engineering, Amirkabir University of Technology - Tehran Polytechnic, 2010
M.Sc., Polymer Engineering, Amirkabir University of Technology - Tehran Polytechnic, 2012
M.Sc., Chemistry, University of New Orleans, 2016

May, 2017

To …

Artin and Kourosh,

My mom and brothers.

Acknowledgements

I am truly appreciative of my supervisor, Professor John B. Wiley, for being not only a very helpful mentor, but also a friend to all of his students. Working in a group that felt more like my family let me concentrate my energy on moving forward with my research rather than losing it in a tense unfriendly atmosphere. He has always been there for all of us by keeping the door of his office open and lending us a pair of ears to listen to all of our concerns and questions and to sincerely offer us his best.

I am also very thankful to my committee members: Professor Matthew A. Tarr, Professor Mark L. Trudell, and Professor Dhruva Chakravorty. Their knowledge and helpful tips have shed light on this path and offered me new perspectives to look at my work as a whole.

I would like to also thank Harry Rees, the technical engineer of the chemistry department, who helps everyone whenever there is something wrong with anything electrical. Without him many research plans would halt due to a puzzling electrical glitch.

Thanks to Dr. Dariush Montasserasadi, Dr. Taha Rostamzadeh, and Dr. Jagnyaseni Tripathy, the senior graduate students of my research group, for their friendly assistance. Thanks to Dr. Elisha Josepha for teaching me how to rely on myself and not be too concerned by the opinions of others. I am also thankful to all of my past and present group members: Treva Brown, Sarah Gauthier, Mayra Franco, and Alexis Blanco for being good friends to me, Mark Granier for always finding the impossible things that I would need as a part of a research project, Clare Davis-Wheeler, Md Shahidul Islam Khan, Anamika Poduval, Dr. Shivaprasad Reddy Adireddy, and Dr. Léa Gustin, as well as our undergraduate researchers, especially Juana Reconco, Elaine Veiga, Mona Chudasama, Cecilia Carbo, Kayla Moore, and Rebecca Mitton. I would like to also thank my other colleagues at the University of the New Orleans who helped a great deal in different stages of my career: Dr. Parisa Pirani, Dr. Satish Rai, Dr. Artur Maksymov, Dr. Amin Yourdkhani, Dr. Sarah Wozny, Dr. Arjun Sharma, Dr. Richard Prevost, Rahmatollah Eskandari, Zhi Zhang, Shuke Yan, Daniel Adams, and Maria Lindsay.

Making a life from scratch in a new country is quite difficult, and having to experience that along with a Ph.D. career makes it twice as hard. I would like to thank all of my dear friends that I had to leave behind in my country who never gave up on me, especially Anahita, Shima,

Soheyla, Maryam, Mahsa, Arezoo, Raha, and Mehrnaz. I'd like to send my thanks to my family that I've never stopped missing: my aunts, uncles, and cousins.

Being who we are at the moment is also partly because of those who hurt us the most in our lives, I would like to acknowledge the ones I had to erase from my life, but having them crossing my path made me a much stronger person. I am foremost thankful to my God who never let me down in the face of all those bad moments, and always had me protected under his mighty arms. He had me survive the worst moments with the least possible harm and the most treasured lessons, becoming the strongest version of myself.

I am blessed to have a loving and supportive family who made it easier to achieve more in my career: my parents and brothers, as well as my husband and his wonderful family that I love no less than my own. I also truly wish that my sweet grandmother that I lost about ten years ago would hear my appreciation for her as I never forget her loving hands. I would like to specifically thank my mom, husband, and brother, Hesam. My mom is where I can define unconditional love, and Hesam was the reason I started enjoying science and learned how good I am at math and chemistry. Foremost, my husband, Kourosh is the reason that every afternoon I can find comfort, love and peace at home, regardless of the teething troubles at work. He might think that he is lucky to have me, but I believe that I am the lucky one to have someone this supportive and loving as my spouse. There are many mediocre things in my life, but the love I found through him and our son is not definitely one of them.

The help from the beamline staff at the Oak Ridge National Laboratory (BL-11A and BL-16B) and the Argonne National Laboratory (11-BM) is very much appreciated, with special thanks to: Debasish Mohanty, Melanie Kirkham, Ashfia Huq, Lynn Ribaud, and Luke Daemen.

The financial support by the National Science Foundation (DMR-1005856 and CHE-1412670) is also gratefully acknowledged.

Table of Contents

List of Figures

List of Tables

Abbreviations

0D, zero-dimensional

1D, one-dimensional

2D, two-dimensional

3D, three-dimensional

NS, nanosheets

DJ, Dion-Jacobson

RP, Ruddlesden-Popper

AV, Aurivillius

LN, $LaNb_2O_7$

PN, $PrNb_2O_7$

CT, $CaTa_2O_7$

CN, $Ca_2Nb_3O_{10}$

LT, $La_2Ti_3O_{10}$

Fe, $Ca_2Nb_2FeO_9$

Mn, $LaCaNb_2MnO_{10}$

LDH, layered double hydroxide

LHS, layered hydroxide salt

SAM, self-assembled monolayers

GO, graphene oxide

h-BN, hexagonal boron nitride

TBA^+, tetra(n-butyl)ammonium

Am, amine or ammonium

BA, benzyl alcohol or benzyl alcoxy

BAm, benzylamine or benzylammonium

DCM, dichloromethane

PEG, polyethylene glycol

DVB, divinyl benzene

AIBN, 2,2′-azobis(2-methyl-propionitrile)

TMPDAE, trimethylolpropane diallyl ether

DEGDVE, di(ethylene glycol) divinyl ether

AT, 4-amino-1,2,4-triazole

HMF, hydroxymethylferrocene

TLC, thin-layer chromatography

IE, ion exchange

MA, microwave assisted

MAOS, microwave-assisted organic-synthesis

XRD, X-ray diffraction

SNS, spallation neutron source

ORNL, Oak Ridge national laboratory

TOF, time-of-flight neutrons

INS, inelastic neutron scattering

ANL, Argonne national laboratory

APS, advanced photon source

EM, electron microscopy

SEM or TEM, scanning or transmission EM

FE, field emission

EDS, energy dispersive spectroscopy

SAED, selected area electron diffraction

AFM, atomic force microscopy

DART, dual amplitude resonance tracking

TA, thermal analysis

DTA, differential thermal analysis

TGA, thermogravimetric analysis

DSC, differential scanning calorimetry

UV, ultraviolet

NIR, near-infrared

FTIR, Fourier transform infrared spectroscopy

DRS, diffuse reflectance spectrum

FL, fluorescence

NMR, nuclear magnetic resonance spectroscopy

JJ, Josephson junction

FC or **ZFC**, field cooling or zero field cooling

SQUID, Superconducting Quantum Interference Device

Abstract

Developing new materials with desired properties is a vital component of emerging technologies. Functional hybrid compounds make an important class of advanced materials that let us synergistically utilize the key features of the organic and inorganic counterparts in a single composite, providing a very strong tool to develop new materials with ”engineered” properties. The research presented here, summarizes efforts in the development of facile and efficient methods for the fabrication of three- and two-dimensional inorganic-organic hybrids based on layered oxide perovskites. Microwave radiation was exploited to rapidly fabricate and modify new and known materials. Despite the extensive utilization of microwaves in organic syntheses as well as the fabrication of the inorganic solids, the work herein was among the first reported that used microwaves in topochemical modification of the layered oxide perovskites. Our group specifically was the first to perform rapid microwave-assisted reactions in all of the modification steps including proton exchange, grafting, intercalation, and exfoliation, which decreased the duration of multi-step modification procedures from weeks to only a few hours. Microwave-assisted grafting and intercalation reactions with n-alkyl alcohols and n-alkylamines, respectively, were successfully applied on double-layered Dion-Jacobson and Ruddlesden-Popper phases ($HLaNb_2O_7$, $HPrNb_2O_7$, and $H_2CaTa_2O_7$), and with somewhat more limited reactivity, applied to triple-layered perovskites ($HCa_2Nb_3O_{10}$ and $H_2La_2Ti_3O_{10}$). Performing neutron diffraction on n-propoxy-$LaNb_2O_7$, structure refinement of a layered hybrid oxide perovskite was then tried for the first time. Furthermore, two-dimensional hybrid oxides were efficiently prepared from $HLnNb_2O_7$ (Ln = La, Pr), $HCa_2Nb_3O_{10}$, $HCa_2Nb_2FeO_9$, and $HLaCaNb_2MnO_{10}$, employing facile microwave-assisted exfoliation and post-exfoliation surface-modification reactions for the first time. A variety of surface groups, saturated or unsaturated linear and cyclic organics, were successfully anchored onto these oxide nanosheets. Properties of various functionalized metal-oxide nanosheets, as well as the polymerization of some monomer-grafted nanosheets, were then investigated for the two-dimensional hybrid systems.

Keywords: *topochemical manipulation, layered oxide perovskites, microwave-assisted reactions, inorganic-organic hybrids, structure refinement, surface modification, functionalized metal-oxide nanosheets, radical polymerization.*

Chapter 1. Introduction

From the electronics to catalysis to medical applications, the search for the new materials, ones that can keep up with emerging technologies, has been of great interest these days. The discovery of novel materials in turn is fueled by the development of new methods of synthesis. The research summarized in the following chapters highlights the development of facile synthetic methods to fabricate and modify new and known materials, specifically these involve the modification of the interlayer of receptive perovskite hosts and the exfoliation of these layers by effective methodologies.

1.1– Layered Materials

Other than molecular solids with discrete molecules held together via weak intermolecular forces, many solids consist of an infinite lattice of atoms networking via ionic or covalent bonds; *non-molecular solids*.[1] A two-dimensional (2D) lattice is an arrangement of atoms with a repeating pattern throughout the width and length of a single layer with a very small thickness. Stacking a large number of 2D arrays results in the formation of a three-dimensional (3D) layered solid, where the adjacent layers are usually held together via van der Waals interactions or electrostatic forces (layered van der Waals solids, or ionic solids, respectively).[2–4] Typically, when in-plane atomic bonds are much stronger than the interactions that the atoms of adjacent layers have with one another, a 3D lattice is considered a layered structure (there are some layered materials though with strong bonding in all directions—*such as La_2CuO_4).*[2,5] As shown in Figure 1-1, individual layers in a layered solid can be considered as *planar "macromolecules"* or *"lamellas"*, where packing many of these *macromolecules* forms a 3D *"molecular"* crystal with a layered structure. Following terms are then demonstrated in a layered solid: interlayer region (space confined between two adjacent layers), interlayer spacing (measured from the barycenter of one layer to the next one), and the gallery height (the free distance between two layers, obtained by subtracting the layer thickness from the interlamellar distance).[2]

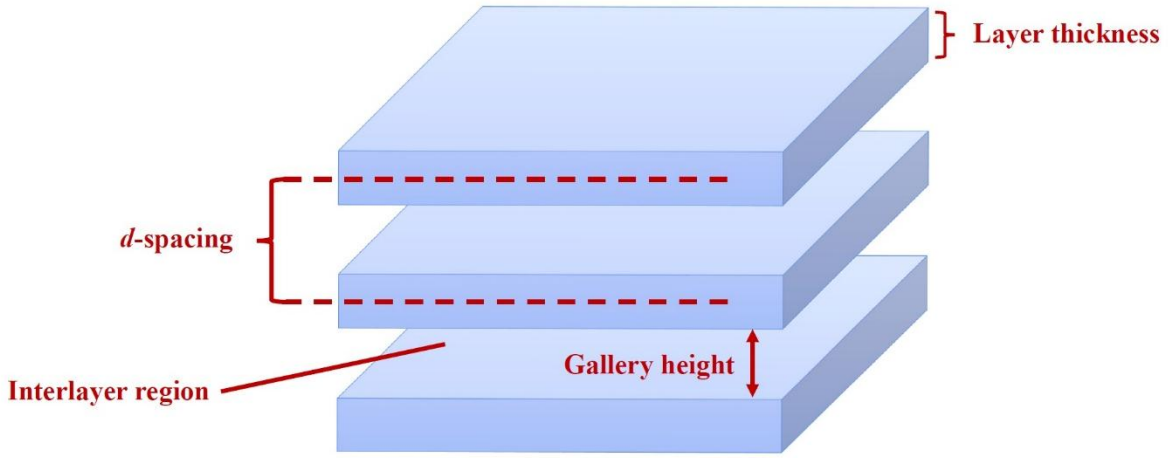

Figure 1-1: Illustration of a layered solid formed by stacking single layers. Important terms in characterizing a layered structure are also shown.

Layered solids can be classified in three different ways, all of which are based on a specific feature of the planar constituent layers: thickness, the organic or inorganic nature, and the net charge.[2] Since the thickness of the constituent sheets is directly related to their *rigidity*, a key property of the layered structure, the first classification is very useful.[2,6,7] Three classes of: atomic monolayers, few atoms thick, and many atoms thick, are demonstrated in this case. Classification based on the organic / inorganic nature can be confusing in cases where the planar layer has a mixed nature (for instance hydrogenated graphite can be considered of organic type while graphite fits more to an inorganic class). When organic groups are covalently attached to an inorganic backbone, the term "inorgano-organic" can be used to describe the layered material, and "organic-inorganic", or "inorganic-organic" more refers to cases where the planar backbone has a mixed nature (according to the organic or inorganic component being prevalent in the structure, respectively).[2] On the basis of the charge of each layer, the layered materials are either electrically neutral (uncharged), or charged.[2,3,7] Uncharged layers are subdivided into electronic conductors and insulators, such as graphite and hexagonal boron nitride (h-BN, also known as white graphite), respectively.[2,8–10] The main difference between conductive and insulator neutral layered structures is the nature of the interactions between the host and guest in the intercalates of these solids; while quite weak dipole-dipole interactions or hydrogen bonding is demonstrated

in the latter, the former exhibits stronger ionic-type interactions with exchangeable interlayer ions (due to the ability of gaining or losing electrons in the conduction band).[2] Other than graphite, some of the very important families of layered materials fall under the conductive neutral category, such as layered metal chalcogenides (metal dichalcogenide, trichalcogenide, and phosphorous trichalcogenide), transition metal oxyhalides, vanadium pentoxide and molybdenum trioxide.[2,4,11–13] Charged layers can either be positive or negative, respectively forming anionic or cationic layered solids based on the type of the counterions placed in the interlayer region neutralizing the fixed charge of each lamella. The interlayer counterions usually form a monolayer or a bilayer, causing the adjacent layers linking together via ionic bonds, and in some cases through hydrogen bonding.[2,3] Layered α-zirconium phosphates and phosphonates, double hydroxide (LDH) and hydroxide salts (LHS) are examples of anionic layered solids,[3,13–15] and layered graphite oxide, smectite clay, titanates, niobate, titanoniobate, niobo-tungstate, tantalo-tungstate, manganate (birnessite and buserite), and perovskites are important types of cationic layered materials.[12,13,16,17] Among these layered compounds, perovskites are the main focus of this work, which are further discussed in the next section. Figure 1-2 represents the structure of a few layered solids introduced above: (a) h-BN as an insulating uncharged atomic monolayer,[12,18] (b) a brucite LDH as an anionic layered solid,[12,19] and (c) montmorillonite (a smectite clay mineral) as a cationic layered lattice.[12,20,21]

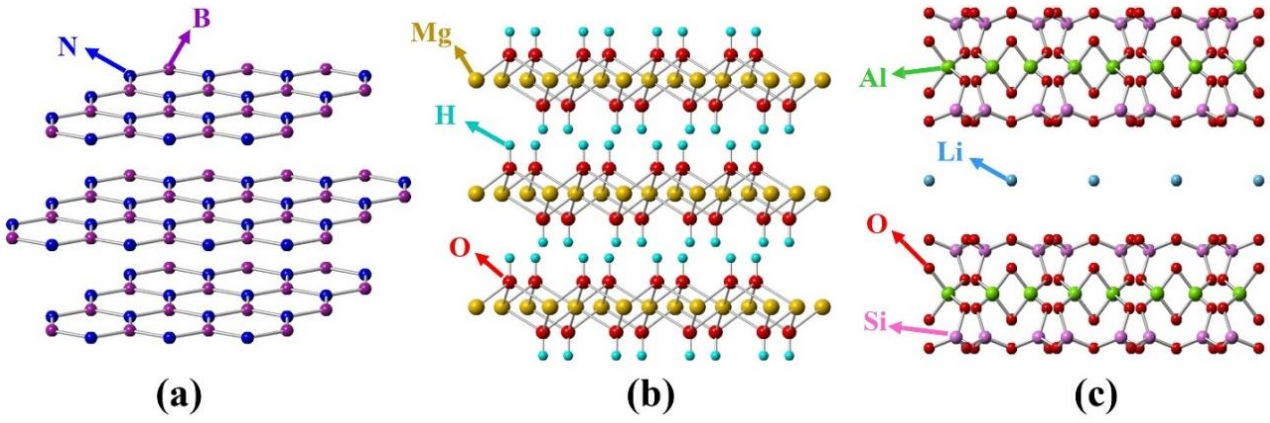

Figure 1-2: Structure of some layered solids: (a) boron nitride, (b) brucite LDH, and (c) montmorillonite.

1.1.1 Layered Perovskites

1.1.1.1 Structure

$CaTiO_3$ mineral was found in 1839 in the Ural Mountains, and named *perovskite* by Gustav Rose (in honor of a Russian geologist, Lev Aleksevich von Perovski).[22] Simple or ideal perovskites, with structures similar to that of $CaTiO_3$, are represented with ABX_3 general formula, where X is an anion surrounding A and B metal cations (A is typically larger in size than B).[23,24] Even though much of the research on perovskites has involved oxides and halides, some carbides, nitrides, and hydrides are also known to form similar crystal structures.[23] Figure 1-3 shows the simple cubic crystal structure of $BaTiO_3$,[25] where Ba has a coordination number of 12 and is surrounded by 8 TiO_6 octahedra residing the corners of the unit cell, corner-sharing of which will provide an extended lattice.[24,26,27]

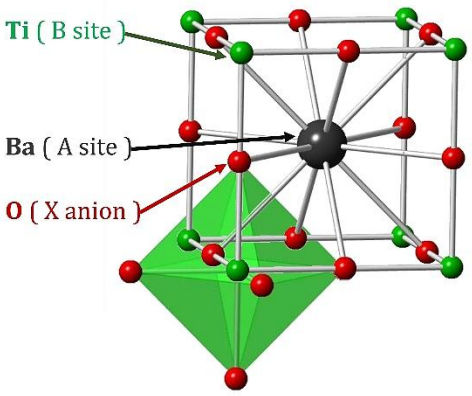

Figure 1-3: Crystal structure of $BaTiO_3$ simple perovskite with ABX_3 general formula.

The structure of the constituent layers of layered perovskites, so called perovskite slabs, resembles an extended lattice of ideal perovskite with the general formula of $[A_{n-1}B_nO_{3n+1}]$, where the negative slabs are interlayered with cations or cationic structural units (*A* is alkali-metal, alkaline earth, or rare-earth cations, *B* is a transition metal cation, and *n* is the thickness of the layers).[24,27,28] On the basis of the net charge of the slab, layered perovskites are commonly divided into three families: Dion-Jacobson (DJ) structure where the slab has a charge of -1 and the overall formula is $A'[A_{n-1}B_nO_{3n+1}]$, Ruddlesden-Popper (RP) with a net charge of -2 and $A'_2[A_{n-1}B_nO_{3n+1}]$ formula, and lastly Aurivillius type (AV) with the same structure as Ruddlesden-Popper and Bi_2O_2 arrays in the interlayer (usually shown as $Bi_2O_2[A_{n-1}B_nO_{3n+1}]$).[24,27–29] Figure 1-

4 provides the crystal structure of two layered perovskites, $RbCa_2Nb_3O_{10}$[30] and $Li_2CaTa_2O_7$,[31] with Dion-Jacobson and Ruddlesden-Popper structures, respectively.

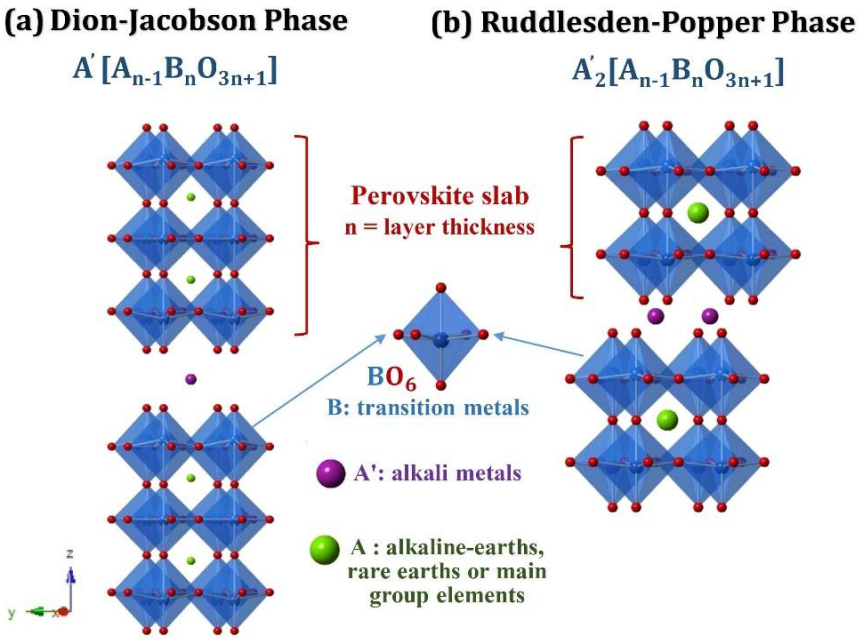

Figure 1-4: Two important families of layered oxide perovskites are presented here; (a) $RbCa_2Nb_3O_{10}$ as a triple-layered Dion-Jacobson, and (b) $Li_2CaTa_2O_7$ as a double-layered Ruddlesden-Popper.

1.1.1.2 Synthesis

Non-molecular inorganic solids can be prepared via different techniques and in various forms such as powders, single crystals, films, and fibers.[32] Layered oxide perovskites are mainly synthesized as powders via *solid state reactions* (ceramic method). Solid state reactions consist of combining non-volatile reagents, and successive grinding and heating for prolonged periods to specific temperatures (as high as 1300 ºC in some cases).[32–35] Grinding is a key factor in such reactions as it increases the surface contact area of the solid reactants and allows for more homogeneity and higher crystallinity of the product.[33,36] Due to the limited diffusion of reagents in solid form, longer reaction durations (usually days) and higher temperatures (in some cases also high pressures[37–39]), are typical for solid state reactions as opposed to regular organic syntheses. Based on the necessity of successive grinding and heating, these reactions are also known as '*heat and beat'* or '*shake and bake'* methods.[32,33,36] Figure 1-5 provides pictures of

important components in carrying out a solid state reaction: (a) *furnace*-ovens that can go to higher temperatures needed for ceramic methods, (b) *mortar and pestle*-for grinding, and (c) *alumina crucible*-typical reaction vessel in solid state reactions. Considering the harsh conditions of ceramic methods discussed above, synthesis of metastable compounds would require alternative approaches, such as those carried out at lower temperatures and shorter time times;[24,40] these will be covered in the following sections.

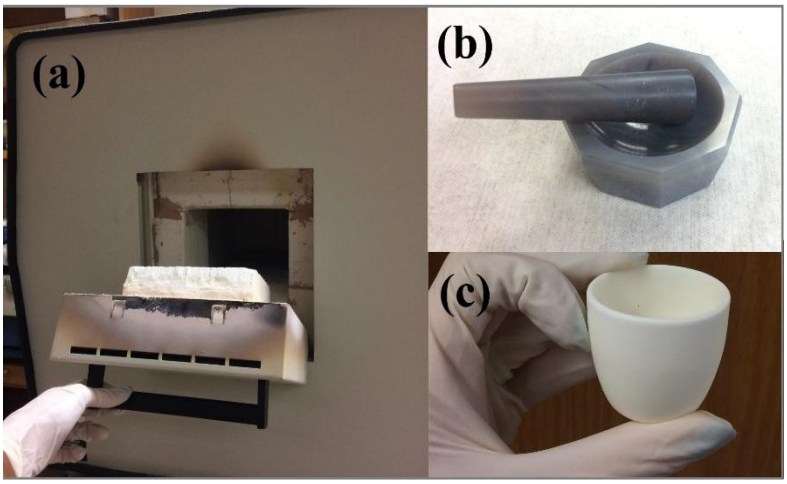

Figure 1-5: Important components of a solid state reaction: (a) furnace, (b) mortar and pestle, and (c) crucible.

The regular ceramic method is certainly the main synthetic approach when it comes to layered perovskites. There is, however, another alternative high-temperature method which is also popular among inorganic chemists: *molten salt synthesis*.[32,41,42] In this technique, a few percent of a salt with a melting point lower than the reaction temperature is combined with other oxide and carbonate reagents of the reaction. Melting of the salt will enhance the diffusion of the starting materials, as well as the homogeneity of the product without having to perform any intermediate grinding. In other words, the molten salt acts as the "solvent" of this modified ceramic method.[41] In case of using a large amount of salt (salt-to-reactant molar ratios as high as 10:1), the molten salt synthesis is specifically called a *flux-assisted approach*.[1,41,43–46] Salts used for this technique typically include alkali chlorides and sulfates (such as KCl and Na_2SO_4), which can be conveniently washed away from the final product after the reaction (usually very soluble in water).[41] Flux-assisted approaches can be done with considerably higher rates (in only

a few hours) and at temperatures lower than their alternative ceramic routes. Also, by tuning the reaction temperature and duration, they allow for controlling the shape and size of the particles in the final products.[41,43–45,47] It should be noted that the synthesis of the oxides and layered perovskites is also possible via other wet low-temperature processes, where the properties of the final product are highly affected by the change of the synthetic approach and the conditions.[48–52]

1.1.1.3 Properties and Applications

The selection of A and B elements and their stoichiometry in perovskites and layered variations, are the key factors to introduce a wide variety of interesting electrical, magnetic, and optical properties to the mixed metal oxides.[23,24,26,28,53,54] Some key features are: dielectricity and ferroelectricity,[26,55–57] superconductivity (defined as zero electrical resistance and expulsion of magnetic field below a critical temperature),[38,58–63] colossal magnetoresistance, ferromagnetism and antiferromagnetism,[64–67] interesting optical properties,[23,68] proton conductivity,[23,69–72] photocatalytic[73–77] and catalytic activity.[23,78,79] Engineering the perovskite structure and composition has made them key materials in electronic, catalytic, and photovoltaic applications over the past decades. Considering the exchangeable interlayer in some cationic layered compounds, a large variety of inorganic or organic arrays can be formed in the layered perovskites, where fine tuning of the final properties is also possible. Even though modified ABX_3 type halide perovskites are mostly used for electronic and photovoltaic applications,[80–87] tailoring the interlayer and the slab composition of layered oxide perovskites makes them interesting photocatalytic materials.[2,17,73–77,88] The overall structure and composition of the perovskite are controlled via the reactants and conditions of the high temperature solid state reactions. However, structures with mixed valence,[89–92] nonstoichiometry of the oxygen or cations,[23] and specific inorganic or organic arrays in the interlayer,[88,93–101] call for lower synthetic temperatures where such kinetic phases are accessible.[24,27,102] Using low temperature reactions, sometimes as a multistep sequence, allows for controlling structural features of the layered perovskite and access to a wide variety of interesting properties.[24,27,96] The fundamentals of low temperature approaches (*soft chemistry*), especially those that matter to the goals of this dissertation, are covered in the following section.

1.2– Soft Chemistry (*Chimie Douce*)

The term *Chimie douce* was first proposed in 1977 by a French scientist, Jacques Livage (translated to *soft chemistry*).[36,103] Later on, Jean Rouxel expanded the soft chemistry field by working on solid precursors, and organizing the first national meeting on *chimie douce* approaches in the nineties.[36] The inspiration behind soft chemistry reactions is to mimic the wet chemistry that nature offers for daily creations of bio-materials in living organisms without any extreme conditions.[36,103] In other words, soft chemistry is defined as synthetic approaches done in lower temperatures where thermodynamically unstable structures and morphologies are accessible at the kinetic level.[24] Sol-gel processes[36,46,104] and topotactic reactions[24,27] are two main types of *chimie douce* approaches widely studied in the past decades.[36] A "sol-gel process" is the transformation of "solution" precursors to an inorganic network, forming a "gel" (this so-called inorganic polymerization is typically done via hydrolysis and condensation reactions).[27,36,50,104–106] Topotactic reactions, which are the main processes used in this work, are defined as methods where fine tuning of the structure of a layered compound, especially in the interlayer region, is done while the main structure of the starting compound is maintained. The layered precursor (host) is typically pre-formed via high temperature solid state-reactions, and then modified via low temperature soft chemistry approaches.[24,27,36]

1.2.1 Topochemical Manipulation of Layered Perovskites

Topochemical manipulation is defined as modification of a layered host while its major structural features are maintained in the obtained product.[17,36] In a layered oxide perovskite, the new structural features are directed via various techniques such as ion exchange, intercalation, deintercalation, and substitution, when the structure of the perovskite slab remains basically intact.[24,27] Figure 1-6 represents four types of topotactic reactions that are significant to this research: (a) ion exchange, (b) intercalation, (c) grafting, and (d) exfoliation.[27] More detailed description of each of these processes is provided below. As illustrated in the figure, in all of these approaches the slab structure of the host is maintained.[27]

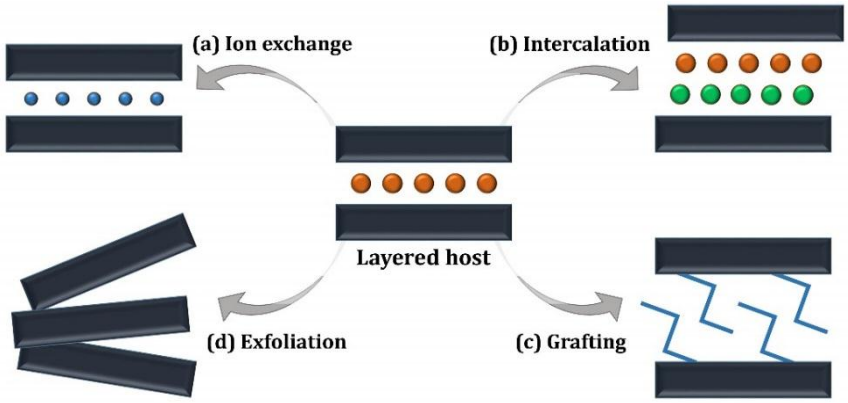

Figure 1-6: An illustration of: (a) ion exchange, (b) intercalation, (c) grafting, and (d) exfoliation reactions in a layered host.

1.2.1.1 Ion Exchange

Considering the nature of layered oxide perovskites (negative slabs with -1 or -2 lamellar charge), the interlayer cations are exchangeable with other cations or cationic structural units in such a way that the overall charge within these layered compounds stays neutral. Other than simply exchanging an ion with another one with the same oxidation state,[107] there are cases where the replacing unit is either an ion of a different oxidation state (aliovalent exchange),[108,109] or an ionic array (co-exchange),[67,94] either way, a specific stoichiometry is formed to keep the overall interlayer charge the same as the initial stage. There have also been reports of partial exchange of the interlayer ions.[27,110]

An exchangeable interlayer is one of the very interesting features of charged layered materials, which allows one to exchange the interlayer ions with new ions and ionic arrays (ion exchange), or insert organics held in place via covalent bonds or acid-base interactions (grafting, and intercalation, respectively). Ion exchange is the simplest way to modify the interlayer of perovskites, and indeed a typical step preceding other modification reactions such as intercalation and grafting.

1.2.1.2 Intercalation

Intercalation consists of inserting an ion or molecular unit in the interlayer area, without removing any of the constituent elements present in the structure.[2] Intercalation sometimes leads

to a reduction or oxidation reaction by altering a specific oxidation state in the slab (respectively reductive[61,111] or oxidative[112,113] intercalation). However, neutral intercalation happens where a complete molecular unit is inserted without changing the oxidation states in the slab or causing any other structural change other than the expansion or contraction of the *d*-spacing.[24,27] Insertion of water molecules in some perovskites (hydration),[107,114] or formation of ammonium ions in the interlayer by acid-base interaction of organic amines and solid acid perovskites, are the examples of neutral intercalation.[2,100,107,115,116]

1.2.1.3 Grafting

Strong covalent bonds are formed in the event of a grafting reaction, where organic groups are tethered to the terminal oxygens of a layered oxide perovskite.[27] Most common terminal bonds include M-O-C,[97–100] M-O-Si,[117–119] and M-O-P,[120] where M is the transition metal in B site (such as Nb).

Figure 1-7 represents grafting and intercalation reactions of a double-layered DJ perovskite ($HLaNb_2O_7$) with n-alkyl alcohols and n-alkylamines, respectively. It is notable that prior to a successful organic modification reaction, an elementary ion exchange reaction is carried out; formation of $HLaNb_2O_7$ from $A'LaNb_2O_7$ using acids such as HNO_3. The protonated form, solid acid perovskite, shows high reactivity with desired organics (such as amines and alcohols). As illustrated below, intercalation reactions with amines only involve the formation of ammonium ions through the combination of interlayer proton and the RNH_2 (R = n-alkyl groups or more complicated organic structures).[100,107,115,116,121] However, the mechanism of grafting reactions is more complicated. Considering the hydroxy functional groups in an n-alkyl alcohol, it is suggested that the mechanism would include an initial hydrolysis followed by esterification.[98,122]

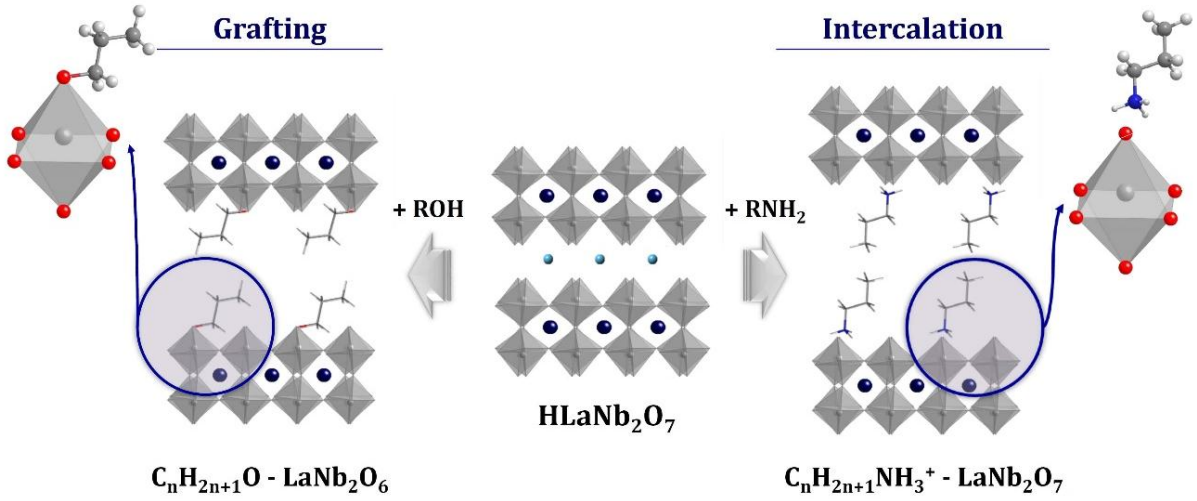

Figure 1-7: Grafting and intercalation reactions of $HLaNb_2O_7$ with n-alkyl alcohols and n-alkylamines, respectively. In this illustration 3-carbon chains are used.

1.2.1.4 Exfoliation

Liquid exfoliation techniques mainly involve the intercalation of polymeric, organic, or ionic species that weaken the interlayer adhesion and result in the delamination of the layered structure.[4,118,119,123–126] Having weak out-of-plane interactions and strong in-plane bonds is the key to have a high-yield exfoliation of the layered host, for instance exfoliation of black phosphorous to phosphorene monolayers is experimentally a challenge due to stronger interlayer interactions as well as relatively weak in-plane phosphorus-phosphorous bonds.[127] The reactivity of the Ruddlesden-Popper phase with an organic base is often very limited,[128] however, double- and triple-layered Dion-Jacobson-type perovskites (such as $RbLaNb_2O_7$, $RbLaTa_2O_7$ and $KCa_2Nb_3O_{10}$) efficiently go through exfoliation reactions, producing freestanding 2D layers used in different applications.[129–135] Figure 1-8 provides an illustration of exfoliation reactions, where bulky tetra(n-butyl)ammonium ions (TBA^+) are intercalated in the galleries of a double-layered DJ perovskite and caused the delamination of the 3D structure into individual layers.

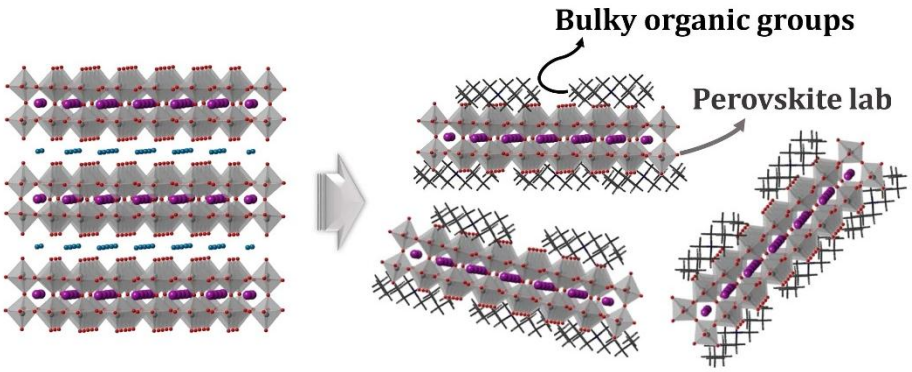

Figure 1-8: A typical exfoliation reaction of $HLaNb_2O_7$ perovskite due to the intercalation of tetra(n-butyl)ammonium hydroxide.

1.2.2 Heating Techniques

Even though traditional wet chemistry routines using hot plate / stirrer accessories are still popular despite their typical long durations, more advanced heating techniques, such as solvothermal methods and microwave-assisted reactions, are absolutely required in order to successfully, efficiently, and rapidly carry out some specific soft chemistry approaches. Further details of these two common heating techniques will be provided in the following sections.

1.2.2.1 Solvothermal Methods

In simple words, a solvothermal reaction is performed under modest temperature and high pressure, and in an appropriate solvent.[46] Typically a mixture of reactants and a solvent is enclosed inside a PTFE-lined cylinder (bomb), and heated in an oven up to 100-500 ºC and under high pressures.[32] Pictures of a PTFE-lined cylinder and a typical sealable autoclave (stainless steel container), are presented in Figure 1-9. In case of using water as the solvent, the solvothermal reaction is specifically called *hydrothermal*.[1,32,136] Even though higher pressures can be easily reached via connection to an external pressure control, the amount of pressure in the vessel can also be estimated based on the filling percentage of the mixture in the bomb and the reaction temperature.[32,137] In other words, the second function of the solvent in such reactions is to transmit pressure via forming convection streams in the confined reaction vessel (for example due to the existence of water / steam in a hydrothermal method).[32] Solvothermal

reactions have been vastly used for the production or modification of various inorganic materials.[88,100,136,138–147]

Figure 1-9: PTFE-lined cylinder and parts of a typical autoclave (left) and a sealed autoclave (right).

1.2.2.2 Microwave-Assisted Reactions

Microwave irradiations have been used as an important method of heating since commercializing the first generation of microwave ovens in 1950s.[148,149] Use of microwaves in performing chemical transformation was first reported as a published work in 1986,[150,151] and have been extensively expanding since then in facilitating processes in different fields such as analytical chemistry, biochemistry, photochemistry, catalysis, as well as the synthesis of inorganic materials, organometallics, polymers, and most importantly microwave-assisted organic synthesis (MAOS).[152–155] Microwave-assisted research was initially based on the use of kitchen microwave ovens, which tremendously increased the confusion among the chemists in 1990's due to non-reliable temperature / pressure monitoring and higher chances of explosion. Even though employing domestic household microwave ovens is not yet eliminated in the published works (about 30% in 2009), the majority of the researchers today take advantage of dedicated microwave stations and their interesting features (monitoring both temperature and pressure on-line and accurately, higher safety controls, robust cavities that withstand possible explosions, and possibility of stirring the reaction vessels which increases the homogeneity).[152] Despite availability of dedicated microwave reactors in lower prices these days, they are still harder to afford than conventional heating equipment.[152]

Heating a reaction vessel using an external heat source (conventional thermal heating) typically causes a temperature gradient within the sample with the temperature increasing in layers closer to the reaction vessel (Figure 1-10a). The key feature of microwave-assisted reaction, is the simultaneous exposure of the whole reaction mixture to microwaves (internal or in core volumetric heating), causing a uniform temperature increase throughout the entire sample (Figure 1-10b).[32,152,156]

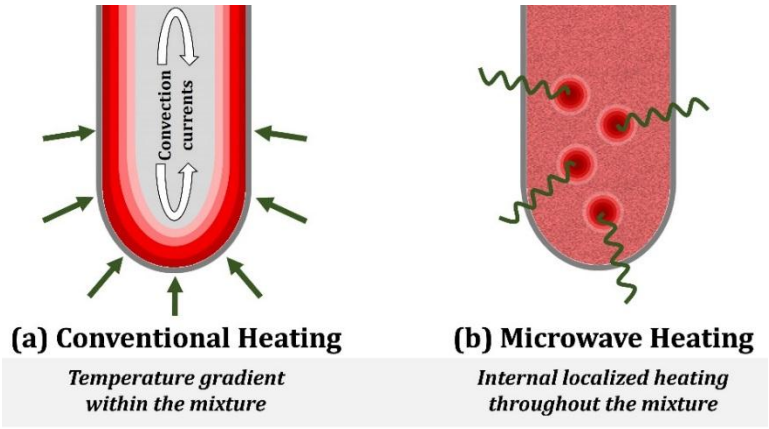

Figure 1-10: Comparison of heat distribution in: (a) conventional methods with an external heat source, and (b) microwave-assisted reactions

The frequency of microwaves is in 0.3 – 300 GHz range of the electromagnetic irradiation, corresponding to wavelengths of 1 mm – 1 m.[32,152,156] Microwaves are used for transmission of either energy or information. All domestic microwave ovens and dedicated microwave stations operate at a specific frequency (2.45 GHz) to avoid interference with telecommunication frequencies.[152] This small frequency does not cleave any molecular bonds and is also lower than Brownian motion, proving that microwaves will not induce any chemical reactions via direct absorption (as opposed to ultraviolet or visible radiation).[152] Like any electromagnetic irradiation, microwaves also transmits as a transverse oscillating wave of electric and magnetic fields.[152,156] The electric component of microwaves is mainly responsible for heating of the materials via two major mechanisms: *dipolar polarization* and *ionic conduction*. Molecules with dipoles constantly try to align themselves with the oscillating electric field and realign as the field quickly changes. In this process, heat is generated due to molecular friction and dielectric loss. In ionic conduction, heating is based on the collisions of

charged particles and ions as they oscillate back and forth under the impression of the alternating electric field.[152] In both of these mechanisms, the microwaves are absorbed by dipolar molecules, ions, or charged particles, and generate heat throughout the sample. However, there is a third mechanism which applies to semiconducting or conducting materials (such as metals) where microwaves are mainly reflected rather than absorbed: *resistive (ohmic) heating mechanism*. In ohmic heating, the electric field will direct the free flow of electrons on the surface of the material, which causes heating due to the intrinsic resistance of the system.[152,155] Even though the electric field is the component that is responsible for heating most of the microwave-assisted processes, the interactions with the magnetic field could also be of interest in some cases (for instance for transition metal oxides).[157–159]

The dielectric properties of a certain material will directly impact their ability to efficiently convert this electromagnetic irradiation into heat (dielectric heating). Microwave-absorbing feature of the materials is typically evaluated by the so-called *loss factor or loss tangent* (tan δ). This factor is obtained by dividing the dielectric loss of the material (ε") by its dielectric constant (ε'), respectively defined as the efficiency of the material to convert the electromagnetic radiation into heat, and polarizability of the molecules in the electric field. Solvents used in microwave chemistry can be classified based on their loss factor: high (tan $\delta > 0.5$, such as ethanol), medium ($0.1 < \tan \delta < 0.5$, such as water), and low microwave-absorbing ($\tan \delta < 0.1$, such as toluene). It should be noted that the loss factor is strongly frequency and temperature dependent. For instance, the loss tangent of pure water and most of the organic solvents drops with increasing the temperature; as in water heating via microwaves gets very difficult past 100 ºC, to a point that water becomes transparent to microwaves at its supercritical temperature. In the opposite scenario (in case of the materials that become more microwave-absorbing at elevated temperatures), the chances of overheating and explosion highly increases.[152]

Microwave-assisted reactions significantly decrease the reaction times due to the minimization of wall effects and efficient internal heating of the reaction mixture. This allows the chemists screen for new target compounds in a few hours, and move on to more decision points without wasting days waiting for the result.[152] Due to the enormous instantaneous energy

provided in microwave heating, thermodynamically controlled reactions can also take place, as opposed to the conventional heating techniques were mainly kinetic products are obtained (the easiest path with the lowest activation energy due to the mild conditions in conventional methods).[156] This so-called "*microwave flash heating*" is believed to be the main reason of the rate-enhancement in the majority of microwave-assisted reactions. However, there are more perplexing aspects to microwave-matter interactions (*microwave effects*),[152] which are also known to enhance the rate of microwave-assisted reactions. Full ramifications of the *microwave effects* have not been realized yet.

1.3– Nanomaterials

Nanotechnology is based on the manipulation of materials in nanoscale – from subnanometer to several hundred nanometers. However, the decisive aspect of nanotechnology is the *appearance of a novel property*, so-called "nano-effect", which is achieved by going down in the crystallite size of a particular material .[160,161] Even though materials in the microscale have properties very similar to that of bulk, nanoscale materials offer distinctively different features than that of their bulk.[160] As an example, gold has no catalytic properties in bulk, however, gold nanocrystals are known to be great low-temperature catalysts.[160] Gold also changes its typical yellow color when a critical size is reached: becoming blue at about 50 nm and purple at about 20 nm (the nano-effect in this specific example is the *plasmon resonance* revealed in the smaller size range).[161] Since the 1980s, nanotechnology has been growing tremendously in different areas such as therapeutic drugs, information storage, refrigeration, chemical/optical computers, improved ceramics and insulators, harder metals, thin film precursors, environmental chemistry (solar cells, remediation, water purification, and destructive adsorbents), catalysts, sensors, smart magnetic fluids, and batteries.[4,161–163] Some of the aforementioned fields should be considered more as *nanoscience*, as they are still a step away from well-realized technologies.[161] The cornerstone of nanoscience is the ability to fabricate and process nanostructures and nanomaterials: materials with at least one dimension in the nano-scale. Properties of a material can strictly change by changing its dimensionality; designing desirable zero-, one-, two-, and three-dimensional nanostructures (like nanoparticles, nanorods, nanosheets, and nanoflowers, respectively).[4,164] Two-dimensional (2D) materials, having two dimensions outside of

nanometric size range by definition, are the specific class of nanomaterials that was the focus of this work.[4]

1.3.1 Two-Dimensional (2D) Nanosheets

Synthesis and fabrication methods in nanoscience are classified in two main areas: *bottom-up* and *top-down* approaches. Nanomaterials in bottom-up approaches are made from the bottom using subnano building blocks (atoms, molecules, or clusters), while top-down approaches involve fabrication of nanomaterials or nanostructures from a microscopic bulk material.[4,160,161] It is notable that the level of surface defects and internal stress is usually minimal in bottom-up approaches as opposed to the latter class.[160] Some important syntheses and fabrication methods of 2D nanomaterials can be highlighted as: micromechanical cleavage, liquid exfoliation, chemical vapor deposition, van der Waals epitaxial growth on substrate, and hydrothermal synthesis.[4,165–167] Fabrication of 2D nanomaterials in a typical top-down method is based on cleaving weak out-of-plane van der Waals interactions in a layered solid, and the formation of freestanding layers maintaining the initial strong in-plane chemical bonds of the 3D host.[4,11,12,14,127,168–173] Liquid exfoliation explained in ***section 1.2.1.4*** is the most common technique in such top-down methods; delamination of the layered structure as a result of the intercalation of polymeric, organic, or ionic species.[4,118,119,123–126,128]

Graphene family[174] (graphene[175,176], graphene oxide[177–179], fluorographene[180,181], hexagonal boron nitride[8–10,182], and boron carbon nitride[183,184]), 2D chalcogenides (transition metal dichalcogenide[185,186]and trichalcogenide[187]), and nanosheets of layered double hydroxides[14,171](LDHs) and oxides[169–171,188] (such as transition metal oxides, perovskites, and niobates) are a number of important types of 2D materials.[4,12,174] Layered oxide perovskites, attainable with tunable elemental compositions and slab thicknesses as described earlier, are one of the important hosts for the fabrication of single or few layers of oxide nanosheets with desired composition and thickness via liquid exfoliation method.[4,12,168–171] Intercalation of a bulky organic base such as tetra(n-butyl)ammonium is the most common method of liquid exfoliation in layered oxide perovskites.[128,129,189–197]

1.4– Hybrid Materials

When organic and inorganic components are mixed at the atomic or molecular level in the composition of a compound, a *hybrid material* is formed.[36,198] Soft chemistry approaches discussed above, allow for the preparation of a wide variety of hybrid materials with different interesting properties.[36] Classification of the hybrid materials is mainly based on the nature of the interactions in the interface of the organic and inorganic moieties: weak (such as electrostatic forces, hydrogen bonding, π-π interaction, or van der Waals contacts) or strong (covalent, iono-covalent, or Lewis acid-base bonding).[17,198–201] The motivation behind the fabrication of hybrids is to ultimately combine the best of both organic and inorganic counterparts in one molecular composite; a mixture with superior properties.[81,106,198,201] Key features of the inorganic materials and nanomaterials can be highlighted as: strong ionic and covalent forces in the extended lattice, tunable electronic and magnetic properties, mechanical hardness, and thermal stability. On the other hand, the organic molecules offer interesting structural diversity, simple and low-cost processing methods, significant polarizability and fluorescence efficiency, light weight, as well as plastic mechanical behavior.[81] A simple example is the incorporation of 0D, 1D, or 2D nanostructures in a polymeric matrix and the formation of a lightweight composite with significantly improved mechanical properties, widely used in many well-stablished technologies like transportation infrastructure.[198] Interestingly, the best teacher in this field is nature with countless examples of organic-inorganic hybrids in all living organisms (like bones).[106,198] The birth of hybrid materials can be traced back to the need of human to create handicrafts with various colors by mixing inorganic pigments and organic dyes.[198,200] However, only during the last decades science could offer the atomic-resolution analysis tools to shed light on hybrid materials and nanotechnology.[198] Functional hybrid materials allow for the fabrication of advanced materials with novel properties meeting the need of the emerging technologies in optics, electronics, catalysis, energy storage, membranes, coatings, and medicinal sciences.[198,200] Synthesis and fabrication of organic-inorganic hybrid materials and nanomaterials have been widely studied in the literature[199,202–209] for various inorganic hosts such as clays,[210–212] perovskites[99,120,133,134,213–216] and other oxides[217–227].

1.5– Characterization and Analysis

1.5.1 Crystallography and Structure Determination

1.5.1.1 Crystal Systems

Any solid is a specific arrangement of atoms, ions, or molecules networking together, creating a three-dimensional lattice. When the arrangement of this network creates a long-range order, the solid is known to be *crystalline*, as opposed to non-crystalline materials (*amorphous*, also referred to as *glasses)* with only a short-range order.[228–230] Figure 1-11 shows two 2D networks with long and short range orders (**a** and **b**, respectively). Considering the ordered arrangement of atoms in a crystalline solid, the smallest repeating unit is called *the unit cell* (for example each hexagon in Figure 1-11a is a unit cell). In other words, a crystalline structure is built up of many identical unit cells, packed side by side, each representing the symmetry of the solid.[231,232] Considering a cuboid shape for the unit cell in 3D, the specifications of the unit cell are three edges (*a*, *b*, and *c*) and three angles (α, β, and γ), as presented in Figure 1-12. Noting the possible variations in three edges and angles, 3D crystals can be classified into seven distinct unit cell shapes, also known as *crystal systems*. Table 1-1 shows these seven crystal systems.[231] It should be noted that these different shapes do not define the unit cell of the solid, it is the *symmetry elements* that give identity to the unit cell (such as mirror plane, rotation axis, etc.). For instance, the *essential* symmetry in a simple cubic system is four threefold axes passing through the body diagonals, though additional symmetry elements are also present in most cubic crystals (the essential symmetries in seven systems are shown in Table 1-1 as well). All seven crystal systems can be derived by stretching/compressing a simple cubic unit cell along a diagonal

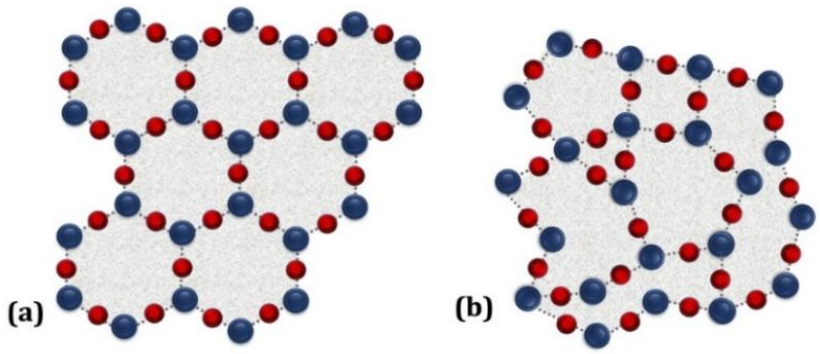

Figure 1-11: Illustration of long range order (a) and short range order (b), respectively called crystalline and amorphous.

and/or axis(es), and sometimes shearing one face relative to the other, which causes the loss of some symmetry elements with each distortion step, and generation of a new shape. Another important feature of each crystal system is the specific locations of the atoms, ions, or molecules, known as *lattice points*, linking of which will construct the unit cell. There are different lattice types: primitive (points only at the corners), face centered (points in the center of each face, as well as the corners), body centered (an extra lattice point in the center of the cell in addition to the corner points), base centered (points in the center of two parallel faces, as well as the corners), and rhombohedrally centered (two points on the longest body diagonal, in addition to the points in the corners_only applies to the trigonal system). As shown in the last column of Table 1-1, specific lattice types are allowed in different crystal systems, making 14 different combinations (*Bravais lattices*).[230,231,233]

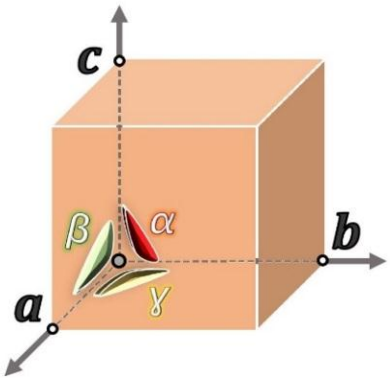

Figure 1-12: Unit cell parameters are shown here. Three edges: *a*, *b*, and *c*, and three angles: *α* (between *b* and *c*), *β* (between *a* and *c*), and *γ* (between *a* and *b*).

Table 1-1: The specifications of different crystal systems

Crystal system	Unit cell restrictions	Symmetry	Allowed lattices*
Cubic	$a = b = c$, $\alpha = \beta = \gamma = 90^o$	Four threefold axes	P, F, I
Tetragonal	$a = b$, $\alpha = \beta = \gamma = 90^o$	One fourfold axis	P, I
Orthorhombic	$\alpha = \beta = \gamma = 90^o$	Three twofold axes or mirror planes	P, F, I, A (B or C)
Hexagonal	$a = b$, $\alpha = \beta = 90^o$, $\gamma = 120^o$	One sixfold axis	P
Trigonal or Rhombohedral	$a = b$, $\alpha = \beta = 90^o$, $\gamma = 120^o$ *or* $a = b = c$, $\alpha = \beta = \gamma \neq 90^o$	One threefold axis	P or R
Monoclinic	$\alpha = \gamma = 90^o$	One twofold axis or mirror plane	P, C
Triclinic	**None**	None	P

P (primitive), F (face-centered), I (body-centered), A, B, or C (Base-centered), and R (rhombohedrally-centered)

Lattice planes are considered as imaginary planes in the unit cell which in cases coincide with actual layers of atoms in the crystal structure. Each set of planes is defined by assigning three numbers known as *Miller indices*. In order to assign miller indices to each set of planes, one should first assign the origin and the three axes, and then find the fractional intersections of these planes with each axis. The reciprocals of these three fractions are written in parentheses and known as miller indices, with (*hkl*) general symbol. Figure 1-13 shows (*040*) set of planes in a random unit cell, where all of the planes are separated with a characteristic distance (called *d*-spacing). The *d*-spacing of more complicated sets of planes can be calculated knowing the unit cell parameters. For instance, in orthogonal crystals (where $\alpha = \beta = \gamma = 90^{o}$), the *d*-spacing is simply calculated as: $\frac{1}{d_{hkl}^2} = \frac{h^2}{a^2} + \frac{k^2}{b^2} + \frac{l^2}{c^2}$.

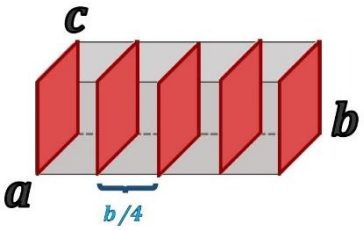

Figure 1-13: (*040*) miller indices in a cuboid unit cell.

Perovskites are mostly obtained as *polycrystalline* powders: a large number of very small crystals with random relative orientations building up a 3D polycrystalline sample.[234] In a perfect single crystal however, there is an unbroken crystal lattice throughout the entire sample to the very edges of it.[235]

1.5.1.2 Diffraction Techniques

In case of non-molecular crystalline solids, the crystal structure can be most important identity to be characterized. One of the most powerful techniques, needed in order to gain information about the spatial arrangement of atoms in a crystal, is the diffraction experiment; this is where the interaction of the sample with radiation reveals information about the atomic structure.[236] In diffraction techniques specifically, scattered radiation coherent with the incident beams are of interest.

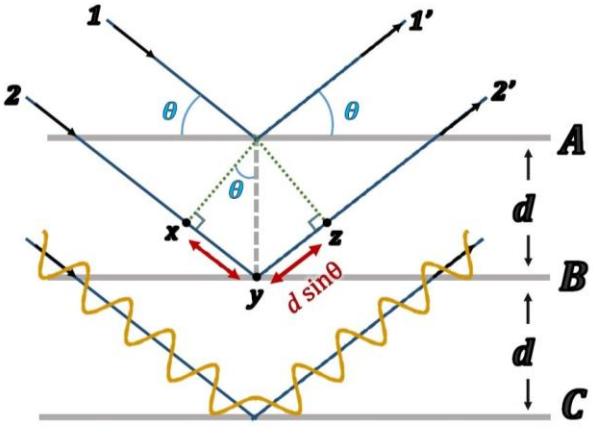

Figure 1-14: Conditions that lead into constructive interference from a set of parallel planes with an interlayer spacing of *d* (derivation of Bragg's law).

Generally, a high degree of order within the sample is required in order to yield interference of scattered radiation from different parts of the samples, and accurately obtain structural details.[237] In other words, even though in most directions the scattered waves interfere destructively and cancel out each other (*out-of-phase* beams), there should be a high periodicity of the atoms in a crystal causing the waves interfering constructively in certain directions (*in-phase* waves).[231,237] The interference of the scattered radiation can be presented by rays "*reflecting"* from a set of parallel planes with an interlayer spacing of *d*, where each plane populates the certain atoms of the lattice (Figure 1-14). The Bragg equation (the easiest way to access structural information in powder diffraction) is derived from Figure 1-14.[231,234,236,237] The logic of Bragg's law is to figure out the conditions that two reflected beams would be in-phase (*1'* and *2'* beams, respectively reflected from the incidence of *1* and *2* beams with an angle of θ). The Bragg equation is satisfied when the extra distance that the second ray travels, equals a whole number of the wavelength (based on figure, the *xyz* distance should be equal to $n\lambda$). Considering the simple geometry relationships involved, *xyz* also equals $2 \times d \sin\theta$, leading to the Bragg equation ($n\lambda = 2d \sin\theta$).[231,234,236,237]

Illumination of an object by light in an optical microscope is the simplest example of scattering of light due to the interaction of the oscillating electric field of this electromagnetic radiation with the dipoles of the specimen, however, no structural details less than the wavelength of the visible light (~400 nm) can be detected. Study of the fine atomic structure requires radiations with wavelengths in the order of the interatomic distances (~1-3 Å), which can be provided by X-rays, neutron beams, or electrons with appropriate energy.[231,237]

X-ray Diffraction. Among X-rays, neutrons and electrons, X-rays are the cheapest to produce and typically non-destructive, and so the most common diffraction technique is based on the X-rays (X-ray diffraction, XRD). X-rays are typically produced in sealed tubes (so called X-ray tubes), where accelerated electrons (up to 60 kV) bombard an anodic metal target inside a vacuum tube (often Cu).[231,234,237] These incident electrons carry enough energy to ionize the 1*s* electrons of Cu, followed by the instantaneous drop of an electron from the outer orbitals (2*p* or 3*p*) to the vacant level created at 1*s*. Based on the nature of the transition, $3p \rightarrow 1s$ or $2p \rightarrow 1s$, specific wavelengths of X-rays are generated, respectively called *Kβ* (1.3922 Å for Cu) or *Kα* (1.5418 Å for Cu). Among the X-rays emitted by striking the metal target, it is desired to filter

out anything but the most intense radiation, and obtain a monochromatic beam for the analysis (for instance filtering out the $K\beta$ from the emission by using Ni foils or a monochromator, and passing through clean Cu $K\alpha$ X-rays).[231] As the oscillating electric field of this monochromatic electromagnetic radiation hits the electrons of the atoms, it vibrates them. These vibrating charges will then re-emit radiation coherent with the incident X-rays, acting as a secondary source reflecting in-phase X-rays to the detector. Based on the mechanism of X-ray diffraction, the *scattering factor* of an atom is proportional to the number of electrons of it (the atomic number), and the *structure factor* shows the intensity of the reflected X-rays based the fractional co-ordinates and the scattering factors of the lattice atoms. This way, the electron density within the lattice is obtained via diffraction, elucidating the structural details.[231,233,237]

In a polycrystalline powder, the crystallites and the lattice planes are randomly arranged in all orientations. So, for each set of planes there are always enough crystallites present at the Bragg angle θ with the incident beam. A movable detector in this case will be able to sweep all of the reflections with different θ values assigned to specific sets of atomic planes (angular dispersive techniques).[238] In some setups of the powder XRD instruments the sample is held stationary with the X-ray tube and detector both moving simultaneously over the angular range θ (theta-theta setup), and in other designs the X-ray tube is held stationary while the sample and detector are both moving by angles θ and 2θ, respectively (2theta-theta setup).[234] Figure 1-15 shows a 2theta-theta X-ray powder diffractometer used in the current research.

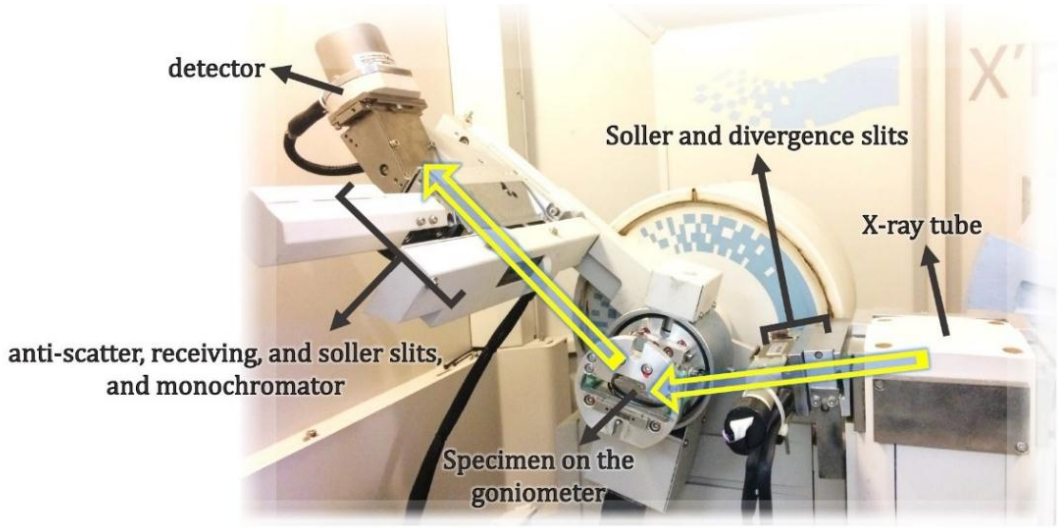

Figure 1-15: An X-ray powder diffraction instrument with theta-2theta setup.

Synchrotron radiation is produced by accelerating charged particles (electrons or positrons) to very high speeds, close to the speed of light, while passing them through a specific closed-loop path (*storage ring*). Strong acceleration of charged particle in an electric field and continuous deflection in magnetic fields, results in the production of a continuous spectrum of X-rays that are 10^{13} times more brilliant than the beams released from common X-ray tubes.[238] Synchrotron sources are huge national facilities where the storage ring is typically hundreds of meters in diameter. The storage ring consists of successive curved and straight segments, which cause the emission of synchrotron radiation, respectively by steering the electrons using a bending magnet, or oscillating them via alternating magnetic fields provided in magnetic arrays. The energy of the emitted synchrotron X-rays depends on the energy of the electrons and specifications of their path in the storage ring. Regardless, using the synchrotron X-rays allows for significantly higher resolution powder diffraction measurements due to the use of extremely intense radiations with tunable wavelengths.[231,234,237]

Neutron Diffraction. Neutrons are neutral subatomic particles with finite mass, one-half spin, a specific magnetic moment, and wavelike behavior (wavelengths in the range of 0.5-3 Å).[231,234,238] Due to their magnetic moment, neutrons are diffracted by the spin of the nuclei of the atoms. In other words, the neutron scattering power of an atom depends on its nuclear structure. Based on this feature, the isotopes of an element and even the light atoms can be identified and distinguished. Neutron diffraction is also of interest when the lattice points have very similar atomic numbers, or in order to study magnetic materials.[234,237] Also, because of being uncharged and small neutron-matter interactions (both nuclear and magnetic), neutrons are highly penetrating into the bulk of the specimen.[234] Despite these advantages, neutron diffraction is a very expensive technique, and requires a large amount of sample due to the typical low intensity of the neutron beams (at least 1 mm^3, which usually is not attainable in single crystals).[231,237]

Making intense neutron beams in laboratories is not possible and requires immense facilities. There are two methods to produce neutron beams with enough energy for decent powder diffraction experiments: either using a *nuclear reactor*, or a *spallation source*.[231,234] Even though the two methods are based on *fission* reaction, they are also quite different and yield neutrons with different features. In the nuclear reactor method, a fissile material is specifically

used (such as highly enriched ^{235}U), and a continuous spectrum of radiation and a lot of heat is released (unlike X-ray source where intense characteristic peaks are obtained). Using a crystal monochromator, only a specific wavelength of this continuous spectrum is filtered out, which will result in the loss of a lot of neutron energy, as well as weak analysis radiation.[231,234] The mechanism of neutron production in the second method is based on *spallation*: interaction of highly accelerated and energetic proton beams with a heavy-metal target (such as liquid mercury).[231,234] For instance, the parts of the spallation neutron source (SNS) at the Oak Ridge National Laboratory (ORNL) is as following: acceleration of a stream of negative hydrogen ions in a long path surrounded by superconducting cavities of niobium and gigantic magnets, conversion of this highly accelerated and focused ions to protons by passing them through carbon foils, accumulation of the energetic protons in a ring for 1046 turns to form one intense pulse of proton, hitting the metal target with proton beams 60 times per second to cause spallation, and finally leading the neutron beams to different detectors (beams should be slowed down and cooled to appropriate temperatures using water or liquid hydrogen, as they are sent to different beam lines).[239] In spallation techniques, about 30 neutrons per proton is produced, and a high neutron flux would be available for analysis techniques.[231] This method is also known as *time-of-flight* neutron analysis, where different wavelengths of the entire neutron spectrum are used with a specific angle of diffraction θ (same fundamental Bragg's law, only with variable λ and d-spacing, at a fixed θ).[230]

Employing both neutron and X-ray diffraction techniques (especially synchrotron X-ray method) is the most elucidating approach in structural study: where all of the atoms contribute to neutron diffraction allowing for a comprehensive structural refinement, more accurate unit cell refinement comes with X-ray diffraction experiments because of the significant X-ray scattering power of heavier atoms.[230,231]

Electron Diffraction. Due to the wavelike characteristic of electrons, electron diffraction is another tool for structural studies. Electrons are scattered by both positively charged nuclei and negatively charged electron clouds of the atoms (so the electron scattering factor of the atoms contain both positive and negative terms).[240] The beam-matter interaction is the most in electron diffraction, which leads to the least penetration depth in this method compared to X-rays

with an acceptable level of penetration depth, and neutrons offering the most.[231,241] Another disadvantage of this method is the high scattering efficiency of electrons which causes further interference of the reflected beams with other sets of planes, and results in unreliable intensities and sometimes extra reflections in the diffraction pattern.[231] Lastly, electrons are usually quite damaging to organic-based and biological samples.[237] One valuable feature of electron diffraction is the possibility to obtain unit cell and symmetry information for crystals smaller than a tenth of mm, which is nearly impossible with neutron or X-ray diffraction methods.[231] This diffraction technique mostly comes as an asset of the transmission electron microscopes which will be explained in the forthcoming sections.[231,241,242]

1.5.1.3 Refinement

Structure determination based on powder diffraction has these major phases: data reduction, unit cell refinement (indexing), structure solution, structure refinement, and intensity extraction.[230] Initially, the raw diffraction file should be translated to a list of distinct reflections with certain positions and intensities, this process is called *data reduction*, including general steps such as: fitting and subtraction of the background, data smoothing, peak search, and elimination of the fake peaks.[234] *Indexing* is based on assigning the most appropriate Miller indices to the diffraction peaks, by fitting a calculated pattern to the available experimental data using least-square trial and error methods.[230,234] In simple words, Miller indices are calculated based on an estimated set of unit cell parameters, and a simulated diffraction pattern is generated, then in successive loops the difference between the simulated pattern and the experimental one is minimized in order to yield the most appropriate unit cell parameters. After indexing and unit cell refinement, *structure solution* should be done: selecting the best crystal systems, realizing the *systematic absences* (zero structure factors), identifying the missing or extra peaks based on related models, and finally narrowing down the possible options for the space group.[230,231] Solving the structure is mathematically very complicated, but is fortunately done using automated computer programs taking advantage of different algorithms (the *Patterson methods* working best in case of having few heavy atoms, and the more advanced *direct methods* for phase determination and in case of having atoms with similar atomic numbers).[231,234,238] While Patterson methods use a specific Fourier summation of the structure factor (generating *F-maps*), direct methods are based on statistical probabilities to calculate a number of phases from the

"observed" structure amplitudes, followed by generating sharp electron density maps (*E-maps*) and successively optimizing them.[233] After the structure is resolved, atomic positions are refined as a full pattern refinement.[238] *Structure refinement* used to be only based on the best least-square fit between the calculated structure factors and the experimentally obtained ones (minimum difference). Rietveld established an alternative structure refinement approach where not only the structure factor, but also the peak widths and shapes, lattice parameters, scale factor, and atomic co-ordinates are refined as required. The *Rietveld method* is now the most common structure refinement approach, that most conveniently deals with problems such as overlapping peaks and phase quantification.[230,233,234] If only the crystal system and the possible space group is known, intensity extraction (*Le Bail* extraction) can be employed to generate a set of integrated intensities, which will assist with the structure solution and final refinement.[230] Nearly all the refinement elements are now done as automated calculations, however, enough knowledge of the significant refinement functions is needed in order to perform a successful structure refinement (such as normalized peak profile function, background function, numerical measures of fit, etc.). It should be noted that refining too many variables at once might more likely generates a false minimum with some incorrect structure parameters; so the strategy should be refining a certain variable and fixing it at the refined value, and then progressing by one-by-one refinement of the other parameters as well.[231]

1.5.2 Electron Microscopy

Generation of electrons is typically done either via *thermionic emission* (heated wire or crystal), or *field-effect emission* (single crystals in intense electric field and under ultrahigh vacuum). Electron microscopy provides valuable information about the structure, composition, and morphology of the samples.[243] There are many variations of electron microscopy techniques used in a wide range of magnifications and for various applications: *stationary beam methods* (such as transmission electron microscopy, high-resolution electron microscopy, reflection electron microscopy, electron energy-loss spectroscopy imaging, and Lorentz microscopy), and *scanning beam methods* (like scanning electron microscopy, scanning reflection electron microscopy, and scanning transmission electron microscopy).[240] The resolution ranges for the most common types of electron microscopy are presented in Figure 1-16: high-resolution

electron microscopy (HREM), scanning-transmission electron microscopy (STEM), transmission electron microscopy (TEM), and scanning electron microscopy (SEM).[243,244]

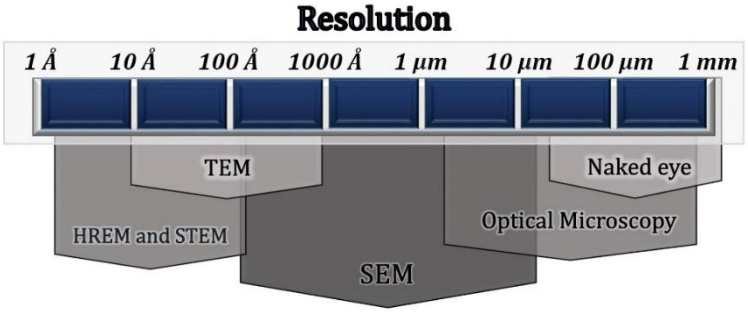

Figure 1-16: Resolution ranges for the most common types of electron microscopy.

If the sample is thin enough and the electron beam is high-voltage (200-400 kV), electrons can transmit through the sample where structural and compositional information in atomic scale is attainable.[240] The working principle is no different from the optical microscopy: illumination of a specimen by electromagnetic radiation which is a monochromatic electron beam in case of TEM and HREM.[241] Image formation in TEM is basically due to diffraction phenomenon, with minimal effect of normal absorption (readily usable in diffraction mode, introduced earlier, as well as imaging mode).[240] HREM is also based on the projection of the bulk structure along the incident electron beam, only it yields the highest resolution (an actual interatomic resolution of ~1Å).[240,245] SEM technique is more of a *mapping* method rather than imaging: low voltage electron beams (up to 30 kV) scan across the sample, and energy loss of the electron due to beam-matter interaction provides morphological and compositional information.[240] Despite the fact that the resolution of SEM is about an order of magnitude less than TEM, it is indeed a very unique technique widely used to investigate the morphology and 3D shape of the specimen.[240] Figure 1-17 illustrate some basic electron-matter interactions, where TEM is more based on elastic scattering (primary electrons transmitting and diffracting with almost no energy

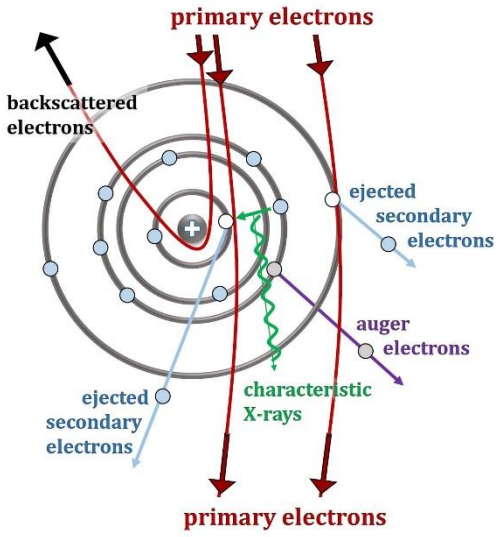

Figure 1-17: Some important interactions of electron beam and the matter.

loss), SEM involves inelastic scattering (mainly based on the secondary electrons).[243,246,247] Energy dispersive spectroscopy (EDS) is an asset on EM instruments which provides compositional contrast based on the characteristic X-rays emitted following the ejection of secondary electrons.[243]

1.5.3 Atomic Force Microscopy (AFM)

Atomic force microscopy (AFM) allows for the surface analysis of micron- and nano-sized structures in atomic resolution.[244,248,249] Chemical and mechanical properties of the surface, as well as some level of crystal lattice structure is possible using this valuable microscopy tool.[248,250] 3D surface topography in AFM is based on the specific tip-surface interactions as the surface of the specimen is being rastered by a delicate probe. AFM can operate in two modes: the *static mode* or *DC* (non-vibrating probe), and the *dynamic mode* or *AC* (vibrating cantilever, amplitude- or frequency-modulated).[244,248] Based on the attraction of the tip to the surface, the AFM imaging modes are classified to *contact* and *non-contact* modes, where respectively repulsive and attractive interactions between the two are manipulated in a controlled manner.[248] The contact mode can be performed in two modes: *constant force* (interpreting the height signal from the piezo-drive) or *constant height* (generating height signal based on the deflection of the cantilever).[248,249] In non-contact mode imaging, the tip is oscillating at its resonant frequency, and the frequency shift due to the interaction force between the tip and the surface is monitored. *Tapping mode* is an intermittent contact imaging mode, where the tip is oscillating at a setpoint amplitude, and the topographic information is obtained by monitoring the change in the amplitude as it periodically encounters the surface. Tapping mode imaging is best when it comes to soft and loosely attached samples (such as nanosheets).[248]

1.5.4 Thermal Analysis

Thermal analysis (TA) is the study of a *specific property* of a sample as a function of *temperature* by heating or cooling it in a controlled manner.[251] Different properties such as temperature difference, heat flow, weight change, dimensions, chemical composition, optical, acoustic, mechanical, electrical, and magnetic properties can be studied in TA methods. Among these various properties, the mass, temperature difference, and heat flow are the most common ones leading to the well-known thermogravimetric analysis (TGA), differential thermal analysis

(DTA), and differential scanning calorimetry (DSC) techniques, respectively.[243,251–254] TGA elucidates the thermal stability of the material and the fraction of its volatile or more temperature-sensitive components, by heating the specimen up to specific temperatures under specific atmospheres. This method is of significant interest for the estimation of the organic loading in organic-inorganic hybrids where the organic substituent can be easily burned off as the inorganic part usually has much higher thermal stability. As some of the thermal events are not accompanied by any weight change (such as melting, crystallization, or glass transition), temperature difference between the sample and the standard pan is also usually monitored (DTA and DSC techniques). The main difference between DTA and DSC is the capability of the instrument to be calibrated in the latter, which allows for assigning a heat flow difference to the temperature difference being measured.[243,251]

1.5.5 Spectroscopy Techniques

Different spectroscopic techniques are based on the absorption or emission of a form of energy by materials under certain conditions. The energy is usually transferred as electromagnetic radiation, and the results (*spectra*) are presented as the intensity of absorption or emission plotted versus the energy (usually expressed as wavelength or frequency of the radiation).[243] Figure 1-18 shows the wavelength and energy of different parts of electromagnetic radiation used in various analysis techniques.[154,243,255] As the wavelength of the radiation increases (higher frequencies and energies), the dimension of the subject of study goes up as well; for instance microwaves can only cause molecular rotations without any actual absorption, while infrared causes vibrational motions of atoms and molecules by absorption/emission, and even higher-frequency waves such as ultraviolet (UV), visible, and X-rays trigger electronic transitions within atoms.[154,243,256]

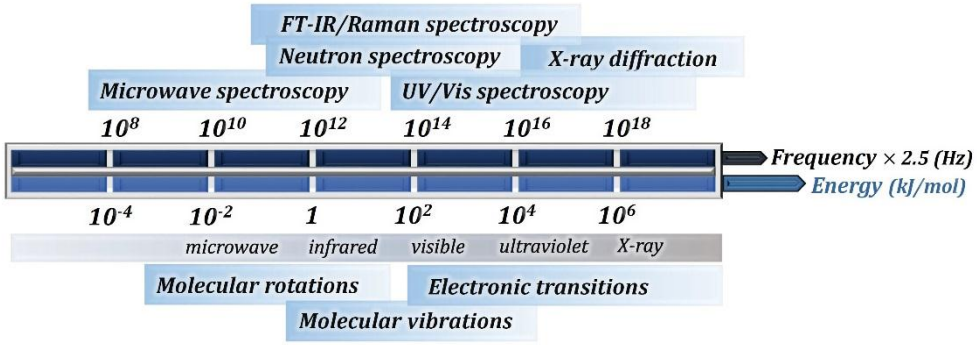

Figure 1-18: Some spectroscopy techniques based on the energy of the electromagnetic radiation involved.

Vibrational Spectroscopy. Radiations with frequencies in the range of the vibration frequency of the atoms in solids and molecules (10^{12}-10^{13} Hz) can excite the vibrational modes to higher energies. In *IR / FT-IR* technique, the absorption of the electric vector of the incident radiation by an oscillating molecular dipole changes its frequency, and the resulting spectrum is obtained by plotting the intensity of the radiation either absorbed or transmitted versus the wavenumber or frequency of the radiation. Compared to IR, the radiation source in *Raman* is of much higher energy (a laser with a fixed wavelength), and the analysis is based on inelastic scattering of the incident photon, followed by a change in its frequency. The resulting Raman spectrum provides peaks whose frequencies show shifts from that of the incident beam, where the shift is equivalent to the frequency of the molecular vibration (it gains energy by absorbing a phonon, or loses energy by emitting one, respectively called *anti-Stokes* or *Stokes shifted*). It should be noted that while polar bonds are usually detected via their specific absorption frequency (IR), the polarizable bonds do inelastic scattering in a certain wavenumber (Raman).[243,256–262] If instead of light, neutron beam is used for vibrational spectroscopy, the *inelastic neutron scattering* (*INS*) will help probing the dynamics of atoms and molecules.[255,260] INS magnetic scattering is not subject to optical selection rules (all vibrations are active), it provides a wide spectral range (covering wavenumbers less than 400 cm^{-1} as well), it is sensitive to hydrogen atom vibrations, it has the highest penetration depth compared to photons, and it can also be accurately modeled.[255] A more comprehensive understanding of the structure is attainable by using all three IR, Raman, and INS vibrational spectroscopy techniques together.

Ultraviolet-Visible Spectroscopy (UV-Vis). This method of spectroscopy uses higher-energy radiations (near-IR through the visible to the UV range; 10^2-10^3 kJ/mol) to allow for the investigation of electronic transitions in materials. The transition of electrons can happen in different ways: excitation of an electron from one orbital of an atom to higher energy orbitals of the same atom (*exciton band*), promotion of the electron of an atom to a higher energy orbital of an adjacent atom (*charge-transfer spectra*), excitation of an electron from a localized orbital to a delocalized energy level (conduction band), and most popular type is the study of the promotion of the electron from the valence band to the conduction band (band gap measurement).[243] The study of absorbance / transmittance in different liquids, or reflectance from solid samples and films (*diffuse-reflectance* UV-Vis spectroscopy) are common practical ways of this spectroscopy technique.[263–268]

Fluorescence Spectroscopy (FL). *Luminescence* is defined as the absorption of UV or visible radiation followed by *emission* of energy in higher wavelength in order for the excited analyte to go back to its initial state (resulting spectra are supplementary to what is obtained from UV-Vis spectroscopy). Spontaneous emission is called *Fluorescence* (spin-allowed emission with an abrupt decay after the removal of the excitation source, 10^{-5}–10^{-8}*s*), while *phosphorescence* refers to a longer time lag (10^{-4} –10^{4} *s*) between the absorption and the following emission due to a change in spin quantum number (spin-forbidden emission).[256,260,266,269,270] *Photoluminescence* term is the same as luminescence, however, it is more common among chemists investigating the absorption / emission of light by semiconductors and nanostructures.[257,268]

1.5.6 Mass Spectrometry

In this analytical technique, gaseous ions are produced from a sample, accelerated in an electric and/or magnetic field, and separated based on their charge-to-mass ratios (*m/Z*). In other words, mass spectrum shows the proportional abundance of an atom, molecule, or molecule fragment of a bigger molecular structure, according to its specific charge-to-mass ratio. Upon variation of the magnetic field, the spectrum of masses is obtained based on the simple fact that heavier ions with less charge are least deflected while reaching the detector. Based on this simple description, important components of any mass spectrometer are an ion source, mass separator,

and detector. Molecular mass, elemental composition, and isotopic distribution of a compound, as well as the sequences of the macromolecules such as DNA can be determined with high accuracies using mass spectrometry. It is notable that the combination of this technique with chromatography methods provide a very powerful tool to analyze mixtures (for instance identifying the toxin residues and contaminants in food products).[271,272]

1.5.7 Superconducting Quantum Interference Device (SQUID)

A superconducting quantum interference device (SQUID) is a very sensitive detector of minute magnetic fields (magnetic flux).[273,274] A SQUID can detect a change of electromagnetic energy 100 billion times weaker than the energy that moves the needle of a compass.[275] Operation of SQUID is based on two physical phenomena: *flux quantization* and *Josephson tunneling*.[274–276] Flux quantization is based on the fact that the magnetic flux of a superconducting loop (or a hole in a bulk of superconductor) is quantized ($h/2e$; h = Planck's constant and e = electron charge). Josephson current is the tunneling of current between two superconducting materials separated by a thin insulating or non-superconductive barrier (this sandwich-like setup is called the *Josephson junction or JJ*).[273–275,277,278] *DC-SQUIDs* consist of two parallel JJ where the quantum interference due to electron tunneling depends on the strength of the magnetic field within a loop. *RF-(or AC-) SQUIDs* includes only one JJ mounted on a superconducting ring, and the magnetic flux is measured based on the voltage changes occurring due to the interactions between the ring and an external circuit with oscillating current. DC-SQUIDS are more complicated and expensive, but much more sensitive.[275,279] Other than identification of magnetic behavior of materials in research laboratories, SQUIDs are also used to study human brain anomalies and some other medical applications.[273]

1.6– Outline of the Current Research

The focus of this dissertation is on the topochemical manipulation of Dion-Jacobson and Ruddlesden-Popper type perovskites via rapid microwave-assisted reactions. The research started back in 2013 in order to produce organic-inorganic hybrids based on the perovskite hosts using the common solvothermal reactions available at the time. Employing microwaves in the organic-modification steps late 2014, allowed us to decrease the typical reaction durations significantly

(from days to hours), and be able to screen various chemistries in the time window of this work. *Chapter Two* provides the results of microwave-assisted grafting and intercalation reactions on a number of Dion-Jacobson and Ruddlesden-Popper hosts, using simple n-alkyl alcohols / amines with various lengths, and confirms the high quality and yield of these reactions. *Chapter Three* includes the results of some novel characterization techniques (neutron diffraction and neutron spectroscopy) done on several organic-inorganic hybrids, made in large quantities and with high qualities via facile microwave approaches, for a number of tests ran using SNS facilities at the Oak Ridge National Laboratory. *Chapter Four* highlights microwave-assisted exfoliation of DJ perovskites and following surface modification reactions, which efficiently yields surface-tailored nanosheets with various saturated and unsaturated surface groups. In *Chapter Five*, the trials to perform polymerization on monomer-grafted nanosheets are reported. The impact of the elemental composition of various double- and triple-layered DJ perovskites on the optical properties of the bulk layered perovskite and exfoliated nanosheets is investigated in *Chapter Six*. After concluding the highlights of this dissertation in *Chapter Seven*, five appendices are provided at the end to summarize a few side projects of the researcher.

1.7- References

(1) Stein, A.; Keller, S. W.; Mallouk, T. E. Turning down the Heat: Design and Mechanism in Solid-State Synthesis. *Science* **1993**, *259* (5101), 1558–1564.

(2) Lehn, J.-M.; Alberti, G.; Bein, T. Chapter 1: Layered Solids and Their Intercalation Chemistry (By Giulio Alberti and Umberto Costantino). In *Comprehensive supramolecular chemistry volume 7, Solid-state supramolecular chemistry: two-and three-dimensional inorganic networks*; Pergamon: Oxford; New York; Tokyo, 1996; pp 1–23.

(3) Arizaga, G. G. C.; Satyanarayana, K. G.; Wypych, F. Layered Hydroxide Salts: Synthesis, Properties and Potential Applications. *Solid State Ion.* **2007**, *178* (15–18), 1143–1162.

(4) Gupta, A.; Sakthivel, T.; Seal, S. Recent Development in 2D Materials beyond Graphene. *Prog. Mater. Sci.* **2015**, *73*, 44–126.

(5) Marder, M. P. Three-Dimensional Lattices. In *Condensed Matter Physics*; John Wiley & Sons, Inc., 2010; pp 17–41.

(6) Solin, S. A. Novel Properties of Intercalated Layered Solids: From Graphite to Sheet Silicates. *J. Mol. Catal.* **1984**, *27* (1), 293–303.

(7) Yao, Y. Controlled Attachment of Nanoparticles to Layered Oxides, University of New Orleans, 2012.

(8) Pakdel, A.; Zhi, C.; Bando, Y.; Golberg, D. Low-Dimensional Boron Nitride Nanomaterials. *Mater. Today* **2012**, *15* (6), 256–265.

(9) Golberg, D.; Bando, Y.; Huang, Y.; Terao, T.; Mitome, M.; Tang, C.; Zhi, C. Boron Nitride Nanotubes and Nanosheets. *ACS Nano* **2010**, *4* (6), 2979–2993.

(10) Wang, X.; Zhi, C.; Weng, Q.; Bando, Y.; Golberg, D. Boron Nitride Nanosheets: Novel Syntheses and Applications in Polymeric Composites. *J. Phys. Conf. Ser.* **2013**, *471* (1), 012003.

(11) Coleman, J. N.; Lotya, M.; O'Neill, A.; Bergin, S. D.; King, P. J.; Khan, U.; Young, K.; Gaucher, A.; De, S.; Smith, R. J.; et al. Two-Dimensional Nanosheets Produced by Liquid Exfoliation of Layered Materials. *Science* **2011**, *331* (6017), 568–571.

(12) Nicolosi, V.; Chhowalla, M.; Kanatzidis, M. G.; Strano, M. S.; Coleman, J. N. Liquid Exfoliation of Layered Materials. *Science* **2013**, *340* (6139), 1226419–1226419.

(13) Auerbach, S. M.; Carrado, K. A.; Dutta, P. K. *Handbook of Layered Materials*; Marcel Dekker, Inc.: New York, NY, U.S.A., 2004.

(14) Wang, Q.; O'Hare, D. Recent Advances in the Synthesis and Application of Layered Double Hydroxide (LDH) Nanosheets. *Chem. Rev.* **2012**, *112* (7), 4124–4155.

(15) Nalawade, P.; Aware, B.; Kadam, V. J.; Hirlekar, R. S. Layered Double Hydroxides: A Review. *J Sci Ind Res* **2009**, *68* (267272), 4.

(16) Themed Issue: Layered Materials: Structure and Properties. *J. Mater. Chem.* **2009**, *19* (17), 2453–2456.

(17) Tahara, S. Preparation of Inorganic-Organic Hybrids via Intercalation and Grafting Reactions of Protonated Forms of Ion-Exchangeable Layered Perovskites, Waseda University, 2007.

(18) Brager, A. X-Ray Examination of the Structure of Boron Nitride. *Acta Physicochim URSS* **1937**, *7*, 699–706.

(19) Zigan, F.; Rothbauer, R. Neutronenbeugungsmessungen Am Brucit. *Neues Jahrb. Für Mineral. Monatshefte* **1967**, *1967*, 137–143.

(20) Odom, I. E. Smectite Clay Minerals: Properties and Uses. *Philos. Trans. R. Soc. Lond. Math. Phys. Eng. Sci.* **1984**, *311* (1517), 391–409.

(21) Gournis, D.; Lappas, A.; Karakassides, M. A.; Többens, D.; Moukarika, A. A Neutron Diffraction Study of Alkali Cation Migration in Montmorillonites. *Phys. Chem. Miner.* **2007**, *35* (1), 49–58.

(22) Nair, S. P. N.; Murugavel, P. 4.03 - Oxides: Their Properties and Uses A2 - Reedijk, Jan. In *Comprehensive Inorganic Chemistry II (Second Edition)*; Poeppelmeier, K., Ed.; Elsevier: Amsterdam, 2013; pp 47–72.

(23) Peña, M. A.; Fierro, J. L. G. Chemical Structures and Performance of Perovskite Oxides. *Chem. Rev.* **2001**, *101* (7), 1981–2018.

(24) Schaak, R. E.; Mallouk, T. E. Perovskites by Design: A Toolbox of Solid-State Reactions. *Chem. Mater.* **2002**, *14* (4), 1455–1471.

(25) Al-Shakarchi, E. K.; Mahmood, N. B. Three Techniques Used to Produce BaTiO3 Fine Powder. *J. Mod. Phys.* **2011**, *02* (11), 1420–1428.

(26) Johnsson, M.; Lemmens, P. Crystallography and Chemistry of Perovskites. *ArXivcond-Mat0506606* **2005**.

(27) Sanjaya Ranmohotti, K. G.; Josepha, E.; Choi, J.; Zhang, J.; Wiley, J. B. Topochemical Manipulation of Perovskites: Low-Temperature Reaction Strategies for Directing Structure and Properties. *Adv. Mater.* **2011**, *23* (4), 442–460.

(28) Lichtenberg, F.; Herrnberger, A.; Wiedenmann, K. Synthesis, Structural, Magnetic and Transport Properties of Layered Perovskite-Related Titanates, Niobates and Tantalates of the Type $A_nB_nO_{3n+2}$, $A'A_{k-1}B_kO_{3k+1}$ and $A_mB_{m-1}O_{3m}$. *Prog. Solid State Chem.* **2008**, *36* (4), 253–387.

(29) Kendall, K. R.; Navas, C.; Thomas, J. K.; zur Loye, H.-C. Recent Developments in Oxide Ion Conductors: Aurivillius Phases. *Chem. Mater.* **1996**, *8* (3), 642–649.

(30) Liang, Z.-H.; Tang, K.-B.; Chen, Q.-W.; Zheng, H.-G. $RbCa_2Nb_3O_{10}$ from X-Ray Powder Data. *Acta Crystallogr. Sect. E* **2009**, *E65*, i44.

(31) Liang, Z.; Tang, K.; Shao, Q.; Li, G.; Zeng, S.; Zheng, H. Synthesis, Crystal Structure, and Photocatalytic Activity of a New Two-Layer Ruddlesden–Popper Phase, $Li_2CaTa_2O_7$. *J. Solid State Chem.* **2008**, *181* (4), 964–970.

(32) West, A. R. Chapter 4: Synthesis, Processing and Fabrication Methods. In *Solid State Chemistry and its Applications*; John Wiley & Sons, Ltd: United Kingdom, 2014; pp 187–228.

(33) Smart, L. E.; Moore, E. A. *Solid State Chemistry: An Introduction*, Third.; Taylor & Francis: Boca Raton, FL, 2005.

(34) Galasso, F. S. Chapter 10 - Preparation of Perovskite-Type Oxides. In *Structure, Properties and Preparation of Perovskite-Type Compounds*; International Series of Monographs in Solid State Physics; Pergamon: New York, 1969; pp 159–181.

(35) Tejuca, L. G.; Fierro, J. L. G. *Properties and Applications of Perovskite-Type Oxides*; CRC Press, 2000.

(36) Livage, J. Chimie Douce: From Shake-and-Bake Processing to Wet Chemistry. *New J. Chem.* **2001**, *25* (1), 1–1.

(37) High-Pressure Synthesis (by J. B. Goodenough, J. A. Kafalas, and J. M. Longo). In *Preparative Methods in Solid State Chemistry*; Hagenmuller, P., Ed.; Academic Press, Inc.: New York, NY, 1972; pp 2–65.

(38) Takayama-Muromachi, E. High-Pressure Synthesis of Homologous Series of High Critical Temperature (Tc) Superconductors. *Chem. Mater.* **1998**, *10* (10), 2686–2698.

(39) McMillan, P. F. High Pressure Synthesis of Solids. *Curr. Opin. Solid State Mater. Sci.* **1999**, *4* (2), 171–178.

(40) Josepha, E. Topochemical Manipulation of Layered Perovskites, 2011.

(41) Chapter 5: Molten Salt Synthesis of Ceramic Powders (by Toshio Kimura). In *Advances in Ceramics - Synthesis and Characterization, Processing and Specific Applications*; Sikalidis, C., Ed.; inTech, 2011.

(42) Montasserasadi, D. New Dion-Jacobson and Ruddlesden- Popper Layered Perovskites Prepared by Topochemical Methods, 2015.

(43) Arney, D.; Maggard, P. A. Effect of Platelet-Shaped Surfaces and Silver-Cation Exchange on the Photocatalytic Hydrogen Production of $RbLaNb_2O_7$. *ACS Catal.* **2012**, *2* (8), 1711–1717.

(44) Porob, D. G.; Maggard, P. A. A Rapid Flux-Assisted Synthetic Approach Towards the Bandgap Engineering of Layered Perovskites. *Chem. Mater.* **2007**, *19* (5), 970–972.

(45) Teshima, K.; Niina, Y.; Yubuta, K.; Suzuki, T.; Ishizawa, N.; Shishido, T.; Oishi, S. Environmentally Friendly Growth of Layered $K_4Nb_6O_{17}$ Crystals from a KCl Flux. *Eur. J. Inorg. Chem.* **2007**, *2007* (29), 4687–4692.

(46) Roy, R. Accelerating the Kinetics of Low-Temperature Inorganic Syntheses. *J. Solid State Chem.* **1994**, *111* (1), 11–17.

(47) Modern Methods of Growing Single Crystals of High-Melting-Point Oxides (by A. M. Anthony and R. Collongues). In *Preparative Methods in Solid State Chemistry*; Hagenmuller, P., Ed.; Academic Press, Inc.: New York, NY, 1972; pp 185–208.

(48) Moreira, M. L.; Paris, E. C.; do Nascimento, G. S.; Longo, V. M.; Sambrano, J. R.; Mastelaro, V. R.; Bernardi, M. I. B.; Andrés, J.; Varela, J. A.; Longo, E. Structural and Optical Properties of $CaTiO_3$ Perovskite-Based Materials Obtained by Microwave-Assisted Hydrothermal Synthesis: An Experimental and Theoretical Insight. *Acta Mater.* **2009**, *57* (17), 5174–5185.

(49) Huang, Y.; Wei, Y.; Fan, L.; Huang, M.; Lin, J.; Wu, J. Photocatalytic Activities of $HLaNb_2O_7$ Prepared by Polymerized Complex Method. *Int. J. Hydrog. Energy* **2009**, *34* (13), 5318–5325.

(50) Xiong, G.; Zhi, Z. L.; Yang, X.; Lu, L.; Wang, X. Characterization of Perovskite-Type $LaCoO_3$ Nanocrystals Prepared by a Stearic Acid Sol--Gel Process. *J. Mater. Sci. Lett.* *16* (13), 1064–1068.

(51) Fu, H.; Zhang, L.; Yao, W.; Zhu, Y. Photocatalytic Properties of Nanosized Bi_2WO_6 Catalysts Synthesized via a Hydrothermal Process. *Appl. Catal. B Environ.* **2006**, *66* (1–2), 100–110.

(52) Jeong, H.; Kim, T.; Kim, D.; Kim, K. Hydrogen Production by the Photocatalytic Overall Water Splitting on: Effect of Preparation Method. *Int. J. Hydrog. Energy* **2006**, *31* (9), 1142–1146.

(53) Galasso, F. S. Chapters 4-9 (Conductivity, Ferroelectricity, Phase Transitions, Ferromagnetism, Optical Properties, and Other Properties). In *Structure, Properties and Preparation of Perovskite-Type Compounds*; International Series of Monographs in Solid State Physics; Pergamon: New York, 1969; pp 60–78.

(54) Johnsson, M.; Lemmens, P. Perovskites and Thin Films—crystallography and Chemistry. *J. Phys. Condens. Matter* **2008**, *20* (26), 264001.

(55) Dimos, D.; Mueller, C. H. Perovskite Thin Films for High-Frequency Capacitor Applications. *Annu. Rev. Mater. Sci.* **1998**, *28* (1), 397–419.

(56) Galasso, F. S. Chapters 5 (Ferroelectricity). In *Structure, Properties and Preparation of Perovskite-Type Compounds*; International Series of Monographs in Solid State Physics; Pergamon: New York, 1969; pp 60–78.

(57) Benedek, N. A.; Rondinelli, J. M.; Djani, H.; Ghosez, P.; Lightfoot, P. Understanding Ferroelectricity in Layered Perovskites: New Ideas and Insights from Theory and Experiments. *Dalton Trans* **2015**, *44* (23), 10543–10558.

(58) Ihringer, J.; Maichle, J. K.; Prandl, W.; Hewat, A. W.; Wroblewski, T. Crystal Structure of the Ceramic Superconductor $BaPb_{0.75}Bi_{0.25}O_3$. *Z. Für Phys. B Condens. Matter 82* (2), 171–176.

(59) Bednorz, J. G.; Müller, K. A. Perovskite-Type oxides- The New Approach to High-Tc Superconductivity. *Rev. Mod. Phys.* **1988**, *60* (3), 585–600.

(60) Teranishi, T.; Takezawa, S.; Toda, K.; Ishikawa, H.; Sato, K.; Uematsu, K.; Sato, M. Superconductivity of Layered Perovskite Synthesized by Soft Chemistry. *Key Eng. Mater.* **2007**, *350*, 163–166.

(61) Takano, Y.; Takayanagi, S.; Ogawa, S.; Yamadaya, T.; Môri, N. Superconducting Properties of Layered Perovskite KCa_2Nb_3O10 and $KLaNb_2O_7$. *Solid State Commun.* **1997**, *103* (4), 215–217.

(62) Nagai, I.; Abe, Y.; Kato, M.; Koike, Y.; Kakihana, M. Electrochemical Intercalation of Lithium in Layered Niobates $AB_2Nb_3O_{10}$ (A=K, Rb, Cs; B=Ca, Sr) and Their Superconductivity. *Phys. C Supercond.* **2001**, *357–360, Part 1*, 393–396.

(63) Kato, M.; Inoue, A.; Nagai, I.; Kakihana, M.; Sleight, A. W.; Koike, Y. Superconductivity in the Electrochemically Li-Intercalated Niobates with the Layered Perovskite Structure. *Phys. C Supercond.* **2003**, *388–389*, 445–446.

(64) Jonker, G. H. Magnetic Compounds with Perovskite Structure IV Conducting and Non-Conducting Compounds. *Physica* **1956**, *22* (6), 707–722.

(65) O'Handley, R. C. Chapter 15: Electronic Transport in Magnetic Materials. In *Modern magnetic materials: principles and applications*; John Wiley & Sons, Inc.: Canada, 2000; pp 609–614.

(66) Galasso, F. S. Chapters 7 (Ferromagnetism). In *Structure, Properties and Preparation of Perovskite-Type Compounds*; International Series of Monographs in Solid State Physics; Pergamon: New York, 1969; pp 60–78.

(67) Kageyama, H.; Viciu, L.; Caruntu, G.; Ueda, Y.; Wiley, J. B. New Magnetic Materials Obtained by Ion-Exchange Reactions from Non-Magnetic Layered Perovskites. *J. Phys. Condens. Matter* **2004**, *16* (11), S585.

(68) Galasso, F. S. Chapters 8 (Optical Properties). In *Structure, Properties and Preparation of Perovskite-Type Compounds*; International Series of Monographs in Solid State Physics; Pergamon: New York, 1969; pp 60–78.

(69) Iwahara, H.; Uchida, H.; Ono, K.; Ogaki, K. Proton Conduction in Sintered Oxides Based on BaCeO3. *J. Electrochem. Soc.* **1988**, *135* (2), 529–533.

(70) Toda, K.; Kameo, Y.; Kurita, S.; Sato, M. Crystal Structure Determination and Ionic Conductivity of Layered Perovskite Compounds $NaLnTiO_4$ (Ln = Rare Earth). *J. Alloys Compd.* **1996**, *234* (1), 19–25.

(71) Tambelli, C. E.; Donoso, J. P.; Magon, C. J.; Ângelo, A. C. D.; Florentino, A. O.; Saeki, M. J. NMR and Conductivity Study of the Protonic Conductor $HPb_2Nb_3O_{10}\cdot nH_2O$. *Solid State Ion.* **2000**, *136–137*, 243–247.

(72) Tani, S.; Komori, Y.; Hayashi, S.; Sugahara, Y. Local Environments and Dynamics of Hydrogen Atoms in Protonated Forms of Ion-Exchangeable Layered Perovskites Estimated by Solid-State 1H NMR. *J. Solid State Chem.* **2006**, *179* (11), 3357–3364.

(73) Kudo, M.; Tsuzuki, S.; Katsumata, K.; Yasumori, A.; Sugahara, Y. Effects of Selective Leaching of Bismuth Oxide Sheets in Triple-Layered Aurivillius Phases on Their Photocatalytic Activities. *Chem. Phys. Lett.* **2004**, *393* (1–3), 12–16.

(74) Domen, K.; Kondo, J. N.; Hara, M.; Takata, T. Photo-and Mechano-Catalytic Overall Water Splitting Reactions to Form Hydrogen and Oxygen on Heterogeneous Catalysts. *Bull. Chem. Soc. Jpn.* **2000**, *73* (6), 1307–1331.

(75) Takata, T.; Furumi, Y.; Shinohara, K.; Tanaka, A.; Hara, M.; Kondo, J. N.; Domen, K. Photocatalytic Decomposition of Water on Spontaneously Hydrated Layered Perovskites. *Chem. Mater.* **1997**, *9* (5), 1063–1064.

(76) Machida, M.; Mitsuyama, T.; Ikeue, K.; Matsushima, S.; Arai, M. Photocatalytic Property and Electronic Structure of Triple-Layered Perovskite Tantalates, $MCa_2Ta_3O_{10}$ (M = Cs, Na, H, and $C_6H_{13}NH_3$). *J. Phys. Chem. B* **2005**, *109* (16), 7801–7806.

(77) Osterloh, F. E. Inorganic Materials as Catalysts for Photochemical Splitting of Water. *Chem. Mater.* **2008**, *20* (1), 35–54.

(78) Spinicci, R.; Tofanari, A.; Delmastro, A.; Mazza, D.; Ronchetti, S. Catalytic Properties of Stoichiometric and Non-Stoichiometric LaFeO3 Perovskite for Total Oxidation of Methane. *Mater. Chem. Phys.* **2002**, *76* (1), 20–25.

(79) Galasso, F. S. Chapters 9 (Other Properties). In *Structure, Properties and Preparation of Perovskite-Type Compounds*; International Series of Monographs in Solid State Physics; Pergamon: New York, 1969; pp 60–78.

(80) Mitzi, D. B. Templating and Structural Engineering in Organic–inorganic Perovskites. *J. Chem. Soc. Dalton Trans.* **2001**, No. 1, 1–12.

(81) Mitzi, D. B.; Chondroudis, K.; Kagan, C. R. Organic-Inorganic Electronics. *IBM J. Res. Dev.* **2001**, *45* (1), 29–45.

(82) Mitzi, D. B.; Dimitrakopoulos, C. D.; Kosbar, L. L. Structurally Tailored Organic−Inorganic Perovskites: Optical Properties and Solution-Processed Channel Materials for Thin-Film Transistors. *Chem. Mater.* **2001**, *13* (10), 3728–3740.

(83) Hodes, G. Perovskite-Based Solar Cells. *Science* **2013**, *342* (6156), 317–318.

(84) Lee, M. M.; Teuscher, J.; Miyasaka, T.; Murakami, T. N.; Snaith, H. J. Efficient Hybrid Solar Cells Based on Meso-Superstructured Organometal Halide Perovskites. *Science* **2012**, *338* (6107), 643–647.

(85) Conings, B.; Baeten, L.; De Dobbelaere, C.; D'Haen, J.; Manca, J.; Boyen, H.-G. Perovskite-Based Hybrid Solar Cells Exceeding 10% Efficiency with High Reproducibility Using a Thin Film Sandwich Approach. *Adv. Mater.* **2014**, *26* (13), 2041–2046.

(86) Zhang, W.; Saliba, M.; Stranks, S. D.; Sun, Y.; Shi, X.; Wiesner, U.; Snaith, H. J. Enhancement of Perovskite-Based Solar Cells Employing Core–Shell Metal Nanoparticles. *Nano Lett.* **2013**, *13* (9), 4505–4510.

(87) Chiarella, F. Growth and Characterization of Films of Perovskite Based Organic-Inorganic Hybrid Materials for Electronics. Tesi di dottorato, Università degli Studi di Napoli Federico II, 2006.

(88) Wang, Y.; Wang, C.; Wang, L.; Hao, Q.; zhu, X.; Chen, X.; Tang, K. Preparation of Interlayer Surface Tailored Protonated Double-Layered Perovskite $H_2CaTa_2O_7$ with N-Alcohols, and Their Photocatalytic Activity. *RSC Adv* **2014**, *4* (8), 4047–4054.

(89) Lalena, J. N.; Cushing, B. L.; Falster, A. U.; Simmons, William B.; Seip, C. T.; Carpenter, E. E.; O'Connor, C. J.; Wiley, J. B. A Multistep Topotactic Route to the New

Mixed-Valence Titanate, $Na_{2-x+y}Ca_{x/2}La_2Ti_3O_{10}$. Electron Localization Effects in a Triple-Layered Perovskite. *Inorg. Chem.* **1998**, *37* (18), 4484–4485.

(90) Neiner, D.; Sweany, R. L.; Golub, V.; Wiley, J. B. Structure and Properties of Mixed Valence Titanates, $(Li_xVO)La_2Ti_3O_{10}$. *J. Mater. Chem.* **2006**, *16* (2), 186–191.

(91) Kobayashi, Y.; Tian, M.; Eguchi, M.; Mallouk, T. E. Ion-Exchangeable, Electronically Conducting Layered Perovskite Oxyfluorides. *J. Am. Chem. Soc.* **2009**, *131* (28), 9849–9855.

(92) McIntyre, R. A.; Falster, A. U.; Li, S.; Simmons, W. B.; O'Connor, C. J.; Wiley, J. B. Opening a Perovskite to Valence Manipulation: Two-Step Topotactic Route to a New Mixed-Valence Titanate, Na_{1-X+Y} $Ca_{x/2}LaTiO_4$. *J. Am. Chem. Soc.* **1998**, *120* (1), 217–218.

(93) Montasserasadi, D.; Mohanty, D.; Huq, A.; Heroux, L.; Payzant, E. A.; Wiley, J. B. Topochemical Synthesis of Alkali-Metal Hydroxide Layers within Double- and Triple-Layered Perovskites. *Inorg. Chem.* **2014**, *53* (3), 1773–1778.

(94) Kodenkandath, T. A.; Kumbhar, A. S.; Zhou, W. L.; Wiley, J. B. Construction of Copper Halide Networks within Layered Perovskites. Syntheses and Characterization of New Low-Temperature Copper Oxyhalides. *Inorg. Chem.* **2001**, *40* (4), 710–714.

(95) Zhang, X. Building Metal-Anion Layers within a Preovskite Host, 2006.

(96) Sugahara, Y. Chemical Processes Employing Inorganic Layered Compounds for Inorganic and Inorganic–organic Hybrid Materials. *J. Ceram. Soc. Jpn.* **2014**, *122* (1427), 523–529.

(97) Takahashi, S.; Nakato, T.; Hayashi, S.; Sugahara, Y.; Kuroda, K. Formation of Methoxy-Modified Interlayer Surface via the Reaction between Methanol and Layered Perovskite $HLaNb_2O_7 \cdot xH_2O$. *Inorg. Chem.* **1995**, *34* (20), 5065–5069.

(98) Suzuki, H.; Notsu, K.; Takeda, Y.; Sugimoto, W.; Sugahara, Y. Reactions of Alkoxyl Derivatives of a Layered Perovskite with Alcohols: Substitution Reactions on the Interlayer Surface of a Layered Perovskite. *Chem. Mater.* **2003**, *15* (3), 636–641.

(99) Tahara, S.; Sugahara, Y. Interlayer Surface Modification of the Protonated Triple-Layered Perovskite $HCa_2Nb_3O_{10} \cdot xH_2O$ with *n* -Alcohols. *Langmuir* **2003**, *19* (22), 9473–9478.

(100) Tahara, S.; Ichikawa, T.; Kajiwara, G.; Sugahara, Y. Reactivity of the Ruddlesden−Popper Phase $H_2La_2Ti_3O_{10}$ with Organic Compounds: Intercalation and Grafting Reactions. *Chem. Mater.* **2007**, *19* (9), 2352–2358.

(101) Kitada, A.; Tsujimoto, Y.; Yamamoto, T.; Kobayashi, Y.; Narumi, Y.; Kindo, K.; Aczel, A. A.; Luke, G. M.; Uemura, Y. J.; Kiuchi, Y.; et al. Quadruple-Layered Perovskite $(CuCl)Ca_2NaNb_4O_{13}$. *J. Solid State Chem.* **2012**, *185*, 10–17.

(102) Gopalakrishnan, J. Chimie Douce Approaches to the Synthesis of Metastable Oxide Materials. *Chem. Mater.* **1995**, *7* (7), 1265–1275.

(103) Bensaude-Vincent, B.; Arribart, H.; Bouligand, Y.; Sanchez, C. Chemists and the School of Nature. *New J. Chem.* **2002**, *26* (1), 1–5.

(104) Jolivet, J.-P.; Henry, M.; Livage, J. *Metal Oxide Chemistry and Synthesis: From Solution to Solid State*; Wiley-Blackwell, 2000.

(105) Lind, C.; Gates, S. D.; Pedoussaut, N. M.; Baiz, T. I. Novel Materials through Non-Hydrolytic Sol-Gel Processing: Negative Thermal Expansion Oxides and Beyond. *Materials* **2010**, *3* (4), 2567–2587.

(106) Sanchez, C.; Rozes, L.; Ribot, F.; Laberty-Robert, C.; Grosso, D.; Sassoye, C.; Boissiere, C.; Nicole, L. "Chimie Douce": A Land of Opportunities for the Designed Construction of Functional Inorganic and Hybrid Organic-Inorganic Nanomaterials. *Comptes Rendus Chim.* **2010**, *13* (1–2), 3–39.

(107) Gopalakrishnan, J.; Bhat, V.; Raveau, B. $AILaNb_2O_7$: A New Series of Layered Perovskites Exhibiting Ion Exchange and Intercalation Behaviour. *Mater. Res. Bull.* **1987**, *22* (3), 413–417.

(108) Hyeon, K.-A.; Byeon, S.-H. Synthesis and Structure of New Layered Oxides, $M^{II}La_2Ti_3O_{10}$ (M = Co, Cu, and Zn). *Chem. Mater.* **1999**, *11* (2), 352–357.

(109) Viciu, L.; Liziard, N.; Golub, V.; Kodenkandath, T. A.; Wiley, J. B. Transition-Metal Dion-Jacobson Layered Perovskites, $M_{0.5}LaNb_2O_7$. *Mater. Res. Bull.* **2004**, *39* (14–15), 2147–2154.

(110) Galven, C.; Fourquet, J.-L.; Suard, E.; Crosnier-Lopez, M.-P.; Le Berre, F. Structural Characterization of a New Acentric Ruddlesden–Popper Layered Perovskite Compound: $LiHSrTa_2O_7$. *Dalton Trans.* **2010**, *39* (13), 3212.

(111) Armstrong, A. R.; Anderson, P. A. Synthesis and Structure of a New Layered Niobium Blue Bronze: Rb2LaNb2O7. *Inorg. Chem.* **1994**, *33* (19), 4366–4369.

(112) Li, R. K.; Greaves, C. Double-Layered Ruthenate Sr3Ru2O7F2 Formed by Fluorine Insertion into Sr3Ru2O7. *Phys. Rev. B* **2000**, *62* (6), 3811–3815.

(113) Hyett, G.; Barrier, N.; Clarke, S. J.; Hadermann, J. Topotactic Oxidative and Reductive Control of the Structures and Properties of Layered Manganese Oxychalcogenides. *J. Am. Chem. Soc.* **2007**, *129* (36), 11192–11201.

(114) Gopalakrishnan, J.; Bhat, V. $A_2Ln_2Ti_3O_{10}$ (A = Potassium or Rubidium; Ln = Lanthanum or Rare Earth): A New Series of Layered Perovskites Exhibiting Ion Exchange. *Inorg. Chem.* **1987**, *26* (26), 4299–4301.

(115) Uma, S.; Gopalakrishnan, J. Synthesis of Anion-Deficient Layered Perovskites, $ACa_2Nb_{3-x}M_xO_{10-X}$ (A = Rb, Cs; M = Al, Fe), Exhibiting Ion-Exchange and Intercalation. Evidence for the Formation of Layered Brownmillerites, $ACa_2Nb_2AlO_9$ (A = Cs, H). *Chem. Mater.* **1994**, *6* (7), 907–912.

(116) Clearfield, A. Intercalation Chemistry of Selected Layered Oxides and Phosphates. In *Progress in Intercalation Research*; Müller-Warmuth, W., Schöllhorn, R., Eds.; Physics and Chemistry of Materials with Low-Dimensional Structures; Springer Netherlands, 1994; pp 223–271.

(117) Yoshioka, S.; Takeda, Y.; Uchimaru, Y.; Sugahara, Y. Hydrosilylation in the 2D Interlayer Space between Inorganic Layers: Reaction between Immobilized C=C Groups on the Interlayer Surface of Layered Perovskite $HLaNb_2O_7 \cdot xH_2O$ and Chlorohydrosilanes. *J. Organomet. Chem.* **2003**, *686* (1–2), 145–150.

(118) Tahara, S.; Takeda, Y.; Sugahara, Y. Preparation of Organic−Inorganic Hybrids Possessing Nanosheets with Perovskite-Related Structures via Exfoliation during a Sol−Gel Process. *Chem. Mater.* **2005**, *17* (24), 6198–6204.

(119) Tahara, S.; Okamoto, T.; Sugahara, Y. Preparation of a Nanocomposite Consisting of a Siloxane Network and Perovskite-Related Nanosheets via a Sol–gel Process. *Sci. Technol. Adv. Mater.* **2006**, *7* (5), 446–450.

(120) Shimada, A.; Yoneyama, Y.; Tahara, S.; Mutin, P. H.; Sugahara, Y. Interlayer Surface Modification of the Protonated Ion-Exchangeable Layered Perovskite $HLaNb_2O_7 \bullet xH_2O$ with Organophosphonic Acids. *Chem. Mater.* **2009**, *21* (18), 4155–4162.

(121) Wang, Y.; Delahaye, E.; Leuvrey, C.; Leroux, F.; Rabu, P.; Rogez, G. Efficient Microwave-Assisted Functionalization of the Aurivillius-Phase $Bi_2SrTa_2O_9$. *Inorg. Chem.* **2016**.

(122) Niederberger, M.; Pinna, N. Aqueous and Nonaqueous Sol-Gel Chemistry. In *Metal Oxide Nanoparticles in Organic Solvents*; Engineering Materials and Processes; Springer Science & Business Media, 2009; pp 7–18.

(123) Geng, F.; Ma, R.; Ebina, Y.; Yamauchi, Y.; Miyamoto, N.; Sasaki, T. Gigantic Swelling of Inorganic Layered Materials: A Bridge to Molecularly Thin Two-Dimensional Nanosheets. *J. Am. Chem. Soc.* **2014**, *136* (14), 5491–5500.

(124) Maluangnont, T.; Matsuba, K.; Geng, F.; Ma, R.; Yamauchi, Y.; Sasaki, T. Osmotic Swelling of Layered Compounds as a Route to Producing High-Quality Two-Dimensional Materials. A Comparative Study of Tetramethylammonium versus Tetrabutylammonium Cation in a Lepidocrocite-Type Titanate. *Chem. Mater.* **2013**, *25* (15), 3137–3146.

(125) Ida, S.; Ogata, C.; Unal, U.; Izawa, K.; Inoue, T.; Altuntasoglu, O.; Matsumoto, Y. Preparation of a Blue Luminescent Nanosheet Derived from Layered Perovskite $Bi_2SrTa_2O_9$. *J. Am. Chem. Soc.* **2007**, *129* (29), 8956–8957.

(126) Han, Y.-S.; Park, I.; Choy, J.-H. Exfoliation of Layered Perovskite, $KCa_2Nb_3O_{10}$, into Colloidal Nanosheets by a Novel Chemical Process. *J. Mater. Chem.* **2001**, *11* (4), 1277–1282.

(127) Woomer, A. H.; Farnsworth, T. W.; Hu, J.; Wells, R. A.; Donley, C. L.; Warren, S. C. Phosphorene: Synthesis, Scale-Up, and Quantitative Optical Spectroscopy. *ACS Nano* **2015**, *9* (9), 8869–8884.

(128) Schaak, R. E.; Mallouk, T. E. Prying Apart Ruddlesden−Popper Phases: Exfoliation into Sheets and Nanotubes for Assembly of Perovskite Thin Films. *Chem. Mater.* **2000**, *12* (11), 3427–3434.

(129) Chen, Y.; Zhao, X.; Ma, H.; Ma, S.; Huang, G.; Makita, Y.; Bai, X.; Yang, X. Structure and Dehydration of Layered Perovskite Niobate with Bilayer Hydrates Prepared by Exfoliation/self-Assembly Process. *J. Solid State Chem.* **2008**, *181* (7), 1684–1694.

(130) Treacy, M. M. J.; Rice, S. B.; Jacobson, A. J.; Lewandowski, J. T. Electron Microscopy Study of Delamination in Dispersions of the Perovskite-Related Layered Phases $K[Ca_2Na_{n-3}Nb_nO_{3n-1}]$: Evidence for Single-Layer Formation. *Chem. Mater.* **1990**, *2* (3), 279–286.

(131) Li, B.-W.; Osada, M.; Ebina, Y.; Akatsuka, K.; Fukuda, K.; Sasaki, T. High Thermal Robustness of Molecularly Thin Perovskite Nanosheets and Implications for Superior Dielectric Properties. *ACS Nano* **2014**, *8* (6), 5449–5461.

(132) Compton, O. C.; Osterloh, F. E. Niobate Nanosheets as Catalysts for Photochemical Water Splitting into Hydrogen and Hydrogen Peroxide. *J. Phys. Chem. C* **2009**, *113* (1), 479–485.

(133) Takei, T.; Muraki, N.; Xu, N.; Miura, A.; Kumada, N. Anodic Hybridization of Fluorinated Layered Perovskite Nanosheet with Polyaniline for Electrochemical Capacitor. *Colloids Surf. Physicochem. Eng. Asp.* **2014**, *459*, 186–193.

(134) Asai, Y.; Ariake, Y.; Saito, H.; Idota, N.; Matsukawa, K.; Nishino, T.; Sugahara, Y. Layered Perovskite Nanosheets Bearing Fluoroalkoxy Groups: Their Preparation and Application in Epoxy-Based Hybrids. *RSC Adv.* **2014**, *4* (51), 26932.

(135) Lee, W.-J.; Yeo, H. J.; Kim, D.-Y.; Paek, S.-M.; Kim, Y.-I. Exfoliation of Dion-Jacobson Layered Perovskite into Macromolecular Nanoplatelet. *Bull. Korean Chem. Soc.* **2013**, *34* (7), 2041–2043.

(136) Masala, O.; Seshadri, R. Synthesis Routes for Large Volumes of Nanoparticles. *Annu. Rev. Mater. Res.* **2004**, *34* (1), 41–81.

(137) Kennedy, G. C. Pressure-Volume-Temperature Relations in Water at Elevated Temperatures and Pressures. *Am. J. Sci.* **1950**, *248* (8), 540–564.

(138) Caruntu, D.; Rostamzadeh, T.; Costanzo, T.; Parizi, S. S.; Caruntu, G. Solvothermal Synthesis and Controlled Self-Assembly of Monodisperse Titanium-Based Perovskite Colloidal Nanocrystals. *Nanoscale* **2015**, *7* (30), 12955–12969.

(139) Rostamzadeh, T.; Adireddy, S.; Zhang, X.; Koplitz, B.; Chrisey, D. B.; Wiley, J. B. Rapid Large-Scale Synthesis of Vanadate Nanoscrolls with Controllable Lengths. *ChemNanoMat* **2016**, *2* (1), 54–60.

(140) Adireddy, S.; Yao, Y.; He, J.; Wiley, J. B. Rapid Solvothermal Fabrication of Hexaniobate Nanoscrolls. *Mater. Res. Bull.* **2013**, *48* (9), 3236–3241.

(141) Deng, D.; Pan, X.; Yu, L.; Cui, Y.; Jiang, Y.; Qi, J.; Li, W.-X.; Fu, Q.; Ma, X.; Xue, Q.; et al. Toward N-Doped Graphene via Solvothermal Synthesis. *Chem. Mater.* **2011**, *23* (5), 1188–1193.

(142) Wu, H.; Liu, G.; Wang, X.; Zhang, J.; Chen, Y.; Shi, J.; Yang, H.; Hu, H.; Yang, S. Solvothermal Synthesis of Cobalt Ferrite Nanoparticles Loaded on Multiwalled Carbon Nanotubes for Magnetic Resonance Imaging and Drug Delivery. *Acta Biomater.* **2011**, *7* (9), 3496–3504.

(143) Yang, Y.; Matsubara, S.; Xiong, L.; Hayakawa, T.; Nogami, M. Solvothermal Synthesis of Multiple Shapes of Silver Nanoparticles and Their SERS Properties. *J. Phys. Chem. C* **2007**, *111* (26), 9095–9104.

(144) Sun, C.; Li, H.; Zhang, H.; Wang, Z.; Chen, L. Controlled Synthesis of CeO 2 Nanorods by a Solvothermal Method. *Nanotechnology* **2005**, *16* (9), 1454.

(145) Choi, H. G.; Jung, Y. H.; Kim, D. K. Solvothermal Synthesis of Tungsten Oxide Nanorod/Nanowire/Nanosheet. *J. Am. Ceram. Soc.* **2005**, *88* (6), 1684–1686.

(146) Rajamathi, M.; Seshadri, R. Oxide and Chalcogenide Nanoparticles from Hydrothermal/solvothermal Reactions. *Curr. Opin. Solid State Mater. Sci.* **2002**, *6* (4), 337–345.

(147) Qian, Y. Solvothermal Synthesis of Nanocrystalline III–V Semiconductors. *Adv. Mater.* **1999**, *11* (13), 1101–1102.

(148) Buffler, C. R. *Microwave Cooking and Processing*; Van Nostrand Reinhold: New York, 1993.

(149) Clark, D. E.; Sutton, W. H. Microwave Processing of Materials. *Annu. Rev. Mater. Sci.* **1996**, *26* (1), 299–331.

(150) Gedye, R.; Smith, F.; Westaway, K.; Ali, H.; Baldisera, L.; Laberge, L.; Rousell, J. The Use of Microwave Ovens for Rapid Organic Synthesis. *Tetrahedron Lett.* **1986**, *27* (3), 279–282.

(151) Giguere, R. J.; Bray, T. L.; Duncan, S. M.; Majetich, G. Application of Commercial Microwave Ovens to Organic Synthesis. *Tetrahedron Lett.* **1986**, *27* (41), 4945–4948.

(152) Kappe, C. O.; Dallinger, D.; Murphree, S. S. Chapters 1, 2, and 5 ("Microwave Synthesis -An Introduction", "Microwave Theory", and "Starting with Microwave Chemistry"). In *Practical Microwave Synthesis for Organic Chemists*; Wiley-VCH Verlag GmbH & Co. KGaA: Weinheim, Germany, 2009; pp 1–42, 161–203.

(153) Kappe, C. O.; Stadler, A.; Dallinger, D. *Microwaves in Organic and Medicinal Chemistry*; Wiley-VCH Verlag GmbH & Co. KGaA: Weinheim, Germany, 2012.

(154) Horikoshi, S.; Serpone, N. Chapters 2 and 3: "General Features of Microwave Chemistry" and "Considerations of Microwave Heating." In *Microwaves in Nanoparticle Synthesis*; Horikoshi, S., Serpone, N., Eds.; Wiley-VCH Verlag GmbH & Co. KGaA: Weinheim, Germany, 2013; pp 25–36.

(155) Bogdal, D.; Prociak, A. *Microwave-Enhanced Polymer Chemistry and Technology*; Blackwell Publishing Professional: Ames, IA, 2007.

(156) Hayes, B. L. *Microwave Synthesis: Chemistry at the Speed of Light*; CEM Pub.: Matthews, NC, 2002.

(157) Timmel, C. R.; Hore, P. J. Oscillating Magnetic Field Effects on the Yields of Radical Pair Reactions. *Chem. Phys. Lett.* **1996**, *257* (3), 401–408.

(158) Stass, D. V.; Woodward, J. R.; Timmel, C. R.; Hore, P. J.; McLauchlan, K. A. Radiofrequency Magnetic Field Effects on Chemical Reaction Yields. *Chem. Phys. Lett.* **2000**, *329* (1–2), 15–22.

(159) Woodward, J. R.; Jackson, R. J.; Timmel, C. R.; Hore, P. J.; McLauchlan, K. A. Resonant Radiofrequency Magnetic Field Effects on a Chemical Reaction. *Chem. Phys. Lett.* **1997**, *272* (5), 376–382.

(160) Cao, G. *Nanostructures and Nanomaterials: Synthesis, Properties, and Applications*; Imperial College Press: London, 2004.

(161) Schmid, G. *Nanotechnology: Principles and Fundamentals*; Wiley-VCH: Weinheim, 2008.

(162) Jr, C. P. P.; Owens, F. J. *Introduction to Nanotechnology*; John Wiley & Sons: Hoboken, New Jersey, 2003.

(163) Introduction to Nanoscale Materials in Chemistry. In *Nanoscale Materials in Chemistry*; Klabunde, K. J., Ed.; John Wiley & Sons, Inc.: New York, NY, 2001; pp 1–14.

(164) Tiwari, J. N.; Tiwari, R. N.; Kim, K. S. Zero-Dimensional, One-Dimensional, Two-Dimensional and Three-Dimensional Nanostructured Materials for Advanced Electrochemical Energy Devices. *Prog. Mater. Sci.* **2012**, *57* (4), 724–803.

(165) Wang, H.; Liu, F.; Fu, W.; Fang, Z.; Zhou, W.; Liu, Z. Two-Dimensional Heterostructures: Fabrication, Characterization, and Application. *Nanoscale* **2014**, *6* (21), 12250–12272.

(166) Zhang, H. Ultrathin Two-Dimensional Nanomaterials. *ACS Nano* **2015**, *9* (10), 9451–9469.

(167) Mas-Ballesté, R.; Gómez-Navarro, C.; Gómez-Herrero, J.; Zamora, F. 2D Materials: To Graphene and beyond. *Nanoscale* **2011**, *3* (1), 20–30.

(168) Nakato, T.; Miyamoto, N. Liquid Crystalline Behavior and Related Properties of Colloidal Systems of Inorganic Oxide Nanosheets. *Materials* **2009**, *2* (4), 1734–1761.

(169) Osada, M.; Sasaki, T. Exfoliated Oxide Nanosheets: New Solution to Nanoelectronics. *J. Mater. Chem.* **2009**, *19* (17), 2503.

(170) Bizeto, M. A.; Shiguihara, A. L.; Constantino, V. R. L. Layered Niobate Nanosheets: Building Blocks for Advanced Materials Assembly. *J. Mater. Chem.* **2009**, *19* (17), 2512.

(171) Ma, R.; Sasaki, T. Nanosheets of Oxides and Hydroxides: Ultimate 2D Charge-Bearing Functional Crystallites. *Adv. Mater.* **2010**, *22* (45), 5082–5104.

(172) Butler, S. Z.; Hollen, S. M.; Cao, L.; Cui, Y.; Gupta, J. A.; Gutiérrez, H. R.; Heinz, T. F.; Hong, S. S.; Huang, J.; Ismach, A. F.; et al. Progress, Challenges, and Opportunities in Two-Dimensional Materials Beyond Graphene. *ACS Nano* **2013**, *7* (4), 2898–2926.

(173) Smith, R. J.; King, P. J.; Lotya, M.; Wirtz, C.; Khan, U.; De, S.; O'Neill, A.; Duesberg, G. S.; Grunlan, J. C.; Moriarty, G.; et al. Large-Scale Exfoliation of Inorganic Layered Compounds in Aqueous Surfactant Solutions. *Adv. Mater.* **2011**, *23* (34), 3944–3948.

(174) Geim, A. K.; Grigorieva, I. V. Van Der Waals Heterostructures. *Nature* **2013**, *499* (7459), 419–425.

(175) Geim, A. K. Graphene: Status and Prospects. *Science* **2009**, *324* (5934), 1530–1534.

(176) Singh, V.; Joung, D.; Zhai, L.; Das, S.; Khondaker, S. I.; Seal, S. Graphene Based Materials: Past, Present and Future. *Prog. Mater. Sci.* **2011**, *56* (8), 1178–1271.

(177) Rattana; Chaiyakun, S.; Witit-anun, N.; Nuntawong, N.; Chindaudom, P.; Oaew, S.; Kedkeaw, C.; Limsuwan, P. Preparation and Characterization of Graphene Oxide Nanosheets. *Procedia Eng.* **2012**, *32*, 759–764.

(178) Compton, O. C.; Nguyen, S. T. Graphene Oxide, Highly Reduced Graphene Oxide, and Graphene: Versatile Building Blocks for Carbon-Based Materials. *Small* **2010**, *6* (6), 711–723.

(179) Kim, J.; Cote, L. J.; Kim, F.; Yuan, W.; Shull, K. R.; Huang, J. Graphene Oxide Sheets at Interfaces. *J. Am. Chem. Soc.* **2010**, *132* (23), 8180–8186.

(180) Nair, R. R.; Ren, W.; Jalil, R.; Riaz, I.; Kravets, V. G.; Britnell, L.; Blake, P.; Schedin, F.; Mayorov, A. S.; Yuan, S.; et al. Fluorographene: A Two-Dimensional Counterpart of Teflon. *Small* **2010**, *6* (24), 2877–2884.

(181) Feng, W.; Long, P.; Feng, Y.; Li, Y. Two-Dimensional Fluorinated Graphene: Synthesis, Structures, Properties and Applications. *Adv. Sci.* **2016**, 1500413(1–22).

(182) Sajjad, M.; Morell, G.; Feng, P. Advance in Novel Boron Nitride Nanosheets to Nanoelectronic Device Applications. *ACS Appl. Mater. Interfaces* **2013**, *5* (11), 5051–5056.

(183) Ci, L.; Song, L.; Jin, C.; Jariwala, D.; Wu, D.; Li, Y.; Srivastava, A.; Wang, Z. F.; Storr, K.; Balicas, L.; et al. Atomic Layers of Hybridized Boron Nitride and Graphene Domains. *Nat. Mater.* **2010**, *9* (5), 430–435.

(184) Lei, W.; Qin, S.; Liu, D.; Portehault, D.; Liu, Z.; Chen, Y. Large Scale Boron Carbon Nitride Nanosheets with Enhanced Lithium Storage Capabilities. *Chem Commun* **2013**, *49* (4), 352–354.

(185) Huang, X.; Zeng, Z.; Zhang, H. Metal Dichalcogenide Nanosheets: Preparation, Properties and Applications. *Chem. Soc. Rev.* **2013**, *42* (5), 1934–1946.

(186) Chhowalla, M.; Liu, Z.; Zhang, H. Two-Dimensional Transition Metal Dichalcogenide (TMD) Nanosheets. *Chem. Soc. Rev.* **2015**, *44* (9), 2584–2586.

(187) Dai, J.; Li, M.; Zeng, X. C. Group IVB Transition Metal Trichalcogenides: A New Class of 2D Layered Materials beyond Graphene. *Wiley Interdiscip. Rev. Comput. Mol. Sci.* **2016**, *6* (2), 211–222.

(188) Rodríguez, J. A.; Fernández-García, M. Introduction the World of Oxide Nanomaterials. In *Synthesis, Properties, and Applications of Oxide Nanomaterials*; Rodríguez, J. A., Fernández-García, rcos, Eds.; John Wiley & Sons, Inc.: Hoboken, New Jersey, 2007; pp 1–5.

(189) Takagaki, A.; Sugisawa, M.; Lu, D.; Kondo, J. N.; Hara, M.; Domen, K.; Hayashi, S. Exfoliated Nanosheets as a New Strong Solid Acid Catalyst. *J. Am. Chem. Soc.* **2003**, *125* (18), 5479–5485.

(190) Shibata, T.; Takano, H.; Ebina, Y.; Kim, D. S.; Ozawa, T. C.; Akatsuka, K.; Ohnishi, T.; Takada, K.; Kogure, T.; Sasaki, T. Versatile van Der Waals Epitaxy-like Growth of Crystal Films Using Two-Dimensional Nanosheets as a Seed Layer: Orientation Tuning of $SrTiO_3$ Films along Three Important Axes on Glass Substrates. *J Mater Chem C* **2014**, *2* (3), 441–449.

(191) Ida, S.; Okamoto, Y.; Matsuka, M.; Hagiwara, H.; Ishihara, T. Preparation of Tantalum-Based Oxynitride Nanosheets by Exfoliation of a Layered Oxynitride, $CsCa_2Ta_3O_{10-x}Ny$, and Their Photocatalytic Activity. *J. Am. Chem. Soc.* **2012**, *134* (38), 15773–15782.

(192) Schaak, R. E.; Mallouk, T. E. Self-Assembly of Tiled Perovskite Monolayer and Multilayer Thin Films. *Chem. Mater.* **2000**, *12* (9), 2513–2516.

(193) Sasaki, T.; Watanabe, M.; Hashizume, H.; Yamada, H.; Nakazawa, H. Macromolecule-like Aspects for a Colloidal Suspension of an Exfoliated Titanate. Pairwise Association of Nanosheets and Dynamic Reassembling Process Initiated from It. *J. Am. Chem. Soc.* **1996**, *118* (35), 8329–8335.

(194) Schaak, R. E.; Mallouk, T. E. Exfoliation of Layered Rutile and Perovskite Tungstates. *Chem. Commun.* **2002**, No. 7, 706–707.

(195) Allen, M. R.; Thibert, A.; Sabio, E. M.; Browning, N. D.; Larsen, D. S.; Osterloh, F. E. Evolution of Physical and Photocatalytic Properties in the Layered Titanates $A_2Ti_4O_9$ (A = K, H) and in Nanosheets Derived by Chemical Exfoliation †. *Chem. Mater.* **2010**, *22* (3), 1220–1228.

(196) Takagaki, A.; Tagusagawa, C.; Hayashi, S.; Hara, M.; Domen, K. Nanosheets as Highly Active Solid Acid Catalysts for Green Chemical Syntheses. *Energy Env. Sci* **2010**, *3* (1), 82–93.

(197) Wang, T.; Henderson, C. N.; Draskovic, T. I.; Mallouk, T. E. Synthesis, Exfoliation, and Electronic/Protonic Conductivity of the Dion–Jacobson Phase Layer Perovskite $HLa_2TiTa_2O_{10}$. *Chem. Mater.* **2014**, *26* (2), 898–906.

(198) Kickelbick, G. *Hybrid Materials: Synthesis, Characterization, and Applications*; Wiley-VCH Verlag GmbH & Co. KGaA: Weinheim, Germany, 2007.

(199) Sanchez, C.; Soler-Illia, G. J. de A. A.; Ribot, F.; Lalot, T.; Mayer, C. R.; Cabuil, V. Designed Hybrid Organic−Inorganic Nanocomposites from Functional Nanobuilding Blocks. *Chem. Mater.* **2001**, *13* (10), 3061–3083.

(200) Gomez-Romero, P.; Sanchez, C. *Functional Hybrid Materials*; Wiley-VCH Verlag GmbH & Co. KGaA: Weinheim, Germany, 2006.

(201) Zhu, Y.-P.; Yuan, Z.-Y. *Mesoporous Organic-Inorganic Non-Siliceous Hybrid Materials: Basic Principles and Promising Multifunctionality (from "Springer Briefs in Molecular Science")*; Springer-Verlag GmbH Berlin Heidelberg, 2015.

(202) Huang, S.; Cen, X.; Peng, H.; Guo, S.; Wang, W.; Liu, T. Heterogeneous Ultrathin Films of Poly(vinyl alcohol)/Layered Double Hydroxide and Montmorillonite Nanosheets via Layer-by-Layer Assembly. *J. Phys. Chem. B* **2009**, *113* (46), 15225–15230.

(203) Moujahid, E. M.; Leroux, F.; Dubois, M.; Besse, J.-P. In Situ Polymerisation of Monomers in Layered Double Hydroxides. *Comptes Rendus Chim.* **2003**, *6* (2), 259–264.

(204) Eftekhari, A. *Nanostructured Conductive Polymers*; John Wiley & Sons, Ltd: United Kingdom, 2010.

(205) Lv, S.; Yuan, Y.; Shi, W. Strengthening and Toughening Effects of Layered Double Hydroxide and Hyperbranched Polymer on Epoxy Resin. *Prog. Org. Coat.* **2009**, *65* (4), 425–430.

(206) Matsuo, Y.; Higashika, S.; Kimura, K.; Miyamoto, Y.; Fukutsuka, T.; Sugie, Y. Synthesis of Polyaniline-Intercalated Layered Materials via Exchange Reaction. *J. Mater. Chem.* **2002**, *12* (5), 1592–1596.

(207) Rurack, K.; Martinez-Manez, R. *The Supramolecular Chemistry of Organic-Inorganic Hybrid Materials*; John Wiley & Sons, Inc.: Hoboken, New Jersey, 2010.

(208) *Organic-Inorganic Hybrid Nanomaterials (Advances in Polymer Science 267)*; Kalia, S., Haldorai, Y., Eds.; Springer International Publishing Switzerland, 2015.

(209) American Chemical Society. Meeting (207th : 1994 : San Diego, C. .; Mark, J. E.; Lee, C. Y.-C.; Biancini, P. A. *Hybrid Organic-Inorganic Composites*; ACS symposium series, 0097-6156 ; 585; ACS symposium series ; 0097-6156 585.; American Chemical Society: Washington, D.C., 1995.

(210) Jordens, K. Hybrid Inorganic-Organic Materials: Novel Poly(Propylene Oxide) Based Ceramers, Abrasion Resistant Sol-Gel Coatings for Metals, and Epoxy-Clay Nanocomposites., Virginia Polytechnic Institute and State University, 1999.

(211) Ramakrishnan, V.; Yamamoto, D.; Sasamoto, S.; Shimada, T.; Nabetani, Y.; Tachibana, H.; Inoue, H. Remarkable Enhancement of the Photoreactivity of a Polyfluoroalkyl Azobenzene Derivative in an Organic–inorganic Nano-Layered Microenvironment. *Phys Chem Phys* **2014**, *16* (43), 23663–23670.

(212) Shori, S. Surface Modification of Nanoplatelets in Polymer Nanocomposites. *Theses Diss.* **2014**.

(213) Geselbracht, M. J.; White, H. K.; Blaine, J. M.; Diaz, M. J.; Hubbs, J. L.; Adelstein, N.; Kurzman, J. A. New Solid Acids in the Triple-Layer Dion–Jacobson Layered Perovskite Family. *Mater. Res. Bull.* **2011**, *46* (3), 398–406.

(214) Takeda, Y.; Momma, T.; Osaka, T.; Kuroda, K.; Sugahara, Y. Organic Derivatives of the Layered Perovskite $HLaNb_2O_7 \cdot xH_2O$ with Polyether Chains on the Interlayer Surface: Characterization, Intercalation of LiClO4, and Ionic Conductivity. *J. Mater. Chem.* **2008**, *18* (30), 3581.

(215) Uma, S.; Gopalakrishnan, J. Polymerization of Aniline in Layered Perovskites. *Mater. Sci. Eng. B* **1995**, *34* (2–3), 175–179.

(216) Wang, Y.; Delahaye, E.; Leuvrey, C.; Leroux, F.; Rabu, P.; Rogez, G. Post-Synthesis Modification of the Aurivillius Phase $Bi_2SrTa_2O_9$ via In Situ Microwave-Assisted "Click Reaction." *Inorg. Chem.* **2016**, *55* (19), 9790–9797.

(217) Ide, Y.; Sadakane, M.; Sano, T.; Ogawa, M. Functionalization of Layered Titanates. *J. Nanosci. Nanotechnol.* **2014**, *14* (3), 2135–2147.

(218) Miyamoto, N.; Kuroda, K. Preparation of Porous Solids Composed of Layered Niobate Walls from Colloidal Mixtures of Niobate Nanosheets and Polystyrene Spheres. *J. Colloid Interface Sci.* **2007**, *313* (1), 369–373.

(219) Hattori, T.; Tong, Z.; Kasuga, Y.; Sugito, Y.; Yui, T.; Takagi, K. Hybridization of Layered Niobates with Cationic Dyes. *Res. Chem. Intermed.* **2006**, *32* (7), 653–669.

(220) Kiba, S.; Haga, J.-I.; Hashimoto, S.; Nakato, T. Adsorptive and Photocatalytic Removal of Phenol by Layered Niobates Organically Modified Through Intercalation and Silylation. *J. Nanosci. Nanotechnol.* **2010**, *10* (12), 8341–8348.

(221) Ma, J.; Wu, J.; Zheng, J.; Liu, L.; Zhang, D.; Xu, X.; Yang, X.; Tong, Z. Functional Layered Niobate Nanocomposite with Cationic Manganese Porphyrin and Its Electrocatalytic Behavior. *Mater. Lett.* **2012**, *71*, 4–6.

(222) Shiguihara, A. L.; Bizeto, M. A.; Constantino, V. R. Chemical Modification of Niobium Layered Oxide by Tetraalkylammonium Intercalation. *J. Braz. Chem. Soc.* **2010**, *21* (7), 1366–1376.

(223) Perkins, L. M. Organic-Inorganic Hybrid Materials: New Functionalised Polyoxotungstates. d_ph, University of Birmingham, 2009.

(224) Wang, B.; Dong, X.; Pan, Q.; Cheng, Z.; Yang, Y. Intercalation Behavior of N-Alkylamines into an A-Site Defective Layered Perovskite $H_2W_2O_7$. *J. Solid State Chem.* **2007**, *180* (3), 1125–1129.

(225) Gannon, G.; O'Dwyer, C.; Larsson, J. A.; Thompson, D. Interdigitating Organic Bilayers Direct the Short Interlayer Spacing in Hybrid Organic–Inorganic Layered Vanadium Oxide Nanostructures. *J. Phys. Chem. B* **2011**, *115* (49), 14518–14525.

(226) de Bonis, C.; D'Epifanio, A.; Mecheri, B.; Traversa, E.; Miyayama, M.; Tavares, A. C.; Licoccia, S. Layered Tetratitanate Intercalating Sulfanilic Acid for Organic/inorganic Proton Conductors. *Solid State Ion.* **2012**, *227*, 73–79.

(227) Nam, H.-J.; Kim, H.; Chang, S. H.; Kang, S.-G.; Byeon, S.-H. Polymerization of Aniline in the Galleries of Layered HNbMoO6. *Solid State Ion.* **1999**, *120* (1–4), 189–195.

(228) Chapter 1: An Introduction to Disorder in Solids (by: C. R. A. Catlow). In *Defects and Disorder in Crystalline and Amorphous Solids*; Catlow, C. R. A., Ed.; Kluwer Academic Publishers, 1994.

(229) Volume 3: Crystalline and Noncrystalline Solids. In *Treatise on Solid State Chemistry:*; Hannay, N., Ed.; PLENUM PRESS: New York, NY, U.S.A., 1976.

(230) Kisi, E. H.; Howard, C. J. *Applications of Neutron Powder Diffraction*; Oxford University Press: New York, USA, 2008.

(231) West, A. R. Chapters 1 and 5 ("Crystal Structures and Crystal Chemistry", and "Crystallography and Diffraction Techniques"). In *Solid State Chemistry and its Applications*; John Wiley & Sons, Ltd: United Kingdom, 2014; pp 1–82, 229–270.

(232) Sands, D. E. *Introduction to Crystallography*; Courier Corporation: US, 1969.

(233) Blake, A. J.; Clegg, W.; Cole, J. M.; Evans, J. S.; Main, P.; Parsons, S.; Watkin, D. J. *Crystal Structure Analysis: Principles and Practice*; Clegg, W., Ed.; Oxford University Press, 2009.

(234) Dinnebier, R. E.; Billinge, S. J. L. *Powder Diffraction: Theory and Practice*; Royal Society of Chemistry, 2008.

(235) Phillips, F. C. *An Introduction to Crystallography*; LONGMANS, GREEN AND CO: New York, 1956.

(236) Fultz, B.; Howe, J. M. Chapter 1: Diffraction and the X-Ray Powder Diffractometer. In *Transmission Electron Microscopy and Diffractometry of Materials*; Springer Science & Business Media, 2013; pp 1–57.

(237) Lehn, J.-M.; Alberti, G.; Bein, T. Chapter 1: Diffraction Techniques (By Zbigniew Dauter and Keith S. Wilson). In *Comprehensive supramolecular chemistry volume 8, Physical Methods in Supramolecular Chemistry.*; Pergamon: Oxford; New York; Tokyo, 1996; pp 1–23.

(238) Will, G. *Powder Diffraction: The Rietveld Method and the Two Stage Method to Determine and Refine Crystal Structures from Powder Diffraction Data*; Springer Science & Business Media: Germany, 2006.

(239) *Experimental Methods in the Physical Sciences, Volume 44: Neutron Scattering - Fundamentals (by Felix Fernandez-Alonso, and David L. Price)*; Lucatorto, T., Parr, A. C., Baldwin, Series Eds.; Elsevier Inc.: San Diego, CA, USA, 2013.

(240) *Electron Microscopy: Principles and Fundamentals*; Amelinckx, S., Dyck, D. van, Landuyt, J. van, Tendeloo, G. van, Eds.; VCH, a Wiley Company: Weinheim, Germany, 1997.

(241) *Diffraction and Imaging Techniques in Material Science, Volume I: Imaging and Diffraction Techniques*; Amelinckx, S., Gevers, R., Van Landuyt, J., Eds.; North-Holland Publishing Company, 1978.

(242) *Transmission Electron Microscopy, Part 2: Diffraction*, 2nd ed.; Williams, D. B., Carter, C. B., Eds.; Springer Science & Business Media: New York, NY, U.S.A., 2009.

(243) West, A. R. Chapter 6: Other Techniques: Microscopy, Spectroscopy, Thermal Analysis. In *Solid State Chemistry and its Applications*; John Wiley & Sons, Ltd: United Kingdom, 2014; pp 187–228.

(244) Voigtländer, B. *Scanning Probe Microscopy - Atomic Force Microscopy and Scanning Tunneling Microscopy. from "NanoScience and Technology" Series*; Avouris, P., Bhushan, B., Bimberg, D., Sakaki, H., von Klitzing, K., Wiesendanger, R., Series Eds.; Springer-Verlag Berlin Heidelberg: New York Dordrecht London, 2015.

(245) Spence, J. C. H. *High-Resolution Electron Microscopy*, 3rd ed.; Oxford University Press: New York, USA, 2003.

(246) *Transmission Electron Microscopy, Part 1: Basics*, 2nd ed.; Williams, D. B., Carter, C. B., Eds.; Springer Science & Business Media: New York, NY, U.S.A., 2009.

(247) Krumeick, F. Properties of Electrons, Their Interactions with Matter and Applications in Electron Microscopy. *Lab. Inorg. Chem. Disponível Em Httpwww Microsc. Ethz ChdownloadsInteractions Pdf Consult. Em* **2011**, 3–08.

(248) *Atomic Force Microscopy - Imaging, Measuring and Manipulating Surfaces at the Atomic Scale*; Bellitto, V., Ed.; InTech: Rijeka, Croatia, 2012.

(249) Magonov, S. N.; Whangbo, M.-H. Introduction. In *Surface Analysis with STM and AFM-Experimental and Theoretical Aspects of Image Analysis*; VCH Verlagsgesellschaft mbH: Weinheim, Germany, 1996; pp 1–8.

(250) *Atomic Force Microscopy/Scanning Tunneling Microscopy*; Cohen, S. H., Bray, M. T., Lightbody, M. L., Eds.; Springer Science & Business Media: Natick, Massachusetts, 1994.

(251) Vol. 1: Principles and Practice. In *Handbook of Thermal Analysis and Calorimetry*; Brown, M. E., Ed.; Gallagher, P. K., Series Ed.; Recent Advances, Techniques and Applications; Elsevier Science B.V., 2008; Vol. 5, pp 13–54.

(252) Hatakeyama, T.; Quinn, F. X. *Thermal Analysis: Fundamentals and Applications to Polymer Science*, 2nd ed.; John Wiley & Sons, Ltd: England, 1999.

(253) Brown, M. E. *Introduction to Thermal Analysis - Techniques and Applications*, 2nd ed.; Kluwer Academic Publishers: US, 2004.

(254) Speyer, R. F. *Thermal Analysis of Materials*; Marcel Dekker, Inc: New York, NY, U.S.A., 1994.

(255) Mitchell, P. C. H.; Parker, S. F.; Ramirez-Cuesta, A. J.; Tomkinson, J. *Vibrational Spectroscopy with Neutrons: With Applications in Chemistry, Biology, Materials Science and Catalysis (Vol.3 from Series on "NeutronTechniques and Applications";* Finney, J. L., Worcester, D. L., Series Eds.; World Scientific: MA, USA, 2005.

(256) McHale, J. L. *Molecular Spectroscopy*; Prentice-Hall Inc.: NJ, 1999.

(257) Perkowitz, S. *Optical Characterization of Semiconductors: Infrared, Raman, and Photoluminescence Spectroscopy (Vol. 14 of Series on "Techniques of Physics")*; March, N. H., Series Ed.; Academic Press: San Diego, CA, USA, 1993.

(258) *Handbook of Vibrational Spectroscopy (Vol. 1- Theory and Instrumentation).*; Chalmers, J. M., Griffiths, P. R., Eds.; John Wiley and Sons Ltd: Chichester, United Kingdom, 2002.

(259) Vincent, A. Molecular Symmetry and Group Theory (Programme 7-"Applications to Molecular Vibrations"); John Wiley and Sons Ltd: England, 2010.

(260) Rankin, D. W. H.; Mitzel, N.; Morrison, C. Chapters 8 and 9 ("Vibrational Spectroscopy" and "Electronic Characterization Techniques"). In *Structural Methods in*

Molecular Inorganic Chemistry (in "Inorganic chemistry" series); John Wiley and Sons Ltd: United Kingdom, 2013; Vol. 52, pp 8200–8201.

(261) General Survey of Vibrational Spectroscopy. In *Infrared and Raman Spectroscopy*; Schrader, B., Ed.; Wiley-VCH Verlag GmbH: Weinheim, Germany, 1995; pp 7–61.

(262) McCreery, R. L. Introduction and Scope. In *Raman Spectroscopy for Chemical Analysis (Vol. 157 of "Chemical Analysis" series)*; Winefordner, J. D., Series Ed.; John Wiley & Sons, Inc.: Canada, 2000; pp 1–14.

(263) Lacombe, S.; Cardy, H.; Soggiu, N.; Blanc, S.; Habib-Jiwan, J. L.; Soumillion, J. P. Diffuse Reflectance UV–Visible Spectroscopy for the Qualitative and Quantitative Study of Chromophores Adsorbed or Grafted on Silica. *Microporous Mesoporous Mater.* **2001**, *46* (2–3), 311–325.

(264) Tauc, J.; Grigorovici, R.; Vancu, A. Optical Properties and Electronic Structure of Amorphous Germanium. *Phys. Status Solidi B* **1966**, *15* (2), 627–637.

(265) Davis, E. A.; Mott, N. F. Conduction in Non-Crystalline Systems V. Conductivity, Optical Absorption and Photoconductivity in Amorphous Semiconductors. *Philos. Mag.* **1970**, *22* (179), 0903–0922.

(266) Harvey, D. *Analytical Chemistry 2.0 (A Free Digital Resource for Analytical Chemistry)*; Digital Textbook.

(267) Perkampus, P. em D. H.-H. Recent Developments in UV-VIS Spectroscopy. In *UV-VIS Spectroscopy and Its Applications*; Springer Lab Manuals; Springer Berlin Heidelberg: Germany, 1992; pp 81–130.

(268) *UV-VIS and Photoluminescence Spectroscopy for Nanomaterials Characterization*; Kumar, C. S. S. R., Ed.; Springer-Verlag Berlin Heidelberg: US, 2013.

(269) Balzani, V.; Ceroni, P.; Juris, A. Chapter 3: Light Absorption and Excited-State Deactivation. In *Photochemistry and Photophysics: Concepts, Research, Applications*; Wiley-VCH Verlag GmbH & Co. KGaA: Weinheim, Germany, 2014.

(270) Farley, J. W.; Brumley, W. C.; Eastwood, D. Environmental Applications of Electronic Spectroscopy. In *Encyclopedia of Spectroscopy and Spectrometry*; Lindon, J., Series Ed.; Academic Press: San Diego, CA, USA, 2000; pp 430–432.

(271) Harris, D. C. *Quantitative Chemical Analysis (Chapter 22: Mass Spectrometry)*, 9th ed.; Macmillan: New York, NY, 2016.

(272) Rankin, D. W. H.; Mitzel, N.; Morrison, C. *Structural Methods in Molecular Inorganic Chemistry (Chapter 11: Mass Spectrometry)*; John Wiley & Sons, Ltd: United Kingdom, 2013.

(273) West, A. R. Chapter 8: Electrical Properties. In *Solid State Chemistry and its Applications*; John Wiley & Sons, Ltd: United Kingdom, 2014; pp 187–228.

(274) Kleiner, R.; Koelle, D.; Ludwig, F.; Clarke, J. Superconducting Quantum Interference Devices: State of the Art and Applications. *Proc. IEEE* **2004**, *92* (10), 1534–1548.

(275) Chen, G.; Church, D. A.; Englert, B.-G.; Henkel, C.; Rohwedder, B.; Scully, M. O.; Zubairy, M. S. *Quantum Computing Devices: Principles, Designs, and Analysis (from Chapman & Hall/CRC Applied Mathematics and Nonlinear Science Series)*; Taylor & Francis Group, LLC: Boca Raton, FL, 2007.

(276) Josephson, B. D. Possible New Effects in Superconductive Tunnelling. *Phys. Lett.* **1962**, *1* (7), 251–253.

(277) Ficek, Z.; Swain, S. *Quantum Interference and Coherence - Theory and Experiments (from Springer Series in Optical Sciences)*; Rhodes, W. T., Series Ed.; Springer Science & Business Media: New York, NY, U.S.A., 2005.

(278) Foner, S.; Schwartz, B. B. *Superconducting Machines and Devices - Large Systems Applications (from NATO Advanced Study Institutes Series)*; Plenum Press: New York, 1974.

(279) Kose, V. *Superconducting Quantum Electronics*; Springer-Verlag Berlin Heidelberg: Germany, 1989.

Chapter 2. Rapid Topochemical Modification of Layered Perovskites via Microwave Reactions[†]

2.1– Introduction

Microwaves have been an important method of heat treatment since the 1950's when the first generation of microwave ovens were commercialized.[1,2] In addition to the heating of foodstuffs, microwaves have been utilized in environmental remediation, medicine, printing, paints, thin films, agriculture, and wood processing.[3–9] Microwaves are also significant in chemistry for facilitating reactions and processing in various fields such as analytical chemistry,[10–13] biochemistry,[8,14] photochemistry,[15,16] catalysis,[17–20] inorganic materials,[9,21–24] organometallics,[25–28] polymers,[29,30] and most importantly organic synthesis.[31–36]

Organic-inorganic hybrids are of interest since they can potentially exhibit tunable or superior features compared to their pure organic and inorganic counterparts.[37,38] Tunable mechanical, electronic, optical, and catalytic properties are attainable by combinations of various components as well as through control of bonding interactions.[39–42] Based on the interactions at the organic-inorganic interface, hybrids can be divided into weak bonding (hydrogen bonding, van der Waals contacts or electrostatic forces) and strong bonding (covalent, iono-covalent, or Lewis acid-base).[43,44] The best examples of these composites are lightweight materials based on polymers reinforced with inorganic nanoparticles that exhibit synergistically superior properties despite weak interfacial bonding.[39] Organic-inorganic hybrids can also be designed at the molecular scale with strong intermolecular covalent linkages.[37,38]

Perovskites have been modified by the insertion of organic substituents such that the resulting hybrids offer interesting magnetic, electrical, optical and catalytic properties.[38,41,44–46] Simple perovskite hybrids with the ABX_3 general formula (where A is an organic substituent, B is a divalent metal in octahedral anion coordination, and X is a halide anion) can be prepared by direct reaction of the various components.[38,41,46] Layered perovskite hybrids can be formed through intercalation or grafting[44,45,47–53]from Dion-Jacobson or Ruddlesden-Popper type phases

[†] This chapter was adapted from: Akbarian-Tefaghi, S.; Teixeira Veiga, E.; Amand, G.; Wiley, J. B. Rapid Topochemical Modification of Layered Perovskites via Microwave Reactions. *Inorg. Chem.* **2016**, *55* (4), 1604–1612.

($A'[A_{n-1}B_nO_{3n+1}]$ and $A'_2[A_{n-1}B_nO_{3n+1}]$, respectively, where n = layer thickness, A and A' = alkali-metal, alkaline earth, or rare-earth cations, and B = transition metal cation).[47,54] While ABX_3 type compounds are mainly used for electronic, optical and photovoltaic applications,[38,41,46,55–58] manipulating the interlayer of layered oxide perovskites with organics can produce photocatalytically active hybrids.[44,45] Some reports of exfoliation/delamination of layered oxide perovskites[53,59–65] show that it is also possible to produce surface-tailored nanosheets for use as reinforcing components in polymer-based hybrids;[53,63,64] since the surfaces of nanosheets are organically modified, the filler will have a better affinity for the polymer matrix, thereby improving the mechanical properties of the hybrid.[52,53,66]

While microwave-assisted reactions have been quite effective in a variety of organic syntheses,[22,32–36] as well as in the preparation of inorganic solids,[9,22] their use in the modification of layered perovskites has been limited. Recently Boykin and Smith[67] reported the production of perovskite-based hybrids by microwave-assisted grafting reactions of n-alcohols on the triple-layered Dion-Jacobson perovskites, $RbAe_2Nb_3O_{10}$ (*Ae* = Ca, Sr);[67] an exciting advance which reduced grafting times down from days or weeks to hours. Herein we build on this approach by showing that microwave synthesis can be applied to a variety of topotactic reactions (ion exchange, intercalation and grafting) on double- and triple-layered perovskites of both Dion-Jacobson and Ruddlesden-Popper structure types. Detailed studies are presented optimizing times and temperatures in a dedicated synthetic microwave system. The series of inorganic hosts in this study, $RbLaNb_2O_7$, $KCa_2Nb_3O_{10}$, $Li_2CaTa_2O_7$ and $Na_2La_2Ti_3O_{10}$, were chosen due to the previous reports on their modification.[44,45,48–51] Microwave-assisted ion exchange and intercalation reactions, as well as grafting reactions with the Ruddlesden-Popper hosts, are reported for the first time.

2.2– Experimental

2.2.1 Materials

Rb_2CO_3 (Alfa Aesar, 99.8%), K_2CO_3 (Alfa Aesar, 99.997%), Na_2CO_3 (Alfa Aesar, 99.997%), Li_2CO_3 (Alfa Aesar, 99.999%), $CaCO_3$ (Alfa Aesar, 99.99%), KCl (Alfa Aesar, 99.995%), TiO_2 (Alfa Aesar 99.995%), and Ta_2O_5 (Alfa Aesar, 99.85%) were used as received. La_2O_3 (Alfa Aesar, 99.99%), Nb_2O_5 (Alfa Aesar, 99.9985%), and Pr_6O_{11} (Alfa Aesar, 99.9%)

were heated at 1000˚C for 12 h in order to eliminate any impurities. Organic n-alkylamines and n-alkyl alcohols were used without any further distillation: methanol (Fisher Scientific 99.9%), 1-propanol (Alfa Aesar 99+%), 1-pentanol (Alfa Aesar 98+%), 1-decanol (Alfa Aesar 98+%), methylamine (Alfa Aesar 40% w/w aq. soln.), ethylamine (Alfa Aesar 70% aq. soln.), 1-propylamine (Alfa Aesar 99+%), 1-butylamine (Alfa Aesar 99%), 1-hexylamine (Alfa Aesar 99%) and 1-octylamine (Alfa Aesar 99%). For aqueous solutions (aq. soln.), milli-Q water (18.2 MV cm, Millipore) was mixed with the pure solvent to obtain the desired concentration (typically 50% v/v aq. soln. of n-alkyl amine or 80% v/v aq. soln. of n-alcohol). ***Caution:*** amines are corrosive and very irritating to the skin, eyes and lungs; these reagents should be handled in a fume hood with proper PPE.

2.2.2 Synthesis of the Inorganic Hosts

$RbLaNb_2O_7$, $KCa_2Nb_3O_{10}$, $Li_2CaTa_2O_7$ and $Na_2La_2Ti_3O_{10}$ were synthesized from the corresponding oxides and carbonates by methods similar to previously reported solid state reactions.[68–71] All ceramic reactions were done in alumina crucibles in air. $RbLaNb_2O_7$ was synthesized by mixing Rb_2CO_3, La_2O_3, and Nb_2O_5 in a molar ratio of 1.3:1:2, respectively. The ground mixture was pre-heated at 850 ˚C for 12 h, re-ground, and then heated at 1050 ˚C (24 h) and 1100 ˚C (24 h) with one intermediate grinding. $KCa_2Nb_3O_{10}$ was prepared by a method similar to the molten salt synthesis reported by Geselbracht *et al.*[69] K_2CO_3, $CaCO_3$, Nb_2O_5, and KCl were mixed in a 1:4:3:15 molar ratio, respectively. The mixture was ground and heated at 900 ˚C (24 h), 950 ˚C (12 h) and 1000 ˚C (2 h). For the synthesis of $Li_2CaTa_2O_7$, Li_2CO_3, $CaCO_3$ and Ta_2O_5 were mixed and ground in a molar ratio of 1.3:1:1, respectively, and then heated at 1175˚C for 4 h with two intermediate grindings. $Na_2La_2Ti_3O_{10}$ was prepared by grinding a mixture of Na_2CO_3, La_2O_3, and TiO_2 with 1.3:1:3 molar ratio of the reagents, respectively. The mixture was pre-heated at 550 ˚C for 12 h and heated at 1050 ˚C for 48 h with three intermediate grindings. $RbPrNb_2O_7$ was synthesized similar to that reported by Montasserasadi et al.[72] in order to study the reproducibility of the topotactic reactions on other compounds isostructural with what provided here. Rb_2CO_3, Pr_6O_{11}, and Nb_2O_5 were ground in a molar ratio of 3.3:1:6, respectively. The mixture was pre-heated at 850 ˚C for 12 h, re-ground, and then heated at 1050 ˚C (6 h) and 1100 ˚C (48 h) with one intermediate grinding. $RbLaNb_2O_7$, $RbPrNb_2O_7$,

$KCa_2Nb_3O_{10}$, $Li_2CaTa_2O_7$, and $Na_2La_2Ti_3O_{10}$ final products were washed with copious amount of distilled water, rinsed with acetone, and dried at 130 ˚C for several hours.

Microwave Syntheses. Topochemical reactions involving ion exchange, grafting and intercalation were carried out in a StartSYNTH Microwave Synthesis Labstation (Figure 2-1). The unit was equipped with Milestone's START platform, which provides the possibility of simultaneously processing up to 32 reactions. The individual reactions are contained in pressure reactors (< 15 bar) where the typical reaction volumes ranged from 4 to 16 ml. For non-aqueous reaction mixtures, a Weflon button (graphite-doped Teflon) was used in the mixture to absorb the microwaves in the non-polar solvents. A Teflon stirring bar (transparent to the microwaves) was used in all trials to ensure the reaction uniformity. ***Caution:*** Glass reaction vessels should be carefully inspected before each reaction; defects in the glass (e.g. pits) can result in hotspots, possibly leading to explosion.

2.2.3 Acid Exchange (Protonation)

Microwave acid treatment was carried out for 3 h at 60˚C with continuous stirring and a maximum power of 300 watts. Following the literature on conventional proton exchange,[45,48–51] nitric acid solutions with different molarities were used in order to carry out these reactions. In all cases, the molar ratio of proton to the interlayer cation remained greater than 150:1. $HLaNb_2O_7$ and $HCa_2Nb_3O_{10}$ were prepared by treatment with 6 M HNO_3, $H_2CaTa_2O_7$ with 4 M HNO_3, and 1 M HNO_3 in the case of $H_2La_2Ti_3O_{10}$. The protonated products were washed with distilled water until pH 7 was obtained, and then dried at 130 ˚C for at least 3 hours.

2.2.4 Organic Modification of the Protonated Hosts

All the organic-inorganic hybrid syntheses involved the protonated hosts above. Reactions were performed in air for 30 minutes to one hour. Samples were heated from 25 ˚C to desired reaction temperature (100, 120 and 150 ˚C) with a heating rate of 2.5 ˚C/min.

2.2.4.1 Direct Grafting of Short-Chain n-Alkyl Alcohols. C_nH_{2n+1}-$LaNb_2O_7$ members (n = 1, 3) were directly synthesized from the protonated Dion-Jacobson host. Typically, 0.15 g of $HLaNb_2O_7$ was reacted with 14 mL of 80% v/v aq. soln. of n-alcohol for 1 h at 100 ˚C with the maximum power of 350 W. The products were washed with distilled water and acetone and then dried at 70 ˚C for 1 h.

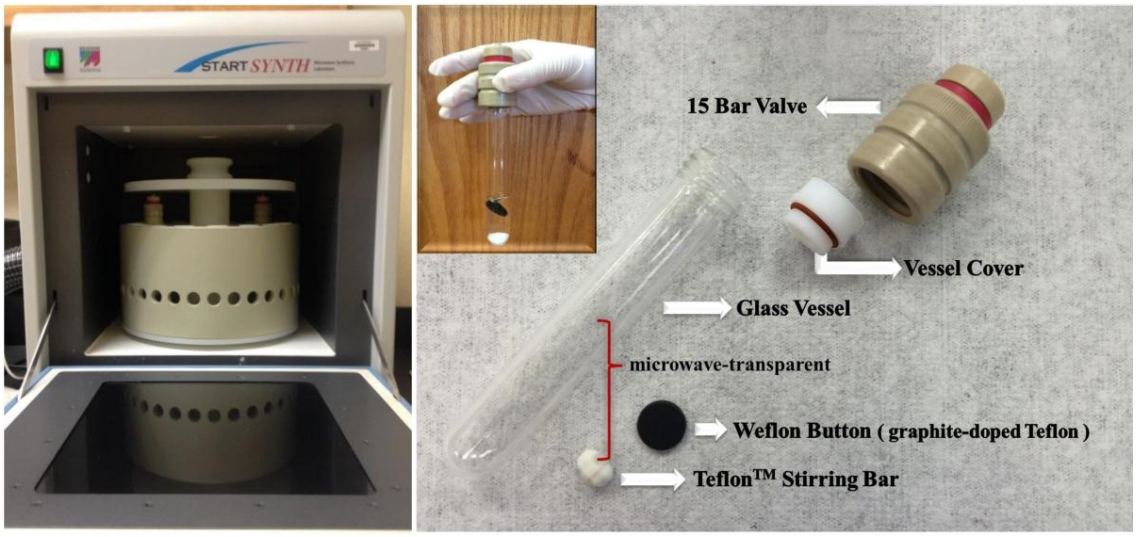

Figure 2-1: Milestone's StartSYNTH Labstation (left) and parts of a 15-bar pressure reactor used in modification reactions of the perovskite hosts (right).

2.2.4.2 Direct Intercalation of n-Alkyl Amines. $C_nH_{2n+1}NH_2$-$LaNb_2O_7$ and $C_nH_{2n+1}NH_2$-$CaTa_2O_7$ members (n = 1 – 4) were prepared directly from the protonated Dion-Jacobson and Ruddlesden-Popper hosts. Typically, 0.15 g of $HLaNb_2O_7$ or $H_2CaTa_2O_7$ was stirred with 14 mL of 50% v/v aqueous solutions of n-alkyl amines for 1 h at 100 ˚C (maximum power of 350 W). The intercalated products were washed with distilled water, ethanol and acetone and dried at 70 ˚C for 1 h.

2.2.4.3 Indirect Exchange Reactions of $HLaNb_2O_7$ Host. Using rapid microwave reactions, the interlayer of C_nH_{2n+1}-$LaNb_2O_7$ members (n = 1, 3) were successfully exchanged with longer chain n-alkoxy and n-alkylamine substituents: $C_nH_{2n+1}OH$ (n = 3, 5 and 10) and $C_nH_{2n+1}NH_2$ (n = 1 – 4). Exchanging $C_nH_{2n+1}NH_2$-$LaNb_2O_7$ hybrids (n = 1, 3 and 4) was also done in order to obtain longer intercalants (n = 3, 4, 6 and 8). Exchanging an n-alkylamine substituent with n-alkoxy was not successful in any of the trials on this host. In the case of water-soluble reactants (n = 1 – 4), typically 0.03 g of C_nH_{2n+1}-$LaNb_2O_7$ (or $C_nH_{2n+1}NH_2$-$LaNb_2O_7$) was stirred with 5 ml of 50% v/v aq. soln. of n-alkyl amine or 80% v/v aq. soln. of n-alcohol for 1 h at 100 ˚C (maximum power of 350 W). For $C_nH_{2n+1}OH$ (n = 5 and 10) and $C_nH_{2n+1}NH_2$ (n = 6 and 8) reactants, the typical microwave procedure was carried out by reacting 0.03 g of the parent hybrid with 5 mL of the pure target solution containing Weflon, either for 1 h at 120 ˚C

with the maximum power of 800 W (n = 5 and 6), or for only 30 min at 150 ˚C with the maximum power of 1000 W (n = 8 and 10). Synthesis of $C_8H_{17}NH_2$-$LaNb_2O_7$ was also possible by reacting 0.03 g of $C_{10}H_{21}$-$LaNb_2O_7$ with 5mL of pure 1-octylamine (30 min at 150 ˚C with the maximum power of 1000 W). The products were washed with either water and acetone, or just acetone for the longer chain reactants, and dried at 70 ˚C for 1 h.

2.2.4.4 Indirect Exchange Reactions of $H_2CaTa_2O_7$ Host. Similar to what has been reported in the literature,[45,51] direct reaction of n-alcohols with a Ruddlesden-Popper host was found to be unsuccessful. However, it was possible to obtain C_3H_7-$CaTa_2O_7$ using an amine-intercalated intermediate. Stirring 0.1 g of 1-propylamine-$CaTa_2O_7$ with 14 mL of 80% v/v aq. soln. of n-propanol for 1 h at 100 ˚C (maximum power of 350 W), the 1-propylamine intercalant was replaced by an n-propoxy substituent. The interlayer of C_3H_7-$CaTa_2O_7$ was then successfully exchanged with longer chain n-alkoxy substituents (n = 5 and 10) by reacting 0.03 g of the parent hybrid for 1 h at 120 ˚C (maximum power of 800 W) with 5 mL of pure n-pentanol or n-decanol solvent containing a Weflon. Exchanging the intercalated n-alkylamine in $C_nH_{2n+1}NH_2$-$CaTa_2O_7$ hybrids (n = 3 and 4) was also done in order to obtain longer intercalants (n = 4, 6 and 8). Targeting $C_4H_9NH_2$-$CaTa_2O_7$, typically 0.03 g of $C_3H_7NH_2$-$CaTa_2O_7$ was reacted with 5 mL of the 50% v/v aq. soln. of 1-butylamine for 1 h at 100 ˚C (maximum power of 350 W). In the case of $C_nH_{2n+1}NH_2$ (n = 6 and 8), the microwave reaction was typically done by reacting 0.03 g of the $C_nH_{2n+1}NH_2$-$CaTa_2O_7$ hybrids (n = 3 and 4), 5 mL of the pure target solvent, and a Weflon button for 1 h at 120 ˚C (maximum power of 800 W). All the final products were washed with ethanol and acetone and dried at 70 ˚C for 1 h (for water-miscible amines, distilled water was also used).

2.2.5 Characterization

X-ray powder diffraction (XRD) data were collected on a Philips X'Pert system equipped with Cu Kα radiation (λ = 1.5418 Å) and a curved graphite monochromator. Typical scans were carried out in continuous mode with a scan rate of 0.02 °/s. The peak positions and lattice parameters were refined using Fullprof[73] and a least-squares method with the ChekCell program.[74] A JEOL (model JSM-5410) scanning electron microscope (SEM), equipped with the energy dispersive analysis (EDS), EDAX (DX-PRIME) microanalytical system, was used for elemental analysis. Raman spectra were obtained with a Thermo-Fisher DXR dispersive Raman

spectrometer using the $\lambda = 532$ nm line with a spectral resolution of 3 cm^{-1}. Thermogravimetric analysis (TGA) and differential scanning calorimetry (DSC) data were collected on a TA Instruments TGA-DSC SQ600 system in alumina pans under a dilute oxygen atmosphere (ca. 50% argon); samples were heated to 800 °C at a rate of 10 °C/min. Combustion of the organic substituents provided information on the organic loading in the interlayer of the inorganic host.

2.3– Results

Ion exchange with microwave heating was carried out on four different perovskite hosts to produce $HLaNb_2O_7$, $HCa_2Nb_3O_{10}$, $H_2CaTa_2O_7$ and $H_2La_2Ti_3O_{10}$. Figure 2-2 provides the XRD patterns of the various hosts versus their acid exchanged products. While typical proton exchange reactions can take several days,[45,48–51,67] microwave reactions can be completed in 3 hrs. Protonated perovskite hosts are needed to carry out grafting or intercalation reactions with long-chain alcohols and amines, respectively.

Initial studies involved grafting reactions with the acid-exchanged double-layered perovskite host, $HLaNb_2O_7$. While the solvothermal method takes days, microwave reactions produce the same quality compounds in as little as an hour. Figure 2-3 compares the XRD patterns of three sets of reaction products, each set prepared through both solvothermal and microwave methods: $HLaNb_2O_7$ (HLN), n-propoxy-$LaNb_2O_7$ (propoxy-LN) and n-decoxy-$LaNb_2O_7$ (decoxy-LN). Unit cell values (Table 2-1) were obtained from indexed XRD patterns. TGA and DSC analyses were also carried out to show that similar weight losses and thermal behaviors occur in the two alkoxy-grafted products regardless of the synthetic method (Figure 2-4). Table 2-1 compares the percent weight loss and the estimated stoichiometries for propoxy-LN and decoxy-LN products; the approximate organic loading per [$LaNb_2O_7$] unit was calculated based on the formation of $LaNb_2O_{6.5}$ after decomposition, as verified by XRD and reported by Hermann et al.[75] The compositions are essentially identical for both synthetic methods. In cases where literature values were available, organic contents were found to be slightly lower than those reported for propoxy-LN and decoxy-LN.[49]

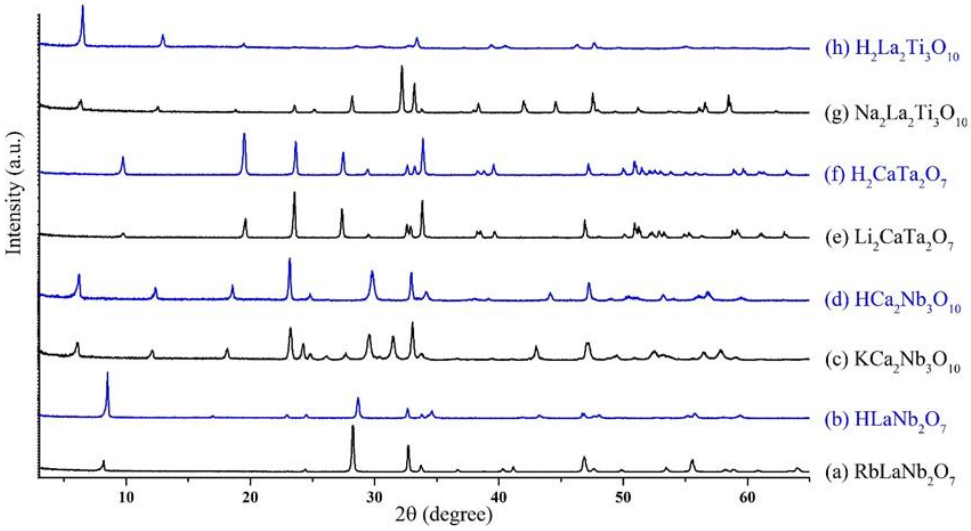

Figure 2-2: XRD patterns of the perovskite hosts versus the acid exchanged products obtained via microwave heating.

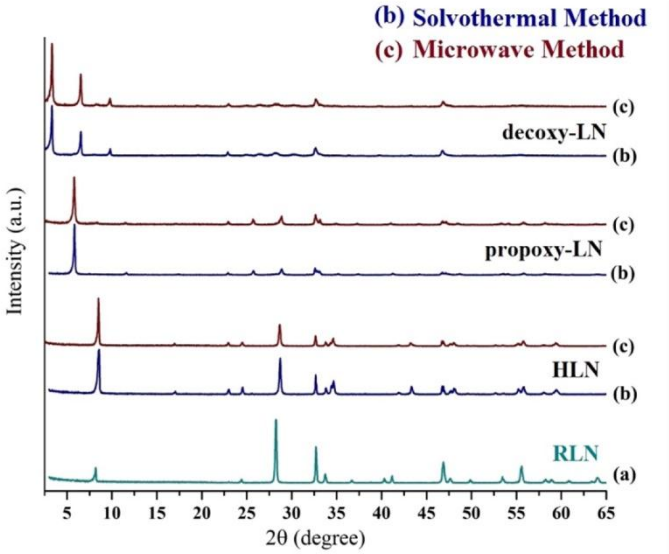

Figure 2-3: Comparison of XRD patterns for solvothermal (autoclave) and microwave methods. (a) RLN (starting material) and the three sets of topochemical-modification products: HLN, propoxy-LN and decoxy-LN obtained via (b) solvothermal (autoclave) and (c) microwave reactions.

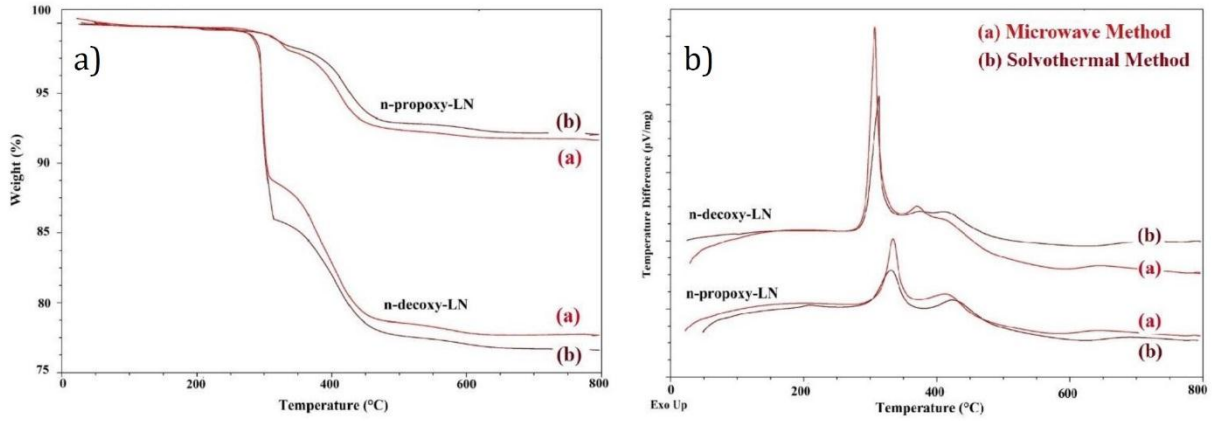

Figure 2-4: a) TGA and b) DSC curves comparing the thermal behavior of propoxy-LN and decoxy-LN prepared via (a) microwave method or (b) autoclave method.

Table 2-1: Unit cell parameters, weight loss and organic loading of propoxy-LN and decoxy-LN hybrids prepared via microwave and solvothermal methods.

	Chemical Formula of the Organic Substituent		Lattice Parameter (Å)		Volume (Å^3)	Weight Loss% * (organic + water)	Estimation of Loading per [$LaNb_2O_7$]
			a	c			
Microwave	C_3H_7O-	n-propoxy	3.888(3)	15.4011(5)	232.796	8.45(1)	0.7745(1)
	$C_{10}H_{21}O$-	n-decoxy	3.876(5)	27.2380(6)	409.185	22(3)	0.833(7)
Solvothermal	C_3H_7O-	n-propoxy	3.887(3)	15.3180(4)	231.449	8.5(3)	0.780(3)
	$C_{10}H_{21}O$-	n-decoxy	3.876(6)	27.1928(6)	408.505	23(2)	0.835(4)

*Average of minimum three TGA-DSC runs

This microwave approach is quite versatile and can be used for the rapid fabrication of a large number of both grafted and intercalated products. Figure 2-5 provides the XRD patterns of 10 hybrids prepared from $HLaNb_2O_7$ (HLN), in all cases the first reflection shifts to lower angles on expansion of the interlayer. Alcohol grafting products are shown in Figures 2-5b – 2-5e and amine intercalation products in Figures 2-5f – 2-5k. Raman spectroscopy further supported the presence of alkyl chains as well as C-N/C-O bonds in the hybrids (Figure 2-6a). Synthesis of C_nH_{2n+1}-LN (n = 1, 3) and $C_nH_{2n+1}NH_2$-LN (n = 1 – 4) was initiated from the protonated host (HLN). In the case of C_nH_{2n+1}-LN (n = 5, 10) and $C_nH_{2n+1}NH_2$-LN (n = 6, 8), efficient grafting/intercalation is obtained if shorter organics (n = 3, 5 and n =3, 4 for the alcohols and amines, respectively) are already present in the interlayer. TGA results are provided in Table 2-2 for the entire series (Figure 2-7 shows the TGA and DSC curves for these 10 hybrids). The estimated organic loading per [$LaNb_2O_7$] unit is in the range of 0.83-1.3, which is in agreement with that previously reported in Dion-Jacobson hosts.[48,49] Table 2-3 presents the unit cell

parameters for the series of alcohols and amines (when available, literature values are shown for comparison). The interlayer spacing clearly increases as the length of the intercalated/grafted organic substituent increases.

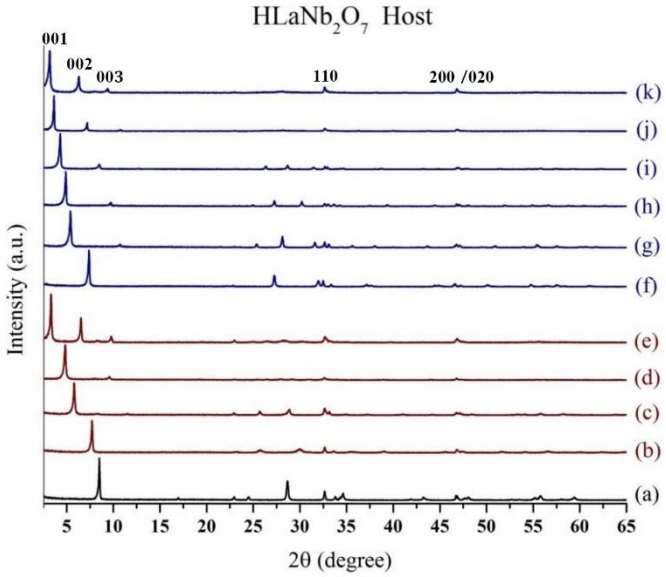

Figure 2-5: XRD patterns of (a) HLN, (b-e) n-alkoxy-LN (C_nH_{2n+1}-$LaNb_2O_7$ where n=1, 3, 5 and 10 in b, c, d and e, respectively), and (f-k) n-alkylamine-LN ($C_nH_{2n+1}NH_2$-$LaNb_2O_7$ where n=1, 2, 3, 4, 6 and 8 in f, g, h, i, j and k, respectively).

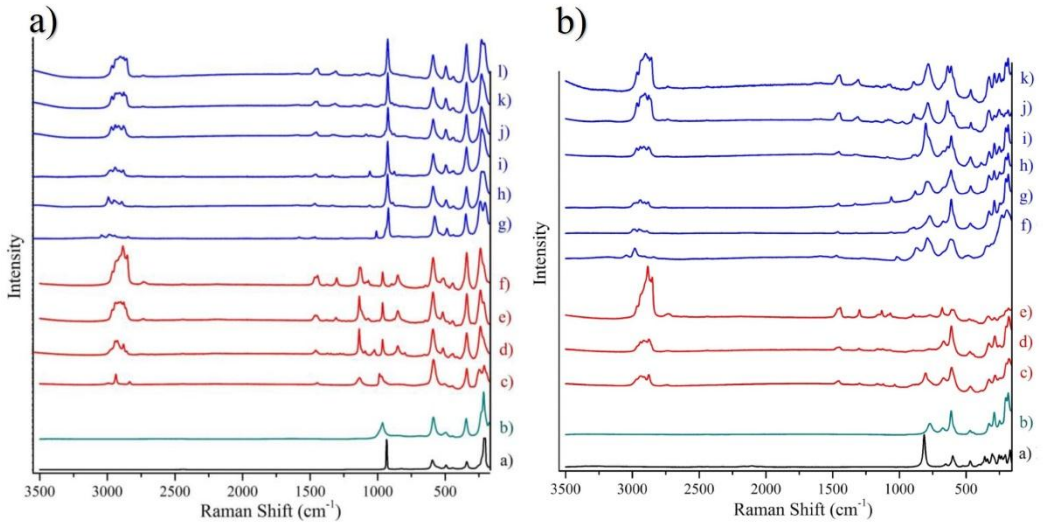

Figure 2-6: Raman spectra provided for the hybrids based on HLN and HCT.

a) RLN-based products: (a) RLN, (b) HLN, (c-f) n-alkoxy-LN (C_nH_{2n+1}-$LaNb_2O_7$ where n=1, 3, 5 and 10 in c, d, e and f respectively) and (g-l) n-alkylamine-LN ($C_nH_{2n+1}NH_2$-$LaNb_2O_7$ where n=1, 2, 3, 4, 6 and 8 in g, h, ©, j, k and l respectively).

b) LCT-based products: (a) LCT, (b) HCT, (c-e) n-alkoxy-CT (C_nH_{2n+1}-$CaTa_2O_7$ where n=3, 5 and 10 in c, d and e respectively) and (f-k) n-alkylamine-CT ($C_nH_{2n+1}NH_2$-$CaTa_2O_7$ where n= 1, 2, 3, 4, 6 and 8 in f, g, h, ©, j and k respectively).

Table 2-2: TGA results and approximate organic loading for HLN-based hybrids prepared by the microwave methods.

	Chemical Formula of the Organic Substituent		Weight Loss% * (organic + water)	Estimation of Loading per $[LaNb_2O_7]$	
	$HLaNb_2O_7$		2.07(2)	1.007(4)	
Grafted Hybrids	CH_3O-	methoxy	5.1(6)	0.99(3)	
	C_3H_7O-	n-propoxy	8.45(1)	0.7745(1)	0.85 [49] **
	$C_5H_{11}O$-	n-pentoxy	13(2)	0.84(1)	
	$C_{10}H_{21}O$-	n-decoxy	22(3)	0.833(7)	0.87 [49] **
Intercalated Hybrids	CH_3NH_2	methylamine	8.30(1)	0.9685(2)	
	$C_2H_5NH_2$	Ethylamine	11(2)	0.96(2)	
	$C_3H_7NH_2$	n-propylamine	13.6(8)	0.995(6)	
	$C_4H_9NH_2$	n-butylamine	19.95(7)	1.301(0)	
	$C_6H_{13}NH_2$	n-hexylamine	20(1)	0.999(4)	
	$C_8H_{17}NH_2$	n-octylamine	23.2(2)	0.9389(7)	

*Average of at least three TGA-DSC runs
** Literature values calculated based on the carbon content

Table 2-3: Unit cell parameters for RLN, HLN and derived hybrids.

	Chemical Formula of the Organic Substituent		Lattice Parameter (Å)		Literature Lattice Parameter (Å)	
			a	c	a	c
	$RbLaNb_2O_7$		3.884(2)	10.9626(3)	3.885(2)	10.989(3) [68,76]
	$HLaNb_2O_7$		3.883(3)	10.4527(5)	3.8886(4)	10.5483(12) [49,77]
					3.891(4)	10.578(6) [49]
Grafted Hybrids	CH_3O-	Methoxy	3.883(4)	23.0579(5) *	-	11.8 [48]
	C_3H_7O-	n-propoxy	3.888(3)	15.4011(5)	-	15.3 [49]
	$C_5H_{11}O$-	n-pentoxy	3.886(6)	18.5051(9)	-	-
	$C_{10}H_{21}O$-	n-decoxy	3.876(5)	27.2380(6)	-	27.3 [49]
Intercalated Hybrids	CH_3NH_2	Methylamine	3.899(6)	12.1073(6)	-	-
	$C_2H_5NH_2$	Ethylamine	3.884(2)	16.5819(2)	-	-
	$C_3H_7NH_2$	n-propylamine	3.884(3)	18.3316(2)	-	-
	$C_4H_9NH_2$	n-butylamine	3.881(3)	20.9230(3)	-	-
	$C_6H_{13}NH_2$	n-hexylamine	3.873(8)	24.7800(6)	-	-
	$C_8H_{17}NH_2$	n-octylamine	3.877(8)	28.3872(7)	-	-

* Larger c parameter needed to index the powder pattern

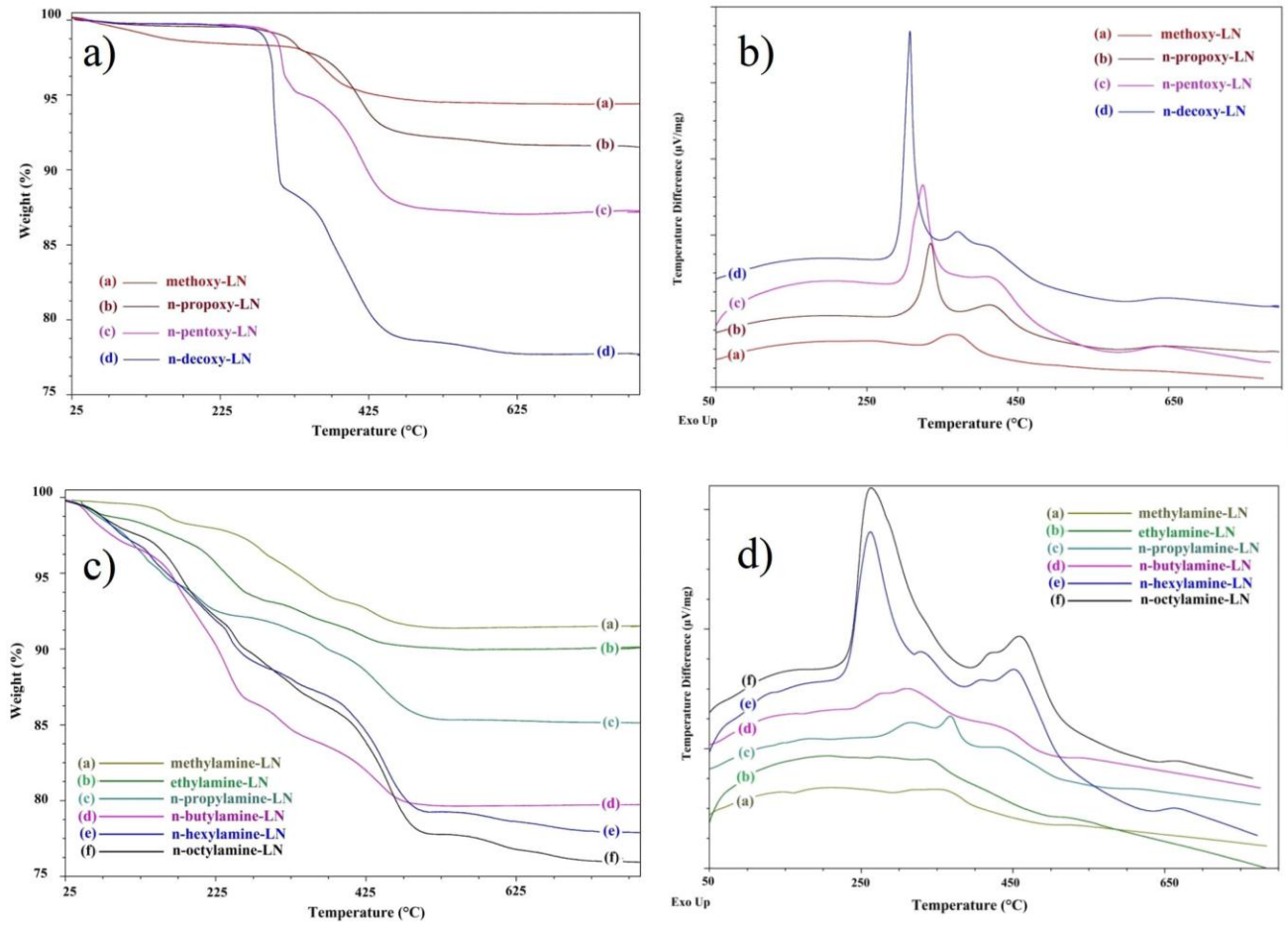

Figure 2-7: a) TGA and b) DSC curves for n-alkoxy-LN and c) TGA and d) DSC curves for n-alkylamine-LN.

Similar ion exchange, grafting, and intercalation reactions were also carried out on $RbPrNb_2O_7$ (RPN). As expected, comparable reactivity as to that seen for RLN is observed (Figure 2-8a and 2-8b).

Grafting of n-pentanol and n-decanol is also possible straight from the protonated form (HLN), as shown in Figure 2-9. However, this single-step reaction was found to be incomplete as the product mainly contains the HLN starting material (Figure 2-9a and 2-9c). Multistep expansion of the interlayer leads to better quality hybrids with the longer-chain substituents. As shown in Figure 2-9, n-hexylamine and n-octylamine intercalation products were also attainable directly from HLN host, but products from this single-step reaction are of poorer quality compared to those obtained from an n-butylamine-LN intermediate.

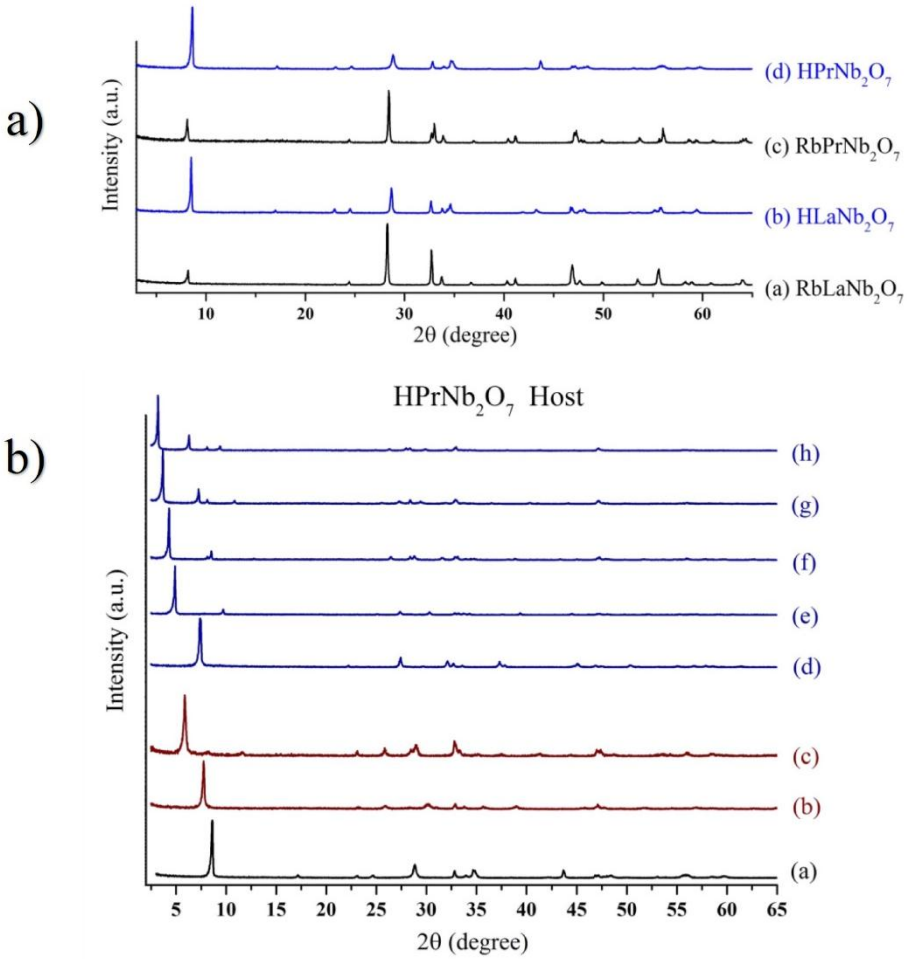

Figure 2-8: Results on topochemical modification of RPN host, isostructural with RLN.

a) Comparing the XRD patterns of RPN and HPN with RLN and HLN; (a) RLN, (b) HLN, (c) RPN, and (d) HPN.

b) HPN-based hybrids; (a) HPN, (b, c) C_nH_{2n+1}-PN (n=1 and 3 for b and c respectively), and (d-h) $C_nH_{2n+1}NH_2$-PN (n=1, 3, 4, 6, and 8 in d, e, f, g and h, respectively).

The formation of organic-inorganic hybrids from the triple-layered Dion-Jacobson host $HCa_2Nb_3O_{10}$ (HCN) was also studied (Figure 2-10). In the case of HCN, intercalation of n-alkylamines ($C_nH_{2n+1}NH_2$, n = 1-4, 6, 8) readily occurred under the same experimental conditions as HLN. The only difference between these two hosts was n-alcohol reactivity; successful grafting of only methanol was seen despite examination of different sets of reaction conditions, even those proceeding through either alkoxy or amine intermediates. Grafting of n-propanol and n-hexanol was recently reported by Boykin and Smith with microwaves;[67] the reaction conditions we examined did not produce successful grafting reactions with n-alcohols where n>1.

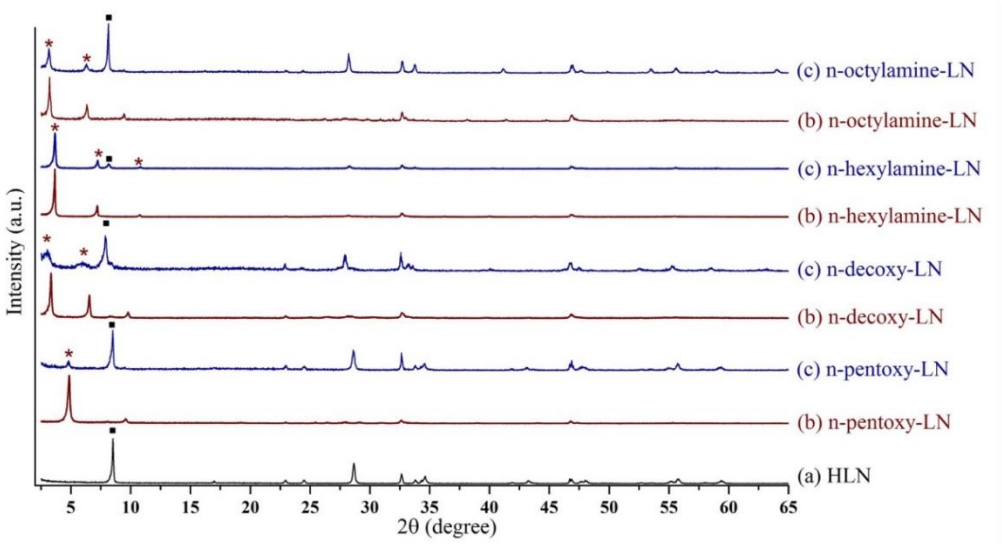

Figure 2-9: Comparing four different hybrids based on (a) HLN host, prepared either from (b) intermediates or (c) straight from HLN.

▪ Square peaks: the incompletion of the reaction due to the presence of HLN starting material.

*** Star peaks: the existence of the target products provided in (b), despite the incomplete reactions in (c).**

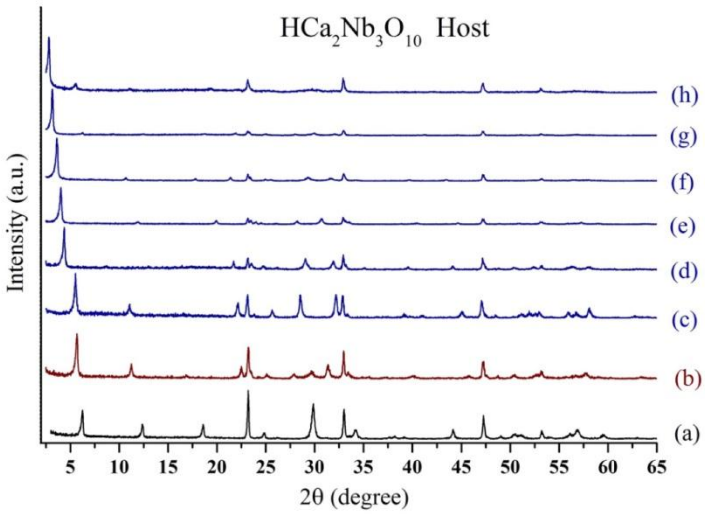

Figure 2-10: HCN-based hybrids; (a) HCN, (b) methoxy-CN, and (c-h) n-alkylamine-CN ($C_nH_{2n+1}NH_2$-CN, where n=1, 2, 3, 4, 6, and 8 for c, d, e, f, g and h, respectively).

The microwave approach is also quite effective for modification of Ruddlesden-Popper type hosts. The XRD patterns of 7 different hybrids synthesized from $H_2CaTa_2O_7$ (HCT) are provided in Figure 2-11. Preparation of n-alkylamine intercalated products, $C_nH_{2n+1}NH_2$-CT (n =

1 – 4) was carried out directly from the protonated host (The products n = 1, 2 are shown in Figure 2-12). Figures 2-11e and 2-11f show the intercalated products where n = 3 and 4, respectively. $C_nH_{2n+1}NH_2$-CT (n = 6, 8), Figures 2-11g and 2-11h, were obtained from n-alkylamine-CT intermediates (n = 3 or 4). In order to create n-alkoxy bonds in the interlayer, amine intercalated intermediates were used since direct reactions with protonated hosts were not successful.[45,51] To obtain C_nH_{2n+1}-CT (n = 3, Figure 2-11b), 1-propylamine-CT was reacted with n-propanol. Further reactions with n-propoxy-CT acting as an intermediate were then possible, leading to longer-chain alkoxy substituents (n = 5, 10, Figure 2-11c, 2-11d). Unit cell parameters for the complete HCT reaction series are presented in Table 2-4. There is good agreement between literature lattice parameters and those values observed here (in some cases by doubling the c parameter). The indexed cells provided for $C_nH_{2n+1}NH_2$-CT (n = 3, 4, 6 and 8) and n-pentoxy-CT have not been previously reported. Successful intercalation/grafting reactions on HCT were also supported by Raman spectroscopic characterization (Figure 2-6b).

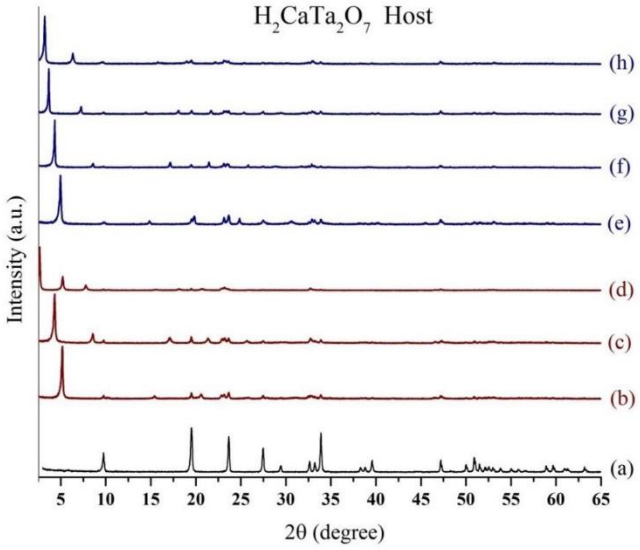

Figure 2-11: XRD patterns of the hybrids based on HCT. (a) HCT, (b-d) n-alkoxy-CT (C_nH_{2n+1}-$CaTa_2O_7$ where n=3, 5 and 10 in b, c and d, respectively), and (e-h) n-alkylamine-CT ($C_nH_{2n+1}NH_2$-$CaTa_2O_7$ where n= 3, 4, 6 and 8 in e, f, g and h, respectively).

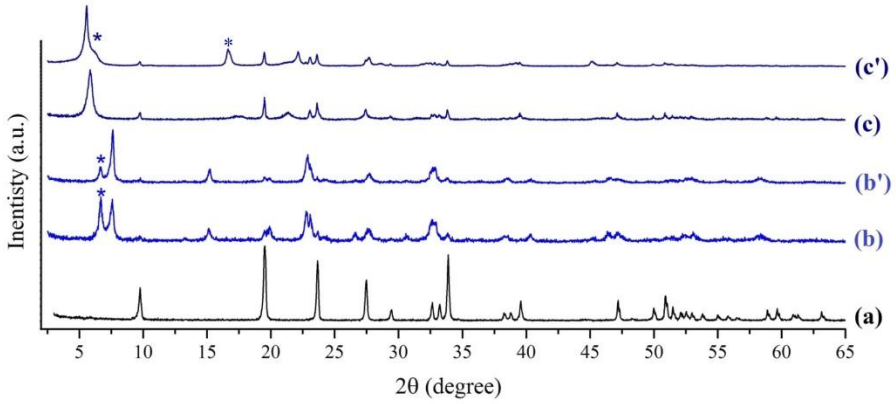

Figure 2-12: XRD patterns of (a) HCT host, (b) methylamine-CT, (b') methylamine-CT in b retreated with fresh methylamine, (c) ethylamine-CT with a broad first peak, and (c') ethylamine-CT with a shouldered first peak.

Table 2-4: Unit cell parameters of LCT, HCT and organic grafted/intercalated products.

	Chemical Formula of the Organic Substituent		Lattice Parameter (Å)			Literature Lattice Parameter (Å)		
			a	b	c	a	b	c
	$Li_2CaTa_2O_7$		5.506(2)	5.455(2)	18.193(6)	5.5153(1)	5.4646(1)	18.2375(3) [70]
	$H_2CaTa_2O_7$		5.403(2)	5.497(2)	18.242(6)	5.409(2)	5.506(6)	18.274(0) [45]
Grafted Hybrids	C_3H_7O-	n-propoxy	4.010(2)	3.848(2)	17.25(1)*	3.920(6)	3.859(1)	34.621(9) [45]
	$C_5H_{11}O$-	n-pentoxy	3.892(4)	3.841(3)	20.75(2)	-	-	-
	$C_{10}H_{21}O$-	n-decoxy	3.904(3)	3.847(4)	34.16(3)*	3.916(4)	3.857(6)	70.052(1) [45]
Intercalated Hybrids	$C_3H_7NH_2$	n-propylamine	3.868(2)	3.845(2)	17.930(9)	-	-	-
	$C_4H_9NH_2$	n-butylamine	3.922(3)	3.849(4)	20.64(1)	-	-	-
	$C_6H_{13}NH_2$	n-hexylamine	3.885(5)	3.849(3)	24.51(2)	-	-	-
	$C_8H_{17}NH_2$	n-octylamine	3.906(3)	3.855(2)	27.33(2)	-	-	-

* Diffraction patterns indexed with smaller c parameters than those reported in reference [45]

In the case of the triple-layered Ruddlesden-Popper (HLT), successful reactions are limited to $C_nH_{2n+1}NH_2$, n = 1, 3, 4, 6 and 8 (Figure 2-13). Many in this series, however, show incomplete conversion and a loss in crystallinity. This seems to be more dependent on the inorganic host rather than the conditions of the modification reaction, as multiple treatments of the HLT-based hybrids did not improve the conversion or crystallinity. Since, the reactions to form the $C_nH_{2n+1}NH_2$-LT amines were incomplete, use of these samples as intermediates for grafting reactions were not attempted.

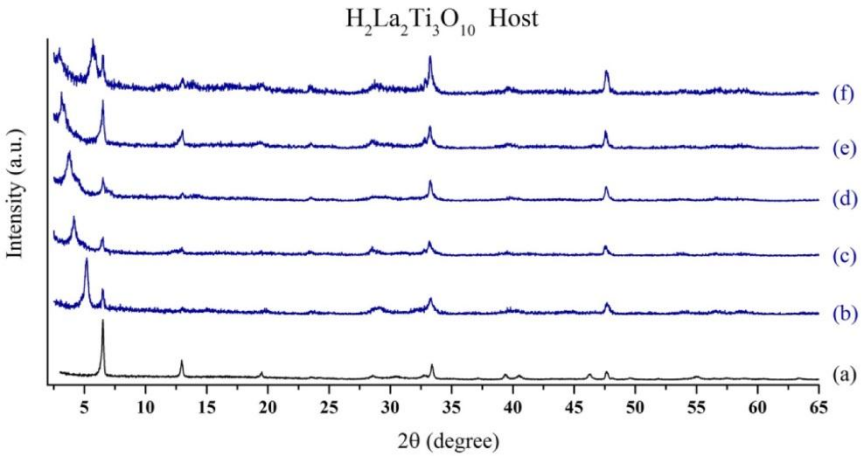

Figure 2-13: XRD patterns of five amine-intercalated products based on HLT host (a), $C_nH_{2n+1}NH_2$-LT, where n = 1, 3, 4, 6, and 8 for (b), (c), (d), (e) and (f), respectively.

2.4– Discussion

Solvothermal synthesis is based more on conductive heating with an external heat source, while microwave irradiation produces efficient internal heating.[32] This so-called "in core volumetric heating" can potentially increase the reaction speed as well as temperature uniformity. Recently, Boykin and Smith used microwaves to carry out grafting reactions with n-alcohols for the triple-layered Dion-Jacobson hosts Rb*Ae*$_2$Nb$_3$O$_{10}$ (*Ae* = Ca, Sr);[67] the control of temperature and power, however, was limited due to the use of a simple domestic microwave. In the present work, a dedicated microwave station (Figure 2-1) was used, allowing one to reproducibly achieve specific temperatures and powers.

In this study, the microwave method was investigated for a series of topochemical reactions. For comparison within the RLN series, solvothermal methods were also used. In all instances, the two approaches gave very similar results, though the microwave method was able to complete the reaction in hours instead of days. Figures 2-3 and 2-4 and Table 2-1 compare diffraction and thermal data for sets of HLN, propoxy-LN, and decoxy-LN samples that were produced by both microwave and solvothermal methods. The diffraction and thermal analysis gave very similar results in terms of the lattice parameters and organic loading per [$LaNb_2O_7$] unit regardless of the synthesis method, further confirming the effectiveness of the microwave method. In previous syntheses reported by Suzuki et al.,[49] the series of reactions from HLN to

decoxy-LN were carried out in sealed ampules with reaction times as long as 13 d total (3 d protonation at 60 ˚C, 3 d n-propanol grafting at 80 ˚C, and 7 d final reaction with n-decanol at 80 ˚C). In the solvothermal reactions carried out as controls in the current study, the reaction times were reduced, cutting the duration to 5 d (2 d protonation at 90 ˚C, 2 d n-propanol grafting at 100 ˚C, and 1 d final reaction with n-decanol at 200 ˚C, all steps done in autoclaves). It then becomes especially significant that this same reaction was carried out in only 4.5 h with microwave methods. Even considering the warmup time of each reaction, the overall process did not exceed 6 h (3 h protonation at 60 ˚C, 1 h n-propanol grafting at 100 ˚C, and 30 min reaction with n-decanol at 150 ˚C).

For the triple-layered Dion-Jacobson ($KCa_2Nb_3O_{10}$), both microwave assisted proton exchange and amine intercalation reactions readily occur. With regards to grafting reactions, the reactivity with n-alcohols was limited to methanol only. This is in contrast to what has been observed by others[67] and may relate to reaction parameters investigated in our study.

Another part of the study involved the organic modification of Ruddlesden-Popper perovskites, $H_2CaTa_2O_7$ (HCT) and $H_2La_2Ti_3O_{10}$ (HLT).[45,51] As presented in Figure 2-11, intercalation/grafting reactions on HCT hosts were quite successful (using $C_nH_{2n+1}NH_2$, n = 1 - 4, 6, 8 and $C_nH_{2n+1}OH$, n = 3, 5, 10). In the case of direct intercalation of methylamine, there appears to be two phases produced in this reaction (Figure 2-12). The peak at $2\Theta = 6.640$ degrees (d spacing ~13.3 Å) corresponds to literature values,[45] while the higher angle peak at $2\Theta = 7.626$ degrees has not been previously reported for this compound. Interestingly, the high angle reflection becomes more intense after the sample is treated again with fresh methylamine (Figure 2-12b'). In case of ethylamine, the reaction from HCT was also successful, however, the diffraction peaks are broader compared to the sharp peaks present in the rest of the products (Figure 2-12c versus Figure 2-11). In contrast, while HLT is readily prepared via microwave-assisted protonation, subsequent amine intercalation reactions are always incomplete with a slight loss in crystallinity. This behavior may relate to the poor reactivity of anhydrous HLT with organics; considering that HLT was obtained as an anhydrous phase in the present experiments and that anhydrous HLT cannot be rehydrated in water.[44,50]

To further highlight the advantages of the microwave method compared to conventional methods, the reaction duration to synthesize n-propoxy-CT from $Li_2CaTa_2O_7$ can be compared to

that previously reported by Wang et al.[45] using an autoclave approach. As they reported a 16 d modification via conventional mehods[45] (3 d protonation with 4 M HNO_3 at room temperature, 3 d autoclave treatment with methylamine at 80 ˚C, 3 d autoclave exchange with methanol at 80 ˚C, and finally 7 d exchange of methanol with n-propanol at 80 ˚C), n-propoxy-CT was obtained in only 5 h in the present work (3 h protonation with 4 M HNO_3 at 60 ˚C, 1 h reaction at 100 ˚C to prepare n-propylamine-CT, and finally exchanging for n-propanol from the amine intermediate was done at 100 ˚C for 1 h). It is worth noting that microwave method is applied on Ruddlesden-Popper family herein for the first time, successfully carrying out proton exchange, intercalation and grafting.

As presented in Tables 2-3 and 2-5, XRD patterns were indexed for the hybrids obtained from the HLN and HCT hosts. $RbLaNb_2O_7$, $HLaNb_2O_7$, and HLN-based hybrids were all indexed on tetragonal cells, while $Li_2CaTa_2O_7$, $H_2CaTa_2O_7$, and derived hybrids were indexed on

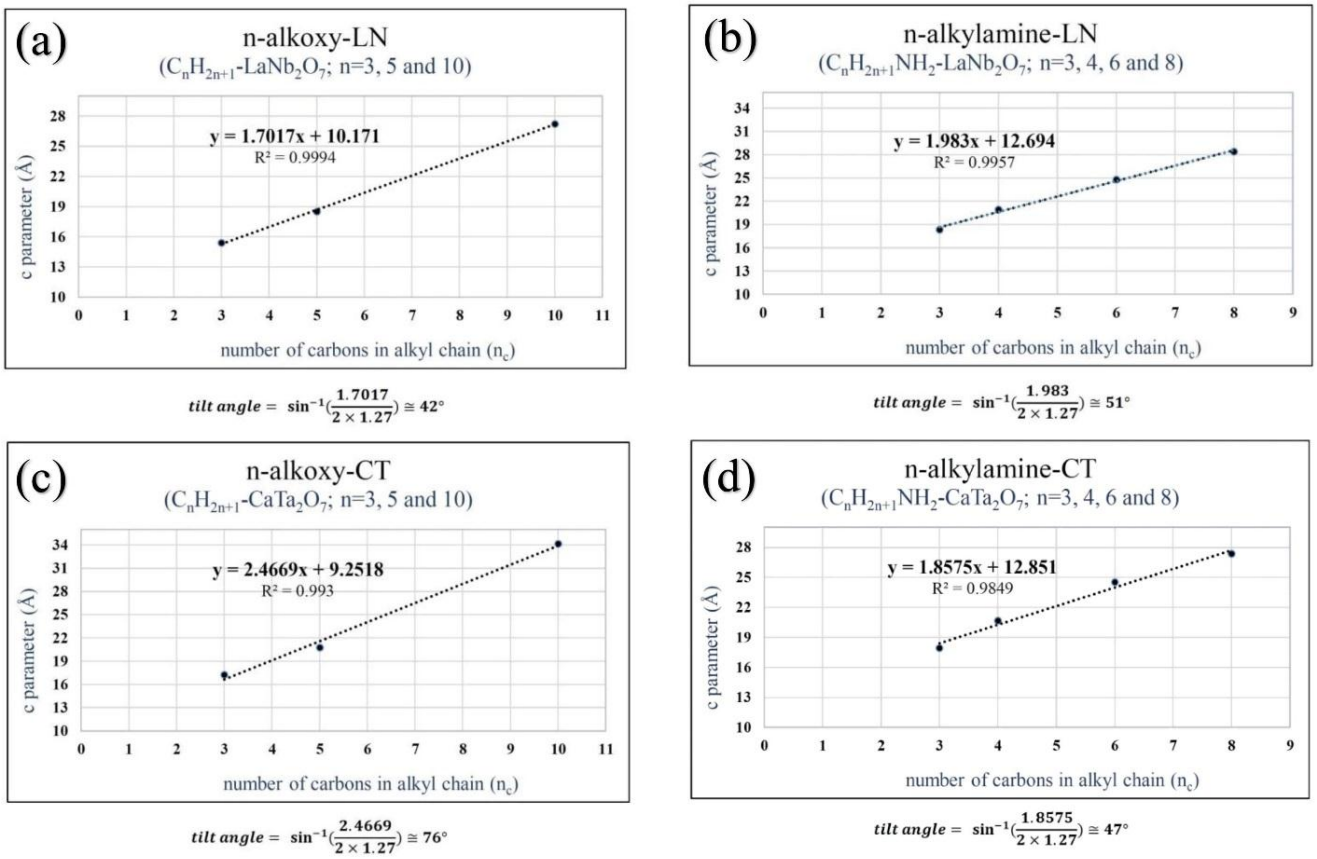

Figure 2-14: Relationship between the c parameter of the hybrid and the number of the carbons in the alkyl chains, calculated for (a) n-alkoxy-LN, (b) n-alkylamine-LN, (c) n-alkoxy-CT, and (d) n-alkylamine-CT.

orthorhombic cells. Using the layer spacings for the various hybrids, the orientation of the organic chains in the interlayer of HLN and HCT hosts was estimated based on the methods proposed in the literature (see Figure 2-14).[44,45,50,51,78,79] In the case of n-alkoxy-LN and n-alkoxy-CT the tilt angles were calculated as 42° and 76°, respectively, which are similar to that of literature values (57° for n-alkoxy-LN,[48] 41° for n-alkoxy-CN,[50] and 70° for n-alkoxy-CT[45]). The schematic model of n-propoxy-CT is presented in Figure 2-15 as an example.

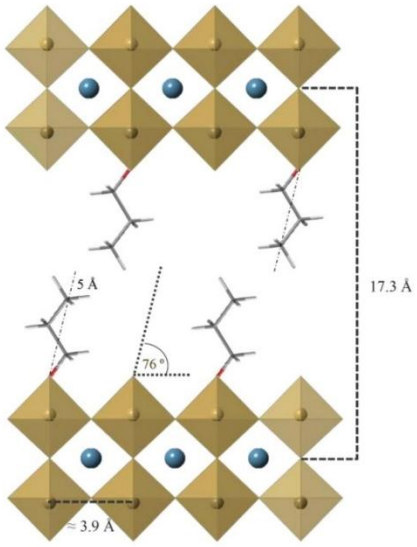

Figure 2-15: The schematic model of n-propoxy-CT product.

In the present work, no water was added to the hydrophobic solvents (1-hexylamine, 1-octylamine, 1-pentanol and 1-decanol). This experimental condition was not limited to the hybrids synthesized via the microwave technique, but was also applied for the solvothermal control reactions involving 1-decanol. Researchers, however, have suggested that exchange reactions require 1-3 mass% of added water at 80 ˚C.[44,45,48,50,51] Though water was not added to our reactions, it is possible that small amounts of water were present in the host or became available due to moisture in the air and that this combined with higher reaction temperatures[44,50] (100-150 ˚C) allowed reactions to readily occur.

2.5– Conclusions

Microwave techniques can be effective for the topochemical manipulation of layered perovskites. Combinations of proton exchange, grafting, and intercalation are possible. These methods quickly lead to a series of organic-inorganic hybrids as demonstrated on four different Dion-Jacobson and Ruddlesden-Popper hosts, $HLaNb_2O_7$, $HCa_2Nb_3O_{10}$, $H_2CaTa_2O_7$ and $H_2La_2Ti_3O_{10}$. Rapidity, coupled with the ability to make gram quantities of materials, highlights the potential of this approach for effectively expanding the production of new and known organic-inorganic hybrids. Taking advantage of rapid reactions permits one to screen a variety of reaction conditions and organic-inorganic hybrids for different applications. One can then begin

to design and screen various organic substituents such that different combinations could lead to new hybrids with technologically significant properties.

2.6– References

(1) Buffler, C. R. *Microwave Cooking and Processing*; Van Nostrand Reinhold: New York, 1993.

(2) Clark, D. E.; Sutton, W. H. Microwave Processing of Materials. *Annu. Rev. Mater. Sci.* **1996**, *26* (1), 299–331.

(3) Jones, D. A.; Lelyveld, T. P.; Mavrofidis, S. D.; Kingman, S. W.; Miles, N. J. Microwave Heating Applications in Environmental Engineering—a Review. *Resour. Conserv. Recycl.* **2002**, *34* (2), 75–90.

(4) Horikoshi, S.; Saitou, A.; Hidaka, H.; Serpone, N. Environmental Remediation by an Integrated Microwave/UV Illumination Method. V. Thermal and Nonthermal Effects of Microwave Radiation on the Photocatalyst and on the Photodegradation of Rhodamine-B under UV/Vis Radiation. *Environ. Sci. Technol.* **2003**, *37* (24), 5813–5822.

(5) Wu, T.-N. Environmental Perspectives of Microwave Applications as Remedial Alternatives: Review. *Pract. Period. Hazard. Toxic Radioact. Waste Manag.* **2008**, *12* (2), 102–115.

(6) Alcazar, J.; Diels, G.; Schoentjes, B. Microwave Assisted Medicinal Chemistry. *Mini Rev. Med. Chem.* **2007**, *7* (4), 345–369.

(7) Alcázar, J.; Oehlrich, D. Recent Applications of Microwave Irradiation to Medicinal Chemistry. *Future Med. Chem.* **2010**, *2* (2), 169–176.

(8) Kappe, C. O.; Stadler, A.; Dallinger, D. *Microwaves in Organic and Medicinal Chemistry*; Wiley-VCH Verlag GmbH & Co. KGaA: Weinheim, Germany, 2012.

(9) Horikoshi, S.; Serpone, N. General Features of Microwave Chemistry. In *Microwaves in Nanoparticle Synthesis*; Horikoshi, S., Serpone, N., Eds.; Wiley-VCH Verlag GmbH & Co. KGaA: Weinheim, Germany, 2013.

(10) Smith, F. E.; Arsenault, E. A. Microwave-Assisted Sample Preparation in Analytical Chemistry. *Talanta* **1996**, *43* (8), 1207–1268.

(11) Jin, Q.; Liang, F.; Zhang, H.; Zhao, L.; Huan, Y.; Song, D. Application of Microwave Techniques in Analytical Chemistry. *TrAC Trends Anal. Chem.* **1999**, *18* (7), 479–484.

(12) Srogi, K. A Review: Application of Microwave Techniques for Environmental Analytical Chemistry. *Anal. Lett.* **2006**, *39* (7), 1261–1288.

(13) Kubrakova, I. V.; Toropchenova, E. S. Microwave Heating for Enhancing Efficiency of Analytical Operations (Review). *Inorg. Mater.* **2008**, *44* (14), 1509–1519.

(14) Trivedi, N.; Patadia, M.; Kothari, V. Biological Applications of Microwaves. *Int J Life Sci Technol* **2011**, *4* (6), 37–46.

(15) Cirkva, V.; Hajek, M. Microwave Photochemistry. Photoinitiated Radical Addition of Tetrahydrofuran to Perfluorohexylethene under Microwave Irradiation. *J. Photochem. Photobiol. -Chem.* **1999**, *123* (1–3), 21–23.

(16) Klán, P.; Literák, J.; Relich, S. Molecular Photochemical Thermometers: Investigation of Microwave Superheating Effects by Temperature Dependent Photochemical Processes. *J. Photochem. Photobiol. Chem.* **2001**, *143* (1), 49–57.

(17) Deshayes, S.; Liagre, M.; Loupy, A.; Luche, J.-L.; Petit, A. Microwave Activation in Phase Transfer Catalysis. *Tetrahedron* **1999**, *55* (36), 10851–10870.

(18) Larhed, M.; Moberg, C.; Hallberg, A. Microwave-Accelerated Homogeneous Catalysis in Organic Chemistry. *Acc. Chem. Res.* **2002**, *35* (9), 717–727.

(19) Will, H.; Scholz, P.; Ondruschka, B. Microwave-Assisted Heterogeneous Gas-Phase Catalysis. *Chem. Eng. Technol.* **2004**, *27* (2), 113–122.

(20) Young, D. D.; Nichols, J.; Kelly, R. M.; Deiters, A. Microwave Activation of Enzymatic Catalysis. *J. Am. Chem. Soc.* **2008**, *130* (31), 10048–10049.

(21) Baghurst, D. R.; Mingos, D. M. P. Application of Microwave Heating Techniques for the Synthesis of Solid State Inorganic Compounds. *J. Chem. Soc. Chem. Commun.* **1988**, No. 12, 829–830.

(22) Rao, K. J.; Vaidhyanathan, B.; Ganguli, M.; Ramakrishnan, P. A. Synthesis of Inorganic Solids Using Microwaves. *Chem. Mater.* **1999**, *11* (4), 882–895.

(23) Bilecka, I.; Niederberger, M. Microwave Chemistry for Inorganic Nanomaterials Synthesis. *Nanoscale* **2010**, *2* (8), 1358–1374.

(24) Baghbanzadeh, M.; Carbone, L.; Cozzoli, P. D.; Kappe, C. O. Microwave-Assisted Synthesis of Colloidal Inorganic Nanocrystals. *Angew. Chem. Int. Ed.* **2011**, *50* (48), 11312–11359.

(25) VanAtta, S. L.; Duclos, B. A.; Green, D. B. Microwave-Assisted Synthesis of Group 6 (Cr, Mo, W) Zerovalent Organometallic Carbonyl Compounds. *Organometallics* **2000**, *19* (12), 2397–2399.

(26) Ardon, M.; Hogarth, G.; Oscroft, D. T. W. Organometallic Chemistry in a Conventional Microwave Oven: The Facile Synthesis of Group 6 Carbonyl Complexes. *J. Organomet. Chem.* **2004**, *689* (15), 2429–2435.

(27) Ni, Z.; Masel, R. I. Rapid Production of Metal-Organic Frameworks via Microwave-Assisted Solvothermal Synthesis. *J. Am. Chem. Soc.* **2006**, *128* (38), 12394–12395.

(28) Seo, Y.-K.; Hundal, G.; Jang, I. T.; Hwang, Y. K.; Jun, C.-H.; Chang, J.-S. Microwave Synthesis of Hybrid Inorganic–organic Materials Including Porous $Cu_3(BTC)_2$ from Cu(II)-Trimesate Mixture. *Microporous Mesoporous Mater.* **2009**, *119* (1–3), 331–337.

(29) Zong, L.; Zhou, S.; Sgriccia, N.; Hawley, M. C.; Kempel, L. C. A Review of Microwave-Assisted Polymer Chemistry (MAPC). *J. Microw. Power Electromagn. Energy Publ. Int. Microw. Power Inst.* **2002**, *38* (1), 49–74.

(30) Bogdal, D.; Prociak, A. *Microwave-Enhanced Polymer Chemistry and Technology*; Blackwell Publishing Professional: Ames, IA, 2007.

(31) Caddick, S. Microwave-Assisted Organic-Reactions. *Tetrahedron* **1995**, *51* (38), 10403–10432.

(32) Kappe, C. O.; Dallinger, D.; Murphree, S. S. *Practical Microwave Synthesis for Organic Chemists*; Wiley-VCH Verlag GmbH & Co. KGaA: Weinheim, Germany, 2009.

(33) Hayes, B. L. *Microwave Synthesis: Chemistry at the Speed of Light*; CEM Pub.: Matthews, NC, 2002.

(34) Kappe, C. O. Microwave Dielectric Heating in Synthetic Organic Chemistry. *Chem. Soc. Rev.* **2008**, *37* (6), 1127–1139.

(35) Kappe, C. O. High-Speed Combinatorial Synthesis Utilizing Microwave Irradiation. *Curr. Opin. Chem. Biol.* **2002**, *6* (3), 314–320.

(36) Lidström, P.; Tierney, J.; Wathey, B.; Westman, J. Microwave Assisted Organic Synthesis—a Review. *Tetrahedron* **2001**, *57* (45), 9225–9283.

(37) Kickelbick, G. *Hybrid Materials: Synthesis, Characterization, and Applications*; Wiley-VCH Verlag GmbH & Co. KGaA: Weinheim, Germany, 2007.

(38) Mitzi, D. B. Templating and Structural Engineering in Organic–inorganic Perovskites. *J. Chem. Soc. Dalton Trans.* **2001**, No. 1, 1–12.

(39) Balazs, A. C.; Emrick, T.; Russell, T. P. Nanoparticle Polymer Composites: Where Two Small Worlds Meet. *Science* **2006**, *314* (5802), 1107–1110.

(40) Mammeri, F.; Bourhis, E. L.; Rozes, L.; Sanchez, C. Mechanical Properties of Hybrid Organic–inorganic Materials. *J. Mater. Chem.* **2005**, *15* (35–36), 3787–3811.

(41) Mitzi, D. B.; Chondroudis, K.; Kagan, C. R. Organic-Inorganic Electronics. *IBM J. Res. Dev.* **2001**, *45* (1), 29–45.

(42) Sanchez, C.; Julián, B.; Belleville, P.; Popall, M. Applications of Hybrid Organic–inorganic Nanocomposites. *J. Mater. Chem.* **2005**, *15* (35–36), 3559–3592.

(43) Sanchez, C.; Soler-Illia, G. J. de A. A.; Ribot, F.; Lalot, T.; Mayer, C. R.; Cabuil, V. Designed Hybrid Organic−Inorganic Nanocomposites from Functional Nanobuilding Blocks. *Chem. Mater.* **2001**, *13* (10), 3061–3083.

(44) Tahara, S. Preparation of Inorganic-Organic Hybrids via Intercalation and Grafting Reactions of Protonated Forms of Ion-Exchangeable Layered Perovskites, Waseda University, 2007.

(45) Wang, Y.; Wang, C.; Wang, L.; Hao, Q.; zhu, X.; Chen, X.; Tang, K. Preparation of Interlayer Surface Tailored Protonated Double-Layered Perovskite $H_2CaTa_2O_7$ with N-Alcohols, and Their Photocatalytic Activity. *RSC Adv* **2014**, *4* (8), 4047–4054.

(46) Mitzi, D. B.; Dimitrakopoulos, C. D.; Kosbar, L. L. Structurally Tailored Organic−Inorganic Perovskites: Optical Properties and Solution-Processed Channel Materials for Thin-Film Transistors. *Chem. Mater.* **2001**, *13* (10), 3728–3740.

(47) Sanjaya Ranmohotti, K. G.; Josepha, E.; Choi, J.; Zhang, J.; Wiley, J. B. Topochemical Manipulation of Perovskites: Low-Temperature Reaction Strategies for Directing Structure and Properties. *Adv. Mater.* **2011**, *23* (4), 442–460.

(48) Takahashi, S.; Nakato, T.; Hayashi, S.; Sugahara, Y.; Kuroda, K. Formation of Methoxy-Modified Interlayer Surface via the Reaction between Methanol and Layered Perovskite $HLaNb_2O_7.xH_2O$. *Inorg. Chem.* **1995**, *34* (20), 5065–5069.

(49) Suzuki, H.; Notsu, K.; Takeda, Y.; Sugimoto, W.; Sugahara, Y. Reactions of Alkoxyl Derivatives of a Layered Perovskite with Alcohols: Substitution Reactions on the Interlayer Surface of a Layered Perovskite. *Chem. Mater.* **2003**, *15* (3), 636–641.

(50) Tahara, S.; Sugahara, Y. Interlayer Surface Modification of the Protonated Triple-Layered Perovskite $HCa_2Nb_3O_{10}\cdot X H_2O$ with *N* -Alcohols. *Langmuir* **2003**, *19* (22), 9473–9478.

(51) Tahara, S.; Ichikawa, T.; Kajiwara, G.; Sugahara, Y. Reactivity of the Ruddlesden−Popper Phase $H_2La_2Ti_3O_{10}$ with Organic Compounds: Intercalation and Grafting Reactions. *Chem. Mater.* **2007**, *19* (9), 2352–2358.

(52) Kimura, N.; Kato, Y.; Suzuki, R.; Shimada, A.; Tahara, S.; Nakato, T.; Matsukawa, K.; Mutin, P. H.; Sugahara, Y. Single- and Double-Layered Organically Modified Nanosheets by Selective Interlayer Grafting and Exfoliation of Layered Potassium Hexaniobate. *Langmuir* **2014**, *30* (4), 1169–1175.

(53) Asai, Y.; Ariake, Y.; Saito, H.; Idota, N.; Matsukawa, K.; Nishino, T.; Sugahara, Y. Layered Perovskite Nanosheets Bearing Fluoroalkoxy Groups: Their Preparation and Application in Epoxy-Based Hybrids. *RSC Adv.* **2014**, *4* (51), 26932.

(54) Schaak, R. E.; Mallouk, T. E. Perovskites by Design: A Toolbox of Solid-State Reactions. *Chem. Mater.* **2002**, *14* (4), 1455–1471.

(55) Hodes, G. Perovskite-Based Solar Cells. *Science* **2013**, *342* (6156), 317–318.

(56) Lee, M. M.; Teuscher, J.; Miyasaka, T.; Murakami, T. N.; Snaith, H. J. Efficient Hybrid Solar Cells Based on Meso-Superstructured Organometal Halide Perovskites. *Science* **2012**, *338* (6107), 643–647.

(57) Conings, B.; Baeten, L.; De Dobbelaere, C.; D'Haen, J.; Manca, J.; Boyen, H.-G. Perovskite-Based Hybrid Solar Cells Exceeding 10% Efficiency with High Reproducibility Using a Thin Film Sandwich Approach. *Adv. Mater.* **2014**, *26* (13), 2041–2046.

(58) Zhang, W.; Saliba, M.; Stranks, S. D.; Sun, Y.; Shi, X.; Wiesner, U.; Snaith, H. J. Enhancement of Perovskite-Based Solar Cells Employing Core–Shell Metal Nanoparticles. *Nano Lett.* **2013**, *13* (9), 4505–4510.

(59) Han, Y.-S.; Park, I.; Choy, J.-H. Exfoliation of Layered Perovskite, $KCa_2Nb_3O_{10}$,into Colloidal Nanosheets by a Novel Chemical Process. *J. Mater. Chem.* **2001**, *11* (4), 1277–1282.

(60) Schaak, R. E.; Mallouk, T. E. Prying Apart Ruddlesden−Popper Phases: Exfoliation into Sheets and Nanotubes for Assembly of Perovskite Thin Films. *Chem. Mater.* **2000**, *12* (11), 3427–3434.

(61) Ebina, Y.; Sasaki, T.; Harada, M.; Watanabe, M. Restacked Perovskite Nanosheets and Their Pt-Loaded Materials as Photocatalysts. *Chem. Mater.* **2002**, *14* (10), 4390–4395.

(62) Xu, F. F.; Ebina, Y.; Bando, Y.; Sasaki, T. Structural Characterization of (TBA, H)$Ca_2Nb_3O_{10}$ Nanosheets Formed by Delamination of a Precursor-Layered Perovskite. *J. Phys. Chem. B* **2003**, *107* (36), 9638–9645.

(63) Tahara, S.; Takeda, Y.; Sugahara, Y. Preparation of Organic−Inorganic Hybrids Possessing Nanosheets with Perovskite-Related Structures via Exfoliation during a Sol−Gel Process. *Chem. Mater.* **2005**, *17* (24), 6198–6204.

(64) Tahara, S.; Okamoto, T.; Sugahara, Y. Preparation of a Nanocomposite Consisting of a Siloxane Network and Perovskite-Related Nanosheets via a Sol–gel Process. *Sci. Technol. Adv. Mater.* **2006**, *7* (5), 446–450.

(65) Tanimaa, K.; Watanabeb, M.; Imanaria, Y.; Kameia, S.; Uematsub, K.; Ishigakic, T.; Todaa, K.; Satob, M.; Masakid, T.; Yoond, D. H. Research on New Precursor for Nanosheets Phosphors. *J. Ceram. Process. Res.* **2013**, *14*, S71–S73.

(66) Takei, T.; Dong, Q.; Yonesaki, Y.; Kumada, N.; Kinomura, N. Preparation of Hybrid Film of Polyaniline and Organically Pillared Zirconium Phosphate Nanosheet by Electrodeposition. *Langmuir* **2011**, *27* (1), 126–131.

(67) Boykin, J. R.; Smith, L. J. Rapid Microwave-Assisted Grafting of Layered Perovskites with N-Alcohols. *Inorg. Chem.* **2015**, *54* (9), 4177–4179.

(68) Armstrong, A. R.; Anderson, P. A. Synthesis and Structure of a New Layered Niobium Blue Bronze: Rb_2LaNb_2O7. *Inorg. Chem.* **1994**, *33* (19), 4366–4369.

(69) Geselbracht, M. J.; Scarola, R. J.; Ingram, D.; Green, C.; Caldwell, J. H. Early Transition Metal Oxides and a Pinch of Salt: New Synthetic Routes to Titanates and Niobates. *MRS Proc.* **1996**, *453*, 147–152.

(70) Liang, Z.; Tang, K.; Shao, Q.; Li, G.; Zeng, S.; Zheng, H. Synthesis, Crystal Structure, and Photocatalytic Activity of a New Two-Layer Ruddlesden–Popper Phase, $Li_2CaTa_2O_7$. *J. Solid State Chem.* **2008**, *181* (4), 964–970.

(71) Hyeon, K.-A.; Byeon, S.-H. Synthesis and Structure of New Layered Oxides, $M^{II}La_2Ti_3O_{10}$ (M = Co, Cu, and Zn). *Chem. Mater.* **1999**, *11* (2), 352–357.

(72) Montasserasadi, D.; Granier, M. W.; Spinu, L.; Rai, S. C.; Zhou, W.; Wiley, J. B. Synthesis and Characterization of the Rare-Earth Dion–Jacobson Layered Perovskites, $APrNb_2O_7$ (A = Rb, Cs and CuCl). *Dalton Trans* **2015**, *44* (23), 10654–10660.

(73) Carvajal, R. *Comm Powder Diffr IUCr* **2001**, *26*, 12.

(74) Laugier, J.; Bochu, B. *LMGP-Suite Suite of Programs for the Interpretation of X-Ray Experiments, by Jean Laugier and Bernard Bochu, ENSP/Laboratoire Des Matériaux et Du Génie Physique, BP 46. 38042 Saint Martin d'Hères, France. WWW: http://www.inpg.fr/LMGP and http://www.ccp14.ac.uk/tutorial/lmgp/*.

(75) Hermann, A. T.; Wiley, J. B. Thermal Stability of Dion–Jacobson Mixed-Metal-Niobate Double-Layered Perovskites. *Mater. Res. Bull.* **2009**, *44* (5), 1046–1050.

(76) Gopalakrishnan, J.; Bhat, V.; Raveau, B. $AILaNb_2O_7$: A New Series of Layered Perovskites Exhibiting Ion Exchange and Intercalation Behaviour. *Mater. Res. Bull.* **1987**, *22* (3), 413–417.

(77) Sato, M.; Abo, J.; Jin, T.; Ohta, M. Structure and Ionic Conductivity of $MLaNb_2O_7$ (M: K, Na, Li, H). *J. Alloys Compd.* **1993**, *192* (1–2), 81–83.

(78) Jacobson, A. J.; Whittingham, M. S. *Intercalation Chemistry*; Academic Press: New York, NY, 1982.

(79) Amghouz, Z.; Espina, A.; García, J. R. Synthesis and Characterization of a New Family of Alkylammonium–chromium Phosphates with Worm-like Morphology. *J. Solid State Chem.* **2015**, *221*, 158–165.

Chapter 3. Further Characterization of Layered Hybrid Perovskites using Neutron Diffraction‡

3.1– Introduction

Hybrid materials, combining organic and inorganic counterparts at the atomic level, let us take advantage of both sets of features that each class has to offer at once.[1–6] Some hybrids allow for anchoring organic molecules to an inorganic lattice and the formation of "self-organizing" systems; inorganic-organic hybrid perovskites are one of the important examples in this regard.[6–12] Despite their usual degradation under ambient condition, the inorganic-organic layered halide perovskites have been studied vastly due to their outstanding potential in optoelectronic devices and solar cells.[13–20] The structure of layered hybrid halide perovskites can be easily determined as these hybrids are readily attainable in the form of single crystals or highly-oriented polycrystalline films at typically mild conditions.[21–25,6,26–28,13,29–31,20] As opposed to the halide-type layered perovskites, the oxide variations offer far better stability in ambient conditions, as well as the possibility to form an actual covalent bond between the anchored organic substituent and the inorganic slab; these interactions are not limited to electrostatic or Lewis acid-base anchoring of the organic ions.[32,33,9] However, as the synthesis of layered hybrid oxide perovskites as single crystals or even highly-oriented polycrystals has not yet been fullfilled in our knowledge, where the crystal stucture of these materials is yet to be determined. The only tools that have been widely used for revealing some structural aspects of hybrid oxide perovskites so far, are X-ray diffraction, solid-state NMR, and vibrational spectroscopy techniques.[34,10,35,11,36,12] The interlayer distances (or the largest unit cell parameters) obtained via XRD and unit cell refinement are typically plotted versus the number of carbons in the alkyl chains, and the slope of the line will be then compared to the distance that a single -CH_2- would add up to the interlayer spacing, which is about 1.27 Å. If the anchored organics form a monolayer, the slope will be about 1.27 Å, and in bilayers it should be about twice this value. *"Tilted"* monolayers and bilayers are demonstrated when the slopes are *lower* than 1.27 and 2.54 Å, respectively.[10–12,34,35,37,38] This method only allows for the "estimation" of the tilt angle,

‡ *Manuscript in preparation*

without providing any information about the positions of the light elements in the organic chain. As a complementary observation, the fraction of trans and gauche conformations are typically collected from IR and solid-state NMR spectroscopies, to evaluate the order of the chains across the interlayer.[34,36,37,39–42] These techniques have demonstrated all-trans conformation for the n-alkyl chains, which is subject to rearrangement upon heating.[34,36]

The extent of X-ray scattering is directly proportional to an atom's atomic number, which makes lighter elements transparent in X-ray powder diffraction of a polycrystal.[43–45] On the contrary, the neutron scattering power of an atom depends on its nuclear structure, where even lighter elements such as carbon and oxygen are "visible". This makes the neutron diffraction technique a powerful way of determining the crytal structure of polycrystalline materials which are rich in lighter elements (such as inorganic-organic hybrids).[43,45–47] Unfortunately, neutron diffraction requires a large amount of sample due to the typical low intensity of the neutron beams,[43,45] which can be an issue in some systems based on the availability of facile large-scale synthesis approaches. Since efficient production of inorganic-organic layered perovskites is now possible via microwave-assisted reactions, larger amounts of these materials are attainable as a single batch to yield decent quality neutron powder diffraction data.[12,48] Ideally, the atomic percent of hydrogen has to be minimized in neutron diffraction techniques due to its large incoherent and inelastic scattering which can almost hide the Bragg peaks. However, using over a hundred milliliters of deuterated solvents is quite costly, and shorter-chain organics can as well minimize this undesirable scattering in our favor.

Herein, efforts have been made to shed light on the crystal structure of inorganic-organic hybrid oxide perovskites via neutron diffraction technique for the first time. Structure refinement of n-propoxy-$LaNb_2O_7$ was successfully carried out positioning the perovskite slab and the first bonding carbon of the organic chain. Temperature studies were also performed on n-propoxy-$LaNb_2O_7$ from 300 K to 10 K and vice versa to investigate the cell contraction/expansion and possible hysteresis in a complete loop. Synchrotron XRD collected were also collected on these systems. Radiation at 0.4146 Å appeared destructive on the hybrid samples, providing questionable merged data. However, even this merged data presented a decent fit with the perovskite models developed for structural refinement.

3.2– Experimental

3.2.1 Materials

The carbonate reagent, Rb_2CO_3 (Alfa Aesar, 99.8%), was used as received. La_2O_3 (Alfa Aesar, 99.99%) and Nb_2O_5 (Alfa Aesar, 99.9985%) oxides were heated at 1000˚C for 12 h for the elimination of impurities or non-stoichiometries. Organic alcohols and amines were used without any further distillation: 1-propanol (Alfa Aesar 99+%), 1-pentanol (Alfa Aesar 98+%), 1-decanol (Alfa Aesar 98+%), benzyl alcohol (Alfa Aesar 99%), 3-phenoxybenzyl alcohol (Alfa Aesar 98%), 1-propylamine (Alfa Aesar 99+%), 1-hexylamine (Alfa Aesar 99%) and 1-octylamine (Alfa Aesar 99%). For aqueous solutions (aq. soln.), milli-Q water (18.2 MV cm, Milli-pore) was mixed with the pure solvent to obtain the de-sired concentration (typically 50% v/v aq. soln. of n-alkyl amine or 80% v/v aq. soln. of n-alcohol). ***Caution:*** handle all of the organic solvents and specifically the amines in a fume hood with proper PPE—amines are toxic, corrosive, and very irritating to the skin, eyes and lungs. It is highly recommended to purchase only small amounts of the amines due to being moderately air sensitive. In case of storage times more than 6 months, amines are best to be kept under protective inert gas.

3.2.2 Synthesis of $RbLaNb_2O_7$

$RbLaNb_2O_7$ was synthesized by grinding stoichiometric amounts of La_2O_3 and Nb_2O_5 oxides with a 30% molar excess of Rb_2CO_3.[12,49] The mixture was preheated at 850 °C overnight, reground, and heated at 1050 °C for 24 h. After regrinding, the sample was finally heated at 1100 °C for 24 h. The product was washed with copious amount of water to remove the excess carbonate, and dried at 100 °C for a few hours. The XRD pattern of $RbLaNb_2O_7$ host showed a tetragonal structure with a = 3.884(2) Å and c = 10.9626(3) Å, consistent with the literature values (a = 3.885(2) Å and c = 10.989(3) Å).[49,50]

Microwave Syntheses. Proton exchange, grafting and intercalation reactions were carried out in a StartSYNTH Microwave Synthesis Labstation as demonstrated in the previous chapter. The Milestone's START platform is capable of simultaneously treating up to 32 reaction vessels in the carrousel (each can safely contain 4-16 mL of the reaction mixture). For non-aqueous reaction mixtures, a Weflon button (graphite-doped Teflon) was used in the mixture to aid the non-polar solvents absorbing the microwaves. The reaction uniformity was also ensured

by using a Teflon stirring bar in all trials. ***Caution:*** Defects and cracks in the glass vessels can result in hotspots or lead to explosion, make sure to inspect them before every run.

3.2.3 Acid Exchange (Protonation)

Microwave acid treatment was carried out by continuous stirring of the $RbLaNb_2O_7$ host in 6 M HNO_3 for 3 h at 60 °C with a maximum power of 300 watts. For the complete exchange of the Rb^+ with proton, at least 150 times molar excess of the H^+ was provided in all trials. $HLaNb_2O_7$ product was washed with distilled water until pH 7 was obtained, and then dried at 90 °C for at least 3 hours. The XRD pattern of the protonated sample showed a tetragonal structure with a = 3.883(3) Å and c = 10.4527(5) Å, in agreement with two sets of literature values available for $HLaNb_2O_7$: a = 3.8886(4) Å and c = 10.5483(12) Å,[8,51] and a = 3.891(4) Å and c = 10.578(6) Å.[8]

3.2.4 Organic Modification of the Protonated Hosts

Organic modification reactions were performed in air for 30 minutes to one hour, involving $HLaNb_2O_7$. Samples were heated from 25 °C to the desired reaction temperature (60, 100, 120 and 150 °C) with a heating rate of 2.5 °C/min. In order to obtain a neutron diffraction pattern with an acceptable quality, at least 1 gram of each sample was required. Providing enough sample was met by running 12 reaction vessels simultaneously each containing 0.1 g of the same sample. Neutron vibrational spectroscopy only required 0.3-0.4 g of sample, so, running 4 reactions vessels containing 0.09 g of the same sample provided enough sample in each case. More details on the conditions of each steps, as well as the reaction mixture of each vessel in a specific reaction, are provided below following what reported earlier for these microwave-assisted reactions.[12] ***Note:*** In cases that the quality of the product was not optimal after performing a specific organic-modification reaction, a so-called *retreatment* step was carried out by redoing the exact same reaction for a second time on the low-quality product, and in all cases improved the quality significantly. The retreatment process was only required for the production of over 1 g of high-quality samples from the following hybrids: n-pentoxy-$LaNb_2O_7$, n-decoxy-$LaNb_2O_7$, 1-octylammonium-$LaNb_2O_7$, and 3-phenoxybenzyl alcoxy-$LaNb_2O_7$.

3.2.4.1 Grafting Reactions with n-Alkyl Alcohols

C_3H_7-$LaNb_2O_7$ was synthesized by reacting 0.09-0.1 g of $HLaNb_2O_7$ with 14 ml of 80% v/v aq. soln. of 1-propanol for 1 h at 100 °C (350 W maximum). The 1-propoxy-$LaNb_2O_7$ intermediate was washed with distilled water and acetone, then dried at 70 °C for 1 h. The interlayer of C_3H_7-$LaNb_2O_7$ was then successfully exchanged with longer chain n-pentoxy or n-decoxy substituents, yielding C_5H_{11}-$LaNb_2O_7$ and $C_{10}H_{21}$-$LaNb_2O_7$, respectively.[12] The typical microwave procedure was carried out by reacting 0.09-0.1 g of n-propoxy-$LaNb_2O_7$ intermediate with 11 mL of the corresponding alcohols: 1-pentanol for 45 min at 120 °C (800 W maximum) or 1-decanol for 30 min at 150 °C (1000 W maximum). The n-pentoxy-$LaNb_2O_7$ and n-decoxy-$LaNb_2O_7$ products were washed with copious amount of acetone and dried at 70 °C for 1 h. The n-decoxy-$LaNb_2O_7$ hybrid has a large interlayer spacing (about 17 Å), which makes it a great intermediate that can be used for the production of benzyl alcoxy-$LaNb_2O_7$ and 3-phenoxybenzyl alcoxy-$LaNb_2O_7$ hybrids via exchanging the n-decoxy bond respectively with benzyl alcoxy and 3-phenoxybenzyl alcoxy.

3.2.4.2 Grafting Reactions with Cyclic Organics—Benzyl Alcohol and 3-Phenoxybenzyl Alcohol

The interlayer of $C_{10}H_{21}$-$LaNb_2O_7$ hybrid was successfully exchanged with two cyclic organics, benzyl alcohol and 3-phenoxybenzyl alcohol, respectively yielding C_7H_7-$LaNb_2O_7$ and $C_{13}H_{11}$-$LaNb_2O_7$. The typical microwave procedure was carried out by reacting 0.09-0.1 g of n-decoxy-$LaNb_2O_7$ intermediate with 11 mL of the corresponding alcohols: benzyl alcohol for 1 h at 60 °C (300 W maximum) or 3-phenoxybenzyl alcohol for 1 h at 100 °C (600 W maximum). The products were washed with copious amount of acetone and dried at 70 °C for 1 h.

3.2.4.3 Intercalation Reactions with n-Alkylamines

Preparation of 1-propylammonium-$LaNb_2O_7$ was done by reacting 0.09-0.1 g of $HLaNb_2O_7$ with 14 ml of 50% v/v aq. soln. of 1-propylamine for 1 h at 100 °C (350 W maximum). The $C_3H_7NH_3$-$LaNb_2O_7$ was washed with distilled water, ethanol, and acetone, then dried at 70 °C for 1 h. The interlayer of 1-propylammonium-$LaNb_2O_7$ (as well as n-propoxy-$LaNb_2O_7$) is then exchangeable with longer chain 1-hexylammonium substituent,[12] yielding $C_6H_{13}NH_3$-$LaNb_2O_7$. The typical microwave procedure was carried out by reacting 0.09-0.1 g of n-propylammonium-$LaNb_2O_7$ intermediate with 11 mL of pure 1-propylammine for 45 min at

120 °C (800 W maximum). The 1-hexylammonium-$LaNb_2O_7$ was washed with copious amount of ethanol and then acetone, then dried at 70 °C for 1 h.

3.2.5 Characterization

X-ray powder diffraction (XRD) data were obtained on a Philips X'Pert system equipped with Cu Kα radiation (λ = 1.5418 Å) and a curved graphite monochromator. XRD scanning was performed in continuous mode with a scan rate of 0.02 °/s. Refinement of the peak positions and lattice parameters was carried out using Fullprof[52] and a least-squares method with the ChekCell program.[53] Raman spectra were collected on a Thermo-Fisher DXR dispersive Raman spectrometer using the λ = 532 nm line with a spectral resolution of 3 cm^{-1}.

Neutron diffraction data were collected on the powder diffractometer POWGEN (BL-11A)[54] located at the Spallation Neutron Source (SNS) of the Oak Ridge National Laboratory (ORNL). 1—1.3 g of each sample was loaded in a 6-mm diameter vanadium can (06 V cans), and measurements were done using the 24-sample changer with cryogenic capabilities. Quick measurements were collected on all samples at room temperature (300 K) to determine the feasibility of the samples. Due to the large number of hydrogen atoms present (samples were not deuterated), some of the samples showed large backgrounds from incoherent and inelastic scattering from hydrogen. Two samples namely n-propoxy-$LaNb_2O_7$ and 1-propylammonium-$LaNb_2O_7$ were measured at both 300 K and 100 K for 4-6 hours— each at a center wavelength of 1.333 Å covering a d-spacing range of 0.4-6.1 Å. Comprehensive temperature studies were then performed between 10 K and 300K for n-propoxy-$LaNb_2O_7$; the sample was cooled down from 300 K to 10 K at a rate of 0.56 K/min and heated to 300 K from 10 K at a rate of 0.55 K/min. Data was continuously collecting compensating in case beam went down, i.e. data collection automatically stopped in case beam down holding the temperature. These data were post processed to 58 slices collected at every 5 K. General processing of the diffraction files (such as conversion from TOF to d-spacing), as well as binning, was carried out using the Mantidplot software via remote analysis service provided by ORNL. Rietveld analysis of the neutron diffraction data collected on the n-propoxy-$LaNb_2O_7$ was performed using the GSAS software and EXPGUI user interface.[55,56]

High-resolution synchrotron XRD data for n-propoxy-$LaNb_2O_7$, n-pentoxy-$LaNb_2O_7$, and 1-propylammonium-$LaNb_2O_7$ samples were collected on beamline 11-BM at the Advanced

Photon Source (APS),[57] Argonne National Laboratory; collection temperatures of 300 K and 100 K, at a calibrated wavelength of 0.414627 or 0.414631 Å. The samples darkened under this intense measurement, which except for 1-propylammonium-$LaNb_2O_7$ did not go away even after cooling down to 100 K. All the samples showed structural changes with exposure; some peaks dramatically changing during the 1800-second lap between the first and last detectors (at times shifting by about 2 millidegrees total). Therefore, the merged data from high resolution XRD could not be used for any refinement purposes.

3.3– Results

3.3.1 Initial Characterzation by XRD and Raman Spectroscopy

Samples were prepared and initially examined with XRD and Raman spectroscopy, before getting shipped and processed at APS and ORNL. The XRD patterns and Raman spectra of n-propoxy-$LaNb_2O_7$, n-pentoxy-$LaNb_2O_7$, n-decoxy-$LaNb_2O_7$, n-propylammonium-$LaNb_2O_7$, n-hexylammonium-$LaNb_2O_7$, benzyl alcoxy-$LaNb_2O_7$, and 3-phenoxybenzyl alcoxy-$LaNb_2O_7$ samples are provided in Figures 3-1 and 3-2, respectively. According to our previous report on complete series of n-alkyl alcoxy- and n-alkylamine-$LaNb_2O_7$ hybrid perovskites,[12] all of the samples with alkyl chains show decent quality. In case of the two samples with cyclic groups, benzyl alcoxy- and 3-phenoxybenzyl alcoxy- $LaNb_2O_7$, the existance of the phenyl rings is well supported in Figure 3-2h and i (bands related to phenyl rings marked with solid circles).[58]

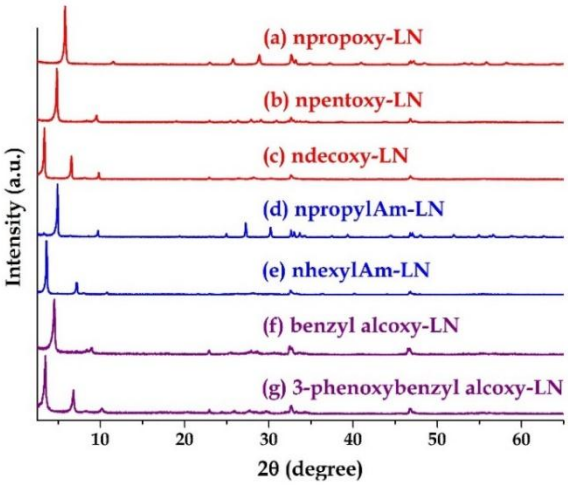

Figure 3- 1: XRD patterns of (a) n-propoxy-$LaNb_2O_7$, (b) n-pentoxy-$LaNb_2O_7$, (c) n-decoxy-$LaNb_2O_7$, (d) n-propylammonium-$LaNb_2O_7$, (e) n-hexylammonium-$LaNb_2O_7$, (f) benzyl alcoxy-$LaNb_2O_7$, and (g) 3-phenoxybenzyl alcoxy-$LaNb_2O_7$.

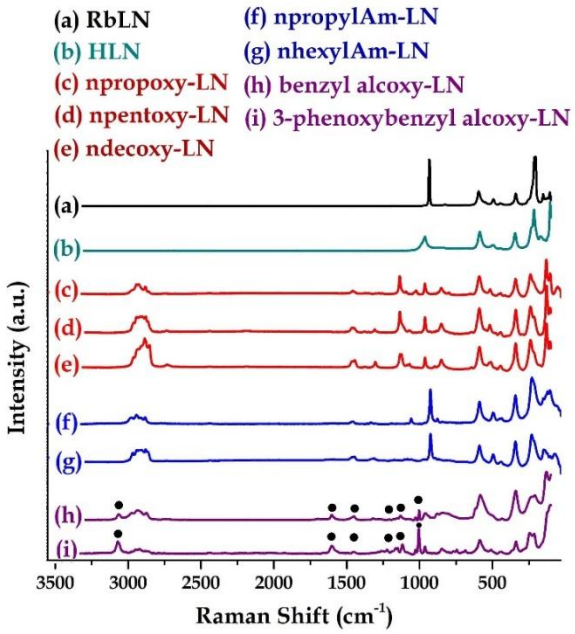

Figure 3- 2: Raman spectra of (a) $RbLaNb_2O_7$, (b) $HLaNb_2O_7$, (c) n-propoxy-$LaNb_2O_7$, (d) n-pentoxy-$LaNb_2O_7$, (e) n-decoxy-$LaNb_2O_7$, (f) n-propylammonium-$LaNb_2O_7$, (g) n-hexylammonium-$LaNb_2O_7$, (h) benzyl alcoxy-$LaNb_2O_7$, and (i) 3-phenoxybenzyl alcoxy-$LaNb_2O_7$.

3.3.2 Structure Evaluation via Diffraction Techniques

The starting model was based on the information obtained from the unit cell parameters presented in Table 2-3.[12] These values were used to modify the atomic positions of $CsLaNb_2O_7$ model refined in a tetragonal cell (P4/mmm).[59] This general modification step involves redrawing the structure of $CsLaNb_2O_7$ with the *a* and *c* parameters of the target hybrid obtained from Table 2-3, and adjusting the positions that would change by new unit cell dimensions. For instance, the terminal oxygens of $CsLaNb_2O_7$ with *x/a*, *y/b* and *z/c* fractional coordinats of 0.5, 0.5, and 0.3569(6), respectively,[59] will be adjusted to 0.5, 0.5, and 0.2586 for n-propoxy-$LaNb_2O_7$ (multiplying 0.3569 by $\frac{C_{original\ model}}{C_{target\ model}}$). In simple words, this model sets the perovskite slabs in the right positions estimated by combining the unit cell parameters of the target structure with the host refined model ($CsLaNb_2O_7$). The simple models of n-propoxy-$LaNb_2O_7$, n-pentoxy-$LaNb_2O_7$, and 1-propylammonium-$LaNb_2O_7$ were generated, and employed in calculating the diffraction pattern in both the X-ray and neutron methods. Figure 3-3 illustrates these three models.

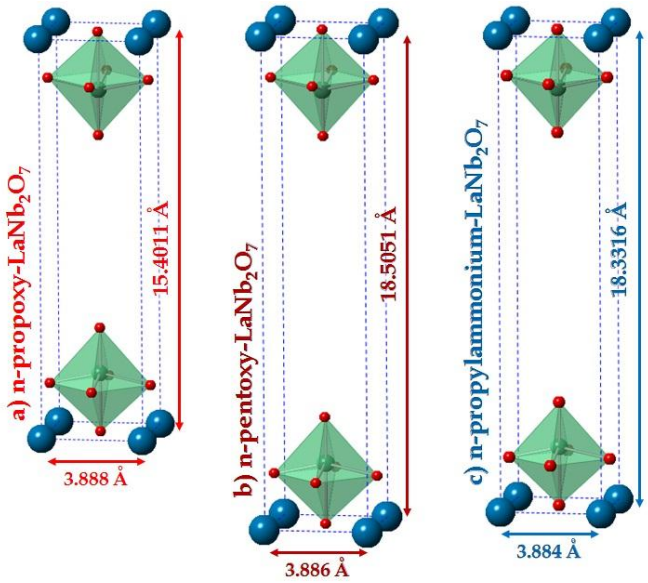

Figure 3- 3: Starting models for (a) n-propoxy-$LaNb_2O_7$, (b) n-pentoxy-$LaNb_2O_7$, and (c) 1-propylammonium-$LaNb_2O_7$ generated based on the tetragonal structure of $CsLaNb_2O_7$ and the unit cell parameters of each system.

3.3.2.1 Regular and Synchrotron X-Ray Diffraction

Since the atomic scattering factors for hydrogen, carbon, and oxygen are relatively small compared to heavier elements, these elements are almost transparent to X-rays. In terms of comparing X-ray diffraction models, there is little if any difference between observed data and calculated models that do not contain alkyl chains. The experimental XRD patterns of n-propoxy-$LaNb_2O_7$, n-pentoxy-$LaNb_2O_7$, and 1-propylammonium-$LaNb_2O_7$ samples (a) are compared to the patterns calculated by the crystallographic models (b), and provided in Figures 3-4 and 3-5, respectively, for regular XRD (1.54056 Å) and synchrotron (0.4146 Å) data. Synchrotron XRD data were collected in order to calculate more accurate unit cell parameters (compared to those presented in Table 2-3 via regular XRD), which would be a better starting point for structure refinement. However, the samples showed sensitivity (degradation) to these very intense X-rays, with some peaks shifting noticeably (by about 2 millidegrees) in the 1800-second time lag between the first and last detectors during data collection. Therefore, the merged data obtained from synchrotron were only used to evaluate the models, rather than calculating more accurate unit cell parameters for our systems. The model proposed for n-pentoxy-$LaNb_2O_7$ shows poor agreement with the experimental results, which lead us to only consider n-propoxy-

$LaNb_2O_7$ and 1-propylammonium-$LaNb_2O_7$ for the comparison of experimental and simulated neutron diffraction patterns.

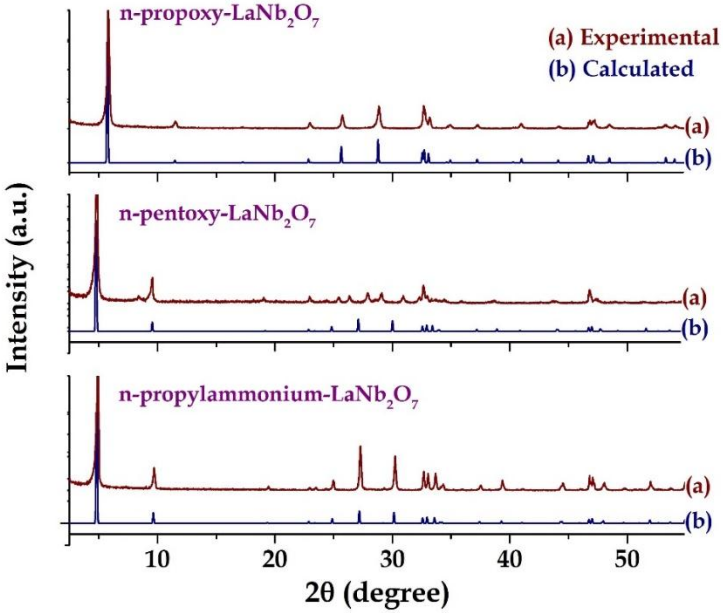

Figure 3- 4: Regular XRD patterns for n-propoxy-$LaNb_2O_7$, n-pentoxy-$LaNb_2O_7$, and 1-propylammonium-$LaNb_2O_7$; (a) experimental versus (b) calculated.

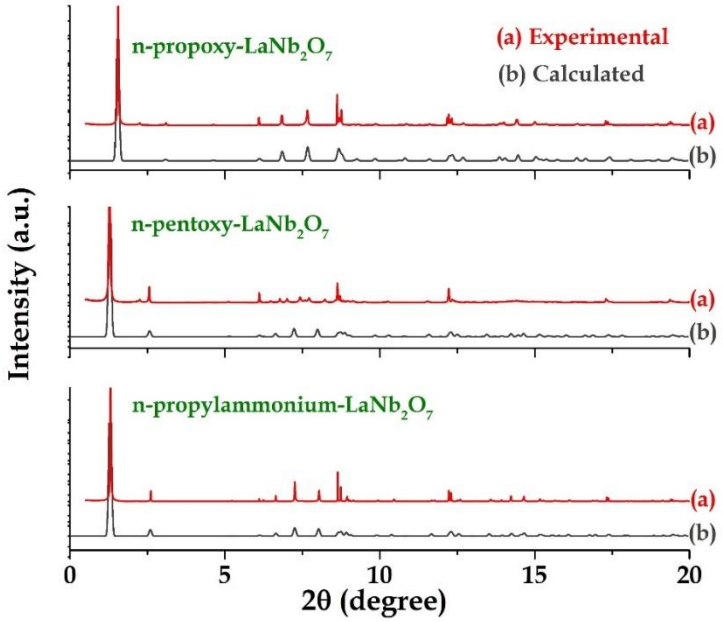

Figure 3- 5: Synchrotron XRD patterns for n-propoxy-$LaNb_2O_7$, n-pentoxy-$LaNb_2O_7$, and 1-propylammonium-$LaNb_2O_7$; (a) experimental versus (b) calculated.

3.3.2.2 Neutron Diffraction

Quick measurements (4-min) were collected on all the samples presented in Figure 3-1 at room temperature (300 K), and at two different wavelengths (1.333 and 2.665 Å) to determine the feasibility of the samples. Except for n-propoxy-$LaNb_2O_7$, n-pentoxy-$LaNb_2O_7$, and 1-propylammonium-$LaNb_2O_7$, the rest of the samples showed large backgrounds because of the large atomic ratio of hydrogen and its incoherent and inelastic scattering. A center wavelength of 1.333 Å covering a d-spacing range of 0.4-6.1 Å was selected for examining the best-quality samples, namely n-propoxy-$LaNb_2O_7$ and 1-propylammonium-$LaNb_2O_7$, measured at both 300 K and 100 K for 4-6 hours.

Since only the models proposed for n-propoxy-$LaNb_2O_7$ and 1-propylammonium-$LaNb_2O_7$ provided agreement between experimental and calculated XRD patterns, only these two were selected for evaluating the neutron diffraction data. Figure 3-6 presents the calculated TOF neutron pattern obtained from the simple models in Figure 3-3, compared to the experimental results. Similar to the promising fit obtained in XRD patterns (Figures 3-4 and 3-5), the TOF patterns also provide great agreement with the calculated patterns. The intensity difference between (a) and (b) patterns can be minimized during structure refinement steps presented later in this chapter.

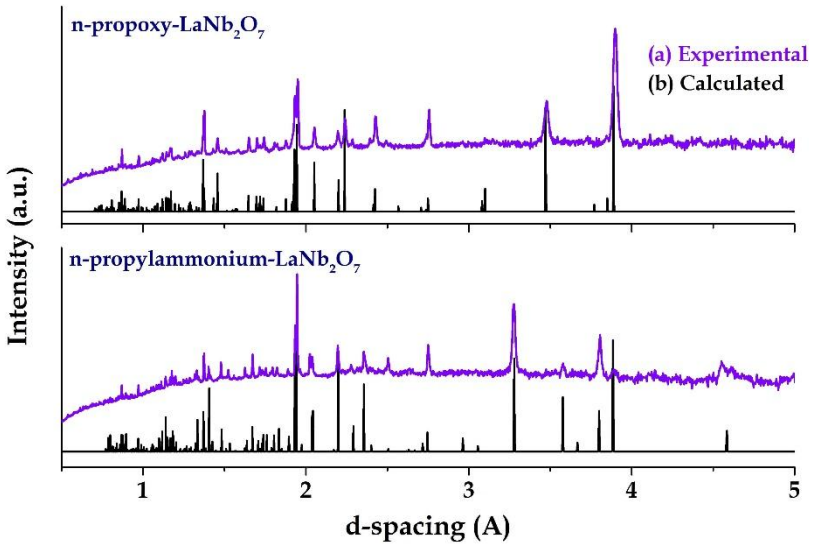

Figure 3- 6: TOF neutron patterns of n-propoxy-$LaNb_2O_7$ and 1-propylammonium-$LaNb_2O_7$; (a) experimental data versus (b) calculated patterns.

In the case of n-propoxy-$LaNb_2O_7$, the alkyl chain is covalently bonded to the terminal oxygens of the perovskite slab, which makes it easier to add the alkyl chains in the starting model presented in Figure 3-3 (as opposed to the alkylammonium chain which is present in the vicinity of the terminal oxygens, not allowing for an easy starting point to add NH_3^+ and the first carbon in the alkyl chain to the slab). The n-propoxy-$LaNb_2O_7$ model presented in Figure 3-3a was modified by adding the first carbon of the propoxy chain. In order to perform this addition reasonably, the C-O was set to 1.54 Å and in a tilt angle of 42º (estimated in our previous work).[12] It should be noted that initially this carbon is added to a reasonable position, and that the structure refinement will allow for fine-tuning its position for a better fit. The rest of the carbons of the alkyl chain can then be simply added using the crystallographic information available for alkyl chains,[60] and then further refinement can help do a final structure refinement. The only complication in that case would be finding the best symmetry options that provide for a better fit with the experimental data. Figure 3-7a shows the model where only one carbon is added to the tetragonal system introduced earlier (P4/mmm), while 3-7b presents the model with the addition of all three carbons using the crystallographic information of n-octanol[60] and estimating a tilt angle of 42º. Figure 3-8 compares the neutron TOF patterns of these two models with the experimental data. The second model with a complete 3-carbon chain does not seem to offer any advantages over the simpler model considering their fit with the experimental pattern. Adversely, they also complicate the structure refinement steps due to limiting the space groups that would provide reasonable symmetry options and chain arrangement. Thus, the simple 1-carbon model was used in Rietveld refinement steps provided in the next section.

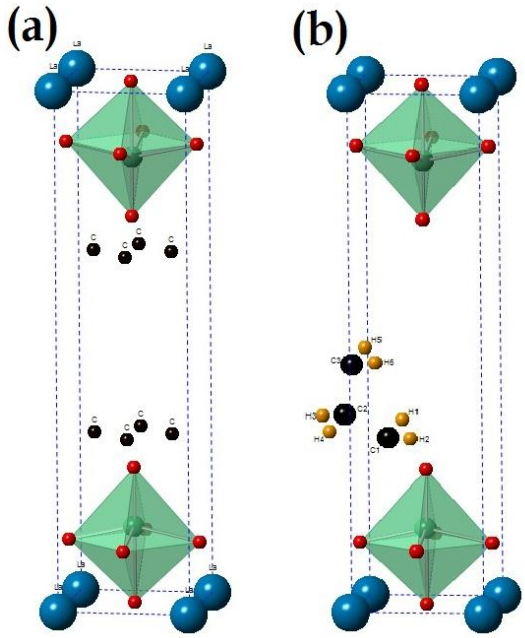

Figure 3- 7: Two starting models with (a) only one carbon, and (b) all three carbons of the n-propoxy chain.

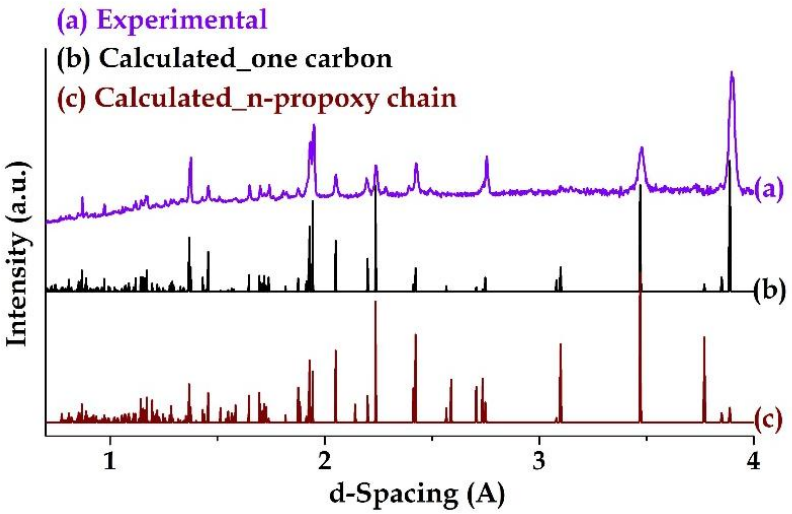

Figure 3- 8: TOF data for n-propoxy-$LaNb_2O_7$; (a) experimental data versus the calculated models with (b) one-carbon or (c) three-carbon alcoxy chains.

3.3.2.3 Rietveld Refinement

Using the GSAS software and EXPGUI user interface, the general parameters such as background, zero shift, phase, sample displacement, peaks shapes (using Lorentzian and Gaussian fits), and unit cell were refined one by one and fixed at their best condition.[55,61] In the next refinement steps, only background and cell were marked to still get refined with modifying every new parameter at each step. The position (x), isotropic thermal parameter (U_{iso}), and occupancy (F) of the C element were refined one by one, and then together, while a restraint was set to the C-O bond-length (1.3-1.8 Å). The occupancy of all the other elements were fixed at one, and their position and thermal parameters were refined step by step. After optimizing these values for all the elements, all of them were also marked to be refined together as the final step (***Note:*** refining the thermal parameters of Nb and La was performed using the "damping" feature, which would apply only small changes). The goodness of the fit is evaluated in form of a parameter named χ^2, which would equal to one for a perfect fit between the calculated model and the experiment. Also, so-called R-Factors should be minimized in a good fit—weighted profile R-Factor (R_{wp}^2) and unweighted profile R-Factor (R_p).[55] The refinement steps applied above improved the χ^2 value from about 50 down to 16, suggesting an acceptable fit between the generated model and the experimental data. The χ^2 can still be improved by further developing

this model. Table 3-1 provides the refined atomic positions and thermal parameters obtained for n-propoxy-$LaNb_2O_7$. Figure 3-9 presents the calculated neutron diffraction pattern in red versus the experimental data in black (the background is also presented in green). The difference between the two calculated and experimental patterns is shown in blue in the very bottom, which would be a flat line in perfect condition.

Table 3- 1:Fractional positions, occupancy, and thermal parameters for n-propoxy-$LaNb_2O_7$

atom	Site	x	y	Z	Occupancy	$100\times U_{iso}$
C	8t	0.5	0.626(7)	0.351(2)	0.1041	2(1)
La	1a	0	0	0	1	0.094*
Nb	2h	0.5	0.5	0.1417(3)	1	0.005*
O_1	4i	0	0.5	0.1201(3)	1	0.48(8)
O_2	2h	0.5	0.5	0.2627(8)	1	4.3(3)
O_3	1c	0.5	0.5	0	1	4.3(5)

P4/mmm, a = 3.899(1) Å, c = 15.403(4) Å, V = 234.2(2) Å^3, R_p = 3.61%, R_{wp} = 2.50%, and χ^2 = 15.37

****** the Uiso parameters for La and Nb showed standard deviations as large as the refined value*

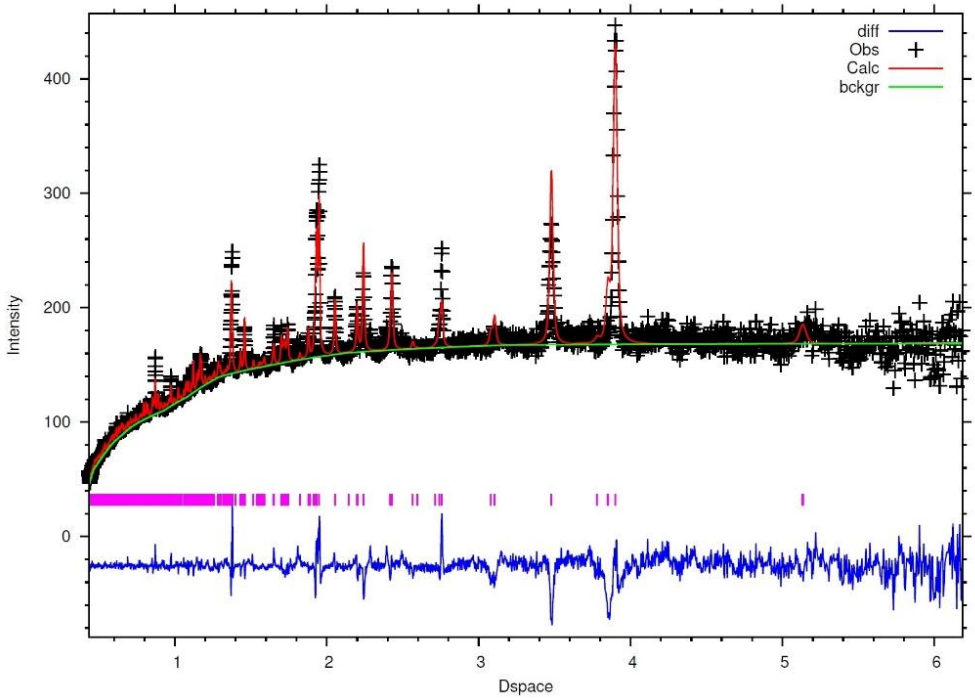

Figure 3- 9: Rietveld refinement of n-propoxy-$LaNb_2O_7$ neutron diffraction data.

3.3.2.4 Temperature Studies Based on Neutron Diffraction

Other than three long scans performed at 300 K, 100 K, and 10 K for the n-propoxy-$LaNb_2O_7$ sample, the temperature was also infinitesimally changed from 300 K to 10 K and vice versa to better study the impact of temperature on the structure. Thus, n-propoxy-$LaNb_2O_7$ was cooled down from 300 K to 10 K at a rate of 0.56 K/min, and then heated to 300 K from 10 K at a rate of 0.55 K/min. These continuous data were then post processed to 58 slices collected at about every 5 K. Figure 3-10 provides the color-fill plot for these two sets of temperature studies. In order to further study the hysteresis of the system in this loop, the first and last slices of each set of experiments, which provide the neutron diffraction patterns at 10 K and 300 K respectively, were compared to the long scans performed at the same temperatures (Figure 3-11). Comparing the end slices to the longs scans ran at 300 K and 10 K (respectively in black and red), suggests almost no hysteresis in the few loops studied here—marked peaks better highlight the major peaks that shift the most between 300 K and 10 K temperatures, better approving of the reversibility of this structural change.

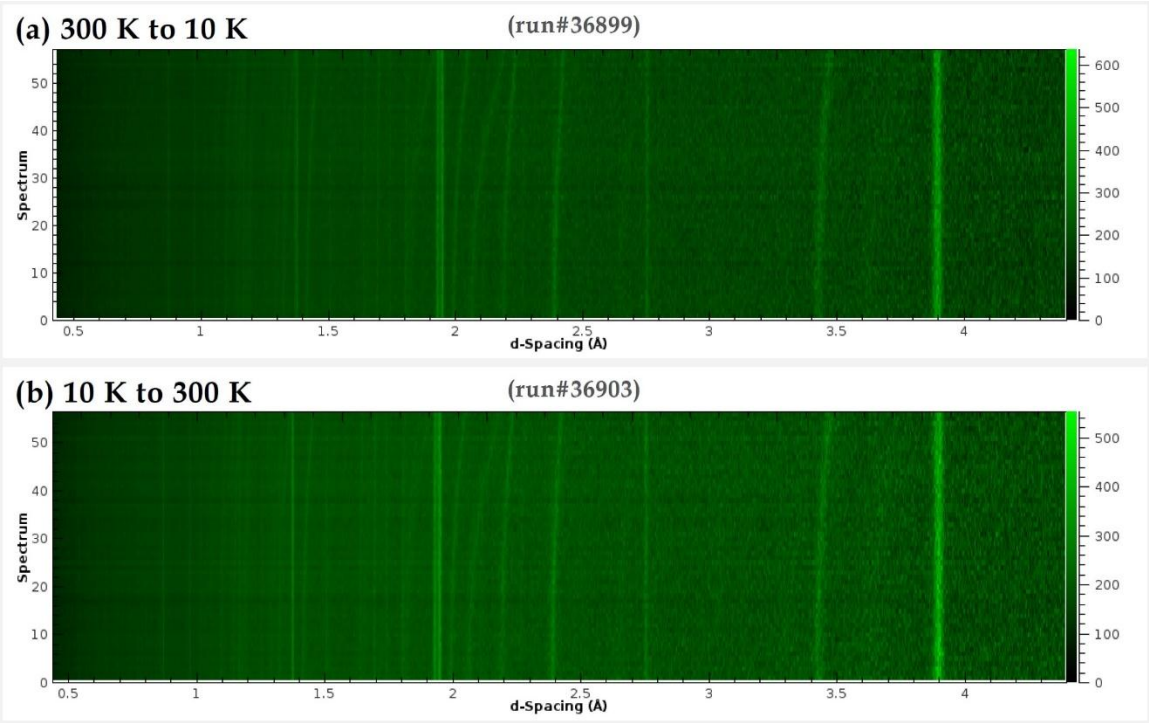

Figure 3- 10: Color-fill plots as the temperature of n-propoxy-$LaNb_2O_7$ is decreased from 300 K to 10 K (a), and increased back to 300 K (b).

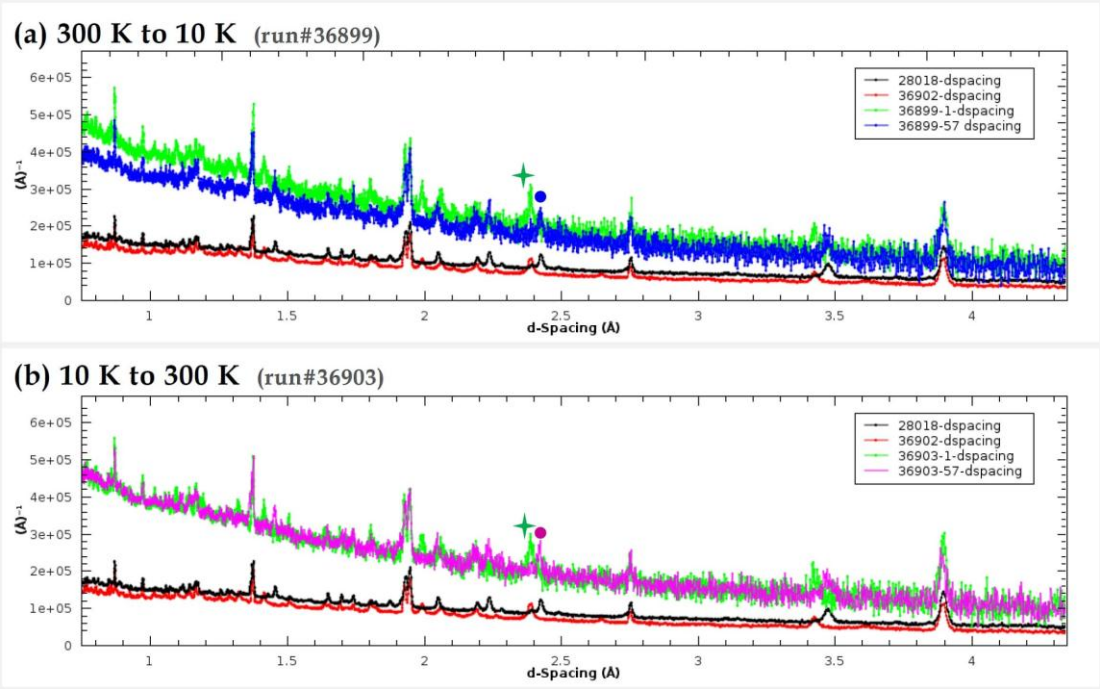

Figure 3- 11: Comparing the first and last slices of each continuous measurement to the long scans ran at the same temperatures; (a) the cool-down and (b) the heat-up processes, versus the long scan at 300 K in black and the long scan in 10 K in red.

Figure 3-12 compares the three long scans carried out at 300 K, 100 K, and 10 K on n-propoxy-$LaNb_2O_7$ sample. Clearly, there seems to be no structural difference between 100 K and 10 K patterns. Considering the intense peak present at the d-spacing of about 3.5 Å which was presented earlier in Figures 3-10a and b, the first 20 slices almost show a flat line as opposed to the gradual shift noticed in the last 38 slices.

Based on the model that was presented earlier for n-propoxy-$LaNb_2O_7$, the *hkl* values of four of the peaks were selected in order to estimate the contraction as the sample is cooled down to 100 K. The *a* and *b* parameters were first calculated based on *(010)* and *(110)* reflections, and the *c* parameters were then obtained using the *(012)* peak. The Δc was approximately 0.92 Å from this set of calculations; almost 1 angstrom of contraction due to the temperature difference. Repeating the same steps based on the *(113)* reflection also yielded a Δc of 0.96 Å. This observation seems to be similar to the phase transitions proposed for hybrid halide perovskites, typically at temperatures higher than 300 K.[7,13,14,62–64]

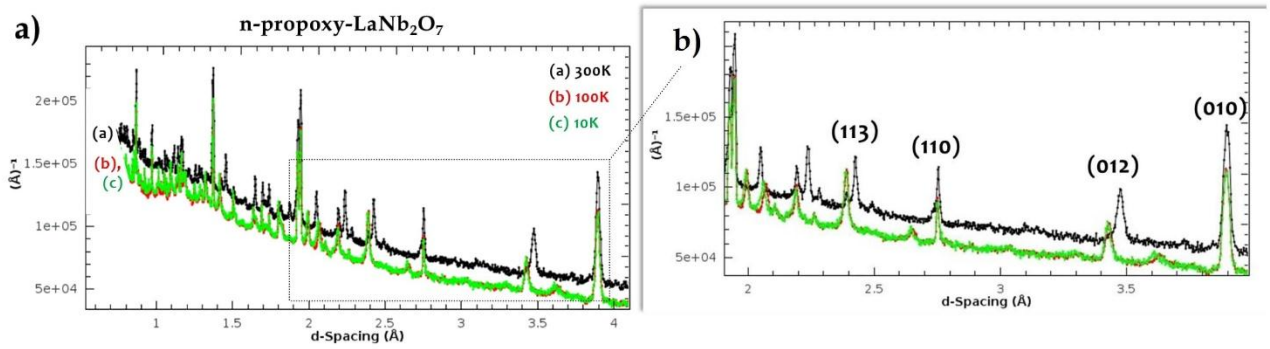

Figure 3- 12: a) Comparing the diffraction pattern of n-propoxy-$LaNb_2O_7$ collected at three temperatures; (a) 300 K, (b) 100 K, and (c) 10K. b) Highlighting the *(113)*, *(110)*, *(012)*, and *(010)* reflections versus d-spacing in a narrower range, in order to estimate the cell contraction upon cooling.

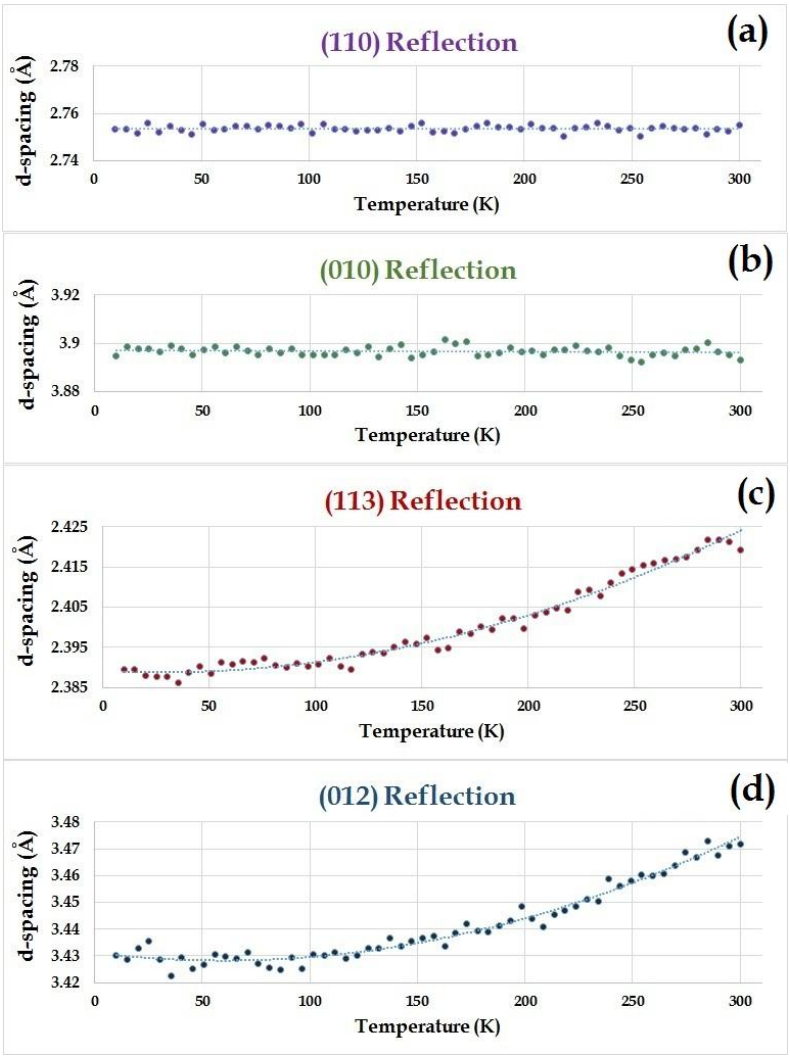

Figure 3- 13: The d-spacing of (a) *(110)*, (b) *(010)*, (c) *(113)*, and (d) *(012)* reflections versus temperature for the 10-to-300 K run.

The 58 slices of the warmup cycle in Figure 3-10b (10-to-300 K) were opened one by one, and the d-spacing of the four peaks highlighted in Figure 3-12 were then collected as a function of the temperature of each slice (slices are approximately 5 K apart from each other based on the binning). Figure 3-13 presents the plots of the d-spacing of *(110)*, *(010)*, *(113)*, and *(012)* reflections at each slice versus their temperature. Notice that each slice is quite noisy as it is a brief portion of the continuous data collection process, and so all the d-spacing values are subject to error when being read. Similar to what was previously seen in Figures 3-10, 3-11, and 3-12, the two *(110)* and *(010)* reflections stay constant by varying the temperature, while *(113)* and *(012)* reflections start increasing noticeably when the temperature passes 100 K. Figure 3-14 shows the linear relationship of the d-spacings of the two temperature-dependant peaks with their temperature in 150-300 K range.

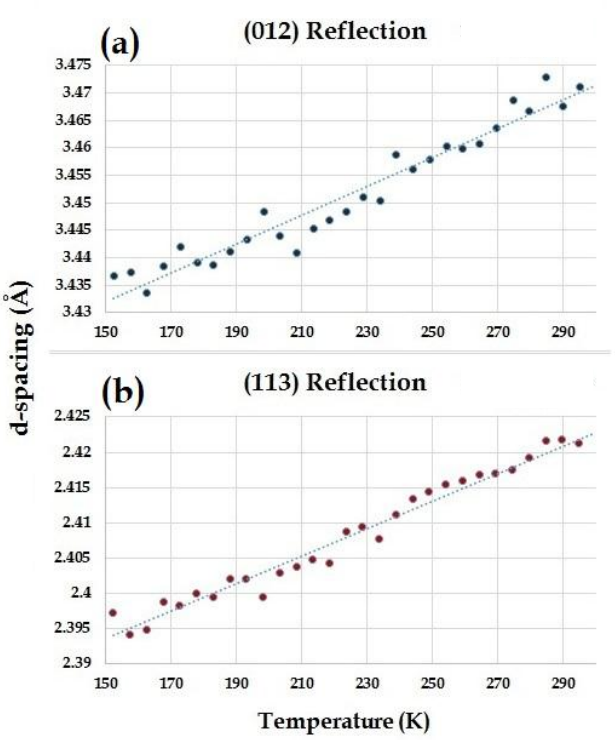

Figure 3- 14: The linear relationship between the d-spacing of the temperature-dependant peaks with temperature in 150-300 K range.

3.4– Discussion

The structure of layered hybrid halide perovskites have been extensively studied as they are typically synthesized as single crystals or highly-oriented polycrystalline films.[21–25,6,26–28,13,29–31,20] Conversely, the structure of polycrystalline layered hybrid oxide perovskites has not yet been fully resolved other than some estimations carried out via X-ray diffraction, solid-state NMR, and vibrational spectroscopy techniques.[34,10,35,11,36,12] Typically, only an estimation of the tilt angle of the organic bilayers is done,[10–12,34,35,37,38] with predicting all-trans conformation based on the solid-state NMR and vibrational spectroscopy techniques.[34,36]

As the synthesis of layered hybrid oxide perovskites via available methods has not yet led to the formation of single crystals or at least highly-oriented polycrystals, neutron diffraction technique is the only tool to shed some light on the positions of the lighter elements in such structures.[43,45–47] Facility and efficiency of novel microwave-assisted reactions[12,48] allowed us to produce high-quality $LaNb_2O_7$-based hybrids in large quantities, enough to obtain decent neutron diffraction results.[43,45] Therefore, we were able to perform structure refinement on layered hybrid oxide perovskites herein. As demonstrated earlier, our generated model is a great starting point for more complicated models that can follow in the future. Even though deuterated solvents in the experimental scale of this experiment are quite expensive, it can be a price that can be paid in order to further resolve the structure of these hybrids later on, without worrying about the incoherent and inelastic scattering of hydrogen in longer organics. Selecting the hybrids with the least amount of hydrogen (shorest organic chains), the adverse impact of hydrogen on the neutron diffraction patterns were minimized in the current work. So, the XRD and neutron diffraction patterns were only generated for of n-propoxy-$LaNb_2O_7$, n-pentoxy-$LaNb_2O_7$, and 1-propylammonium-$LaNb_2O_7$ hybrids, modeled as plain perovskite slabs set in the right distance based on earlier unit cell refinement results (Figure 3-3). After evaluating the overall feasibility of these starting models (Figures 3-4, 3-5, and 3-6), n-propoxy-$LaNb_2O_7$ was selected as the best model and successfully refined positioning the perovskite slab and the first bonding carbon of the organic chain (Figures 3-7, 3-8, and 3-9, as well as Table 3-1).

Performing neutron diffraction temperature studies in Figures 3-10, 3-11, 3-12, 3-13,and 3-14 also suggested a gradual contraction in the *c* parameter, as the temperature is dropped from 300 K to 100 K (similar to the phase transitions demonstrated for layered hybrid halide perovskites).[7,13,14,62–64] The total contraction was estimated to be about 1 angstrom in this range, and was found to be reversible. The expansion coefficient along the *c*-axis is approximately 0.0052 Å/K based on the data points of the warmup cycle collected above 150 K up to 300 K.

3.5– Conclusions

Inorganic-organic $LaNb_2O_7$-based hybrids were successfully obtained in large quantities, and further studied with neutron diffraction; n-propoxy-$LaNb_2O_7$, n-pentoxy-$LaNb_2O_7$, n-decoxy-$LaNb_2O_7$, n-propylammonium-$LaNb_2O_7$, n-hexylammonium-$LaNb_2O_7$, and benzyl alcoxy-$LaNb_2O_7$. Despite the presence of hydrogen atoms in all systems, acceptable patterns

with manageable backgrounds were obtained for the n-propoxy-$LaNb_2O_7$, n-pentoxy-$LaNb_2O_7$, and 1-propylammonium-$LaNb_2O_7$ hybrids. Three simple models were generated for these three systems, and evaluated using XRD and neutron diffraction simulated patterns. Focusing on the neutron diffraction pattern of n-propoxy-$LaNb_2O_7$ obtained at 300 K, the structure was successfully refined positioning the perovskite slab and the first bonding carbon of the organic chain. Continuous temperature studies were also performed on n-propoxy-$LaNb_2O_7$, suggesting a reversible contraction of the interlayer as the system is cooled down to 100 K.

3.6– References

(1) Livage, J. Chimie Douce: From Shake-and-Bake Processing to Wet Chemistry. *New J. Chem.* **2001**, *25* (1), 1–1.

(2) Mitzi, D. B.; Chondroudis, K.; Kagan, C. R. Organic-Inorganic Electronics. *IBM J. Res. Dev.* **2001**, *45* (1), 29–45.

(3) Sanchez, C.; Rozes, L.; Ribot, F.; Laberty-Robert, C.; Grosso, D.; Sassoye, C.; Boissiere, C.; Nicole, L. "Chimie Douce": A Land of Opportunities for the Designed Construction of Functional Inorganic and Hybrid Organic-Inorganic Nanomaterials. *Comptes Rendus Chim.* **2010**, *13* (1–2), 3–39.

(4) Kickelbick, G. *Hybrid Materials: Synthesis, Characterization, and Applications*; Wiley-VCH Verlag GmbH & Co. KGaA: Weinheim, Germany, 2007.

(5) Zhu, Y.-P.; Yuan, Z.-Y. *Mesoporous Organic-Inorganic Non-Siliceous Hybrid Materials: Basic Principles and Promising Multifunctionality (from "Springer Briefs in Molecular Science")*; Springer-Verlag GmbH Berlin Heidelberg, 2015.

(6) Mitzi, D. B. Synthesis, Crystal Structure, and Optical and Thermal Properties of $(C_4H_9NH_3)_2MI_4$ (M = Ge, Sn, Pb). *Chem. Mater.* **1996**, *8* (3), 791–800.

(7) Naik, V. V.; Vasudevan, S. Melting of an Anchored Bilayer: Molecular Dynamics Simulations of the Structural Transition in $(C_nH_{2n+1}NH_3)_2PbI_4$ (n = 12, 14, 16, 18). *J. Phys. Chem. C* **2010**, *114* (10), 4536–4543.

(8) Suzuki, H.; Notsu, K.; Takeda, Y.; Sugimoto, W.; Sugahara, Y. Reactions of Alkoxyl Derivatives of a Layered Perovskite with Alcohols: Substitution Reactions on the Interlayer Surface of a Layered Perovskite. *Chem. Mater.* **2003**, *15* (3), 636–641.

(9) Sugahara, Y. Chemical Processes Employing Inorganic Layered Compounds for Inorganic and Inorganic–organic Hybrid Materials. *J. Ceram. Soc. Jpn.* **2014**, *122* (1427), 523–529.

(10) Tahara, S.; Ichikawa, T.; Kajiwara, G.; Sugahara, Y. Reactivity of the Ruddlesden−Popper Phase $H_2La_2Ti_3O_{10}$ with Organic Compounds: Intercalation and Grafting Reactions. *Chem. Mater.* **2007**, *19* (9), 2352–2358.

(11) Wang, Y.; Wang, C.; Wang, L.; Hao, Q.; zhu, X.; Chen, X.; Tang, K. Preparation of Interlayer Surface Tailored Protonated Double-Layered Perovskite $H_2CaTa_2O_7$ with N-Alcohols, and Their Photocatalytic Activity. *RSC Adv* **2014**, *4* (8), 4047–4054.

(12) Akbarian-Tefaghi, S.; Teixeira Veiga, E.; Amand, G.; Wiley, J. B. Rapid Topochemical Modification of Layered Perovskites via Microwave Reactions. *Inorg. Chem.* **2016**, *55* (4), 1604–1612.

(13) Depmeier, W. Inorganic-Organic Layered Halide Perovskites, with Specific Focus on PAMC, and Its Key and Slot Joint Interlayers. *Z. Für Krist. Int. J. Struct. Phys. Chem. Asp. Cryst. Mater.* **2009**, *224* (5-6), 287–294.

(14) Liao, W.-Q.; Zhang, Y.; Hu, C.-L.; Mao, J.-G.; Ye, H.-Y.; Li, P.-F.; Huang, S. D.; Xiong, R.-G. A Lead-Halide Perovskite Molecular Ferroelectric Semiconductor. *Nat. Commun.* **2015**, *6*, 7338.

(15) Pedesseau, L.; Sapori, D.; Traore, B.; Robles, R.; Fang, H.-H.; Loi, M. A.; Tsai, H.; Nie, W.; Blancon, J.-C.; Neukirch, A.; et al. Advances and Promises of Layered Halide Hybrid Perovskite Semiconductors. *ACS Nano* **2016**, *10* (11), 9776–9786.

(16) Wang, P.; Guo, Y.; Yuan, S.; Yan, C.; Lin, J.; Liu, Z.; Lu, Y.; Bai, C.; Lu, Q.; Dai, S.; et al. Advances in the Structure and Materials of Perovskite Solar Cells. *Res. Chem. Intermed.* **2016**, *42* (2), 625–639.

(17) Rajamanickam, N.; Kumari, S.; Vendra, V. K.; Lavery, B. W.; Spurgeon, J.; Thad Druffel; Sunkara, M. K. Stable and Durable $CH_3NH_3PbI_3$ Perovskite Solar Cells at Ambient Conditions. *Nanotechnology* **2016**, *27* (23), 235404.

(18) Ye, H.-Y.; Liao, W.-Q.; Hu, C.-L.; Zhang, Y.; You, Y.-M.; Mao, J.-G.; Li, P.-F.; Xiong, R.-G. Bandgap Engineering of Lead-Halide Perovskite-Type Ferroelectrics. *Adv. Mater.* **2016**, *28* (13), 2579–2586.

(19) Chen, S.; Shi, G. Two-Dimensional Materials for Halide Perovskite-Based Optoelectronic Devices. *Adv. Mater.* **2017**.

(20) Saparov, B.; Mitzi, D. B. Organic–Inorganic Perovskites: Structural Versatility for Functional Materials Design. *Chem. Rev.* **2016**, *116* (7), 4558–4596.

(21) Kind, R.; Plesko, S.; Günter, P.; Roos, J.; Fousek, J. Structural Phase Transitions in the Perovskite-Type Layer Compounds $NH_3(CH_2)_3NH_3CdCl_4$,$NH_3(CH_2)_4NH_3MnCl_4$, and $NH_3(CH_2)_5NH_3CdCl_4$. *Phys. Rev. B* **1981**, *23* (10), 5301–5315.

(22) Day, P. Organic--Inorganic Layer Compounds: Physical Properties and Chemical Reactions. *Philos. Trans. R. Soc. Lond. Math. Phys. Eng. Sci.* **1985**, *314* (1528), 145–158.

(23) Zuñiga, F. J.; Chapuis, G. Structural Analysis of the Intermediate Phases of $(n\text{-}C_{13}H_{27}NH_3)_2ZnCl_4$ by Single Crystal Diffraction. *Mol. Cryst. Liq. Cryst.* **1985**, *128* (3-4), 349–366.

(24) Dolzhenko, Y. I.; Inabe, T.; Maruyama, Y. In Situ X-Ray Observation on the Intercalation of Weak Interaction Molecules into Perovskite-Type Layered Crystals $(C_9H_{19}NH_3)_2PbI_4$ and $(C_{10}H_{21}NH_3)_2CdCl_4$. *Bull. Chem. Soc. Jpn.* **1986**, *59* (2), 563–567.

(25) Conducting Tin Halides with a Layered Organic-Based Perovski. *Nat. Lond.* **1994**, *369* (6480), 467.

(26) Neve, F.; Crispini, A.; Armentano, S.; Francescangeli, O. Synthesis, Structure, and Thermotropic Mesomorphism of Layered N-Alkylpyridinium Tetrahalopalladate(II) Salts. *Chem. Mater.* **1998**, *10* (7), 1904–1913.

(27) Braun, M.; Frey, W. Crystal Structure of Bis(benzylammonium) Lead Tetrachloride, $(C_7H_7NH_3)_2PbCl_4$. *Z. Für Krist. - New Cryst. Struct.* **2014**, *214* (3), 331–332.

(28) Neve, F.; Francescangeli, O.; Crispini, A. Crystal Architecture and Mesophase Structure of Long-Chain N-Alkylpyridinium Tetrachlorometallates. *Inorganica Chim. Acta* **2002**, *338*, 51–58.

(29) Kong, Y.; Di, Y.; Yang, W.; Lü, Y.; Tan, Z. Crystal Structure, Phase Transition, and Thermodynamic Properties of Bis-Dodecylammonium Tetrachlorozincate $(C_{12}H_{25}NH_3)_2ZnCl_4$(s). *Chin. J. Chem.* **2010**, *28* (4), 521–530.

(30) G. Billing, D.; Lemmerer, A. Synthesis, Characterization and Phase Transitions of the Inorganic–organic Layered Perovskite-Type Hybrids $[(CNH_{2n+1}NH_3)_2PbI_4]$ (N = 12, 14, 16 and 18). *New J. Chem.* **2008**, *32* (10), 1736–1746.

(31) Huang, T. J.; Thiang, Z. X.; Yin, X.; Tang, C.; Qi, G.; Gong, H. $(CH_3NH_3)_2PdCl_4$: A Compound with Two-Dimensional Organic–Inorganic Layered Perovskite Structure. *Chem. – Eur. J.* **2016**, *22* (6), 2146–2152.

(32) Schaak, R. E.; Mallouk, T. E. Perovskites by Design: A Toolbox of Solid-State Reactions. *Chem. Mater.* **2002**, *14* (4), 1455–1471.

(33) Sanjaya Ranmohotti, K. G.; Josepha, E.; Choi, J.; Zhang, J.; Wiley, J. B. Topochemical Manipulation of Perovskites: Low-Temperature Reaction Strategies for Directing Structure and Properties. *Adv. Mater.* **2011**, *23* (4), 442–460.

(34) Tahara, S. Preparation of Inorganic-Organic Hybrids via Intercalation and Grafting Reactions of Protonated Forms of Ion-Exchangeable Layered Perovskites, Waseda University, 2007.

(35) Tahara, S.; Sugahara, Y. Interlayer Surface Modification of the Protonated Triple-Layered Perovskite $HCa_2Nb_3O_{10}{\cdot}x\ H_2O$ with *n* -Alcohols. *Langmuir* **2003**, *19* (22), 9473–9478.

(36) S. Cattaneo, A.; Ferrara, C.; Mossuto Marculescu, A.; Giannici, F.; Martorana, A.; Mustarelli, P.; Tealdi, C. Solid-State NMR Characterization of the Structure and Thermal Stability of Hybrid Organic–inorganic Compounds Based on a $HLaNb_2O_7$ Dion–Jacobson Layered Perovskite. *Phys. Chem. Chem. Phys.* **2016**, *18* (31), 21903–21912.

(37) Jacobson, A. J.; Whittingham, M. S. *Intercalation Chemistry*; Academic Press: New York, NY, 1982.

(38) Amghouz, Z.; Espina, A.; García, J. R. Synthesis and Characterization of a New Family of Alkylammonium–chromium Phosphates with Worm-like Morphology. *J. Solid State Chem.* **2015**, *221*, 158–165.

(39) Pursch, M.; Brindle, R.; Ellwanger, A.; Sander, L. C.; Bell, C. M.; Händel, H.; Albert, K. Stationary Interphases with Extended Alkyl Chains: A Comparative Study on Chain Order by Solid-State NMR Spectroscopy. *Solid State Nucl. Magn. Reson.* **1997**, *9* (2), 191–201.

(40) McPhail, R. A.; Strauss, H. L.; Snyder, R. G.; Elliger, C. A. C–H-Stretching Modes and the Structure of N-Alkyl-Chains. 2. Long, All-Trans Chains. *J Chem Phys* **1984**, *84*, 334–341.

(41) Snyder, R. G.; Strauss, H. L.; Elliger, C. A. C–H-Stretching Modes and the Structure of N-Alkyl-Chains. 1. Long, Disordered Chains. *J Chem Phys* **1982**, *86*, 5145–5150.

(42) Lehn, J.-M.; Alberti, G.; Bein, T. Chapter 2: Vibrational Spectroscopy (By J. Eric D. Davies and Horst Forster). In *Comprehensive supramolecular chemistry volume 8, Physical Methods in Supramolecular Chemistry.*; Pergamon: Oxford; New York; Tokyo, 1996; pp 1–23.

(43) West, A. R. Chapters 1 and 5 ("Crystal Structures and Crystal Chemistry", and "Crystallography and Diffraction Techniques"). In *Solid State Chemistry and its Applications*; John Wiley & Sons, Ltd: United Kingdom, 2014; pp 1–82, 229–270.

(44) Blake, A. J.; Clegg, W.; Cole, J. M.; Evans, J. S.; Main, P.; Parsons, S.; Watkin, D. J. *Crystal Structure Analysis: Principles and Practice*; Clegg, W., Ed.; Oxford University Press, 2009.

(45) Lehn, J.-M.; Alberti, G.; Bein, T. Chapter 1: Diffraction Techniques (By Zbigniew Dauter and Keith S. Wilson). In *Comprehensive supramolecular chemistry volume 8, Physical Methods in Supramolecular Chemistry.*; Pergamon: Oxford; New York; Tokyo, 1996; pp 1–23.

(46) Dinnebier, R. E.; Billinge, S. J. L. *Powder Diffraction: Theory and Practice*; Royal Society of Chemistry, 2008.

(47) Will, G. *Powder Diffraction: The Rietveld Method and the Two Stage Method to Determine and Refine Crystal Structures from Powder Diffraction Data*; Springer Science & Business Media: Germany, 2006.

(48) Boykin, J. R.; Smith, L. J. Rapid Microwave-Assisted Grafting of Layered Perovskites with N-Alcohols. *Inorg. Chem.* **2015**, *54* (9), 4177–4179.

(49) Armstrong, A. R.; Anderson, P. A. Synthesis and Structure of a New Layered Niobium Blue Bronze: $Rb_2LaNb_2O_7$. *Inorg. Chem.* **1994**, *33* (19), 4366–4369.

(50) Gopalakrishnan, J.; Bhat, V.; Raveau, B. $AILaNb_2O_7$: A New Series of Layered Perovskites Exhibiting Ion Exchange and Intercalation Behaviour. *Mater. Res. Bull.* **1987**, *22* (3), 413–417.

(51) Sato, M.; Abo, J.; Jin, T.; Ohta, M. Structure and Ionic Conductivity of $MLaNb_2O_7$ (M: K, Na, Li, H). *J. Alloys Compd.* **1993**, *192* (1–2), 81–83.

(52) Carvajal, R. *Comm Powder Diffr IUCr* **2001**, *26*, 12.

(53) Laugier, J.; Bochu, B. *LMGP-Suite Suite of Programs for the Interpretation of X-Ray Experiments, by Jean Laugier and Bernard Bochu, ENSP/Laboratoire Des Matériaux et Du Génie Physique, BP 46. 38042 Saint Martin d'Hères, France. WWW: http://www.inpg.fr/LMGP and http://www.ccp14.ac.uk/tutorial/lmgp/*.

(54) Huq, A.; Hodges, J. P.; Gourdon, O.; Heroux, L. Powgen: A Third-Generation High-Resolution High-Throughput Powder Diffraction Instrument at the Spallation Neutron Source. *Z Krist. Proc* **2011**, *1*, 127–135.

(55) Larson, A. C.; Von Dreele, R. B. General Structure Analysis System (GSAS); Los Alamos National Laboratory: Los Alamos, NM, 2000. *There No Corresp. Rec. This Ref.* 86–748.

(56) Toby, B. H. EXPGUI, a Graphical User Interface for GSAS. *J. Appl. Crystallogr.* **2001**, *34* (2), 210–213.

(57) A Dedicated Powder Diffraction Beamline at the Advanced Photon Source: Commissioning and Early Operational Results. *Rev. Sci. Instrum.* **2008**, *79* (8), 085105.

(58) Mistry, B. D. *A Handbook of Spectroscopic Data Chemistry: (UV, IR, PMR, 13CNMR and Mass Spectroscopy)*; Oxford Book Company, 2009.

(59) Kumada, N.; Kinomura, N.; Sleight, A. W. $CsLaNb_2O_7$. *Acta Crystallogr. C* **1996**, *52* (5), 1063–1065.

(60) Shallard-Brown, H. A.; Watkin, D. J.; Cowley, A. R. N-Octanol. *Acta Crystallogr. Sect. E Struct. Rep. Online* **2005**, *61* (2), o213–o214.

(61) Toby, B. Brian Toby's EXPGUI: Easy to start a new refinement https://neutrons.ornl.gov/sites/default/files/POWGEN-gsas-2banks.pdf (accessed Mar 25, 2017).

(62) Barman, S.; Venkataraman, N. V.; Vasudevan, S.; Seshadri, R. Phase Transitions in the Anchored Organic Bilayers of Long-Chain Alkylammonium Lead Iodides $(C_nH_{2n+1}NH_3)_2PbI_4$; N = 12, 16, 18. *J. Phys. Chem. B* **2003**, *107* (8), 1875–1883.

(63) Tomaszewski, P. E. Structural Phase Transitions in Crystals. I. Database. *Phase Transit.* **1992**, *38* (3), 127–220.

(64) Suresh, R.; Venkataraman, N.; Vasudevan, S.; Ramanathan, K. V. Conformational Mobility in Alkyl-Chains of an Anchored Bilayer. *J. Phys. Chem. C* **2007**, *111* (2), 495–500.

Chapter 4. Rapid Exfoliation and Surface-Tailoring of Perovskite Nanosheets via Microwave-Assisted Reactions[§]

4.1– Introduction

The nanoscale manipulation of materials is the foundation of nanotechnology. Advances in synthesis have allowed this field to grow rapidly in a variety of areas (e.g., medicine, electronics, and materials) since the 1980s.[1–3] The properties of nanostructured materials can dramatically change with variations in their dimensionality.[3,4] With respect to two-dimensional (2D) materials, these are often obtained by cleaving weak out-of-plane van der Waals interactions in a layered host, leading to freestanding layers with strong in-plane chemical bonds.[3,5–14] The weak out-of-plane interactions and strong in-plane bonds are key to high-yield delaminations of layered hosts. There are many sets of well-studied 2D materials[113,11,15] including the graphene family[15] (graphene,[16,17] graphene oxide,[18–20] fluorographene,[21,22] hexagonal boron nitride,[23–26] and boron carbon nitride[27,28]), 2D chalcogenides (transition metal dichalcogenide[29,30] and trichalcogenide[31]), layered double hydroxides[8,10] (LDHs), and oxides[6–8] (e.g., aluminosilicate clays, transition metal oxides with rock salt- and perovskite-related structures). Interest in such 2D materials and their nanostructures arises from properties that make them suitable for diverse applications in electronics, optoelectronics, catalysis, gas separation or storage, coatings, support membranes, sensors, etc.[3,4,12,32,33]

A variety of methods has been reported for the fabrication of 2D nanosheets. These include liquid exfoliation, micromechanical cleavage, chemical vapor deposition, van der Waals epitaxial growth on a substrate, and hydrothermal synthesis.[3,33–35] Liquid exfoliation is especially prevalent where techniques mainly involve intercalation of organic, polymeric, or ionic species that weaken the interlayer adhesion and result in the delamination of the layered structure.[3,36–43] Ultrasonic cleavage of the layers is another important approach to liquid exfoliation, which can

[§] This chapter was adapted from: Akbarian-Tefaghi, S.; Rostamzadeh, T.; Brown, T. T.; Davis-Wheeler, C.; Wiley, J. B. "Rapid Exfoliation and Surface-Tailoring of Perovskite Nanosheets via Microwave-Assisted Reactions" *(submitted)*.

increase the yield of exfoliation after the intercalation step, or in some cases, when done in suitable solvents, can on its own lead to exfoliation.[3,11,44,45]

Layered oxide perovskites are one set of important compounds that can be manipulated to lead to individual oxide nanosheets or thin slabs consisting of just a few layers. Typically, these materials are produced via the liquid exfoliation method.[3,5–8,11] Since the slab thickness and the elemental composition of the perovskite host can be manipulated in the solid state synthesis step prior to exfoliation, engineering of the nanosheet composition and thickness is readily obtainable. Intercalation of a bulky organic base such as tetra(n-butyl)ammonium ion (TBA^+) is the most common method of liquid exfoliation in layered perovskites.[42,46–55] As the reactivity of the Ruddlesden-Popper phase with an organic base is often very limited,[42] double- and triple-layered Dion-Jacobson-type compounds such as $RbLaNb_2O_7$, $RbLaTa_2O_7$, and $KCa_2Nb_3O_{10}$ are the most-commonly used precursors to produce nanosheets and more complicated assemblies of 2D structures for various applications.[45,47,48,56–72] In some cases, fluorination[70,73] or doping[49,71,74] of these perovskites has been carried out prior to exfoliation to improve the conductivity or catalytic activity of the nanosheets.

Once 2D nanosheets are obtained, they can be used as building blocks for more complicated structures, allowing for improved electronic, optoelectronic, catalytic, or mechanical properties of composite structures. Integration of these components can occur via 2D heterostructures (lateral and vertical),[15,32–34,75–78] layer-by-layer assemblies,[6,72,79–90] or the incorporation of chemically-modified monolayers into polymers. Among the different methods of surface modification of various nanosheets,[88,90–98] graphene oxide (GO) has attracted much attention where there are many studies discussing the functionalization and surface modification of GO nanosheets[99–110] and GO based composites.[111–119] Some of the composites involve actual covalent bonds between GO nanosheets and polymer chains, either by crosslinking nanosheets to polymer chains,[120–122] or by in-situ polymerization on nanosheet surfaces.[123–125] Unlike GO nanosheets and self-assembled-monolayers (SAMs),[126–130] controlled surface modification of perovskite-based nanosheets has been limited to only a few reports.[36–38,45,69,70] At best, the surface groups of the perovskite nanosheets are introduced prior to exfoliation. These systems typically contain organic substituents in the interlayer of the host. In $HLaNb_2O_7$ for example, nanosheets are obtained via ultrasonic exfoliation of hosts containing fluoroalkoxy groups in the

interlayer,[45] or by growing a polymeric network in the interlayer, which then delaminates the layered structure into nanosheets within a polymer matrix.[36–38] There is only one report where surface groups are covalently attached to nanosheets *after* exfoliation; this study involves the attachment of phenylphosphonate groups, where the entire process required over a week of reaction time (7 d exfoliation followed by 3 d of surface modification reaction).[131,132] In other cases, there is no actual covalent bond between the nanosheets and the surface groups or polymer chains; electrostatic interactions dominate these systems.[69,70,133,134]

Rapid microwave-assisted (MA) methods have been found to be effective for organic modification of bulk layered perovskites.[135–138] Herein we extend microwave methods to both the rapid exfoliation and post-exfoliation surface-modification of perovskite nanosheets. MA reactions allow exfoliation to be carried out in as little as 15 min and subsequent surface modifications in as little as 1 h. Exfoliation utilizes the protonated double-layered Dion-Jacobson perovskite ($HLnNb_2O_7$; Ln = La, Pr) where reactions with TBAOH quickly lead to dispersed materials. Exchange reactions can then be applied with a wide variety of organics leading to new surface groups; this approach allows one to replace TBA^+ groups with other organics that contain hydroxyl or amine functionality. This is significant in that it allows the production of a variety of nanosheet-based hybrids with controlled surface engineering in only a few hours.

4.2– Experimental

4.2.1 Materials

Rb_2CO_3 (Alfa Aesar, 99.8%) was used as received. La_2O_3 (Alfa Aesar, 99.99%), Nb_2O_5 (Alfa Aesar, 99.9985%), and Pr_6O_{11} (Alfa Aesar, 99.9%) were heated at 1000 °C in air for 12 h in order to eliminate any impurities or nonstoichiometries. Organic solvents were used without further purification: toluene (Fisher 99.5%), 1-propanol (Alfa Aesar 99+%), 1-pentanol (Alfa Aesar 98+%), 1-decanol (Alfa Aesar 98+%), 1-propylamine (Alfa Aesar 99+%), 1-butylamine (Alfa Aesar 99%), 1-hexylamine (Alfa Aesar 99%), and 1-octylamine (Alfa Aesar 99%). Tetrabutylammonium hydroxide 30-hydrate, 95+% (TBAOH, ACROS Organics) was used for exfoliation trials. ***Note:*** To preserve the integrity of the TBAOH reagent, it is recommended that the storage temperature be in the range of 2-8 °C, and that handling at room temperature be minimized to avoid melting. A variety of organic components with hydroxyl functional groups

were used to study the reproducibility of the proposed surface-modification technique; polyethylene glycol 400 (Alfa Aesar PEG-400), benzyl alcohol (Alfa Aesar 99%), 3-phenoxybenzyl alcohol (Alfa Aesar 98%), phenylphosphonic acid (Aldrich 98%), 2-allylphenol (Alfa Aesar 98+%), 9-decen-1-ol (Alfa Aesar 90+%), trimethylolpropane diallyl ether (Sigma Aldrich 90%), and 6-chloro-1-hexanol (Alfa Aesar 97%) were used as received. ***Note:*** To minimize unwanted degradation, unsaturated organics are best stored in a refrigerator in the absence of oxygen. Toluene and milli-Q water (18.2 MV cm, Millipore) were used for non-aqueous solutions and aqueous solutions (aq. soln.), respectively.

4.2.2 Synthesis of Inorganic Hosts

$RbLnNb_2O_7$ (Ln = La, Pr) were synthesized by grinding stoichiometric amounts of the corresponding oxides (La_2O_3, Pr_6O_{11} and Nb_2O_5) with a 30% molar excess of Rb_2CO_3 as previously reported.[139,140] The excess carbonate was used to compensate for the loss of alkali-metal oxides due to volatilization. The mixture was preheated at 850 °C overnight, ground, and heated at 1050 °C (24 h and 6 h for Ln = La and Pr, respectively). After regrinding, the sample was heated at 1100 °C (24 h and 48 h for Ln = La and Pr, respectively). The product was washed with copious amount of water to remove the excess carbonate, and dried at 100 °C for a few hours.

Microwave Syntheses. Topochemical reactions involving ion exchange, exfoliation, and surface modification (details given below) were carried out in a StartSYNTH Microwave Synthesis Labstation as previously reported.[136] The unit was equipped with Milestone's START platform where the individual reactions were contained in quartz pressure reactors (< 15 bar) and placed in a rotor. Grafting unsaturated organics was carried out in a Milestone QV-50 setup, where a quartz reactor vessel was sealed in the glovebox in order to eliminate the exposure of the reaction mixture to oxygen. Figure 4-1 shows the picture of the sample rack in Milestone QV-50 setup, where a sealed quartz vessel is placed in front of the IR sensor inside the microwave cavity. As shown here, the reaction mixture, stirring bar and Weflon button are all placed in the vessel in a glovebox (Figure 4-1b), and then completely sealed under argon (Figure 4-1c). After taking the sealed sample holder out, the reaction is maintained under argon until after opening the cap. ***Caution:*** One should inspect glass microwave vessels before each reaction; glass defects might lead to hotspots and result in an explosion.

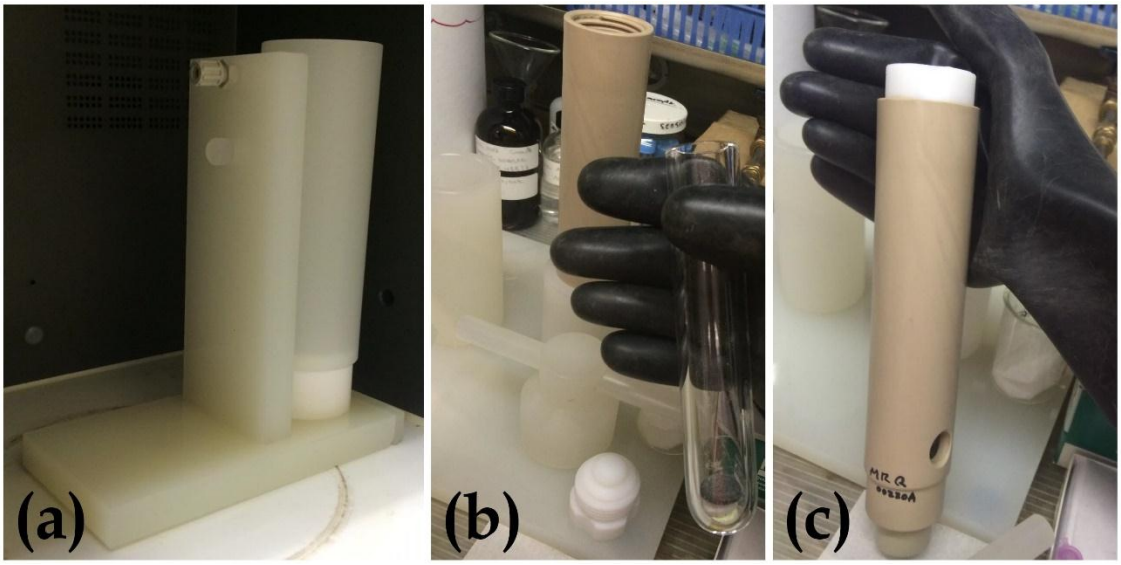

Figure 4- 1: Milestone QV-50 setup.

4.2.3 Acid Exchange (Protonation)

Microwave acid treatment was carried out for 3 h at 60 °C with continuous stirring and a maximum power of 300 W.[136] To maintain a molar ratio of greater than 150:1, proton to interlayer cation (Rb), a 6M nitric acid solution was used for the ion exchange. The protonated product was washed with distilled water until pH 7 was achieved. The samples were then dried at 100 °C for 3 hours.

4.2.4 Exfoliation of $HLnNb_2O_7$

$HLnNb_2O_7$ (HLnNb) was exfoliated in an aqueous solution of TBAOH with a molar ratio of 1:10 for HLnNb to hydrated TBAOH in as little as 15 minutes. Typical microwave-assisted exfoliation reactions were carried out at 1 h at 60 °C (max 300 W), then ramped to 80 °C over a 10-minute period, before heating at 80 °C for 1 h (max 350 W). Exfoliation with high conversions could also be realized in shorter times, though this approach favors smaller nanosheets: 1 h at 80 °C (max 350 W), 30 min at 100 °C (max 450 W), and 15 min at 120 °C (max 550 W). All products were washed with water and ethanol, and dried at 70 °C for several hours.

4.2.5 Surface Exchange of Nanosheets with n-Alkyl Alcohols and n-Alkylamines

Once exfoliated LnNb nanosheets were obtained (TBA-LnNb NS), various n-alkyl alcoxy and n-alkylammonium surface groups were placed on LnNb NS by exchange reactions with $C_nH_{2n+1}OH$ (n = 3, 5, 10) and $C_nH_{2n+1}NH_2$ (n = 3, 4, 6, 8) solvents via microwave-assisted exchange reactions. Typically, 25 mg of dried TBA-LnNb NS were reacted with 8 mL pure solvent containing a Weflon button: 1 h at 100 °C (max 600 W) in n-propanol, 1-propylamine and 1-butylamine, 45 min at 120 °C (max 800 W) for n-pentanol and 1-hexylamine, and 30 min at 150 °C (max 1000 W) for n-decanol and 1-octylamine. The products were washed with acetone and dried at 70 °C for several hours.

4.2.6 Exchange of Nanosheets with Other Organic Surface Groups

Typically 15 mg of TBA-PrNb NS were stirred in 8 mL of desired solution mixture with microwave heating: 15% (w/w) aq. soln. of PEG-400 (100 °C for 1 h, max 350 w), 2% (w/w) soln. of phenylphosphonic acid in toluene (100 °C for 1 h, max 1000 W with a Weflon button), pure 6-chloro-1-hexanol (120 °C for 45 min, max 800 W with a Weflon button), pure benzyl alcohol (60 °C for 1 h, max 300 W with a Weflon button), and pure 3-phenoxybenzyl alcohol (80 °C for 1 h max power of 400 W with a Weflon button). All products were washed with ethanol, then acetone, and dried at 70 °C for several hours.

4.2.7 Exchange of Nanosheets with Unsaturated Surface Groups

In order to protect unsaturated bonds from undesired polymerization in oxygen, reactions with 9-decen-1-ol, 2-allylphenol, and trimethylolpropane diallyl ether were carried out under argon. For the microwave-heated samples, 15 mg of TBA-LnNb NS were combined with 5 mL of pure organic reactants within reactor vessels, sealed in a glovebox under argon, and heated at 90 °C for 45 min (max 500 W). Alternative to these microwave-assisted reactions, similar exchange reactions were carried out with convection heating under argon in a glovebox; samples were heated on a hot plate with stirring for 2 d at 80 °C. The glovebox reactions were done as controls and in all cases yielded identical results to microwave reactions. The monomer-grafted sheets were washed with ethanol, then acetone, dried under vacuum at room temperature, and stored under argon in a glove-box.

4.2.8 Characterization

A Philips X'Pert system equipped with Cu Kα radiation (λ = 1.5418 Å) and a curved graphite monochromator was used in continuous mode with a scan rate of 0.02 °/s to collect the X-ray powder diffraction (XRD) data. Thermogravimetric analysis (TGA) and differential scanning calorimetry (DSC) were carried out on a TA Instruments TGA-DSC SDT Q600 system in alumina pans under a dilute oxygen atmosphere (ca. 50% argon); samples were heated to 900 °C at a rate of 15 °C/min. Raman spectra were collected in a Thermo-Fisher DXR dispersive Raman spectrometer using the λ = 532 nm line with a spectral resolution of 3 cm^{-1}. The thickness of the nanosheets was examined under an Asylum Research MFP-3D Atomic Force Microscope (AFM) working in the dual amplitude resonance tracking (DART) mode; nanosheet samples were observed as a dilute dispersion made by an ethanol drop cast onto a mica sheet. Transmission electron microscopy (TEM) images and selected area electron diffraction (SAED) were taken at JEOL 2010 high-resolution microscope (200 keV) and FEI TECNAI G2 F30 FEG TEM (300 keV). For TEM measurements, a dilute dispersion of nanosheets in ethanol was drop cast onto a grid (carbon film coated fine mesh copper), and dried at room temperature for a few hours. Field emission SEM images of sample morphologies were obtained on a HITACHI S-4800 FEG CRYO-SEM. For the FESEM sample preparation, either a dispersion of nanosheets in ethanol was drop cast on small pieces of aluminum foil, or a trace of the dried powder was mounted on a piece of double-sided carbon tape. The samples were lightly coated with gold and observed in 1-3 kV range.

4.3– Results

4.3.1 Exfoliation of $HLnNb_2O_7$

It has been found that microwave heating can be used to readily exfoliate layered perovskites. A variety of conditions were investigated to examine the influence of reaction times and temperature, and in all cases nanosheets were efficiently obtained through exfoliation of the perovskite host: 2 h at 60 °C, 1 h at 80 °C, 30 min at 100 °C, and 15 min at 120 °C (halving the reaction times with every 20 °C increase in the exfoliation temperature). TEM images of the TBA-PrNb nanosheets synthesized under these different conditions are presented in Figure 4-2a−d, demonstrating the efficient production of nanosheets in 15, 30, 60 and 120 minutes at temperatures ranging from 60 °C to 120°C. Evaluation of nanosheets across the entire TEM grid

supports effective and essentially complete exfoliation in all the conditions above. It appears that nanosheets obtained at higher temperatures are on average relatively smaller in size and generally more fragmented. Reactions carried out at 60 °C produced the largest nanosheets with some as large as few microns on an edge. The insertion of TBA^+ ions into the perovskite galleries results in delamination of the layered structure and loss of crystallinity. XRD patterns of the reassembled nanosheets consistently confirmed the expected loss of crystallinity, and indicated a high-yield exfoliation when compared to the $HPrNb_2O_7$ host (Figure 4-3). The exfoliation conditions employed in all the following results were chosen to be a 2 h reaction as presented in Figure 4-2e,f (1 h at 60 °C , ramped to 80 °C and heated for 1 h—*as a single reaction with two steps).* This ensured a very efficient exfoliation without high fragmentation of the nanosheets. Figure 4-4 provides the X-ray diffraction data for both TBA-LaNb and TBA-PrNb nanosheets obtained via this selected method, and compares them to the XRD patterns of the hosts. The high angle reflections are minimized with *0k0* reflections dominating the pattern. The first reflections related to *0k0* set of planes shift from about 8.5 ° for $HLnNb_2O_7$ to 4.5 ° for TBA-LnNb NS, confirming the expansion in the interlayer spacings after the intercalation of TBA^+. The first peak in the XRD pattern of TBA-LnNb NS is also broader than the very sharp first peak of the $HLnNb_2O_7$, suggesting the formation of nanostructures in the former.

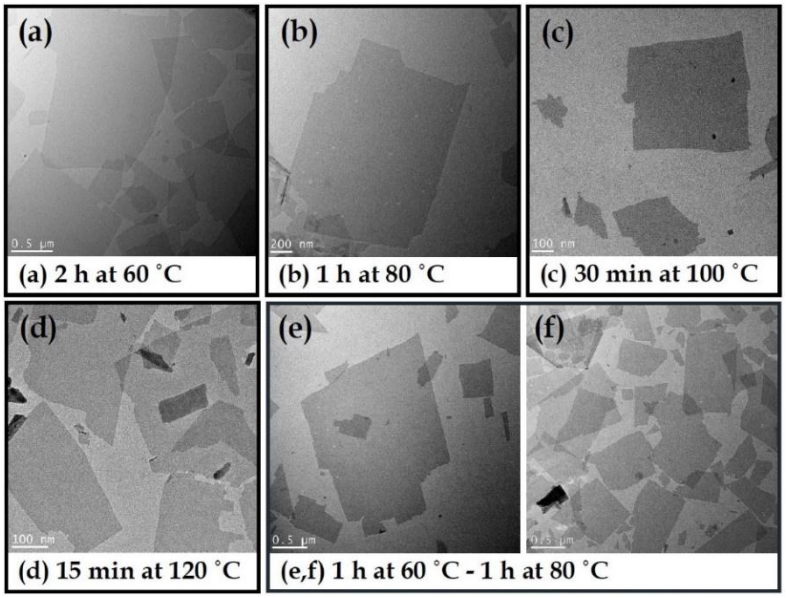

Figure 4- 2: TEM images of the nanosheets obtained via various microwave conditions: (a) 2 h at 60 ˚C, (b) 1 h at 80 ˚C, (c) 30 min at 100 ˚C, (d) 15 min at 120 ˚C, (e,f) the main synthesis approach, consisting of a two-step heating method: 1 h at 60 ˚C - 1 h at 80 ˚C.

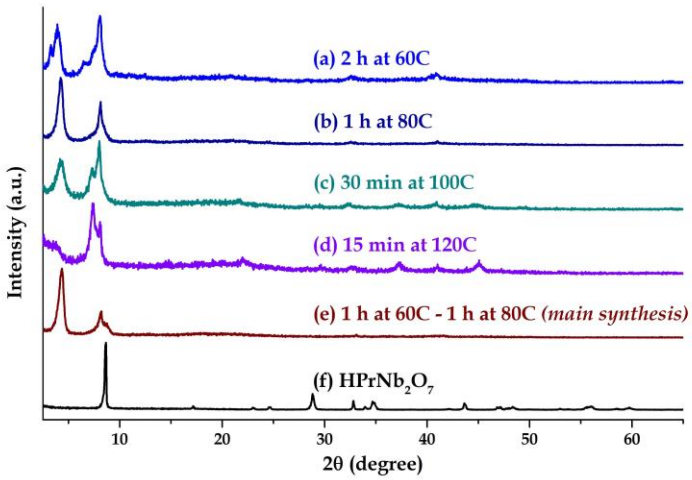

Figure 4- 3: XRD patterns of nanosheets obtained under various microwave exfoliation conditions, versus the host.

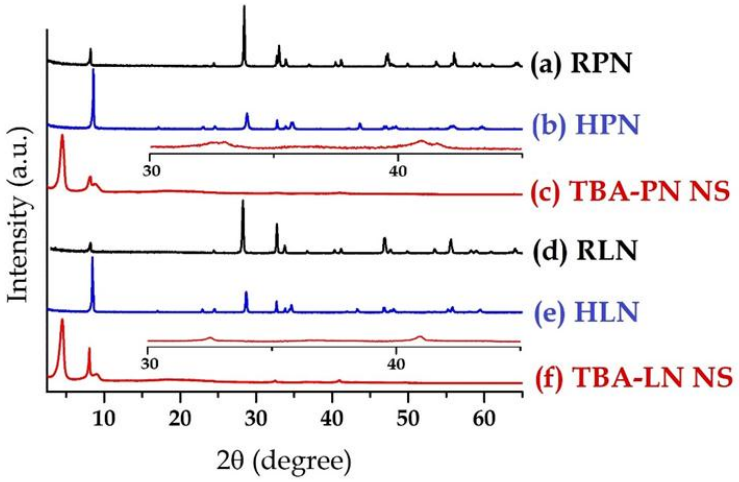

Figure 4- 4: XRD patterns of the layered perovskite hosts versus the exfoliated nanosheets: RPN, HPN, and TBA-PN NS in (a-c), and RLN, HLN, and TBA-LN NS in (d-f).

The topology of individual nanosheets was further examined with AFM. The height contact-mode image and height profile from a TBA-PrNb nanosheet sample are provided in Figure 4-5. The average nanosheet thickness was found to be 1.4(3) nm based on 29 values measured from different height profiles of TBA-PN nanosheets. Considering the crystal structure of $RbPrNb_2O_7$ reported in the literature,[140] the thickness of the $PrNb_2O_7$ slab is about 0.82 nm (oxygen-oxygen distance across the slab). Taking into account the thickness of each slab, any assembly of two nanosheets is expected to be greater than 1.64 nm (two slabs as well as an

interlayer spacing between adjacent organic layers). This implies the delamination of the hosts to at most two layers – though most likely single layers in the current study.

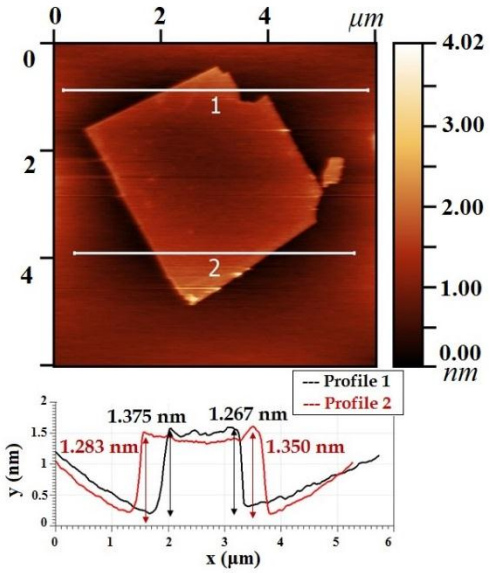

Figure 4- 5: Height contact-mode AFM image and height profile for a TBA-PN NS sample.

FESEM images of TBA-$LnNb_2O_7$ (Ln = La, Pr) nanosheets are presented in Figure 4-6 showing the existence of transparent nanosheets which stand individually or as assemblies of a few to multiple after being drop cast and dried. For nanosheets of a few layers, the thickness is small enough that underlying nanosheets can be observed. Interestingly, some small islands are observed on the surface of these nanosheets in absolute focus; these spots are not evident in TEM images. Figure 4-7 presents the TEM images and selected area electron diffraction (SAED) patterns of TBA-LnNb (Ln = La, Pr) nanosheets. The SAED analysis was performed to ensure the intact delamination of the perovskite slabs without disturbing the order of the in-plane elements. The known body-centered orthorhombic unit cell parameters are a = 5.4941 Å, b =

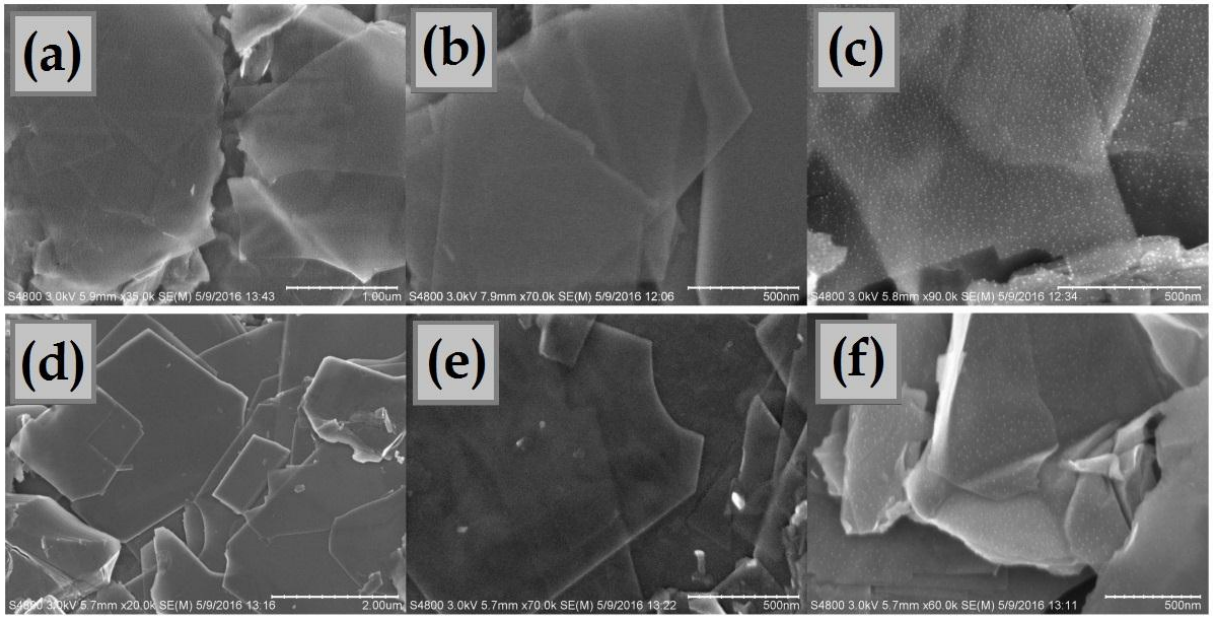

Figure 4- 6: FESEM images of (a-c) TBA-PN NS, and (d-f) TBA-LN NS.

21.9901 Å, and c = 5.4925 Å for $RbLaNb_2O_7$ and a = 5.4534 Å, b = 22.012 Å, and c = 5.4549 Å for $RbPrNb_2O_7$.[139,140]The delamination of the crystalline structure occurs in b direction so that the SAED patterns are along the [010] zone axis. These SAED patterns can be indexed on a body-centered cell. The d value of the *200* reflection was then calculated (the wavelength of the electron beam was 0.0251 Å at 200 keV and the camera length was either 100 cm or 200 cm), which then allowed estimation of the a parameters; 5.71 Å and 5.68 Å for Ln = La and Pr, respectively. Similar calculations were then done for the *101* reflection to estimate the c parameter (5.71 Å and 5.74 Å for Ln = La and Pr, respectively). These estimated a and c values are close to those of the starting material,[48,142] and consistent with delamination of the layered host in b direction. EDS analysis on TBA-LnNb nanosheets under TEM (Figure 4-8) confirms that nanosheets retain both Nb and Ln. This investigation of thickness and atomic arrangement well proves that the exfoliation has efficiently taken place, maintaining the integrity of the slab composition as individual nanosheets.

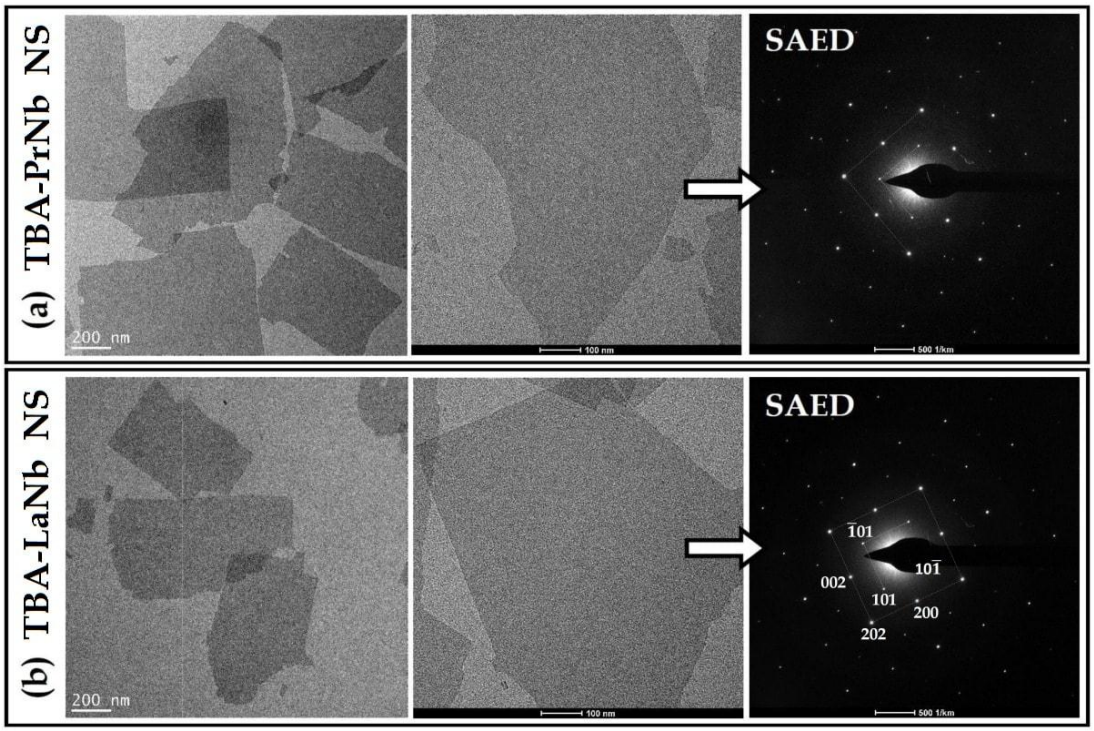

Figure 4- 7: TEM images of TBA-LnNb nanosheets are presented as well as the SAED patterns from the specified portions (Ln = (a) Pr, and (b) La).

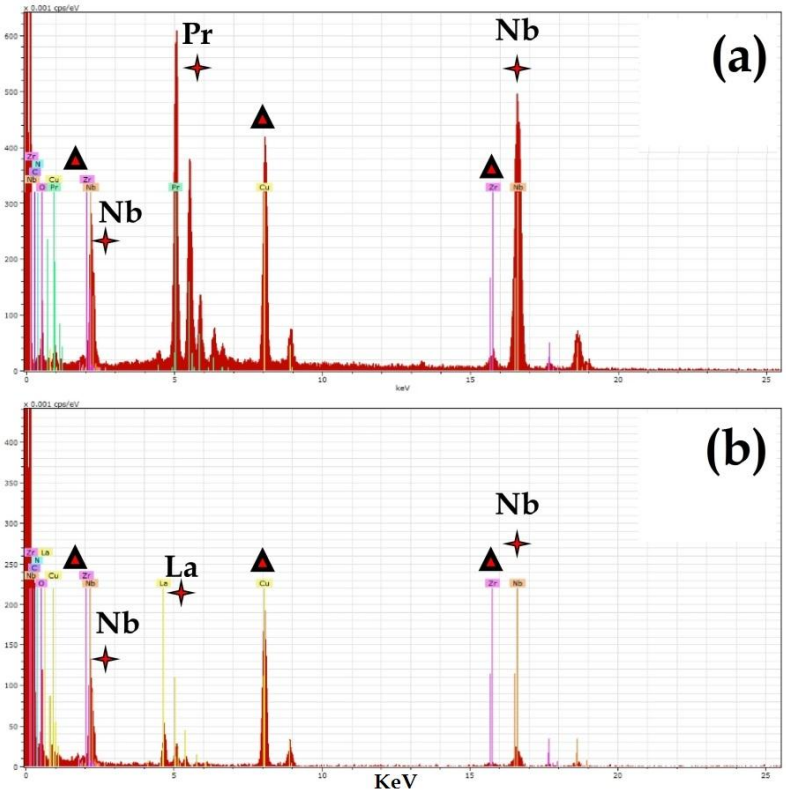

Figure 4- 8: Elemental analysis results for TBA-LnNb nanosheets: (a) Ln = Pr, (b) Ln = La.

As explained above, TBA-LnNb nanosheets are typically obtained by reacting $HLnNb_2O_7$ with TBAOH base. As a further study, exfoliation was also investigated using various layered hybrids with terminal alkoxy-grafted organics (n-alkyl alkoxy-$PrNb_2O_7$ instead of $HPrNb_2O_7$ acid exchanged hosts) to see whether alkoxy covalent bonds survive the intercalation of TBA^+ and nanosheets with alkoxy surface groups are obtained, or similar TBA-LnNb nanosheets are obtained regardless of the interlayer functionality of the exfoliating host. In all conditions, alkoxy groups were exchanged with TBA^+ ions and the nanosheets exfoliated from the layered hosts, resulting in similar products as is seen starting from $HLnNb_2O_7$ (Figures 4-9 and 4-10). This suggests that the reactivity of the oxygen atoms present on the surface of the nanosheets is very similar to those present in the interlayer of the perovskite-based hybrids. The methods available for organic modification of the layered perovskites can then be readily applied in the same fashion to modify the surface of the nanosheets with a variety of organics containing hydroxyl or amine functional groups.

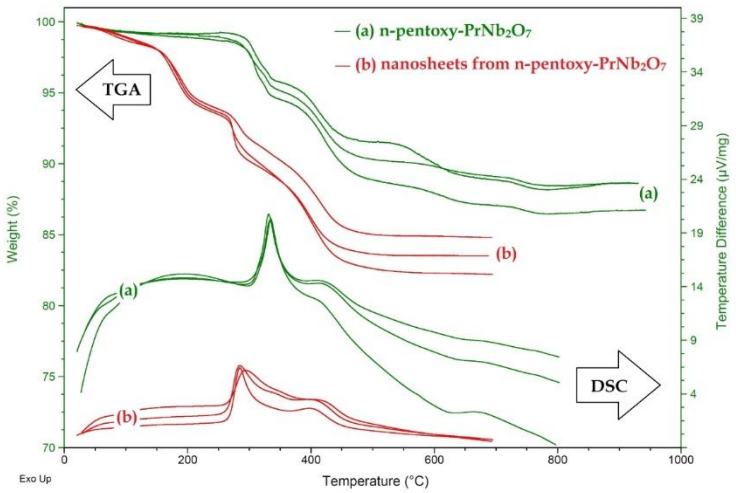

Figure 4- 9: TGA-DSC curves for n-pentoxy-$PrNb_2O_7$ and the nanosheets produced from this host after reaction with TBAOH.

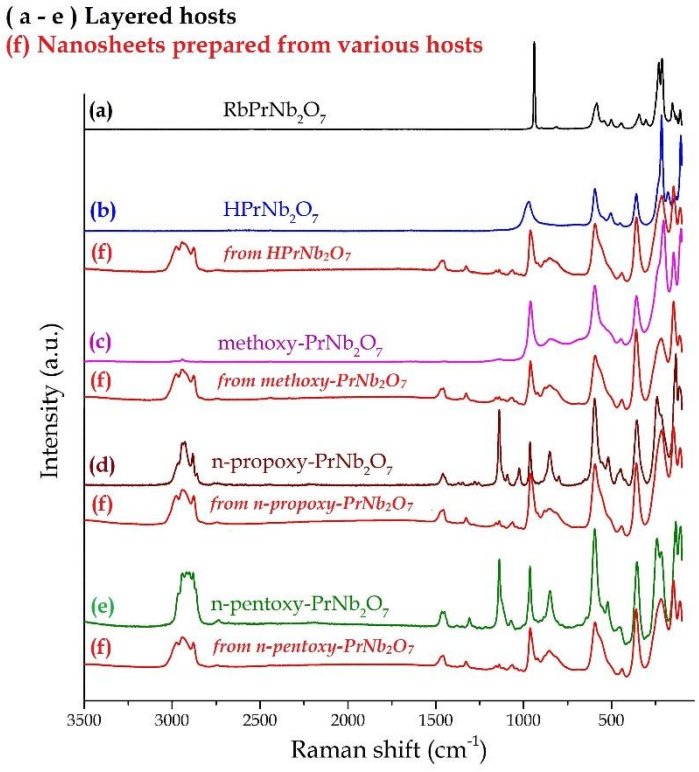

Figure 4- 10: Raman spectra of (a) $RbPrNb_2O_7$, (b) $HPrNb_2O_7$ and (c-e) $C_nH_{2n+1}PrNb_2O_7$ (n = 1, 3, and 5 in c, d, and e, respectively), versus (f) the nanosheets obtained from the hosts provided in b-e.

Table 4- 1: Summary of microwave-assisted surface modification reactions.

Hybrid Perovskite Nanosheets	Microwave Reaction (condition and duration)
TBA-LnNb NS (TBA^+-$LnNb_2O_7$) *Ln = Pr, Nb*	$HLnNb_2O_7$ + TBAOH + water **Variable durations (15 min- 2 h) and temperatures (60-120 °C) are applicable**
n-propoxy-Ln NS, 1-propylammonium-Ln NS, 1-butylammonium-Ln NS	TBA-LnNb NS + n-propanol / 1-propylamine / 1-butylamine **1 h at 100 °C- max 600 W** (using Weflon button)
n-pentoxy-Ln NS, 6-chloro-1-hexoxy-Ln NS 1-hexylammonium-Ln NS	TBA-LnNb NS + n-pentanol / 1-hexylamine / 6-chloro-1-hexanol **45 min at 120 °C- max 800 W** (using Weflon button)
n-decoxy-Ln NS, 1-octylammonium-Ln NS	TBA-LnNb NS + n-decanol / 1-octylamine **30 min at 150 °C- max 1000 W** (using Weflon button)
PEG-Ln NS	TBA-LnNb NS + 15% (w/w) aq. soln. of PEG-400 **1 h at 100 °C- max 350 W**
Benzyl alcoxy-Ln NS	TBA-LnNb NS + benzyl alcohol **1 h at 60 °C- max 300 W** (using Weflon button)
3-phenoxybenzyl alcoxy-Ln NS	TBA-LnNb NS + 3-phenoxybenzyl alcohol **1 h at 80 °C- max 400 W** (using Weflon button)
Phenylphosphonic-Ln NS	TBA-LnNb NS + 2% (w/w) soln. of phenylphosphonic acid in toluene **1 h at 100 °C- max 1000 W** (using Weflon button)
9-decen-1-oxy-Ln NS, 2-allylphenoxy-Ln NS, TMPDAE-Ln NS	TBA-LnNb NS + 9-decen-1-ol / 2-allylphenol / trimethylolpropane diallyl ether **1 h at 80 °C- max 400 W** (sealed vessel, using Weflon button)

4.3.2 Organic Modification of Nanosheets

Treatment of exfoliated TBA-LnNb nanosheets in different organic solvents allows one to exchange the TBA^+ surface ions with various alkoxy and alkylammonium groups. Table 4-1 gives a summary of various microwave reactions carried out in this work to perform surface modification on TBA-LaNb and TBA-PrNb nanosheets. Raman measurements verify the attachment of the different surface groups on these perovskite nanosheets (Figure 4-11). Initially, treatment was carried out with linear organics with simple structures (n-alkyl alcohols and n-alkylamines). Organic modification with $C_nH_{2n+1}OH$ (n = 3, 5 and 10) and $C_nH_{2n+1}NH_2$ (n = 3, 4, 6 and 10) was performed on the nanosheets in a fashion similar to what was used for topochemical reactions on bulk layered perovskites.[136] As further proof that TBA^+ is readily exchangeable, TBA-PrNb nanosheets were treated in pure 6-chloro-1-hexanol resulting in grafted surface groups with characteristic C-Cl Raman peaks (which is clearly distinguished from regular bonds in TBA^+ ions present on the starting host, Figure 4-11c and 4-11k). Grafting more complicated organic substituents on the surface was also carried out; polyethylene glycol-400 (PEG; $C_{2n}H_{4n+2}O_{n+1}$, n = 8.2 to 9.1), phenylphosphonic acid, benzyl alcohol, 3-phenoxybenzyl alcohol, as well as a number of unsaturated molecules, 9-decen-1-ol, 2-allylphenol, and trimethylolpropane diallyl ether (TMPDAE) were attached to the nanosheet surfaces. Figure 4-11 compares the Raman spectra of the bulk RbPrNb and HPrNb hosts, TBA-

PrNb nanosheets, and the various organic-inorganic hybrids synthesized based on modification of TBA-PrNb nanosheets. Characteristic bands of some of the nanosheet-based hybrids are highlighted in order to support the presence of different surface groups. The two rectangles with dashed borders highlight the peaks related to alkanes:[143] C-H symmetric and asymmetric stretch and deformation in -CH_3, C-H symmetric and asymmetric stretch, scissoring, twisting and wagging in –CH_2-, and stretch and deformation in –C-H. Based on the structure of the surface groups, these bands are expected to be seen for all the hybrids except for phenylphosphonic-PN NS which only has –$PO(OH)_2$ connected to a phenyl ring (stretch of P-O and P=O bonds are highlighted with solid circles in Figure 4-11). C-Cl bond is expected in nanosheets grafted with monochlorinated hexanol (marked with stars). The bands related to a phenyl ring are slightly different based on the substitutions present on the ring; characteristic peaks[143] in monosubstituted (in phenylphosphonic-, benzyl alcoxy-, and 3-phenoxybenzyl alcoxy-PN NSs), 1, 2 disubstituted (in 2-allylphenoxy-PN NS), and 1, 3 disubstituted rings (in 3-phenoxybenxyl alcoxy-PN NS) are highlighted with solid triangles. Upon grafting 9-decen-1-ol and trimethylolpropane diallyl ether

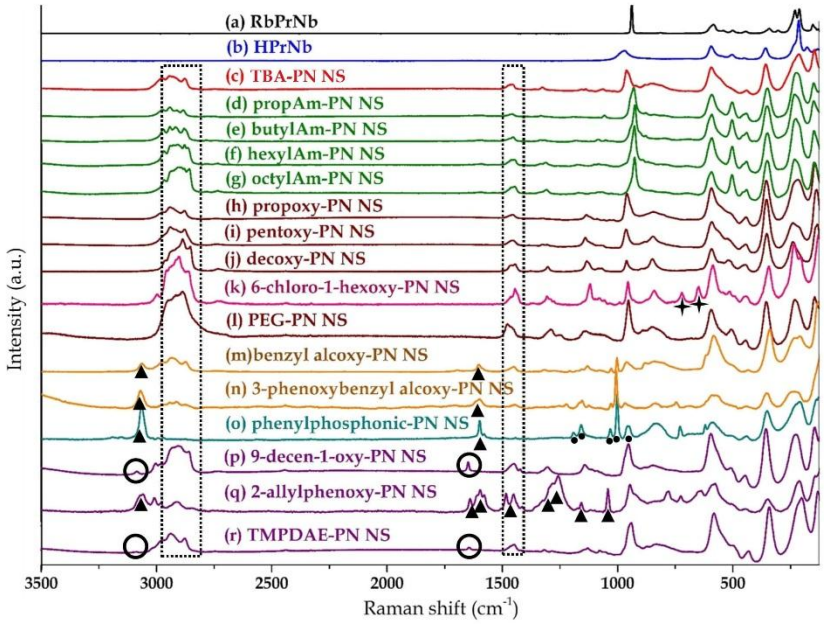

Figure 4- 11: Raman spectra of organically modified nanosheets versus the hosts: (a) RPN, (b) HPN, (c) TBA-PN NS, (d-g) $C_nH_{2n+1}NH_3^+$-PN NS (n = 3, 4, 6, and 8 in d, e, f, and g, respectively), (h-j) $C_nH_{2n+1}O$-PN NS (n = 3, 5, and 10 in h, i, and j, respectively), (k) $C_6H_{12}ClO$-PN NS, (l) PEG-PN NS , (m) C_7H_7O-PN NS, (n) $C_{13}H_{11}O_2$-PN NS, (o) $C_6H_6O_2PO$-PN NS , (p)$C_{10}H_{19}O$-PN NS, (q) C_9H_9O-PN NS, and (r) $C_{12}H_{22}O_3$-PN NS. (Raman bands related to alkanes are highlighted in dashed squares, solid triangle was used to mark the peaks pertinent to phenyl rings, solid circles for phosphonic related bonds, hollow circles for alkene related peaks, and star to mark the C-Cl bond.)

(TMPDAE), alkene related bonds are also observed at 3082 and 1644 cm^{-1}. Performing thermal analysis on various hybrid nanosheets provides further evidence of different groups present on the surface of the nanosheets after exchange; differences in the thermal behaviors and weight losses of three of the hybrids compared to TBA-PN NS, are presented in TGA-DSC results (Figure 4-12).

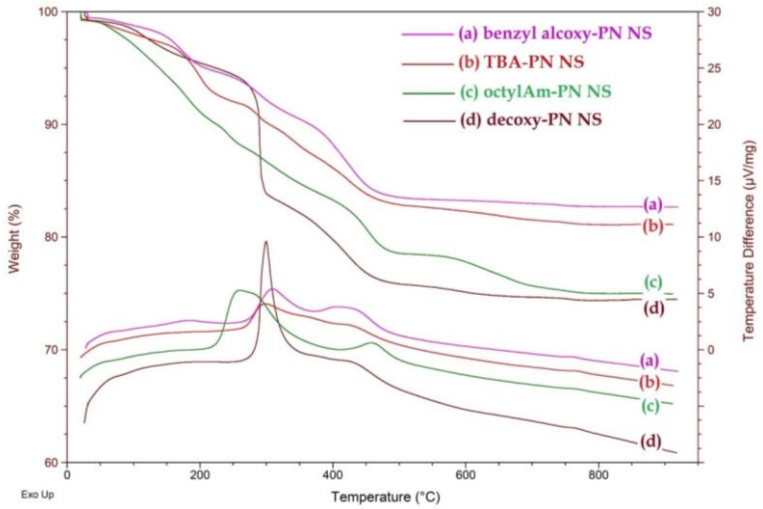

Figure 4- 12: TGA-DSC results of some nanosheet-based hybrids compared to TBA-PN NS host.

In theory, the length of the surface group will have an impact on how close the nanosheets can get to one another. This is similar to a recent report where $LaNb_2O_7$ nanosheets and organic molecules formed self-assembled hybrid films with a characteristic *d*-spacing in XRD.[144] Different interlayer spacings of the obtained hybrid nanosheets can be best studied via XRD measurements on samples drop cast out of their suspensions (Figure 4-13). The diffraction patterns show sharper peaks for the hybrids with moderately larger surface organics ($C_nH_{2n+1}OH$ (n = 5 and 10), $C_nH_{2n+1}NH_2$ (n = 4, 6 and 10), 6-chloro-1-hexanol, 3-phenoxybenzyl alcohol, and 9-decen-1-ol), than seen with TBA^+ groups, suggesting a higher level of organization in these systems. Figure 4-14 provides the XRD

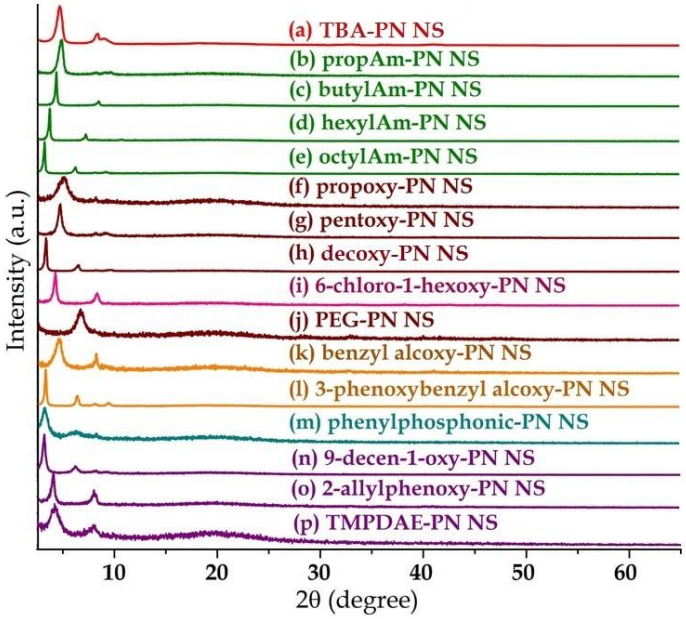

Figure 4- 13: XRD patterns of hybrid PN nanosheets with various surface groups: ammonium groups in (a) TBA^+ and (b-e) $C_nH_{2n+1}NH_3^+$(n = 3, 4, 6, and 8 in b, c, d, and e, respectively), as well as grafted alkoxy groups in (f-h) $C_nH_{2n+1}O$ (n = 3, 5, and 10 in f, g, and h, respectively), (i) $C_6H_{12}ClO$, (j) PEG , (k) C_7H_7O, (l) $C_{13}H_{11}O_2$, (m) $C_6H_6O_2PO$, (n)$C_{10}H_{19}O$, (o) C_9H_9O, and (p) $C_{12}H_{22}O_3$.

patterns of two hybrid nanosheets containing n-butylammonium and n-decoxy surface groups, compared to bulk layered organic-inorganic hybrids having *the same organic substituent* in the interlayer, to highlight the similarity in the interlayer spacings. This suggests that drop cast nanosheets form stacked assemblies with interlayer spacings very similar to that of the layered hybrid perovskite containing the same organic substituent. In other words, nanosheet assemblies with tunable interlayer spacings are readily attainable by tailoring the surface with various functional groups. Formation of nanosheet assemblies is further supported in Figure 4-15 by comparing the TEM images of n-decoxy-PN and TBA-PN NSs. Even though TBA-PN NS mainly form individual nanosheets in a dried state, assemblies of hybrid nanosheets are obtained by tuning the surface groups. Here the interdigitating grafted n-decoxy surface groups allow for the formation of assemblies of multiple nanosheets with certain interlayer spacings.

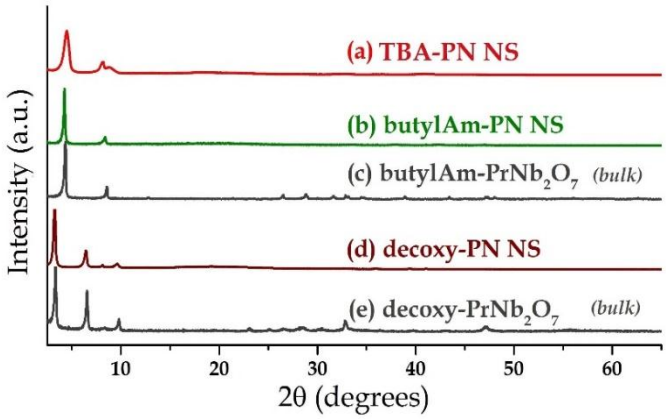

Figure 4- 14: XRD patterns of two types of organically modified sheets compared to similar layered hybrids: (a) TBA-PN NS, (b,d) nanosheets with n-butylammonium and n-decoxy surface groups, respectively, and (c,e) layered hybrids with similar organic substituents in the interlayer.

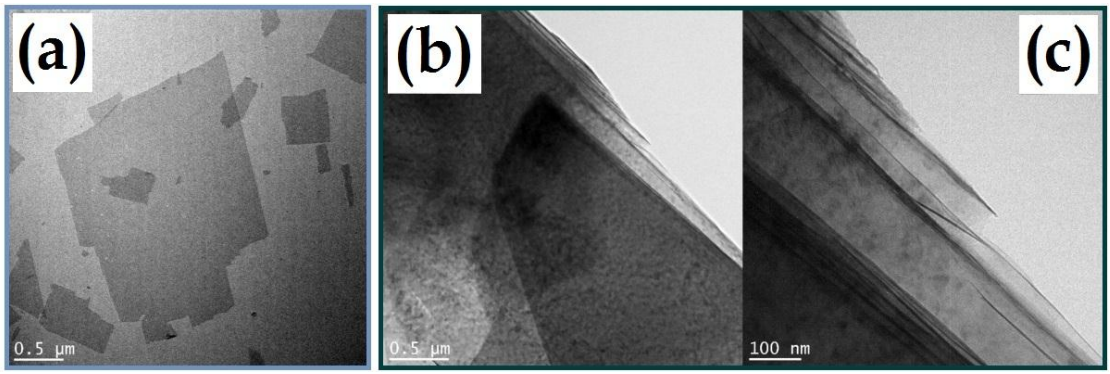

Figure 4- 15: TEM images of (a) TBA-PN NS, and (b, c) n-decoxy-PN NS (obtained by treatment of TBA-PN NS in n-decanol).

It should be noted that the hybrid films only offer short-range order due to the assembly of surface-tailored perovskite slabs in specific spacings, while the hybrid layered perovskites present prior to exfoliation are more crystalline with long-range order in their crystallites[136] (Figures 4-16 and 17). It is expected that once the layered bulk structure is broken into individual slabs (nanosheets), assembly of the nanosheets cannot provide a high crystallinity as once existed in the bulk layered material. FESEM images shown in Figure 4-16 compare bulk grafted polycrystalline samples to functionalized nanosheets. Long-range order of layered n-decoxy-$PrNb_2O_7$ with n-decoxy grafted in the perovskite galleries (Figure 4-16a,b) is compared to the hybrid films formed from n-decoxy-PN nanosheets (Figure 4-16c,d). The crystals exhibit an expanded, mille-feuille-like layered structure while the nanosheets show a few, poorly ordered restacked layers – the latter being the result of reassembly after an effective exfoliation step.

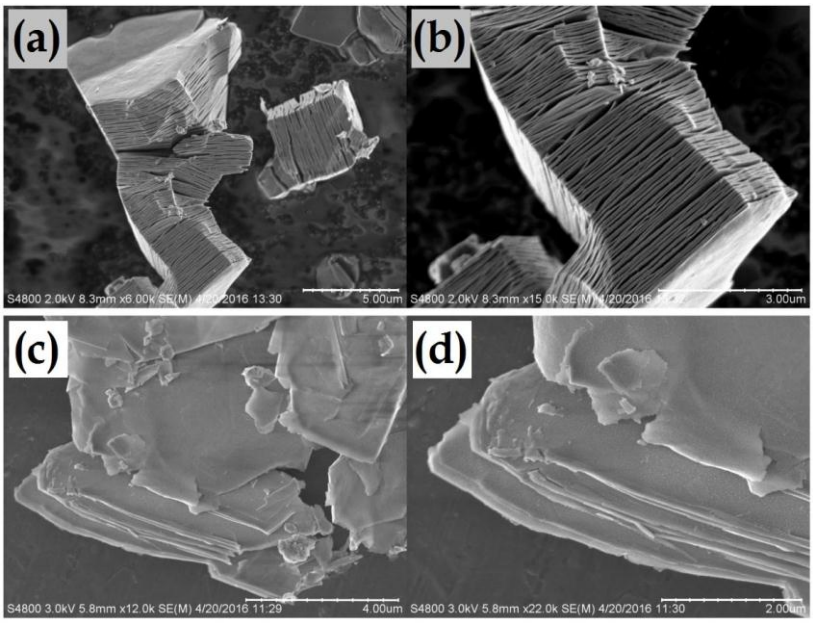

Figure 4- 16: FESEM images of (a,b) layered n-decoxy-$PrNb_2O_7$, compared to (c,d) restacked n-decoxy-PN nanosheets.

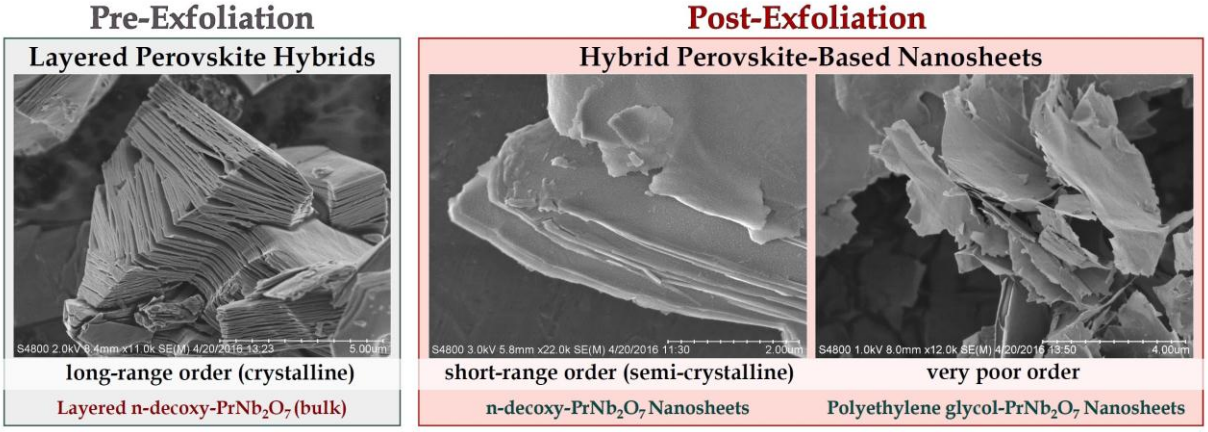

Figure 4- 17: The range of the order in hybrid nanosheets is compared to that of a hybrid layered perovskite present prior to exfoliation.

Variation in the organic surface groups is expected to impact the level of order in stacked hybrid nanosheets (Figure 4-17b); very short surface groups of the adjacent slabs are less capable of interacting well with each other, and very long organics fail to offer a repetitive locking behavior due to higher chances of bending and entanglement. Figure 4-18 shows the FESEM image of nanosheets with a long chain organic on the surface (PEG-400, 16-18 carbons in the backbone), and randomness in the nanosheet assemblies formed after drop casting and drying (no order in stacking). It is notable that the density of PEG-PN nanosheets was much smaller than any other products; the volume of the starting TBA-PN NS powder increased extensively after treatment in PEG-400 aqueous solution.

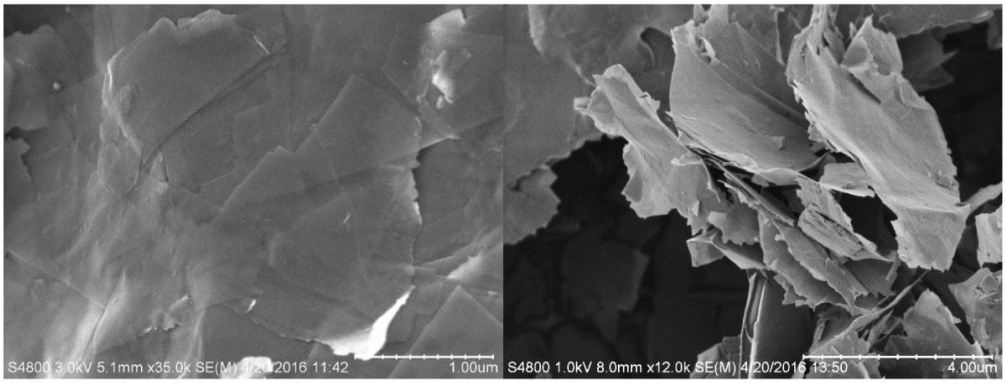

Figure 4- 18: FESEM images of PEG-PN NS, showing poor restacking behavior.

Unsaturated surface groups can also be readily attached to the oxide nanosheets. Figure 4-19 shows the XRD patterns of the three unsaturated hybrid nanosheets (Figure 4-13n−p) before and after air exposure. A clear change in diffraction data can be seen in these systems after 2 days storage in air. Since this spontaneous saturation of monomer-grafted nanosheets occurs at room temperature, it is not an instant reaction and takes over a day. This means the samples can be handled outside the glovebox for quick characterization tests (XRD and Raman) without instant saturation of the double bonds. For XRD characterization, freshly exposed samples were scanned for 30 minutes (Figure 4-19a, c, and e); then the exact same sample was then left in open air for 2 d and rescanned (Figure 4-19b, d, and f). In all cases, the first peak is shifted to higher angles which indicates a contraction in interlayer spacings, likely due to the linkage of the double bonds between adjacent stacked nanosheets. This premise was supported by Raman data from an air-exposed 9-decen-1-oxy-PN NS sample, which clearly shows a decrease in the intensity of the peaks attributed to alkenes (Figure 4-20). It is noteworthy that TMPDAE-PN NS is light

sensitive as well as air sensitive, which may explain the noisier XRD pattern seen even with short (1 h) air exposure times.

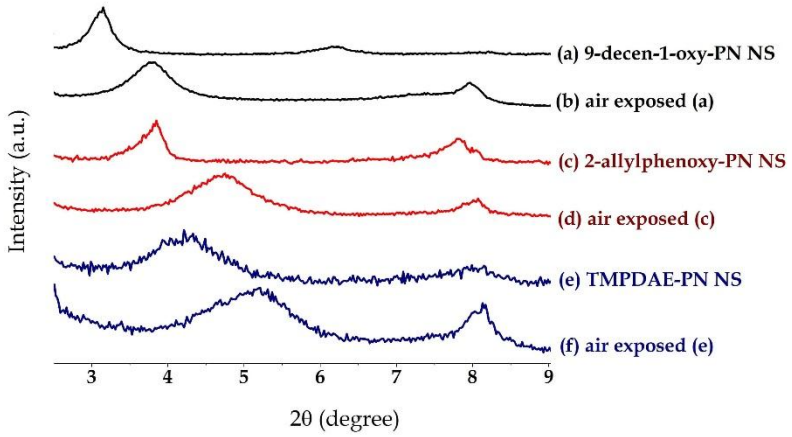

Figure 4- 19: Effect of air exposure on monomer-grafted nanosheets: 9-decen-1-oxy-PN NS (a) before and (b) after air exposure, 2-allylphenoxy-PN NS (c) before and (d) after storage in air, and TMPDAE-PN NS (e) before and (f) upon exposure to air and light.

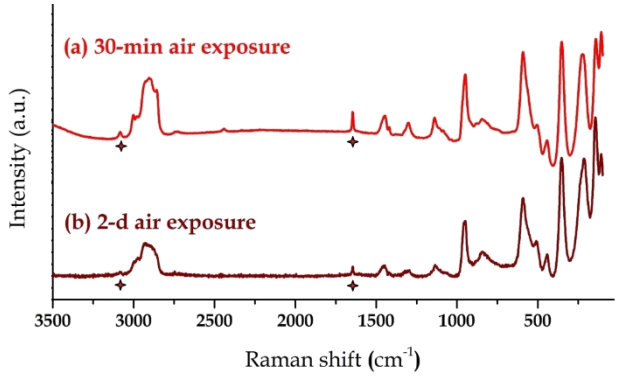

Figure 4- 20: Raman spectra of 9-decen-1-oxy-PN NS after (a) 30 min and (b) 2 d exposure to air.

4.4– Discussion

4.4.1 Exfoliation of $HLnNb_2O_7$

Previous studies generally report the need for days of stirring to obtain similar exfoliated nanosheets.[40,42,46,48–50,57,60,63,145,146] In contrast, the microwave-assisted exfoliation methods presented here yield nanosheets in as little as 15 min. Even though the necessity of long sonication in specific solvents such as acetonitrile was claimed in order to obtain exfoliated

nanosheets of the similar hosts after the intercalation of TBA^+,[70] sonication was done only in between the washing centrifugation steps (in acetone or ethanol) for only a few minutes. Microwave approaches are not new in the synthesis of other types of nanomaterials (various nanoparticles and nanostructures,[147–152] graphene nanosheets[153–155]), however, utilizing this method for the rapid exfoliation of perovskites and post-exfoliation surface modification is novel to our knowledge. Interestingly, the average dimensions of the nanosheets obtained via MA reactions, are comparable to similar perovskite nanosheets attainable by conventional long bench-top stirring methods.[45,48–50,57,65,68] It should be noted that the average dimension are usually observed via microscopy methods, as more quantitative methods such as dynamic light scattering (DLS) cannot be effective due to the wide range of lateral dimensions present after an exfoliation process.

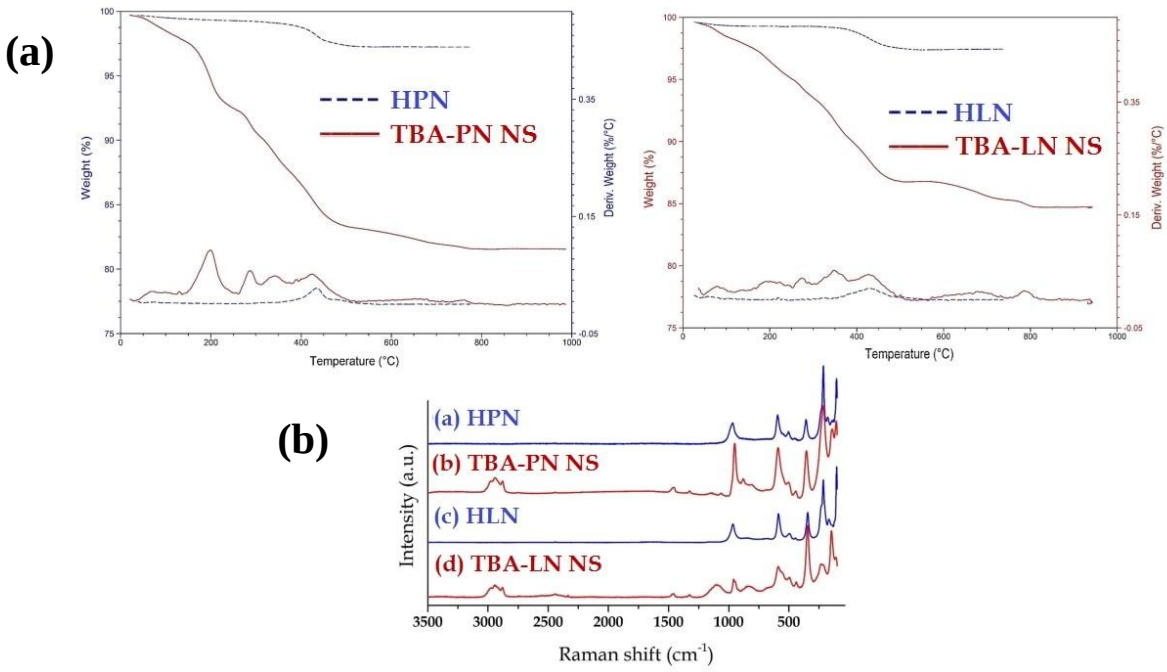

Figure 4- 21: (a) TGA and DTGA curves, and (b) Raman results for $HLnNb_2O_7$ hosts and TBA-LnNb nanosheets, proving the existence of TBA^+ on the nanosheets after the exfoliation.

As explained above, TEM and AFM studies indicate the formation of single-layered nanosheets after TBA^+ intercalation in the perovskite galleries. Similar to the previous reports,[156] the presence of tetrabutylammonium (TBA^+) ion on the surface of nanosheets can be easily confirmed using Raman spectroscopy and TGA (Figure 4-21). Figure 4-6 shows the FESEM images of TBA-LnNb nanosheets where the existence of dots on the surface of the nanosheets is

clear. As seen in Figure 4-22, these dots are 3D and are not thought to be a type of surface defect. They are not from gold sputtering of the samples, as they were seen only in the images of the nanosheets and not bulk materials. Since the exfoliation process only involves water and TBAOH, it is most likely that these spots are islands containing TBA^+ ions, held to the surface via acid-base interactions. Even after washing the sheets with copious amounts of various solvents (water, ethanol and acetone) repeatedly, these 3D surface entities can still be seen in FESEM. The observed sensitivity of these surface entities to the electron beam during the FESEM imaging is also consistent with their organic nature. Images of the nanosheets after combustion up to 1000 °C under dilute oxygen (Figure 4-23) showed no evidence of spots. The surface of the hybrid nanosheets in some cases also had some trace of these dots (Figure 4-16c,d), suggesting that exchange of TBA^+ with other surface groups were at times not a 100%.

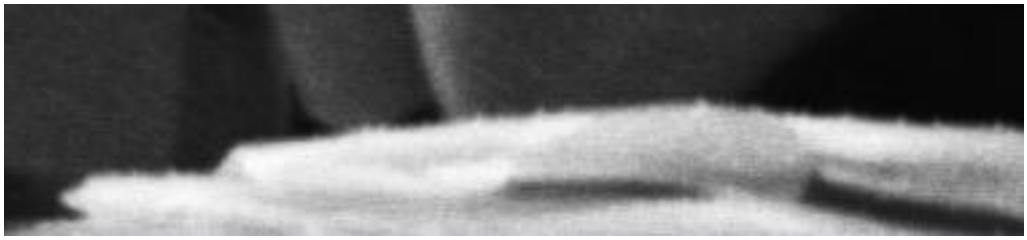

Figure 4- 22: Horizontal FESEM view of TBA-PN NS showing protrusion of dots on NS surface. Arrows indicates some of the dots.

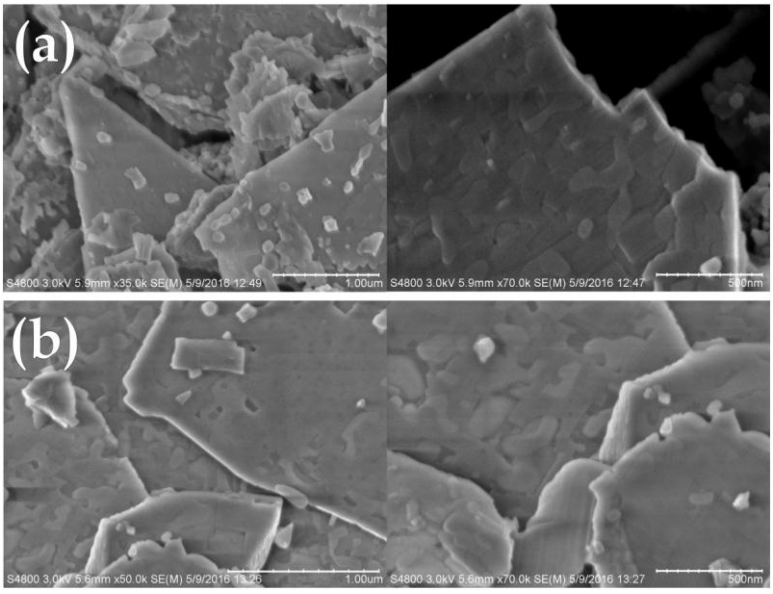

Figure 4- 23: FESEM images of (a) TBA-PN NS and (b) TBA-LN NS burned under dilute oxygen up to 1000 ºC.

The loss of crystallinity in the exfoliated samples is clearly shown in Figure 4-4 where the high-angle peaks in the starting materials disappear except for two low intensity reflections at about 2θ= 33 and 41 degrees. For TBA-LnNb nanosheets, there are three low angle peaks appearing at about 2θ= 4.5, 8 and 9 degrees. The peak at 2θ= 8° seems to be an impurity peak present in almost all of the hybrid nanosheets as well. Since the characteristic peak of the $HLnNb_2O_7$ (protonated host) is at 8.5°, this impurity peak cannot be a sign of remaining unexfoliated host. However, it can imply the presence of some nanosheet assemblies that are more rich in proton than TBA^+. The two other values are related to *0k0* set of planes. This also works for the rest of the hybrid nanosheets where any peaks less than 10 degree and other than the impurity peak could be indexed as *0k0* (for instance in case of n-decoxy-PN NS: *d* spacing values of 27.16, 13.78, and 9.20 Å for the peaks at 2θ= 3.25, 6.41 and 9.60 degrees, indexed as *020*, *040*, and *060*, respectively). The peaks observed in the XRD pattern, as well as the intensities, are also subject to change based on the number of the individual nanosheets restacked together.[142]

4.4.2 Organic Modification of Nanosheets

Combining the organic modification of nanosheets with a rapid microwave approach leads to the facile production of a variety of nanosheet-based hybrids with controlled surface engineering. Organic modification was first carried out using linear n-alkyl alcohols and n-alkylamines, $C_nH_{2n+1}OH$ (n = 3, 5 and 10) and $C_nH_{2n+1}NH_2$ (n = 3, 4, 6 and 10), respectively, and then further extended to saturated and unsaturated cyclic and linear alcohols. Even though only linear amines were studied here, the future scope of surface modifications could be very wide especially considering the high reactivity of layered perovskites with a variety of amines (linear and cyclic).[134,137] The XRD patterns of these hybrids are presented in Figure 4-13, which suggests a restacking behavior when the organic surface groups are moderately long; sharper peaks are observed for $C_nH_{2n+1}OH$ (n = 5 and 10), $C_nH_{2n+1}NH_2$ (n = 4, 6 and 10), 6-chloro-1-hexanol, and 3-phenoxybenzyl alcohol. In case of shorter substituents (n-propylammonium-, n-propoxy-, benzyl alcoxy-, and phenylphosphonic-), as well as very long ones (such as PEG-400), the XRD patterns seem to be noisier with broader first reflections, which is consistent with poor restacking order within reassembled samples. The mechanism of these surface exchange reactions are expected to be similar to the grafting/intercalation reactions that take place in the

interlayer of a layered oxide perovskite.[157,158] For the organic amines, protonated molecules displace the TBA+ ions and are held to the surface of the negatively-charged perovskite nanosheets via electrostatic interactions, and alcoxy organic molecules initially undergo hydrolysis followed by esterification to attach to the terminal oxygens of the perovskite octahedra.

Restacking of the nanosheets can also be seen in TEM and FESEM images. On examination of n-decoxy-PN NS (Figures 4-15 and 4-16) for example, while single-standing nanosheets are seen in TEM and FESEM images of TBA-PN NS (Figures 4-2 and 4-15a), assemblies of multiple nanosheets are formed after grafting n-decoxy surface groups (Figure 4-15b,c). Comparing n-decoxy-PN NS to the bulk n-decoxy-$PrNb_2O_7$ layered sample in Figure 4-16, the loss of order in nanosheet-based hybrids (Figure 4-16c,d and Figure 4-17) is clearly seen (even after restacking). The PEG-PN NS sample (Figure 4-18) does not exhibit the same type of stacking behavior seen in the n-decoxy-PN NS (Figure 4-16c,d); this is consistent with the broad, almost featureless XRD seen for PEG-PN NS (Figure 4-13j). FESEM images show the absence of ordered assemblies in the sample; this is most likely due to the presence of the large organic surface groups quelling strong registry between nanosheets. Very small surface groups such as n-propoxy also seem to result in poor registry between adjacent sheets (Figure 4-13b and f).

Grafting unsaturated organics on the surface of the nanosheets (Figure 4-13n−p) produces nanomaterials that can be covalently bonded into a polymeric network. Previous studies have been limited to grafting monomers within the interlayer of perovskite hosts, subsequent polymerization leads to exfoliation into nanosheets bound within a polymeric matrix. [36–38] Contrary to topochemical modification of layered perovskites, which is limited to the target substituents small enough to permeate the interlayer of the host,[136,157,158] surface modification of exfoliated nanosheets readily occurs regardless of the size of the target surface group. Via the simple synthetic method reported here, a variety of unsaturated hybrid nanosheets can be rapidly prepared and further incorporated in different polymeric networks in future studies. Considering the fact that surface modification of GO nanosheets often involves more complicated chemistry[121,122,124,125] and yet studied vastly, this facile method can potentially attract as much attention to the study of a new class of reinforcing agents which can covalently bond to polymeric composites.

4.5– Conclusions

Utilizing microwave-assisted reactions, exfoliated TBA^+-$LnNb_2O_7$ nanosheets (TBA-LnNb NS, Ln = La, Pr) were rapidly obtained from $HLnNb_2O_7$ layered hosts. Further microwave treatments were then implemented to perform post-exfoliation surface modification of TBA-LnNb NS. Through fast microwave reactions (< 1 h), the TBA^+ surface groups were readily replaced with various organics containing hydroxyl and amine functional groups – different linear and cyclic organics were attached to nanosheets surfaces in order to produce tailored nanosheets including those with $C_nH_{2n+1}OH$ (n = 3, 5 and 10), $C_nH_{2n+1}NH_2$ (n = 3, 4, 6 and 10), 6-chloro-1-hexanol, PEG-400, phenylphosphonic acid, benzyl alcohol, 3-phenoxybenzyl alcohol, and unsaturated surface groups such as 2-allylphenol. As the only condition to produce surface-tailored nanosheets is the selection of organics with any hydroxyl or amine functional group, this facile modification method allows for the production of various nanosheet-based hybrids with potentially novel electronic, magnetic, optical and mechanical properties. The integration of active monomers, for use in the production of nanosheet-infused polymers, could lead to important new composite materials in which the polymer network is covalently bonded and reinforced by oxide-nanosheets.

4.6– References

(1) Poole, C. P. J.; Owens, F. J. *Introduction to Nanotechnology*; John Wiley & Sons: Hoboken, New Jersey, 2003.

(2) Schmid, G. *Nanotechnology: Principles and Fundamentals*; Wiley-VCH: Weinheim, 2008.

(3) Gupta, A.; Sakthivel, T.; Seal, S. Recent Development in 2D Materials beyond Graphene. *Prog. Mater. Sci.* **2015**, *73*, 44–126.

(4) Tiwari, J. N.; Tiwari, R. N.; Kim, K. S. Zero-Dimensional, One-Dimensional, Two-Dimensional and Three-Dimensional Nanostructured Materials for Advanced Electrochemical Energy Devices. *Prog. Mater. Sci.* **2012**, *57* (4), 724–803.

(5) Nakato, T.; Miyamoto, N. Liquid Crystalline Behavior and Related Properties of Colloidal Systems of Inorganic Oxide Nanosheets. *Materials* **2009**, *2* (4), 1734–1761.

(6) Osada, M.; Sasaki, T. Exfoliated Oxide Nanosheets: New Solution to Nanoelectronics. *J. Mater. Chem.* **2009**, *19* (17), 2503.

(7) Bizeto, M. A.; Shiguihara, A. L.; Constantino, V. R. L. Layered Niobate Nanosheets: Building Blocks for Advanced Materials Assembly. *J. Mater. Chem.* **2009**, *19* (17), 2512.

(8) Ma, R.; Sasaki, T. Nanosheets of Oxides and Hydroxides: Ultimate 2D Charge-Bearing Functional Crystallites. *Adv. Mater.* **2010**, *22* (45), 5082–5104.

(9) Coleman, J. N.; Lotya, M.; O'Neill, A.; Bergin, S. D.; King, P. J.; Khan, U.; Young, K.; Gaucher, A.; De, S.; Smith, R. J.; et al. Two-Dimensional Nanosheets Produced by Liquid Exfoliation of Layered Materials. *Science* **2011**, *331* (6017), 568–571.

(10) Wang, Q.; O'Hare, D. Recent Advances in the Synthesis and Application of Layered Double Hydroxide (LDH) Nanosheets. *Chem. Rev.* **2012**, *112* (7), 4124–4155.

(11) Nicolosi, V.; Chhowalla, M.; Kanatzidis, M. G.; Strano, M. S.; Coleman, J. N. Liquid Exfoliation of Layered Materials. *Science* **2013**, *340* (6139), 1226419–1226419.

(12) Butler, S. Z.; Hollen, S. M.; Cao, L.; Cui, Y.; Gupta, J. A.; Gutiérrez, H. R.; Heinz, T. F.; Hong, S. S.; Huang, J.; Ismach, A. F.; et al. Progress, Challenges, and Opportunities in Two-Dimensional Materials Beyond Graphene. *ACS Nano* **2013**, *7* (4), 2898–2926.

(13) Woomer, A. H.; Farnsworth, T. W.; Hu, J.; Wells, R. A.; Donley, C. L.; Warren, S. C. Phosphorene: Synthesis, Scale-Up, and Quantitative Optical Spectroscopy. *ACS Nano* **2015**, *9* (9), 8869–8884.

(14) Smith, R. J.; King, P. J.; Lotya, M.; Wirtz, C.; Khan, U.; De, S.; O'Neill, A.; Duesberg, G. S.; Grunlan, J. C.; Moriarty, G.; et al. Large-Scale Exfoliation of Inorganic Layered Compounds in Aqueous Surfactant Solutions. *Adv. Mater.* **2011**, *23* (34), 3944–3948.

(15) Geim, A. K.; Grigorieva, I. V. Van Der Waals Heterostructures. *Nature* **2013**, *499* (7459), 419–425.

(16) Geim, A. K. Graphene: Status and Prospects. *Science* **2009**, *324* (5934), 1530–1534.

(17) Singh, V.; Joung, D.; Zhai, L.; Das, S.; Khondaker, S. I.; Seal, S. Graphene Based Materials: Past, Present and Future. *Prog. Mater. Sci.* **2011**, *56* (8), 1178–1271.

(18) Rattana; Chaiyakun, S.; Witit-anun, N.; Nuntawong, N.; Chindaudom, P.; Oaew, S.; Kedkeaw, C.; Limsuwan, P. Preparation and Characterization of Graphene Oxide Nanosheets. *Procedia Eng.* **2012**, *32*, 759–764.

(19) Compton, O. C.; Nguyen, S. T. Graphene Oxide, Highly Reduced Graphene Oxide, and Graphene: Versatile Building Blocks for Carbon-Based Materials. *Small* **2010**, *6* (6), 711–723.

(20) Kim, J.; Cote, L. J.; Kim, F.; Yuan, W.; Shull, K. R.; Huang, J. Graphene Oxide Sheets at Interfaces. *J. Am. Chem. Soc.* **2010**, *132* (23), 8180–8186.

(21) Nair, R. R.; Ren, W.; Jalil, R.; Riaz, I.; Kravets, V. G.; Britnell, L.; Blake, P.; Schedin, F.; Mayorov, A. S.; Yuan, S.; et al. Fluorographene: A Two-Dimensional Counterpart of Teflon. *Small* **2010**, *6* (24), 2877–2884.

(22) Feng, W.; Long, P.; Feng, Y.; Li, Y. Two-Dimensional Fluorinated Graphene: Synthesis, Structures, Properties and Applications. *Adv. Sci.* **2016**, 1500413(1–22).

(23) Golberg, D.; Bando, Y.; Huang, Y.; Terao, T.; Mitome, M.; Tang, C.; Zhi, C. Boron Nitride Nanotubes and Nanosheets. *ACS Nano* **2010**, *4* (6), 2979–2993.

(24) Pakdel, A.; Zhi, C.; Bando, Y.; Golberg, D. Low-Dimensional Boron Nitride Nanomaterials. *Mater. Today* **2012**, *15* (6), 256–265.

(25) Wang, X.; Zhi, C.; Weng, Q.; Bando, Y.; Golberg, D. Boron Nitride Nanosheets: Novel Syntheses and Applications in Polymeric Composites. *J. Phys. Conf. Ser.* **2013**, *471* (1), 012003.

(26) Sajjad, M.; Morell, G.; Feng, P. Advance in Novel Boron Nitride Nanosheets to Nanoelectronic Device Applications. *ACS Appl. Mater. Interfaces* **2013**, *5* (11), 5051–5056.

(27) Ci, L.; Song, L.; Jin, C.; Jariwala, D.; Wu, D.; Li, Y.; Srivastava, A.; Wang, Z. F.; Storr, K.; Balicas, L.; et al. Atomic Layers of Hybridized Boron Nitride and Graphene Domains. *Nat. Mater.* **2010**, *9* (5), 430–435.

(28) Lei, W.; Qin, S.; Liu, D.; Portehault, D.; Liu, Z.; Chen, Y. Large Scale Boron Carbon Nitride Nanosheets with Enhanced Lithium Storage Capabilities. *Chem Commun* **2013**, *49* (4), 352–354.

(29) Huang, X.; Zeng, Z.; Zhang, H. Metal Dichalcogenide Nanosheets: Preparation, Properties and Applications. *Chem. Soc. Rev.* **2013**, *42* (5), 1934–1946.

(30) Chhowalla, M.; Liu, Z.; Zhang, H. Two-Dimensional Transition Metal Dichalcogenide (TMD) Nanosheets. *Chem. Soc. Rev.* **2015**, *44* (9), 2584–2586.

(31) Dai, J.; Li, M.; Zeng, X. C. Group IVB Transition Metal Trichalcogenides: A New Class of 2D Layered Materials beyond Graphene. *Wiley Interdiscip. Rev. Comput. Mol. Sci.* **2016**, *6* (2), 211–222.

(32) Xia, F.; Wang, H.; Xiao, D.; Dubey, M.; Ramasubramaniam, A. Two-Dimensional Material Nanophotonics. *Nat. Photonics* **2014**, *8* (12), 899–907.

(33) Wang, H.; Liu, F.; Fu, W.; Fang, Z.; Zhou, W.; Liu, Z. Two-Dimensional Heterostructures: Fabrication, Characterization, and Application. *Nanoscale* **2014**, *6* (21), 12250–12272.

(34) Zhang, H. Ultrathin Two-Dimensional Nanomaterials. *ACS Nano* **2015**, *9* (10), 9451–9469.

(35) Mas-Ballesté, R.; Gómez-Navarro, C.; Gómez-Herrero, J.; Zamora, F. 2D Materials: To Graphene and beyond. *Nanoscale* **2011**, *3* (1), 20–30.

(36) Tahara, S.; Takeda, Y.; Sugahara, Y. Preparation of Organic−Inorganic Hybrids Possessing Nanosheets with Perovskite-Related Structures via Exfoliation during a Sol−Gel Process. *Chem. Mater.* **2005**, *17* (24), 6198–6204.

(37) Tahara, S.; Okamoto, T.; Sugahara, Y. Preparation of a Nanocomposite Consisting of a Siloxane Network and Perovskite-Related Nanosheets via a Sol–gel Process. *Sci. Technol. Adv. Mater.* **2006**, *7* (5), 446–450.

(38) Idota, N.; Fukuda, S.; Tsukahara, T.; Sugahara, Y. Preparation of Thermoresponsive Nanosheets Exhibiting Phase Transitions in Water via Surface Modification of Layered Perovskite Nanosheets with Poly(*N*-Isopropylacrylamide) (PNIPAAm). *Chem. Lett.* **2015**, *44* (2), 203–205.

(39) Geng, F.; Ma, R.; Ebina, Y.; Yamauchi, Y.; Miyamoto, N.; Sasaki, T. Gigantic Swelling of Inorganic Layered Materials: A Bridge to Molecularly Thin Two-Dimensional Nanosheets. *J. Am. Chem. Soc.* **2014**, *136* (14), 5491–5500.

(40) Maluangnont, T.; Matsuba, K.; Geng, F.; Ma, R.; Yamauchi, Y.; Sasaki, T. Osmotic Swelling of Layered Compounds as a Route to Producing High-Quality Two-Dimensional Materials. A Comparative Study of Tetramethylammonium versus Tetrabutylammonium Cation in a Lepidocrocite-Type Titanate. *Chem. Mater.* **2013**, *25* (15), 3137–3146.

(41) Han, Y.-S.; Park, I.; Choy, J.-H. Exfoliation of Layered Perovskite, KCa2Nb3O10,into Colloidal Nanosheets by a Novel Chemical Process. *J. Mater. Chem.* **2001**, *11* (4), 1277–1282.

(42) Schaak, R. E.; Mallouk, T. E. Prying Apart Ruddlesden−Popper Phases: Exfoliation into Sheets and Nanotubes for Assembly of Perovskite Thin Films. *Chem. Mater.* **2000**, *12* (11), 3427–3434.

(43) Ida, S.; Ogata, C.; Unal, U.; Izawa, K.; Inoue, T.; Altuntasoglu, O.; Matsumoto, Y. Preparation of a Blue Luminescent Nanosheet Derived from Layered Perovskite $Bi_2SrTa_2O_9$. *J. Am. Chem. Soc.* **2007**, *129* (29), 8956–8957.

(44) Kimura, N.; Kato, Y.; Suzuki, R.; Shimada, A.; Tahara, S.; Nakato, T.; Matsukawa, K.; Mutin, P. H.; Sugahara, Y. Single- and Double-Layered Organically Modified Nanosheets by Selective Interlayer Grafting and Exfoliation of Layered Potassium Hexaniobate. *Langmuir* **2014**, *30* (4), 1169–1175.

(45) Asai, Y.; Ariake, Y.; Saito, H.; Idota, N.; Matsukawa, K.; Nishino, T.; Sugahara, Y. Layered Perovskite Nanosheets Bearing Fluoroalkoxy Groups: Their Preparation and Application in Epoxy-Based Hybrids. *RSC Adv.* **2014**, *4* (51), 26932.

(46) Takagaki, A.; Sugisawa, M.; Lu, D.; Kondo, J. N.; Hara, M.; Domen, K.; Hayashi, S. Exfoliated Nanosheets as a New Strong Solid Acid Catalyst. *J. Am. Chem. Soc.* **2003**, *125* (18), 5479–5485.

(47) Shibata, T.; Takano, H.; Ebina, Y.; Kim, D. S.; Ozawa, T. C.; Akatsuka, K.; Ohnishi, T.; Takada, K.; Kogure, T.; Sasaki, T. Versatile van Der Waals Epitaxy-like Growth of Crystal Films Using Two-Dimensional Nanosheets as a Seed Layer: Orientation Tuning of $SrTiO_3$ Films along Three Important Axes on Glass Substrates. *J Mater Chem C* **2014**, *2* (3), 441–449.

(48) Chen, Y.; Zhao, X.; Ma, H.; Ma, S.; Huang, G.; Makita, Y.; Bai, X.; Yang, X. Structure and Dehydration of Layered Perovskite Niobate with Bilayer Hydrates Prepared by Exfoliation/self-Assembly Process. *J. Solid State Chem.* **2008**, *181* (7), 1684–1694.

(49) Ida, S.; Okamoto, Y.; Matsuka, M.; Hagiwara, H.; Ishihara, T. Preparation of Tantalum-Based Oxynitride Nanosheets by Exfoliation of a Layered Oxynitride, $CsCa_2Ta_3O_{10-x}N_y$, and Their Photocatalytic Activity. *J. Am. Chem. Soc.* **2012**, *134* (38), 15773–15782.

(50) Schaak, R. E.; Mallouk, T. E. Self-Assembly of Tiled Perovskite Monolayer and Multilayer Thin Films. *Chem. Mater.* **2000**, *12* (9), 2513–2516.

(51) Sasaki, T.; Watanabe, M.; Hashizume, H.; Yamada, H.; Nakazawa, H. Macromolecule-like Aspects for a Colloidal Suspension of an Exfoliated Titanate. Pairwise Association of Nanosheets and Dynamic Reassembling Process Initiated from It. *J. Am. Chem. Soc.* **1996**, *118* (35), 8329–8335.

(52) Schaak, R. E.; Mallouk, T. E. Exfoliation of Layered Rutile and Perovskite Tungstates. *Chem. Commun.* **2002**, No. 7, 706–707.

(53) Allen, M. R.; Thibert, A.; Sabio, E. M.; Browning, N. D.; Larsen, D. S.; Osterloh, F. E. Evolution of Physical and Photocatalytic Properties in the Layered Titanates $A_2Ti_4O_9$ (A = K, H) and in Nanosheets Derived by Chemical Exfoliation †. *Chem. Mater.* **2010**, *22* (3), 1220–1228.

(54) Takagaki, A.; Tagusagawa, C.; Hayashi, S.; Hara, M.; Domen, K. Nanosheets as Highly Active Solid Acid Catalysts for Green Chemical Syntheses. *Energy Env. Sci* **2010**, *3* (1), 82–93.

(55) Wang, T.; Henderson, C. N.; Draskovic, T. I.; Mallouk, T. E. Synthesis, Exfoliation, and Electronic/Protonic Conductivity of the Dion–Jacobson Phase Layer Perovskite $HLa_2TiTa_2O_{10}$. *Chem. Mater.* **2014**, *26* (2), 898–906.

(56) Treacy, M. M. J.; Rice, S. B.; Jacobson, A. J.; Lewandowski, J. T. Electron Microscopy Study of Delamination in Dispersions of the Perovskite-Related Layered Phases $K[Ca_2Na_{n-3}Nb_nO_{3n-1}]$: Evidence for Single-Layer Formation. *Chem. Mater.* **1990**, *2* (3), 279–286.

(57) Lee, W.-J.; Yeo, H. J.; Kim, D.-Y.; Paek, S.-M.; Kim, Y.-I. Exfoliation of Dion-Jacobson Layered Perovskite into Macromolecular Nanoplatelet. *Bull. Korean Chem. Soc.* **2013**, *34* (7), 2041–2043.

(58) Li, B.-W.; Osada, M.; Ebina, Y.; Akatsuka, K.; Fukuda, K.; Sasaki, T. High Thermal Robustness of Molecularly Thin Perovskite Nanosheets and Implications for Superior Dielectric Properties. *ACS Nano* **2014**, *8* (6), 5449–5461.

(59) Compton, O. C.; Osterloh, F. E. Niobate Nanosheets as Catalysts for Photochemical Water Splitting into Hydrogen and Hydrogen Peroxide. *J. Phys. Chem. C* **2009**, *113* (1), 479–485.

(60) Kikuta, K.; Noda, K.; Okumura, S.; Yamaguchi, T.; Hirano, S. Orientation Control of Perovskite Thin Films on Glass Substrates by the Application of a Seed Layer Prepared from Oxide Nanosheets. *J. Sol-Gel Sci. Technol.* **2007**, *42* (3), 381–387.

(61) Zhao, J.; Osterloh, F. E. Photochemical Charge Separation in Nanocrystal Photocatalyst Films: Insights from Surface Photovoltage Spectroscopy. *J. Phys. Chem. Lett.* **2014**, *5* (5), 782–786.

(62) Ida, S.; Ishihara, T. Recent Progress in Two-Dimensional Oxide Photocatalysts for Water Splitting. *J. Phys. Chem. Lett.* **2014**, *5* (15), 2533–2542.

(63) Suzuki, H.; Tomita, O.; Higashi, M.; Abe, R. Two-Step Photocatalytic Water Splitting into H_2 and O_2 Using Layered Metal Oxide $KCa_2Nb_3O_{10}$ and Its Derivatives as O_2-Evolving Photocatalysts with IO_3^-/I^- or Fe^{3+}/Fe^{2+} Redox Mediator. *Catal Sci Technol* **2015**, *5* (5), 2640–2648.

(64) Maeda, K.; Sahara, G.; Eguchi, M.; Ishitani, O. Hybrids of a Ruthenium(II) Polypyridyl Complex and a Metal Oxide Nanosheet for Dye-Sensitized Hydrogen Evolution with Visible Light: Effects of the Energy Structure on Photocatalytic Activity. *ACS Catal.* **2015**, *5* (3), 1700–1707.

(65) Ida, S.; Ogata, C.; Eguchi, M.; Youngblood, W. J.; Mallouk, T. E.; Matsumoto, Y. Photoluminescence of Perovskite Nanosheets Prepared by Exfoliation of Layered Oxides, $K_2Ln_2Ti_3O_{10}$, $KLnNb_2O_7$, and $RbLnTa_2O_7$ (Ln: Lanthanide Ion). *J. Am. Chem. Soc.* **2008**, *130* (22), 7052–7059.

(66) Ebina, Y.; Akatsuka, K.; Fukuda, K.; Sasaki, T. Synthesis and In Situ X-Ray Diffraction Characterization of Two-Dimensional Perovskite-Type Oxide Colloids with a Controlled Molecular Thickness. *Chem. Mater.* **2012**, *24* (21), 4201–4208.

(67) Tanimaa, K.; Watanabeb, M.; Imanaria, Y.; Kameia, S.; Uematsub, K.; Ishigakic, T.; Todaa, K.; Satob, M.; Masakid, T.; Yoond, D. H. Research on New Precursor for Nanosheets Phosphors. *J. Ceram. Process. Res.* **2013**, *14*, S71–S73.

(68) Ebina, Y.; Sasaki, T.; Harada, M.; Watanabe, M. Restacked Perovskite Nanosheets and Their Pt-Loaded Materials as Photocatalysts. *Chem. Mater.* **2002**, *14* (10), 4390–4395.

(69) Wu, X.; Fei, F.; Chen, Z.; Su, W.; Cui, Z. A New Nanocomposite Dielectric Ink and Its Application in Printed Thin-Film Transistors. *Compos. Sci. Technol.* **2014**, *94*, 117–122.

(70) Takei, T.; Muraki, N.; Xu, N.; Miura, A.; Kumada, N. Anodic Hybridization of Fluorinated Layered Perovskite Nanosheet with Polyaniline for Electrochemical Capacitor. *Colloids Surf. Physicochem. Eng. Asp.* **2014**, *459*, 186–193.

(71) Ida, S. Development of Light Energy Conversion Materials Using Two-Dimensional Inorganic Nanosheets. *Bull. Chem. Soc. Jpn.* **2015**, *88* (12), 1619–1628.

(72) Li, B.-W.; Osada, M.; Ozawa, T. C.; Ebina, Y.; Akatsuka, K.; Ma, R.; Funakubo, H.; Sasaki, T. Engineered Interfaces of Artificial Perovskite Oxide Superlattices *via* Nanosheet Deposition Process. *ACS Nano* **2010**, *4* (11), 6673–6680.

(73) Kobayashi, Y.; Tian, M.; Eguchi, M.; Mallouk, T. E. Ion-Exchangeable, Electronically Conducting Layered Perovskite Oxyfluorides. *J. Am. Chem. Soc.* **2009**, *131* (28), 9849–9855.

(74) Ida, S.; Okamoto, Y.; Koga, S.; Hagiwara, H.; Ishihara, T. Black-Colored Nitrogen-Doped Calcium Niobium Oxide Nanosheets and Their Photocatalytic Properties under Visible Light Irradiation. *RSC Adv.* **2013**, *3* (29), 11521.

(75) Ziegler, C.; Werner, S.; Bugnet, M.; Wörsching, M.; Duppel, V.; Botton, G. A.; Scheu, C.; Lotsch, B. V. Artificial Solids by Design: Assembly and Electron Microscopy Study of Nanosheet-Derived Heterostructures. *Chem. Mater.* **2013**, *25* (24), 4892–4900.

(76) Long, M.; Liu, E.; Wang, P.; Gao, A.; Xia, H.; Luo, W.; Wang, B.; Zeng, J.; Fu, Y.; Xu, K.; et al. Broadband Photovoltaic Detectors Based on an Atomically Thin Heterostructure. *Nano Lett.* **2016**, *16* (4), 2254–2259.

(77) Le, N. B.; Huan, T. D.; Woods, L. M. Interlayer Interactions in van Der Waals Heterostructures: Electron and Phonon Properties. *ACS Appl. Mater. Interfaces* **2016**, *8* (9), 6286–6292.

(78) Lotsch, B. V. Vertical 2D Heterostructures. *Annu. Rev. Mater. Res.* **2015**, *45* (1), 85–109.

(79) Akatsuka, K.; Takanashi, G.; Ebina, Y.; Haga, M.; Sasaki, T. Electronic Band Structure of Exfoliated Titanium- And/or Niobium-Based Oxide Nanosheets Probed by Electrochemical and Photoelectrochemical Measurements. *J. Phys. Chem. C* **2012**, *116* (23), 12426–12433.

(80) Zhang, Y.; Ugeda, M. M.; Jin, C.; Shi, S.-F.; Bradley, A. J.; Martín-Recio, A.; Ryu, H.; Kim, J.; Tang, S.; Kim, Y.; et al. Electronic Structure, Surface Doping, and Optical Response in Epitaxial WSe_2 Thin Films. *Nano Lett.* **2016**, *16* (4), 2485–2491.

(81) Li, L.; Ma, R.; Ebina, Y.; Fukuda, K.; Takada, K.; Sasaki, T. Layer-by-Layer Assembly and Spontaneous Flocculation of Oppositely Charged Oxide and Hydroxide Nanosheets into Inorganic Sandwich Layered Materials. *J. Am. Chem. Soc.* **2007**, *129* (25), 8000–8007.

(82) Sasaki, T. Fabrication of Nanostructured Functional Materials Using Exfoliated Nanosheets as a Building Block. *J. Ceram. Soc. Jpn.* **2007**, *115* (1337), 9–16.

(83) Borges, J.; Mano, J. F. Molecular Interactions Driving the Layer-by-Layer Assembly of Multilayers. *Chem. Rev.* **2014**, *114* (18), 8883–8942.

(84) Ma, R.; Sasaki, T. Organization of Artificial Superlattices Utilizing Nanosheets as a Building Block and Exploration of Their Advanced Functions. *Annu. Rev. Mater. Res.* **2015**, *45* (1), 111–127.

(85) Park, J. S.; Cho, S. M.; Kim, W.-J.; Park, J.; Yoo, P. J. Fabrication of Graphene Thin Films Based on Layer-by-Layer Self-Assembly of Functionalized Graphene Nanosheets. *ACS Appl. Mater. Interfaces* **2011**, *3* (2), 360–368.

(86) Wang, Y.; Tong, S. W.; Xu, X. F.; Özyilmaz, B.; Loh, K. P. Interface Engineering of Layer-by-Layer Stacked Graphene Anodes for High-Performance Organic Solar Cells. *Adv. Mater.* **2011**, *23* (13), 1514–1518.

(87) Gunjakar, J. L.; Kim, I. Y.; Lee, J. M.; Jo, Y. K.; Hwang, S.-J. Exploration of Nanostructured Functional Materials Based on Hybridization of Inorganic 2D Nanosheets. *J. Phys. Chem. C* **2014**, *118* (8), 3847–3863.

(88) Huang, S.; Cen, X.; Peng, H.; Guo, S.; Wang, W.; Liu, T. Heterogeneous Ultrathin Films of Poly(vinyl alcohol)/Layered Double Hydroxide and Montmorillonite Nanosheets via Layer-by-Layer Assembly. *J. Phys. Chem. B* **2009**, *113* (46), 15225–15230.

(89) Wang, L.; Sasaki, T. Titanium Oxide Nanosheets: Graphene Analogues with Versatile Functionalities. *Chem. Rev.* **2014**, *114* (19), 9455–9486.

(90) Wang, L.; Sasaki, T.; Ebina, Y.; Kurashima, K.; Watanabe, M. Fabrication of Controllable Ultrathin Hollow Shells by Layer-by-Layer Assembly of Exfoliated Titania Nanosheets on Polymer Templates. *Chem. Mater.* **2002**, *14* (11), 4827–4832.

(91) Wang, R.; Pi, X.; Ni, Z.; Liu, Y.; Yang, D. Density Functional Theory Study on Organically Surface-Modified Silicene. *RSC Adv* **2015**, *5* (43), 33831–33837.

(92) Wang; Omomo, Y.; Sakai, N.; Fukuda, K.; Nakai, I.; Ebina, Y.; Takada, K.; Watanabe, M.; Sasaki, T. Fabrication and Characterization of Multilayer Ultrathin Films of Exfoliated MnO_2 Nanosheets and Polycations. *Chem. Mater.* **2003**, *15* (15), 2873–2878.

(93) Lv, S.; Yuan, Y.; Shi, W. Strengthening and Toughening Effects of Layered Double Hydroxide and Hyperbranched Polymer on Epoxy Resin. *Prog. Org. Coat.* **2009**, *65* (4), 425–430.

(94) Honda, M.; Oaki, Y.; Imai, H. Surface-Functionalized Monolayered Nanodots of a Transition Metal Oxide and Their Properties. *Phys Chem Phys* **2015**, *17* (48), 32498–32504.

(95) Sugiyama, Y.; Okamoto, H.; Mitsuoka, T.; Morikawa, T.; Nakanishi, K.; Ohta, T.; Nakano, H. Synthesis and Optical Properties of Monolayer Organosilicon Nanosheets. *J. Am. Chem. Soc.* **2010**, *132* (17), 5946–5947.

(96) Jiang, S.; Gui, Z.; Chen, G.; Liang, D.; Alam, J. Ultrathin Nanosheets of Organic-Modified β-$Ni(OH)_2$ with Excellent Thermal Stability: Fabrication and Its Reinforcement Application in Polymers. *ACS Appl. Mater. Interfaces* **2015**, *7* (27), 14603–14613.

(97) Honda, M.; Oaki, Y.; Imai, H. Hydrophobic Inorganic–Organic Composite Nanosheets Based on Monolayers of Transition Metal Oxides. *Chem. Mater.* **2014**, *26* (11), 3579–3585.

(98) Honda, M.; Oaki, Y.; Imai, H. Hydrophobic Monolayered Nanoflakes of Tungsten Oxide: Coupled Exfoliation and Fracture in a Nonpolar Organic Medium. *Chem. Commun.* **2015**, *51* (49), 10046–10049.

(99) Zhang, D.-D.; Zu, S.-Z.; Han, B.-H. Inorganic–organic Hybrid Porous Materials Based on Graphite Oxide Sheets. *Carbon* **2009**, *47* (13), 2993–3000.

(100) Hu, H.; Allan, C. C. K.; Li, J.; Kong, Y.; Wang, X.; Xin, J. H.; Hu, H. Multifunctional Organically Modified Graphene with Super-Hydrophobicity. *Nano Res.* **2014**, *7* (3), 418–433.

(101) Singh, S. K.; Singh, M. K.; Kulkarni, P. P.; Sonkar, V. K.; Grácio, J. J. A.; Dash, D. Amine-Modified Graphene: Thrombo-Protective Safer Alternative to Graphene Oxide for Biomedical Applications. *ACS Nano* **2012**, *6* (3), 2731–2740.

(102) Kuila, T.; Bose, S.; Mishra, A. K.; Khanra, P.; Kim, N. H.; Lee, J. H. Chemical Functionalization of Graphene and Its Applications. *Prog. Mater. Sci.* **2012**, *57* (7), 1061–1105.

(103) Dreyer, D. R.; Park, S.; Bielawski, C. W.; Ruoff, R. S. The Chemistry of Graphene Oxide. *Chem Soc Rev* **2010**, *39* (1), 228–240.

(104) Zhang, J.; Zhao, X. S. Conducting Polymers Directly Coated on Reduced Graphene Oxide Sheets as High-Performance Supercapacitor Electrodes. *J. Phys. Chem. C* **2012**, *116* (9), 5420–5426.

(105) Xue, Y.; Liu, Y.; Lu, F.; Qu, J.; Chen, H.; Dai, L. Functionalization of Graphene Oxide with Polyhedral Oligomeric Silsesquioxane (POSS) for Multifunctional Applications. *J. Phys. Chem. Lett.* **2012**, *3* (12), 1607–1612.

(106) Ramanathan, T.; Abdala, A. A.; Stankovich, S.; Dikin, D. A.; Herrera-Alonso, M.; Piner, R. D.; Adamson, D. H.; Schniepp, H. C.; Chen, X.; Ruoff, R. S.; et al. Functionalized Graphene Sheets for Polymer Nanocomposites. *Nat. Nanotechnol.* **2008**, *3* (6), 327–331.

(107) Liu, J.; Tang, J.; Gooding, J. J. Strategies for Chemical Modification of Graphene and Applications of Chemically Modified Graphene. *J. Mater. Chem.* **2012**, *22* (25), 12435.

(108) Xu, J.; Wang, K.; Zu, S.-Z.; Han, B.-H.; Wei, Z. Hierarchical Nanocomposites of Polyaniline Nanowire Arrays on Graphene Oxide Sheets with Synergistic Effect for Energy Storage. *ACS Nano* **2010**, *4* (9), 5019–5026.

(109) Mei, Q.; Zhang, K.; Guan, G.; Liu, B.; Wang, S.; Zhang, Z. Highly Efficient Photoluminescent Graphene Oxide with Tunable Surface Properties. *Chem. Commun.* **2010**, *46* (39), 7319.

(110) Bai, H.; Xu, Y.; Zhao, L.; Li, C.; Shi, G. Non-Covalent Functionalization of Graphene Sheets by Sulfonated Polyaniline. *Chem. Commun.* **2009**, No. 13, 1667.

(111) Kim, H.; Abdala, A. A.; Macosko, C. W. Graphene/Polymer Nanocomposites. *Macromolecules* **2010**, *43* (16), 6515–6530.

(112) Stankovich, S.; Dikin, D. A.; Dommett, G. H. B.; Kohlhaas, K. M.; Zimney, E. J.; Stach, E. A.; Piner, R. D.; Nguyen, S. T.; Ruoff, R. S. Graphene-Based Composite Materials. *Nature* **2006**, *442* (7100), 282–286.

(113) Li, D.; Kaner, R. B. Graphene-Based Materials. *Science* **2008**, *320* (5880), 1170–1171.

(114) Putz, K. W.; Compton, O. C.; Palmeri, M. J.; Nguyen, S. T.; Brinson, L. C. High-Nanofiller-Content Graphene Oxide-Polymer Nanocomposites via Vacuum-Assisted Self-Assembly. *Adv. Funct. Mater.* **2010**, *20* (19), 3322–3329.

(115) Pham, V. H.; Dang, T. T.; Hur, S. H.; Kim, E. J.; Chung, J. S. Highly Conductive Poly(methyl Methacrylate) (PMMA)-Reduced Graphene Oxide Composite Prepared by Self-Assembly of PMMA Latex and Graphene Oxide through Electrostatic Interaction. *ACS Appl. Mater. Interfaces* **2012**, *4* (5), 2630–2636.

(116) Kuila, T.; Bose, S.; Hong, C. E.; Uddin, M. E.; Khanra, P.; Kim, N. H.; Lee, J. H. Preparation of Functionalized Graphene/linear Low Density Polyethylene Composites by a Solution Mixing Method. *Carbon* **2011**, *49* (3), 1033–1037.

(117) Kuilla, T.; Bhadra, S.; Yao, D.; Kim, N. H.; Bose, S.; Lee, J. H. Recent Advances in Graphene Based Polymer Composites. *Prog. Polym. Sci.* **2010**, *35* (11), 1350–1375.

(118) Yun, Y. S.; Bae, Y. H.; Kim, D. H.; Lee, J. Y.; Chin, I.-J.; Jin, H.-J. Reinforcing Effects of Adding Alkylated Graphene Oxide to Polypropylene. *Carbon* **2011**, *49* (11), 3553–3559.

(119) Gao, Y.; Yip, H.-L.; Chen, K.-S.; O'Malley, K. M.; Acton, O.; Sun, Y.; Ting, G.; Chen, H.; Jen, A. K.-Y. Surface Doping of Conjugated Polymers by Graphene Oxide and Its Application for Organic Electronic Devices. *Adv. Mater.* **2011**, *23* (16), 1903–1908.

(120) Satti, A.; Larpent, P.; Gun'ko, Y. Improvement of Mechanical Properties of Graphene Oxide/poly(allylamine) Composites by Chemical Crosslinking. *Carbon* **2010**, *48* (12), 3376–3381.

(121) Kumar, N. A.; Choi, H.-J.; Shin, Y. R.; Chang, D. W.; Dai, L.; Baek, J.-B. Polyaniline-Grafted Reduced Graphene Oxide for Efficient Electrochemical Supercapacitors. *ACS Nano* **2012**, *6* (2), 1715–1723.

(122) Shan, C.; Yang, H.; Han, D.; Zhang, Q.; Ivaska, A.; Niu, L. Water-Soluble Graphene Covalently Functionalized by Biocompatible Poly-L-Lysine. *Langmuir* **2009**, *25* (20), 12030–12033.

(123) Pramoda, K. P.; Hussain, H.; Koh, H. M.; Tan, H. R.; He, C. B. Covalent Bonded Polymer-Graphene Nanocomposites. *J. Polym. Sci. Part Polym. Chem.* **2010**, *48* (19), 4262–4267.

(124) Gonçalves, G.; Marques, P. A. A. P.; Barros-Timmons, A.; Bdkin, I.; Singh, M. K.; Emami, N.; Grácio, J. Graphene Oxide Modified with PMMA via ATRP as a Reinforcement Filler. *J. Mater. Chem.* **2010**, *20* (44), 9927.

(125) Huang, Y.; Qin, Y.; Zhou, Y.; Niu, H.; Yu, Z.-Z.; Dong, J.-Y. Polypropylene/Graphene Oxide Nanocomposites Prepared by In Situ Ziegler−Natta Polymerization. *Chem. Mater.* **2010**, *22* (13), 4096–4102.

(126) Guo, Q.; Li, F. Self-Assembled Alkanethiol Monolayers on Gold Surfaces: Resolving the Complex Structure at the Interface by STM. *Phys. Chem. Chem. Phys.* **2014**, *16* (36), 19074.

(127) Khassanov, A.; Steinrück, H.-G.; Schmaltz, T.; Magerl, A.; Halik, M. Structural Investigations of Self-Assembled Monolayers for Organic Electronics: Results from X-Ray Reflectivity. *Acc. Chem. Res.* **2015**, *48* (7), 1901–1908.

(128) Dubey, M.; Weidner, T.; Gamble, L. J.; Castner, D. G. Structure and Order of Phosphonic Acid-Based Self-Assembled Monolayers on Si(100). *Langmuir* **2010**, *26* (18), 14747–14754.

(129) Ko, S.; Han, G.; Lee, J. K. Surface Organic Chemistry for Application to Organic Electronics. *Tetrahedron Lett.* **2015**, *56* (24), 3721–3731.

(130) Pujari, S. P.; Scheres, L.; Marcelis, A. T. M.; Zuilhof, H. Covalent Surface Modification of Oxide Surfaces. *Angew. Chem. Int. Ed.* **2014**, *53* (25), 6322–6356.

(131) Shori, S. Surface Modification of Nanoplatelets in Polymer Nanocomposites. *Theses Diss.* **2014**.

(132) Shori, S.; Pellechia, P. J.; zur Loye, H.-C.; Ploehn, H. J. Covalent Grafting of Phenylphosphonate on Calcium Niobate Platelets. *J. Colloid Interface Sci.* **2015**, *437*, 97–110.

(133) Malinauskas, A. Chemical Deposition of Conducting Polymers. *Polymer* **2001**, *42* (9), 3957–3972.

(134) Uma, S.; Gopalakrishnan, J. Polymerization of Aniline in Layered Perovskites. *Mater. Sci. Eng. B* **1995**, *34* (2–3), 175–179.

(135) Boykin, J. R.; Smith, L. J. Rapid Microwave-Assisted Grafting of Layered Perovskites with N-Alcohols. *Inorg. Chem.* **2015**, *54* (9), 4177–4179.

(136) Akbarian-Tefaghi, S.; Teixeira Veiga, E.; Amand, G.; Wiley, J. B. Rapid Topochemical Modification of Layered Perovskites via Microwave Reactions. *Inorg. Chem.* **2016**, *55* (4), 1604–1612.

(137) Wang, Y.; Delahaye, E.; Leuvrey, C.; Leroux, F.; Rabu, P.; Rogez, G. Efficient Microwave-Assisted Functionalization of the Aurivillius-Phase $Bi_2SrTa_2O_9$. *Inorg. Chem.* **2016**, *55* (8), 4039–4046.

(138) Wang, Y.; Delahaye, E.; Leuvrey, C.; Leroux, F.; Rabu, P.; Rogez, G. Post-Synthesis Modification of the Aurivillius Phase Bi2SrTa2O9 via In Situ Microwave-Assisted "Click Reaction." *Inorg. Chem.* **2016**, *55* (19), 9790–9797.

(139) Armstrong, A. R.; Anderson, P. A. Synthesis and Structure of a New Layered Niobium Blue Bronze: $Rb_2LaNb_2O_7$. *Inorg. Chem.* **1994**, *33* (19), 4366–4369.

(140) Montasserasadi, D.; Granier, M. W.; Spinu, L.; Rai, S. C.; Zhou, W.; Wiley, J. B. Synthesis and Characterization of the Rare-Earth Dion–Jacobson Layered Perovskites, $APrNb_2O_7$ (A = Rb, Cs and CuCl). *Dalton Trans* **2015**, *44* (23), 10654–10660.

(141) Ebina, Y.; Sasaki, T.; Watanabe, M. Study on Exfoliation of Layered Perovskite-Type Niobates. *Solid State Ion.* **2002**, *151* (1), 177–182.

(142) Mistry, B. D. *A Handbook of Spectroscopic Data Chemistry: (UV, IR, PMR, 13CNMR and Mass Spectroscopy)*; Oxford Book Company, 2009.

(143) Binbin Pan; Zhao, W.; Zhang, X.; Li, J.; Xu, J.; Ma, J.; Liu, L.; Zhang, D.; Tong, Z. Research on the Self-Assembly of Exfoliated Perovskite Nanosheets ($LaNb_2O_7^-$) and Cobalt Porphyrin Utilized for the Electrocatalytic Oxidation of Ascorbic Acid. *RSC Adv.* **2016**, *6* (52), 46388–46393.

(144) Igarashi, S.; Sato, S.; Takashima, T.; Ogawa, M. Preparation of Finite Particles of Layered Niobate ($KCa_2Nb_3O_{10}$) for Improved Materials Performance. *Ind. Eng. Chem. Res.* **2013**, *52* (9), 3329–3333.

(145) Xu, F. F.; Ebina, Y.; Bando, Y.; Sasaki, T. Structural Characterization of (TBA, H)$Ca_2Nb_3O_{10}$ Nanosheets Formed by Delamination of a Precursor-Layered Perovskite. *J. Phys. Chem. B* **2003**, *107* (36), 9638–9645.

(146) Horikoshi, S.; Abe, H.; Torigoe, K.; Abe, M.; Serpone, N. Access to Small Size Distributions of Nanoparticles by Microwave-Assisted Synthesis. Formation of Ag Nanoparticles in Aqueous Carboxymethylcellulose Solutions in Batch and Continuous-Flow Reactors. *Nanoscale* **2010**, *2* (8), 1441–1447.

(147) Zhu, H.; Wang, X.; Li, Y.; Wang, Z.; Yang, F.; Yang, X. Microwave Synthesis of Fluorescent Carbon Nanoparticles with Electrochemiluminescence Properties. *Chem. Commun.* **2009**, *0* (34), 5118–5120.

(148) Washington II, A. L.; Strouse, G. F. Microwave Synthesis of CdSe and CdTe Nanocrystals in Nonabsorbing Alkanes. *J. Am. Chem. Soc.* **2008**, *130* (28), 8916–8922.

(149) Sun, C.-L.; Chang, C.-T.; Lee, H.-H.; Zhou, J.; Wang, J.; Sham, T.-K.; Pong, W.-F. Microwave-Assisted Synthesis of a Core–Shell MWCNT/GONR Heterostructure for the Electrochemical Detection of Ascorbic Acid, Dopamine, and Uric Acid. *ACS Nano* **2011**, *5* (10), 7788–7795.

(150) Liu, X.; Ma, R.; Bando, Y.; Sasaki, T. Layered Cobalt Hydroxide Nanocones: Microwave-Assisted Synthesis, Exfoliation, and Structural Modification. *Angew. Chem. Int. Ed.* **2010**, *49* (44), 8253–8256.

(151) Ramulifho, T.; Ozoemena, K. I.; Modibedi, R. M.; Jafta, C. J.; Mathe, M. K. Fast Microwave-Assisted Solvothermal Synthesis of Metal Nanoparticles (Pd, Ni, Sn) Supported on Sulfonated MWCNTs: Pd-Based Bimetallic Catalysts for Ethanol Oxidation in Alkaline Medium. *Electrochimica Acta* **2012**, *59*, 310–320.

(152) Murugan, A. V.; Muraliganth, T.; Manthiram, A. Rapid, Facile Microwave-Solvothermal Synthesis of Graphene Nanosheets and Their Polyaniline Nanocomposites for Energy Strorage. *Chem. Mater.* **2009**, *21* (21), 5004–5006.

(153) A. Hassan, H. M.; Abdelsayed, V.; S. Khder, A. E. R.; M. AbouZeid, K.; Terner, J.; Samy El-Shall, M.; I. Al-Resayes, S.; A. El-Azhary, A. Microwave Synthesis of Graphene Sheets Supporting Metal Nanocrystals in Aqueous and Organic Media. *J. Mater. Chem.* **2009**, *19* (23), 3832–3837.

(154) Janowska, I.; Chizari, K.; Ersen, O.; Zafeiratos, S.; Soubane, D.; Costa, V. D.; Speisser, V.; Boeglin, C.; Houllé, M.; Bégin, D.; et al. Microwave Synthesis of Large Few-Layer Graphene Sheets in Aqueous Solution of Ammonia. *Nano Res.* **2010**, *3* (2), 126–137.

(155) Shiguihara, A. L.; Bizeto, M. A.; Constantino, V. R. Chemical Modification of Niobium Layered Oxide by Tetraalkylammonium Intercalation. *J. Braz. Chem. Soc.* **2010**, *21* (7), 1366–1376.

(156) Suzuki, H.; Notsu, K.; Takeda, Y.; Sugimoto, W.; Sugahara, Y. Reactions of Alkoxyl Derivatives of a Layered Perovskite with Alcohols: Substitution Reactions on the Interlayer Surface of a Layered Perovskite. *Chem. Mater.* **2003**, *15* (3), 636–641.

(157) Tahara, S.; Ichikawa, T.; Kajiwara, G.; Sugahara, Y. Reactivity of the Ruddlesden−Popper Phase $H_2La_2Ti_3O_{10}$ with Organic Compounds: Intercalation and Grafting Reactions. *Chem. Mater.* **2007**, *19* (9), 2352–2358.

Chapter 5. Grafting and Polymerization on Perovskite-Based Nanosheets*

5.1– Introduction

As presented in the previous chapter, post-exfoliation surface-modification of perovskite nanosheets is readily achievable via facile microwave-assisted chemistries in as little as 1 h. This chapter will concentrate on the perovskite nanosheets that are modified with unsaturated organics, and summarize the results obtained when these monomer-grafted nanosheets undergo radical polymerization using free radical initiators and at times with the addition of divinyl monomers.

When it comes to the incorporation of nanosheets in a polymer matrix via actual covalent bonds, graphene oxide (GO) nanosheets are the most-studied. The composites with actual covalent bonds between GO nanosheets and polymer chains are typically attainable in two ways: either by crosslinking nanosheets to polymer chains,[1–3] or by in-situ polymerization on nanosheet surfaces.[4–6] Unlike GO nanosheets, there are only a few reports investigating the modification of perovskite-based nanosheets with organic surface groups and polymer chains.[7–12] The covalent surface groups of the perovskite nanosheets are typically introduced prior to exfoliation; these organic substituents are already present in the interlayer of the bulk layered host. In $HLaNb_2O_7$ for example, nanosheets are obtained by growing a polymeric network in the interlayer, which then delaminates the layered structure into nanosheets within a polymer matrix covalently grafted to it.[7–9] There is only one report where surface groups are covalently attached to nanosheets after exfoliation; this study does not involve unsaturated groups or polymer chains, and is carried out via conventional heating methods carried out over a few days.[13,14] In other cases, there is no actual covalent bond between the nanosheets and the surface groups or polymer chains; here, electrostatic interactions are dominant.[11,12,15,16]

* This chapter was adapted from: Akbarian-Tefaghi, S.; Wiley, J. B. "Grafting and polymerization on perovskite-based nanosheets" *252nd American Chemical Society National Meeting and Exposition, Philadelphia, PA,* August **2016** (Poster Presentation).

Rapid microwave-assisted (MA) methods have been found to be effective for organic modification of bulk layered perovskites.[17–20] As highlighted in Chapters 2 and 4, we were able to also extend the microwave methods to both rapid exfoliation and surface exchange of perovskite nanosheets. Initially protonated double-layered perovskites $HLnNb_2O_7$ (Ln = La, Pr) were exfoliated in an aqueous solution of tetra(n-butyl)ammonium hydroxide via rapid microwave reactions yielding TBA^+-$LnNb_2O_7$ nanosheets (TBA-LnNb NS), and then five different unsaturated organics with hydroxyl functional groups were exchanged with the tetra(n-butyl)ammonium surface groups. Grafting unsaturated groups to the surface of the nanosheets allows one to then grow polymer chains off the surfaces of the inorganic nanosheets. The resulting composite is especially interesting in that polymer chains are covalently bonded to the inorganic component. A number of unsaturated organics such as 5-hexen-1-ol, 9-decen-1-ol, acrylic acid, 2-allylphenol, and trimethylolpropane diallyl ether (TMPDAE) were grafted on the surface of the nanosheets. Figure 5-1 illustrates the surface modification of the TBA-LnNb NS with these five specific organics (double bonds are marked with star (+)).

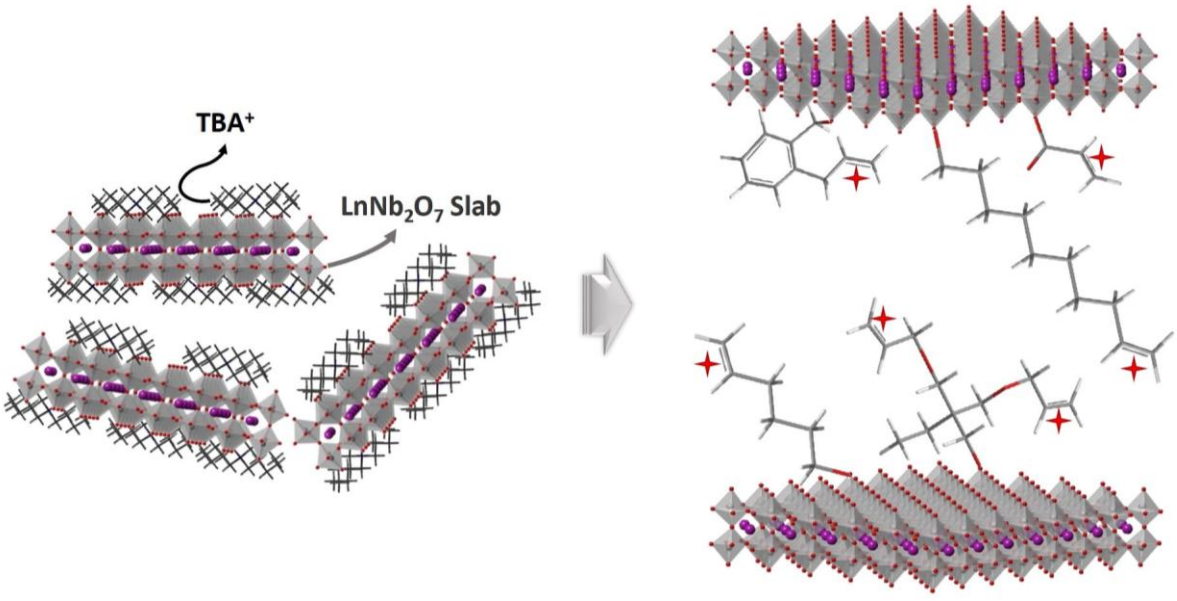

Figure 5- 1: Exchange of TBA+ surface groups on TBA-LnNb nanosheets with unsaturated organic groups (5-hexen-1-ol, 9-decen-1-ol, acrylic acid, 2-allylphenol, and TMPDAE).

The double bonds are marked with star (+).

Radical polymerization of the monomer-grafted nanosheets with AIBN only, or a mixture of AIBN and a divinyl monomer such as divinylbenzene (DVB) or di(ethylene glycol) divinyl ether (DEGDVE) was then carried out. Figure 5-2 presents the overall reaction scheme once monomer-grafted nanosheets (2-allylphenoxy-PrNb NS as an example) are incorporated in a polymerization reaction with the initiator and a divinyl monomer. As illustrated in this figure, AIBN will break into two radicals which then activate the double bonds into reacting radicals, allowing for the crosslinking and networking of the monomer-grafted nanosheets and divinyl monomers.

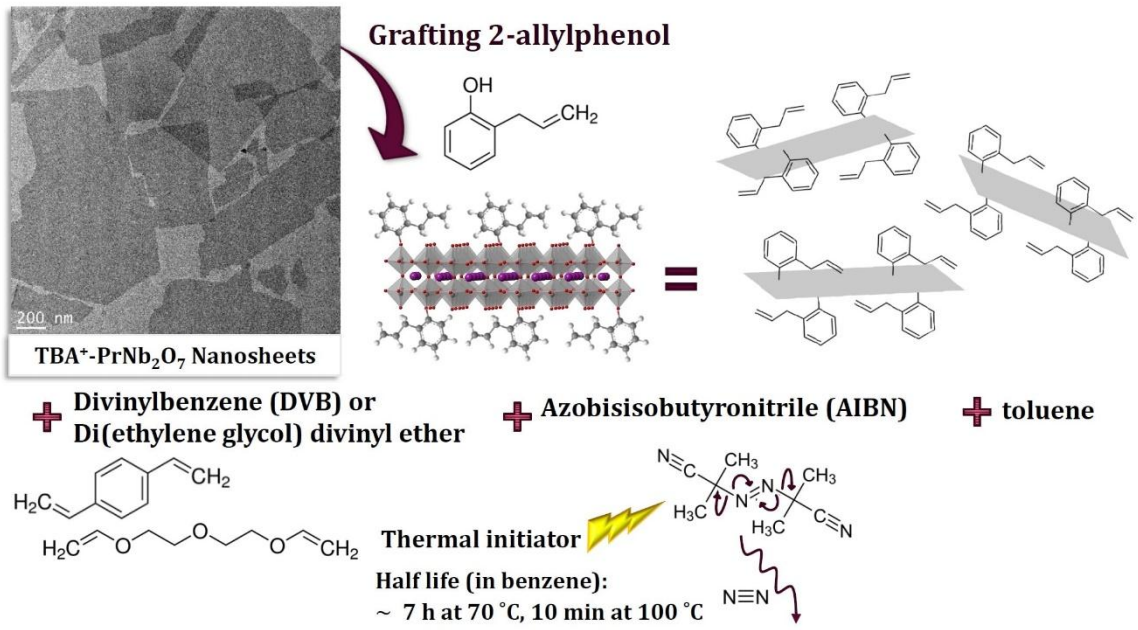

Figure 5- 2: Incorporation of monomer-grafted nanosheets in radical polymerization, using a thermal free-radical initiator (AIBN) as well as a divinyl monomer (DVB or DEGDVE).

Other than producing hybrid nanosize additives (organic-inorganic nanosheets) that allow for a tunable compatibility with a polymeric matrix, through this work the in-situ polymerization of the monomer-grafted nanosheets was also realized. Controlled surface functionalization of inorganic nanosheets is important to the effective engineering of functional composite materials with improved mechanical properties.

5.2– Experimental

5.2.1 Materials

For the synthesis of $RbLnNb_2O_7$ (Ln = La, Pr), the carbonate reagent was used as received, and the oxides were heated at 1000 ˚C in air for 12 h in order to eliminate any impurities or non-stoichiometries: Rb_2CO_3 (Alfa Aesar, 99.8%), La_2O_3 (Alfa Aesar, 99.99%), Nb_2O_5 (Alfa Aesar, 99.9985%), and Pr_6O_{11} (Alfa Aesar, 99.9%). Tetrabutylammonium hydroxide 30-hydrate, 95+% (TBAOH, ACROS Organics) was used for the exfoliation trials (***Note:*** To preserve the integrity of the TBAOH reagent, it is recommended that the storage temperature be in the range of 2-8 ˚C, and that handling at room temperature be minimized to avoid melting). A number of unsaturated organic components with hydroxyl functional groups were used to graft monomers on the nanosheets: 5-hexen-1-ol (Alfa Aesar 98%), 9-decen-1-ol (Alfa Aesar 90+%), acrylic acid (Alfa Aesar 99%, stab. with ca 200 ppm 4-methoxyphenol), 2-allylphenol (Alfa Aesar 98+%), and trimethylolpropane diallyl ether (Sigma Aldrich 90%) were used as received. Two divinyl monomers, divinylbenzene (Alfa Aesar 80%, mixture of isomers, stab. with 1000ppm 4-tert-butylcatechol) and diethylene glycol divinyl ether (Alfa Aesar 98%, stab. 0.1% potassium hydroxide), were used as crosslinking agents without further purification (***Note:*** To minimize unwanted degradation, unsaturated organics are best to be stored in a refrigerator in the absence of oxygen). 2,2′-azobis(2-methyl-propionitrile) free radical initiator, AIBN, (Sigma Aldrich 98%), was used in order to initiate and expedite the radical polymerization reactions (***Note:*** AIBN has to be stored in a fridge at 2-8 ˚C at all times, unless quick weighing is performed in ambient condition). Recrystallization of AIBN initiator was carried out before using: AIBN was dissolved in 50 ˚C methanol, then the solution was quickly filtered to remove any insoluble impurities, and the filtrate was slowly cooled down to yield pure AIBN crystals used in the following reactions.

5.2.2 Synthesis of Inorganic Hosts

$RbLnNb_2O_7$ (Ln = La, Pr) were synthesized by grinding stoichiometric amounts of the corresponding oxides (La_2O_3, Pr_6O_{11} and Nb_2O_5) with a 30% molar excess of Rb_2CO_3.[21,22] The excess carbonate was used to compensate for the volatilization of various rubidium oxides that are produced by heating the carbonate. The mixture was preheated at 850 °C overnight, ground,

and heated at 1050 °C (24 h and 6 h for Ln = La and Pr, respectively). After another intermediate grinding, the sample was heated at 1100 °C (24 h and 48 h for Ln = La and Pr, respectively). To remove the excess carbonate, the product was washed with copious amount of water and dried at 100 ˚C for several hours.

5.2.3 Microwave Syntheses

Topochemical reactions involving ion exchange and exfoliation (details given below) were carried out in a StartSYNTH Microwave Synthesis Labstation as previously reported (pictures and details of the setup presented in chapter 2).[18] The unit was equipped with Milestone's START platform where the individual reactions were contained in quartz pressure reactors (< 15 bar) and placed in a rotor. Grafting unsaturated organics, as well as polymerization reaction, was carried out in a Milestone QV-50 setup, where a quartz reactor vessel was sealed in the glovebox in order to eliminate the exposure of the reaction mixture to oxygen (the setup and the steps to seal the reactor were introduced in chapter 4). ***Caution:*** One should inspect glass microwave vessels before each reaction; glass defects might lead to hotspots and result in an explosion.

5.2.3.1 Acid Exchange (Protonation)

Microwave-assisted acid treatment was carried out for 3 h at 60˚C with continuous stirring (maximum power of 300 W).[18] A 6M nitric acid solution was used for the ion exchange, where the molar ratio of proton to interlayer cation (Rb) was maintained greater than 150:1. The acid-exchanged product was washed with distilled water until pH 7 was achieved, and then dried at 100 ˚C for 3 hours.

5.2.3.2 Exfoliation of $HLnNb_2O_7$

$HLnNb_2O_7$ (HLnNb) was exfoliated in an aqueous solution of TBAOH with a molar ratio of 1:10 for HLnNb to hydrated TBAOH. Microwave-assisted exfoliation reactions were carried out at 1 h at 60 ˚C (max 300 W), ramped to 80 ˚C over a 10-minute period, and then heated at 80 ˚C for 1 h (max 350 W). Exfoliated products were washed with water and ethanol, and dried at 70 ˚C for several hours.

5.2.3.3 Surface-Exchange of Nanosheets with Unsaturated Surface Groups

In order to protect the unsaturated bonds from undesired polymerization in oxygen at elevated temperatures, reactions with the five unsaturated organics were carried out under argon. Typical synthesis of monomer-grafted nanosheets involved reacting 60 mg of TBA-LnNb NS with 8 mL of the pure unsaturated organic solvent within reactor vessels, sealed in a glovebox under argon, and heated at 90 ˚C for 45 min (max 500 W, using a Weflon button). Alternative to these microwave-assisted reactions, similar exchange reactions were carried out with convection heating under argon in a glovebox; samples were heated on a hot plate with stirring for 2 d at 80 ˚C. The glovebox reactions were performed as controls for microwave-assisted trials, and in all cases yielded identical results to microwave reactions. The monomer-grafted nanosheets were then rapidly washed with ethanol and acetone in ambient condition (up to 10 minutes maximum), dried under vacuum at room temperature for a few minutes, and stored under protective argon gas in a glovebox.

5.2.3.4 Polymerization of Monomer-Grafted Nanosheets

Radical polymerization of the monomer-grafted nanosheets was carried out in sealed vessels with AIBN as a thermal free-radical initiator, and at times with the addition of a crosslinking agent, divinylbenzene (DVB) or diethylene glycol divinyl ether (DEGDVE); microwave heating was typically performed by heating the reaction mixture at 100 ˚C for 20 min (max 600 W). Polymerization of the unsaturated nanosheets was realized by adding 20% (w/w) AIBN to 10 mg of the monomer-grafted nanosheets produced above, dissolved in 5 mL toluene. In some trials, the crosslinking agents (divinyl monomers) were also added to enhance the linkage of the monomer-grafted nanosheets to each other, and to cause more noticeable morphology change after the polymerization. This was done based on two typical recipes: either addition of 200% (w/w) divinyl monomer and 30% (w/w) AIBN, or 400% (w/w) divinyl monomer and 50% (w/w) AIBN, to 10 mg of various monomer-grafted nanosheets dissolved in 5 mL toluene.

5.2.4 Characterization

A Philips X'Pert system equipped with Cu Kα radiation (λ = 1.5418 Å) and a curved graphite monochromator was used in continuous mode with a scan rate of 0.02 °/s to collect the

X-ray powder diffraction (XRD) data. Thermogravimetric analysis (TGA) and differential scanning calorimetry (DSC) were carried out on a TA Instruments TGA-DSC SDT Q600 system in alumina pans under a dilute oxygen atmosphere (ca. 50% argon); samples were heated up to 900 ˚C at a rate of 15 ˚C/min. Raman spectra were collected in a Thermo-Fisher DXR dispersive Raman spectrometer using the $\lambda = 532$ nm line with a spectral resolution of 3 cm^{-1}. Field emission SEM images of sample morphologies were obtained on a HITACHI S-4800 FEG CRYO-SEM. For the FESEM sample preparation, a dilute dispersion of nanosheets in ethanol was drop cast on small pieces of aluminum foil, lightly coated with gold, taped onto the FESEM stud using carbon tapes, and finally observed in 1-3 kV range.

5.3– Results

A number of unstaurated organics were successfully grafted on perovskite nanosheets via MA exchange reactions performed on TBA-LnNb NS: 5-hexen-1-ol, 9-decen-1-ol, acrylic acid, 2-allylphenol, and trimethylolpropane diallyl ether (TMPDAE). Figure 5-3 provides the XRD patterns for these monomer-grafted nanosheets; samples were taken out of the glovebox and scanned upon <1 h air-exposure (a), and the very same sample preparation was then rescanned after 2 d storage in ambient condition (b). The first XRD reflections in all cases shift to higher angles upon long air exposure, indicating a shrink in the interlayer spacings of the re-stacked nanosheets, which suggests spontaneous linkage of the neighboring nanosheets due to the side reaction of their unsaturated surface groups in the presence of oxygen. Figure 5-4 presents the

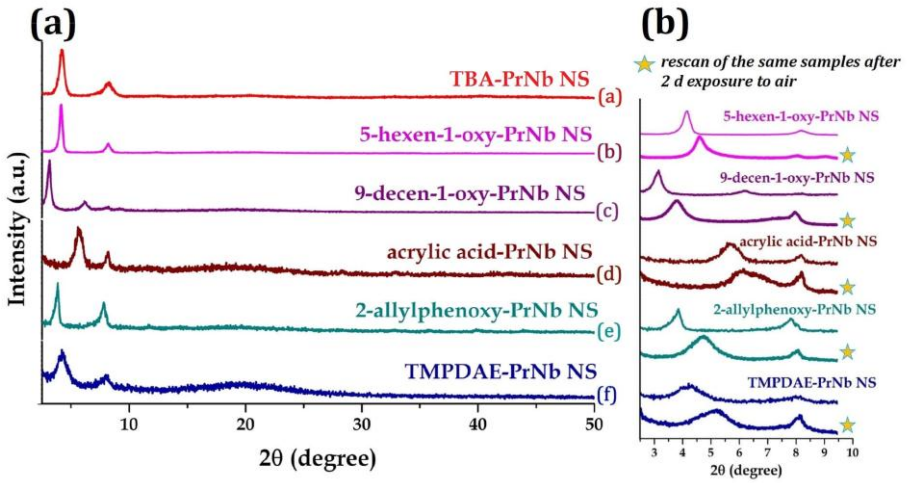

Figure 5- 3: XRD patterns of the monomer-grafted nanosheets upon (a) <1 h air exposure, and (b) 2 d storage in air; TBA-PrNb host versus the products of reaction with (b) 5-hexen-1-ol, (c) 9-decen-1-ol, (d) acrylic acid, (e) 2-allylphenol, and (f) TMPDAE.

Raman spectra for these modified nanosheets (<1 h air-exposure), highlighting the characteristic peaks that are expected in each case.[23]

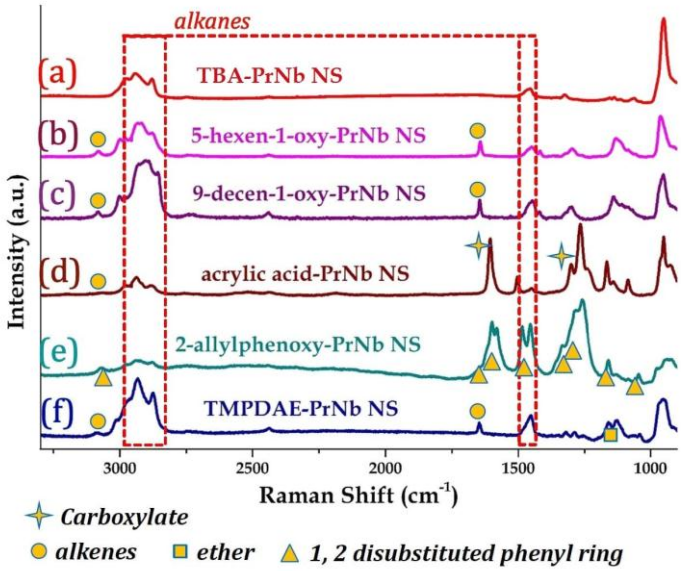

Figure 5- 4: Raman spectra of the monomer-grafted nanosheets, highlighting the characteristic peaks expected in each case.

Figure 5-5 compares the TGA-DSC results obtained for (a) 2-allylphenoxy-PrNb, (b) 5-hexen-1-oxy-PrNb, (c) 9-decen-1-oxy-PrNb, (d) acrylic acid-PrNb, and (e) TMPDAE-PrNb nanosheets, confirming their different thermal behaviors and weight losses.

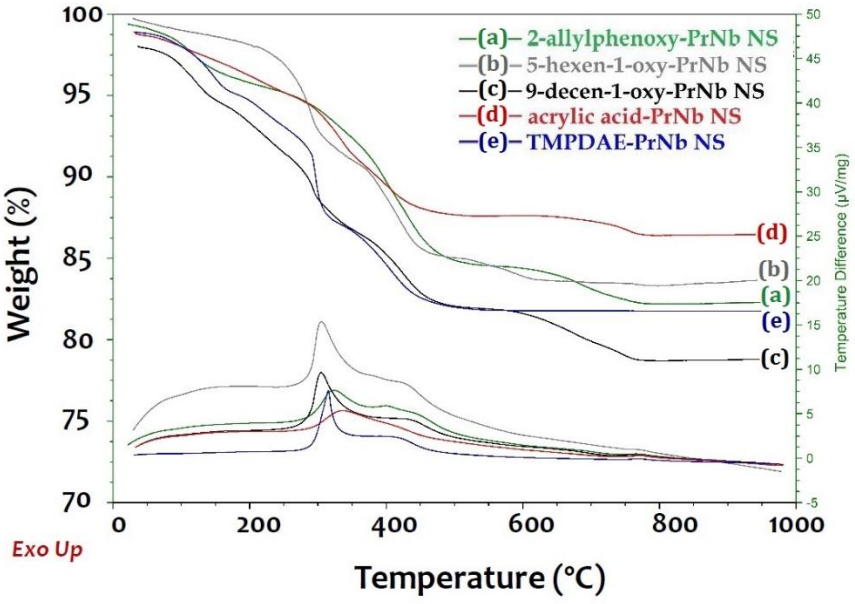

Figure 5- 5: TGA-DSC results for monomer-grafted nanosheets.

FESEM images were used to study the morphological differences due to polymerization of monomer-grafted nanosheets. However, even without introducing AIBN or any crosslinking agent, and only upon air exposure, there seems to be a significant topological difference between a monomer-grafted nanosheet (after several days storage in air) and the TBA-PrNb nanosheet (Figure 5-6).

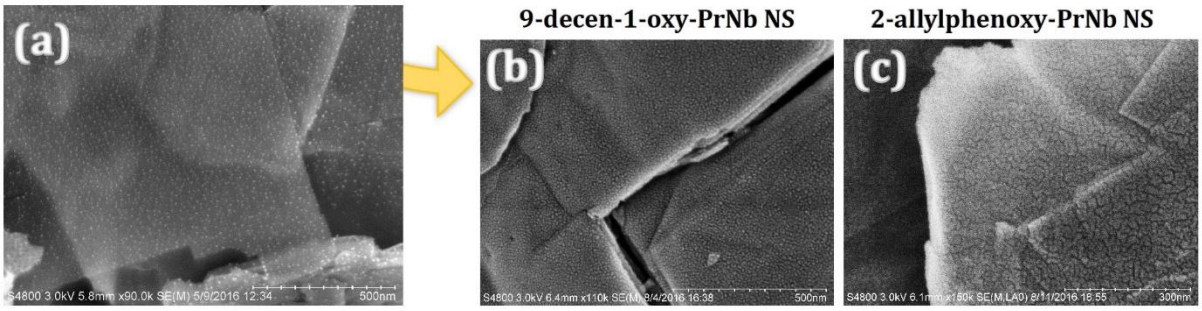

Figure 5- 6: FESEM images of (a) TBA-PrNb NS, (b) 9-decen-1-oxy-PrNb NS, and (c) 2-allylphenoxy-PrNb NS.

Polymerization among monomer-grafted nanosheets was attempted by adding AIBN free radical initiator to the modified nanosheets. FESEM was performed only on one type of these monomer-grafted nanosheets, 9-decen-1-oxy-PrNb NS, and the results are provided in Figure 5-7, showing an even more dramatic topological difference as opposed to the sample that was only exposed to air without the addition of AIBN (Figure 5-6b). Interstingly, the TGA results show less weight losses after reaction with AIBN, which suggests the removal of some monomeric groups as some others are reacting among different nanosheets (Figure 5-8).

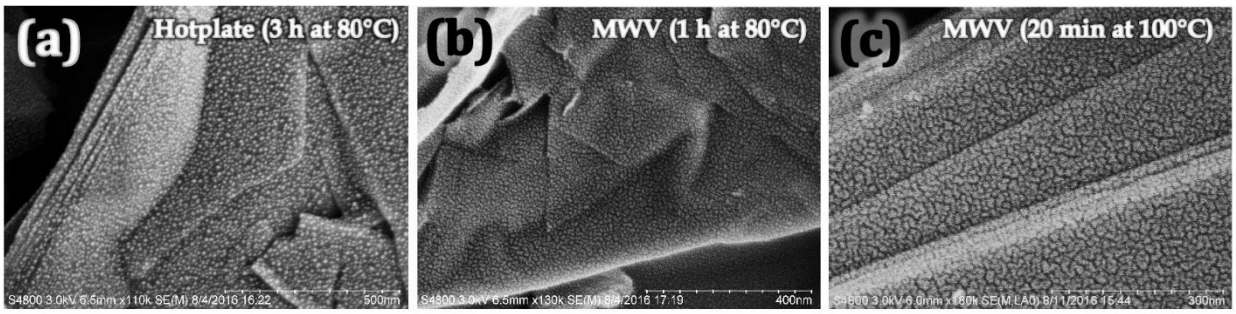

Figure 5- 7: Morphological differences studied via FESEM after the addition of AIBN to 9-decen-1-oxy-PrNb NS. Reactions were performed in three different ways under argon; (a) 3 h stirring on hot plate at 80 ˚C, (b) 1 h microwave heating at 80 ˚C, and (c) 20 min microwave heating at 100 ˚C.

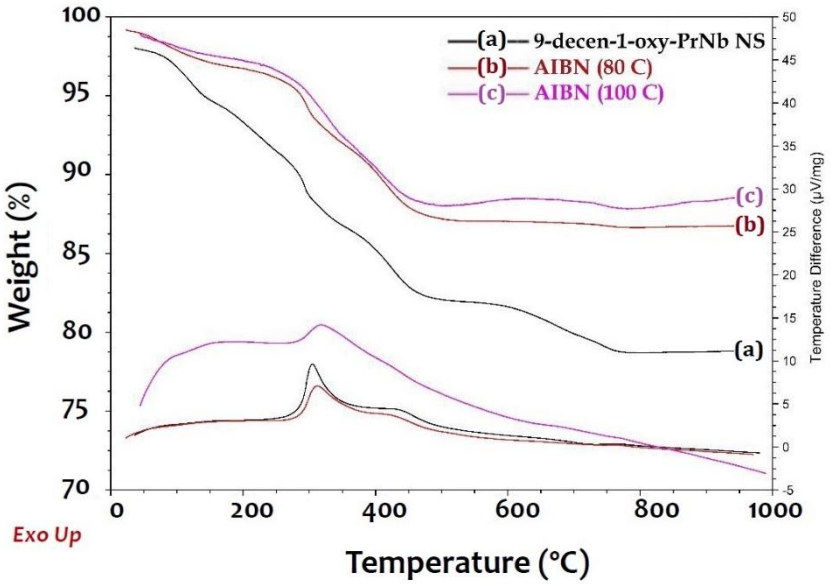

Figure 5- 8: TGA-DSC results comparing the 9-decen-1-oxy-PrNb NS to AIBN-treated ones.

Figure 5-9 shows the effect of microwave reaction condition on the morphology of polymerized 9-decen-1-oxy-PrNb NS, when both AIBN and DVB are introduced. The same study was also performed when the other divinyl monomer, DEGDVE, is used instead of DVB; the FESEM images are provided in Figure 5-10. Thermal behaviors of the polymerization products in all of these cases are then compared in Figure 5-11. It is evident that increased reaction temperature enhances the size of the islands forming on the surface of the nanosheets (based on FESEM), and conversely reduces the organic loading on the nanosheets (based on TGA).

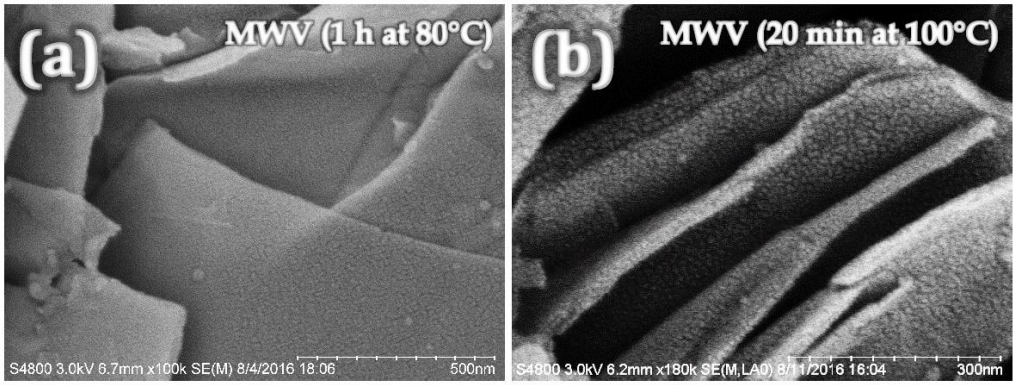

Figure 5- 9: Impact of the microwave reaction condition on the morphology of 9-decen-1-oxy-PrNb NS polymerized with DVB and AIBN, (a) 1 h at 80 ºC, and (b) 20 min at 100 ºC.

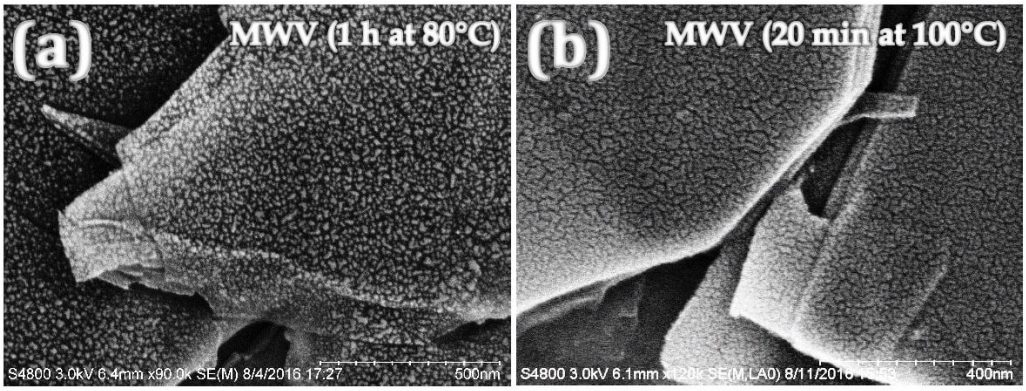

Figure 5- 10: Impact of the microwave reaction condition on the morphology of 9-decen-1-oxy-PrNb NS polymerized with DEGDVE and AIBN, (a) 1 h at 80 ºC, and (b) 20 min at 100 ºC.

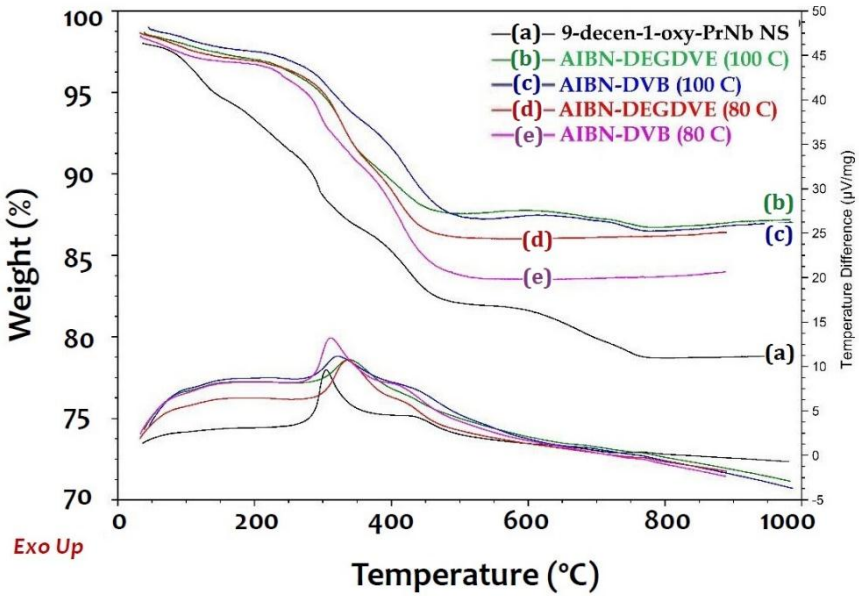

Figure 5- 11: TGA-DSC results for (a) 9-decen-1-oxy-PrNb NS sample treated with AIBN and DEGDVE for (b) 100 ˚C and (d) 80 ˚C, or with AIBN and DVB for (c) 100 ˚C and (e) 80 ˚C.

Raman spectrum of 9-decen-1-oxy-PrNb NS is compared to its polymerized trials in Figure 5-12. The most significant change in polymerized samples reflecting in Raman spectra, is the appearance of the characteristic peaks of the phenyl ring when DVB is incorporated in the structure (1750-1500 cm^{-1}).[23] Considering the thorough washing step in toluene, DVB should be covalently bonded to the NS to show these significant peaks (Figure 5-12h and i versus the monomer-grafted NS in Figure 5-12a).

Since only a limited number of samples could be observed under FESEM, other than 9-decen-1-oxy-PrNb NS, only the morphology of polymerized 2-allylphenoxy-PrNb NS samples were further investigated. Figure 5-13 shows the FESEM images of three polymerized 2-allylphenoxy-PrNb NS samples when 20 min microwave heating was performed with the addition of: (a) only AIBN, (b) both AIBN and DEGDVE, or (c) both AIBN and DVB. Figure 5-14 provides the TGA-DSC results for these samples. The polymerized sample with the highest organic loading appears to be the one whith both DVB and AIBN incorporated in the reaction. However, even in this case the weight loss is only about the same as the monomer-grafted nanosheet and is no higher than that, which indicates the loss of some organic groups as some crosslinking is occuring among various nanosheets introduced to both AIBN and DVB.

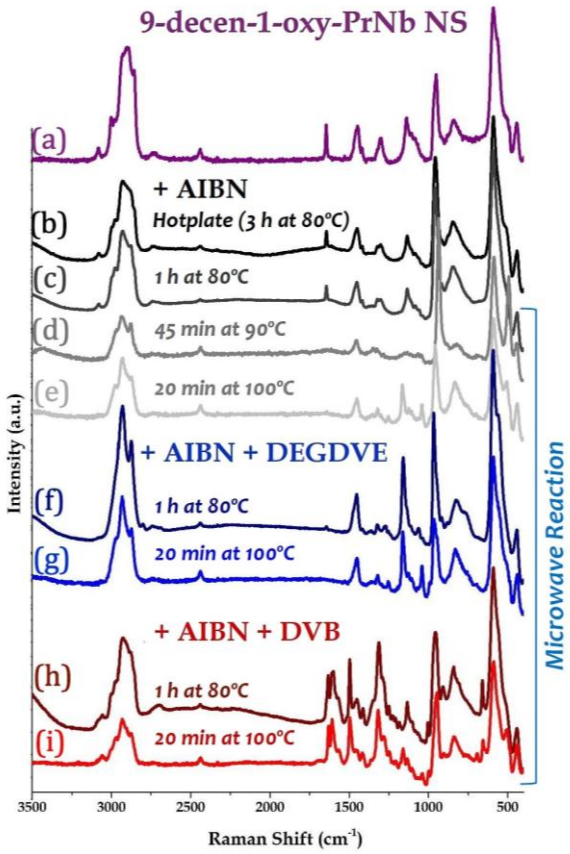

Figure 5- 12: Raman spectra of (a) 9-decen-1-oxy-PrNb NS compared to its polymerized products; when only AIBN is used (b) 3 h hot plate stirring at 80 ˚C, (c) 1 h microwave heating at 80 ˚C, (d) 45 min microwave radiation at 90 ˚C, or (e) 20 min microwave reaction at 100 ˚C, in case of using both AIBN and DEGDVE when microwave heating is performed for (f) 1 h at 80 ˚C or (g) 20 min at 100 ˚C, and lastly, when both AIBN and DVB are used in microwave reactions for (h) 1 h at 80 ˚C, or (i) 20 min at 120 ˚C.

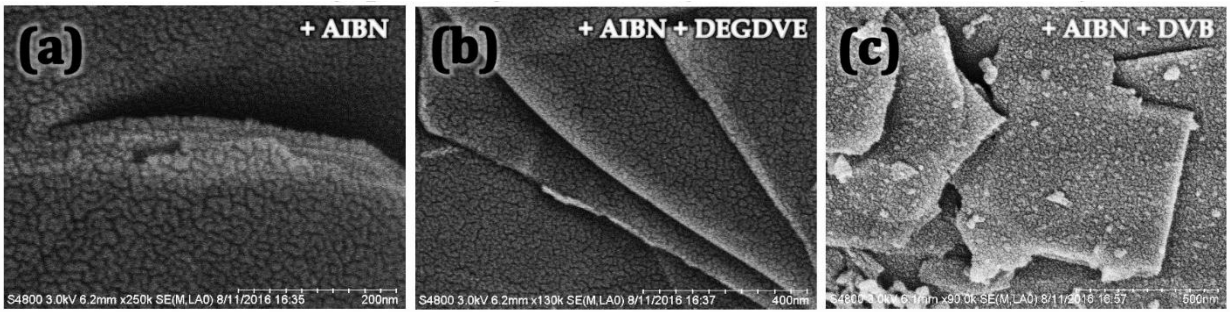

Figure 5- 13: FESEM images of 2-allylphenoxy-PrNb NS sample polymerized in microwave for 20 min at 100 ˚C with: (a) AIBN, (b) AIBN and DEGDVE, and (c) AIBN and DVB.

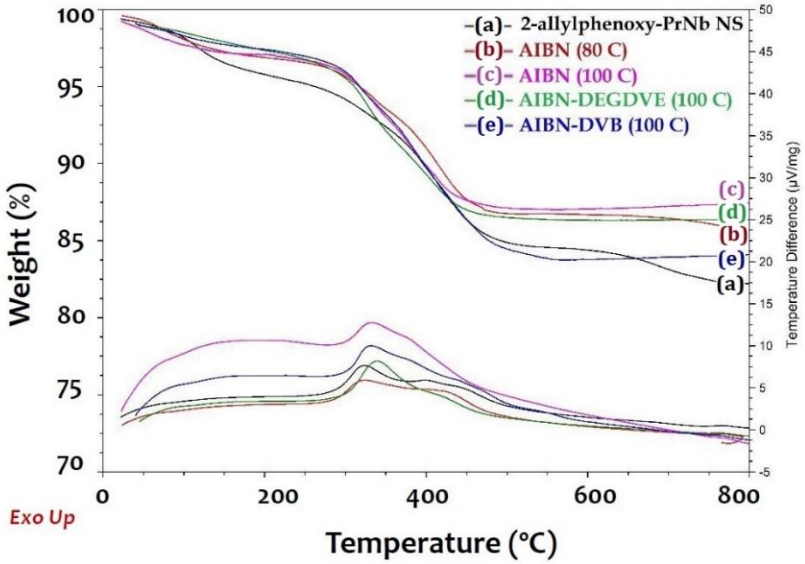

Figure 5- 14: TGA-DSC behaviors of a few polymerized 2-allylphenoxy-PrNb NS samples.

Figure 5-15 shows the XRD patterns of 9-decen-1-oxy-PrNb and 2-allylphenoxy-PrNb nanosheets versus a few polymerized samples using either only AIBN or a combination of AIBN and a divinyl monomer. It is clear that polymerization typically leads to broader peaks and less order in re-stacked hybrid nanosheets due to the formation of larger organic surface groups.

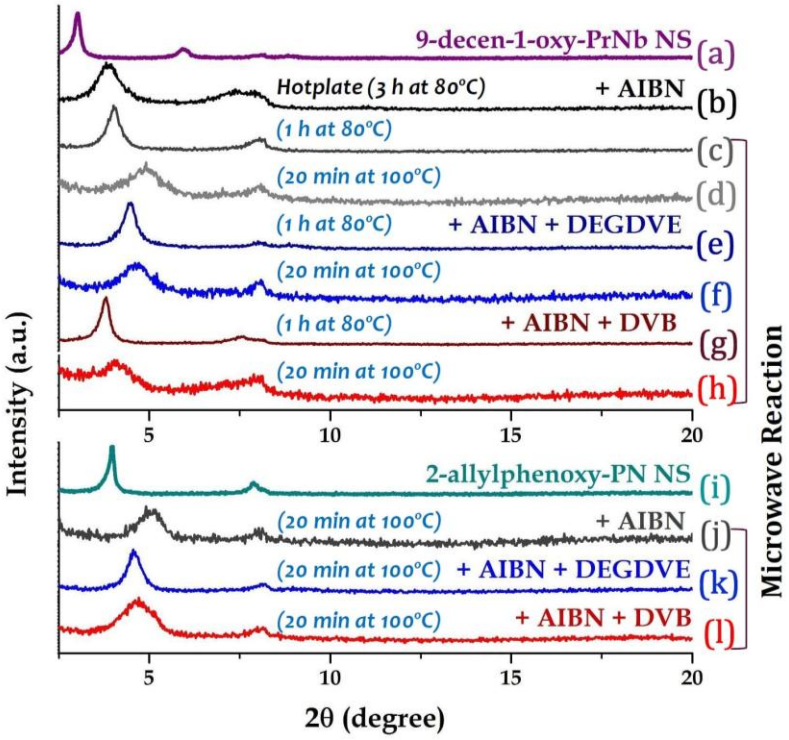

Figure 5- 15: XRD patterns of (a) 9-decen-1-oxy-PrNb and (i) 2-allylphenoxy-PrNb nanosheets versus their polymerized samples respectively provided in (b-h) and (j-l).

It should be noted that in all the polymerized samples reported herein so far, the amount of the secondary monomer (divinyl monomer) was intentionally low, so the polymer chains would not bury the nanosheets. The reactivity of these monomer-grafted nanosheets was basically established by following the morphological differences in the nanosheets. Figure 5-16 is an example of a polymerization reaction with the addition of three active components to 10 mg 9-decen-1-oxy-PrNb NS: AIBN 30% (w/w), DVB 100% (w/w), and AA 100% (w/w). Reaction was carried out in 5 mL of toluene, stirring for 3 h at 80 ˚C on hot plate (under argon). Formation of polymer beads and embedding the nanosheets in polymeric features are obvious. Sample surface charging and electron beam damage are fairly high in this sample due to the majority of polymer component, resulting a noisy FESEM image.

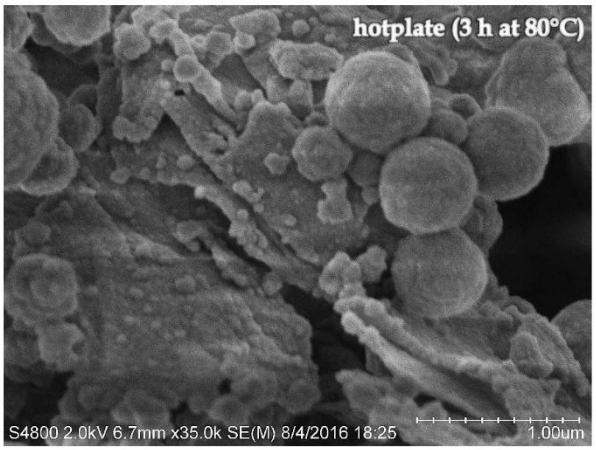

Figure 5- 16: FESEM image of 9-decen-1-oxy-PrNb NS polymerized with the addition of AIBN, DVB and AA in the same batch.

The desired way for the incorporation of these nanosheets in a polymeric network is via a method that provides constant mixing of the components as the polymerization continues. This mixing also has to be of a great quality to ensure the even distribution of these additives all over the polymeric matrix. In order to have these additives boosting the mechanical properties without yielding a brittle composite, usually less than 10% w/w reinforcing agent has to be added to the polymeric matrix. Figure 5-17 illustrates a simple polymerization reaction were only 3% w/w 2-allylphenoxy-PrNb NS is added to DVB monomers going through radical polymerization (1 d polymerization at 70 ˚C by conventional reaction on the hot plate in the glovebox, using 1% w/w AIBN dissolved in 3 mL toluene). AIBN forms radicals due to heating (radical initoators are shown as $I^{\cdot}$) which can then activate the unsaturated bonds in DVB and 2-allylphenoxy-PrNb NS, and yield radicals from them as well. The crosslinking then will continue incorporating all these radicals in a random way, and the poly-DVB gel (PDVB) will covalently incorporate the nanosheets (PDVB-NS composite gel). Figure 5-18 presents the pure PDVB obtained by reacting DVB and AIBN in toluene, and compares it to the PDVB-NS composite prepared by the addition of 2-allylphenoxy-PrNb NS. Even though TGA confirms the existance of about 3% inorganic nanosheet in the PDVB-NS composite as expected (Figure 5-19), the Raman spectra cannot highlight any difference between pure PDVB and the composite as presented in Figure 5-20. This can be due to the small percentage of nanosheets which peaks are shielded by PDVB bands. Another interesting feature of PDVB-NS composite compared to the pure PDVB appeared to be its partial crystallinity as presented in Figure 5-21; pure PDVB seems to be quite amorphous as

expected, while the composite shows one XRD peak indicating more crystallinity. Higher crystallinity can be due to the presence of nanosheets in the polymer matrix which creates some level of ordered polymer chains around these additives. However, it should be noted that replicates of this batch turned out to be completely amorphous (no peaks appearing in XRD), and additional study has to be performed for further reproducibility.

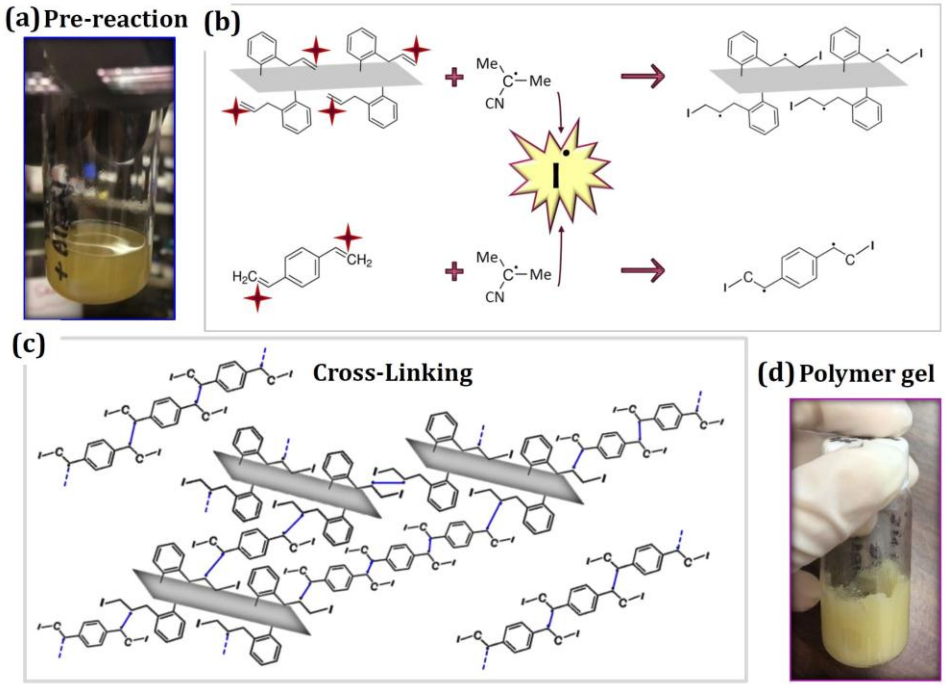

Figure 5- 17: The steps of producing PDVB-crosslinking-2-allylphenoxy-PrNb NS: (a) the mixture of AIBN, 2-allylphenoxy-PrNb NS, DVB and toluene prior to reaction, (b) the formation of radicals from DVB and 2-allylphenoxy-PrNb NS once the radicals forming from AIBN (I˚) activates the double bond, (c) random crosslinking among present radicals, and (d) formation of a PDVB-NS composite gel.

Figure 5- 18: Pure PDVB (left) compared to PDVB-NS composite formed after incorporation of 2-allylphenoxy-PrNb NS (right).

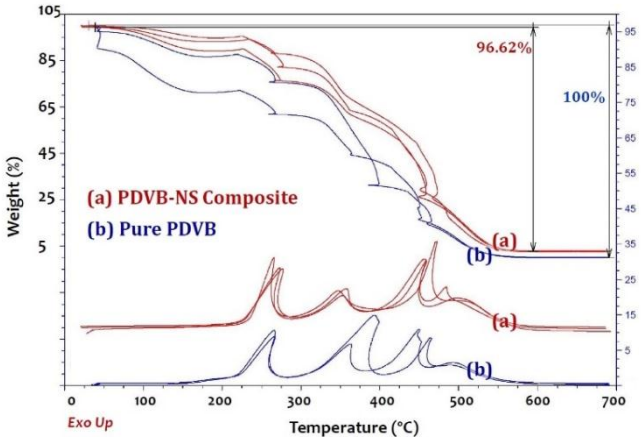

Figure 5- 19: TGA-DSC results for (a) PDVB-NS composite compared to (b) pure PDVB.

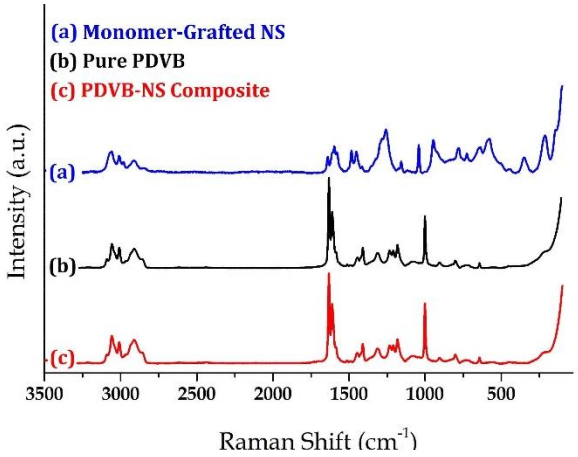

Figure 5- 20: Raman spectra of (a) 2-allylphenoxy-PrNb NS, (b) pure PDVB, and (c) PDVB-NS composite.

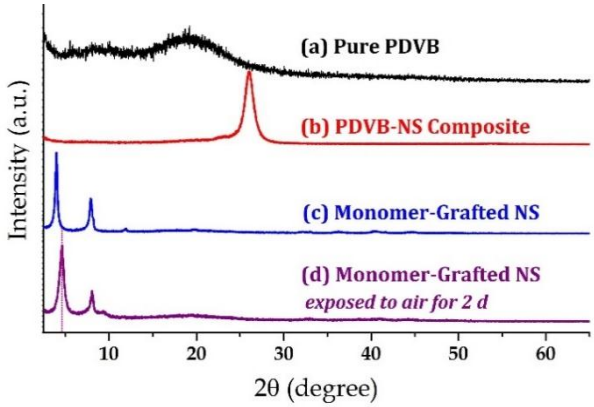

Figure 5- 21: XRD patterns of (a) pure PDVB, (b) PDVB-NS composite, and 2-allylphenoxy-PrNb NS (c) before and (d) after air exposure.

5.4– Discussion

Grafting unsaturated organics on the surface of the nanosheets leads to hybrid nanosheets that have some level of air-sensitivity due to the unsaturated double bonds. This is not an instant reactivity, as oxygen acts like an intitiator with a long half life under ambient conditions. Based on the XRD patterns of these monomer-grafted nanosheets upon air-exposure versus a 2-d exposure, provided respectively in Figures 5-3a and b, the very same sample preparations show a layer contration upon longer air-axposure. This is most likely due to the linkage of the unsaturated bonds present in the neighboring re-stacked nanosheets, causing a gradual reduction in the interlayer spacings. FESEM images of two types of monomer-grafted nansoheets presented in Figure 5-6 also confirms larger islands of organic surface-groups compared to TBA^+-PrNb NS which has no air sensitivity. In general, FESEM images well prove the morphological evolution of TBA^+-PrNb NS after introducing unsaturated organics, as well as after further polymerization of these monomer-grafted nanosheets with either AIBN only, or a combination of AIBN and a divinyl monomer. XRD also revealed noisier patterns and broader peaks after polymerization, which confirms poorer crystallinity, as expected. Raman spectra were indicative of the various functional groups of monomer-grafted nanosheets, and typically confirmed the addition of the divinyl monomer after the polymerization. The only limitation with Raman is where the divinyl monomer has functional groups that are similar to what is already present due to the unsaturated surface groups of the monomer-grafted nanosheets; for instance adding DEGDVE to 9-decen-1-oxy-PrNb Ns cannot show any significant extra peaks in Raman, but the addition of DVB does.

TGA results for polymerized nanosheets seemed to indicate a destructive nature for these polymerization techniques; in all cases the polymerized samples showed a lower weight loss compared to that of the monomer-grafted nanosheets. Even though polymerization should lead into linking polymer chains to the surface of the nanosheets without removing any unsaturated groups that are already present, this observation indicates the deletion of some unsaturated groups as some others undergo polymerization. This adverse effect seems to also be dominant over polymerization, as in all cases the weight losses are even less than the initial monomer-grafted nanosheet. It is highly recommended that less extreme polymerization conditions also be

investigated to see if the loading of organics on the nanosheets can be further improved (lower temperatures for longer durations).

5.5– Conclusions

Various unstaurated organics were successfully grafted on perovskite nanosheets via microwave-assisted exchange reactions perofrmed on TBA^+-$LnNb_2O_7$ NS; 5-hexen-1-ol, 9-decen-1-ol, acrylic acid, 2-allylphenol, and trimethylolpropane diallyl ether (TMPDAE). The reactivity of the monomer-grafted nanosheets was investigated via XRD, FESEM, and Raman and verified the successful formation of polymer on the surface. TGA results indicated poor organic loading on the polymerized samples versus the monomer-grafted nanosheets, which will have to be improved in the future research. Controlled surface functionalization and in-situ polymerization of inorganic nanosheets is significant in order to improve the mechanical properties of functional composite materials.

5.6– References

(1) Satti, A.; Larpent, P.; Gun'ko, Y. Improvement of Mechanical Properties of Graphene Oxide/poly(allylamine) Composites by Chemical Crosslinking. Carbon 2010, 48 (12), 3376–3381.

(2) Kumar, N. A.; Choi, H.-J.; Shin, Y. R.; Chang, D. W.; Dai, L.; Baek, J.-B. Polyaniline-Grafted Reduced Graphene Oxide for Efficient Electrochemical Supercapacitors. ACS Nano 2012, 6 (2), 1715–1723.

(3) Shan, C.; Yang, H.; Han, D.; Zhang, Q.; Ivaska, A.; Niu, L. Water-Soluble Graphene Covalently Functionalized by Biocompatible Poly-L-Lysine. Langmuir 2009, 25 (20), 12030–12033.

(4) Pramoda, K. P.; Hussain, H.; Koh, H. M.; Tan, H. R.; He, C. B. Covalent Bonded Polymer-Graphene Nanocomposites. J. Polym. Sci. Part Polym. Chem. 2010, 48 (19), 4262–4267.

(5) Gonçalves, G.; Marques, P. A. A. P.; Barros-Timmons, A.; Bdkin, I.; Singh, M. K.; Emami, N.; Grácio, J. Graphene Oxide Modified with PMMA via ATRP as a Reinforcement Filler. J. Mater. Chem. 2010, 20 (44), 9927.

(6) Huang, Y.; Qin, Y.; Zhou, Y.; Niu, H.; Yu, Z.-Z.; Dong, J.-Y. Polypropylene/Graphene Oxide Nanocomposites Prepared by In Situ Ziegler−Natta Polymerization. Chem. Mater. 2010, 22 (13), 4096–4102.

(7) Tahara, S.; Okamoto, T.; Sugahara, Y. Preparation of a Nanocomposite Consisting of a Siloxane Network and Perovskite-Related Nanosheets via a Sol–gel Process. Sci. Technol. Adv. Mater. 2006, 7 (5), 446–450.

(8) Tahara, S.; Takeda, Y.; Sugahara, Y. Preparation of Organic−Inorganic Hybrids Possessing Nanosheets with Perovskite-Related Structures via Exfoliation during a Sol−Gel Process. Chem. Mater. 2005, 17 (24), 6198–6204.

(9) Idota, N.; Fukuda, S.; Tsukahara, T.; Sugahara, Y. Preparation of Thermoresponsive Nanosheets Exhibiting Phase Transitions in Water via Surface Modification of Layered Perovskite Nanosheets with Poly(N-Isopropylacrylamide) (PNIPAAm). Chem. Lett. 2015, 44 (2), 203–205.

(10) Asai, Y.; Ariake, Y.; Saito, H.; Idota, N.; Matsukawa, K.; Nishino, T.; Sugahara, Y. Layered Perovskite Nanosheets Bearing Fluoroalkoxy Groups: Their Preparation and Application in Epoxy-Based Hybrids. RSC Adv. 2014, 4 (51), 26932.

(11) Wu, X.; Fei, F.; Chen, Z.; Su, W.; Cui, Z. A New Nanocomposite Dielectric Ink and Its Application in Printed Thin-Film Transistors. Compos. Sci. Technol. 2014, 94, 117–122.

(12) Takei, T.; Muraki, N.; Xu, N.; Miura, A.; Kumada, N. Anodic Hybridization of Fluorinated Layered Perovskite Nanosheet with Polyaniline for Electrochemical Capacitor. Colloids Surf. Physicochem. Eng. Asp. 2014, 459, 186–193.

(13) Shori, S. Surface Modification of Nanoplatelets in Polymer Nanocomposites. Theses Diss. 2014.

(14) Shori, S.; Pellechia, P. J.; zur Loye, H.-C.; Ploehn, H. J. Covalent Grafting of Phenylphosphonate on Calcium Niobate Platelets. J. Colloid Interface Sci. 2015, 437, 97–110.

(15) Malinauskas, A. Chemical Deposition of Conducting Polymers. Polymer 2001, 42 (9), 3957–3972.

(16) Uma, S.; Gopalakrishnan, J. Polymerization of Aniline in Layered Perovskites. Mater. Sci. Eng. B 1995, 34 (2–3), 175–179.

(17) Boykin, J. R.; Smith, L. J. Rapid Microwave-Assisted Grafting of Layered Perovskites with N-Alcohols. Inorg. Chem. 2015, 54 (9), 4177–4179.

(18) Akbarian-Tefaghi, S.; Teixeira Veiga, E.; Amand, G.; Wiley, J. B. Rapid Topochemical Modification of Layered Perovskites via Microwave Reactions. Inorg. Chem. 2016, 55 (4), 1604–1612.

(19) Wang, Y.; Delahaye, E.; Leuvrey, C.; Leroux, F.; Rabu, P.; Rogez, G. Efficient Microwave-Assisted Functionalization of the Aurivillius-Phase Bi2SrTa2O9. Inorg. Chem. 2016, 55 (8), 4039–4046.

(20) Wang, Y.; Delahaye, E.; Leuvrey, C.; Leroux, F.; Rabu, P.; Rogez, G. Post-Synthesis Modification of the Aurivillius Phase Bi2SrTa2O9 via In Situ Microwave-Assisted "Click Reaction." Inorg. Chem. 2016, 55 (19), 9790–9797.

(21) Armstrong, A. R.; Anderson, P. A. Synthesis and Structure of a New Layered Niobium Blue Bronze: Rb2LaNb2O7. Inorg. Chem. 1994, 33 (19), 4366–4369.

(22) Montasserasadi, D.; Granier, M. W.; Spinu, L.; Rai, S. C.; Zhou, W.; Wiley, J. B. Synthesis and Characterization of the Rare-Earth Dion–Jacobson Layered Perovskites, APrNb2O7 (A = Rb, Cs and CuCl). Dalton Trans 2015, 44 (23), 10654–10660.

(23) Mistry, B. D. A Handbook of Spectroscopic Data Chemistry: (UV, IR, PMR, 13CNMR and Mass Spectroscopy); Oxford Book Company, 2009.

Chapter 6. Optical Properties of Functionalized Metal-Oxide Nanosheets*

6.1– Introduction

Liquid exfoliation is one of the main top-down approaches for the fabrication of 2D nanomaterials via cleaving weak out-of-plane van der Waals or electrostatic interactions in a layered solid.[1–16] Exfoliation of layered oxide perovskites using bulky organics allow for the production of metal-oxide nanosheets whose elemental composition and thickness are easily controlled in the preceding solid-state reaction.[10,17–26] Double- and triple-layered Dion-Jacobson perovskites such as $RbLaNb_2O_7$ and $KCa_2Nb_3O_{10}$ are the most common hosts in this case for the preparation of such oxide nanosheets and more complicated assemblies.[10,18,19,27–44] Other than ruling out the elemental composition of the 2D slab via the solid-state formation of the perovskite host from its oxide and carbonate reagents, fluorination[41,45] and doping[20,43,46] can also be carried out after the ceramic method and prior to exfoliation to introduce specific properties in the final nanosheets (such as conductivity or catalytic activity). Due to the presence of the bulky organics on the surface of these exfoliated nanosheets, these metal-oxide freestanding layers are considered hybrid. Intercalation of tetra(n-butyl)ammonium ion (TBA^+) is the most common method for the delamination of layered perovskites, producing TBA^+-functionalized oxide nanosheets.[10,17–26] These nanosize metal-oxide inorganic scaffolds provide mechanical hardness and thermal stability to the hybrid nanosheets, as well as tunable electronic and magnetic properties.[47,48] On the other hand, functionalization with various organic surface groups with structural diversity and varying properties (such as polarizability and luminescence) provide further control over the final properties of the hybrid nanosheets.[47,48] As demonstrated in the literature, the elemental composition of the 2D layers can significantly impact their photocatalytic activity, optical or electronic properties.[20,36,41,45,46,49–51] Sometimes various types

* This chapter was adapted from two poster presentations: 1) Akbarian-Tefaghi, S.; Brown, T.; Renquet, P.; Rostamzadeh, T.; Davis-Wheeler, C.; Wiley, J. B. "Novel Hybrid Perovskite-Based Nanosheets via Rapid Microwave-Assisted Reactions" *2017 Materials Research Society Spring Meeting and Exhibit, Phoenix, AZ,* April **2017**— 2) Akbarian-Tefaghi, S.; Poduval, A.; Renquet, P.; Rostamzadeh, T.; Davis-Wheeler, C.; Wiley, J. B. "Impact of the Functionality of Perovskite-Based Nanosheets on Their Optical Properties" *2017 Materials Research Society Spring Meeting and Exhibit, Phoenix, AZ,* April **2017**.

of nanosheets are also integrated as 2D heterostructures (lateral and vertical)[52–59] or layer-by-layer assemblies[44,60–72] to direct specific properties in a final nanocomposite film. Even though the impact of the intercalants of some layered oxides on their optical properties has been studied before,[11,24,73–76] the influence of various organic functionalities of the 2D hybrid oxide nanosheets has not yet been investigated properly. Taking advantage of novel microwave-assisted (MA) post-exfoliation surface-modification reactions, various linear and cyclic alcoxy or ammonium organic functionalities with different degrees of saturation can now be introduced very rapidly and efficiently,[77] allowing for screening and tuning a vast number of functionalized metal-oxide nanosheets with directed properties.

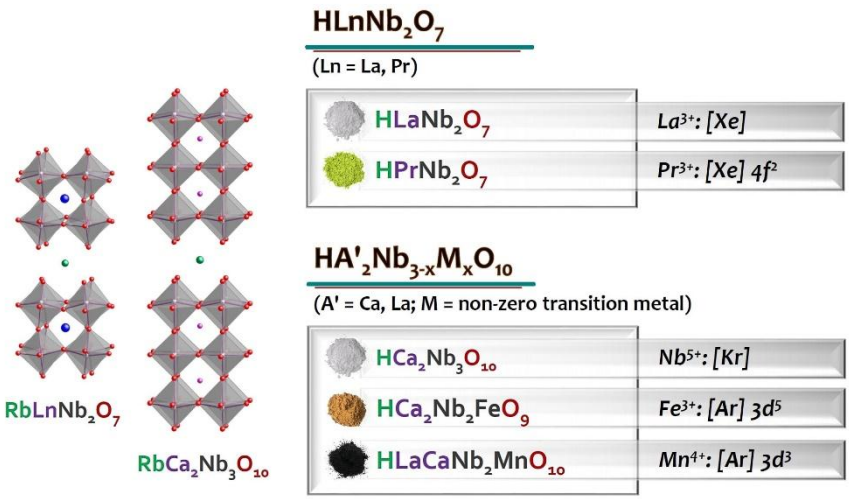

Figure 6- 1: Double- and triple-layered Dion-Jacobson perovskites used for the preparation of functionalized nanosheets.

Figure 6-1 compares the general structure of the double- and triple-layered Dion-Jacobson hosts that were used here: $HPrNb_2O_7$, $HCa_2Nb_2FeO_9$, and $HLaCaNb_2MnO_{10}$. These double- and triple-layered hosts are isostructural with $HLaNb_2O_7$ and $HCa_2Nb_3O_{10}$ perovskites, respectively; the most-widely used precursors for the preparation of perovskite nanosheets. Pr, Fe, and Mn elements with partially filled *d* or *f* orbitals were introduced in order to direct new properties in the final hybrid nanosheets, as well as investigate the impact of the elemental composition among isostructural nanosheets. Novel TBA^+-$PrNb_2O_7$, TBA^+-$Ca_2Nb_2FeO_9$, and TBA^+-$LaCaNb_2MnO_{10}$ nanosheets were obtained by rapid MA exfoliation of the hosts in TBAOH aqueous solution, and then modified with various organics; C_nH_{2n+1}-OH (n = 3, 5, and

10), C_nH_{2n+1}-NH_2 (n = 3, 6, and 8), C_7H_7-OH, and C_7H_7-NH_2. The properties of the hybrid nanosheets as a function of elemental composition and surface groups were then investigated with atomic force and electron microscopies, X-ray diffraction, and vibrational, fluorescence, and diffuse-reflectance UV-Visible spectroscopies.

6.2– Experimental

6.2.1 Materials

Rb_2CO_3 (Alfa Aesar, 99.8%), K_2CO_3 (Alfa Aesar, 99.997%), $CaCO_3$ (Alfa Aesar, 99.99%), Fe_2O_3 (Alfa Aesar, 99.99%), MnO_2 (Alfa Aesar, 99.997%,), and KCl (Alfa Aesar, 99.995%) were used as received. Nb_2O_5 (Alfa Aesar, 99.9985%), La_2O_3 (Alfa Aesar, 99.99%) and Pr_6O_{11} (Alfa Aesar, 99.9%) were heated overnight at 1000 °C to eliminste impurities. Tetrabutylammonium hydroxide 30-hydrate (TBAOH), either ACROS Organics 95+% or Sigma Aldrich 99+%, was used for the exfoliation of the perovskite hosts. ***Note:*** To preserve the integrity of the TBAOH reagent, it is recommended that the storage temperature be in the range of 2-8 °C, and that handling at room temperature be minimized to avoid melting. Milli-Q water (18.2 MV cm, Milli-pore) was used to dissolve TBAOH in the exfoliation trials. Organic alcohols and amines were used without any further distillation: 1-propanol (Alfa Aesar 99+%), 1-pentanol (Alfa Aesar 98+%), 1-decanol (Alfa Aesar 98+%), benzyl alcohol (Alfa Aesar 99%), benzylamine (Alfa Aesar 98+%), 1-propylamine (Alfa Aesar 99+%), 1-hexylamine (Alfa Aesar 99%) and 1-octylamine (Alfa Aesar 99%). ***Caution:*** All of the organic solvents and specifically the amines must be handled in a fume hood with proper PPE—amines are toxic, corrosive, and very irritating to the skin, eyes and lungs. It is also recommended to purchase only small amounts of amines and keep the storage time within 6 months. In case of longer storage times, amines are best to be kept under protective inert gas.

6.2.2 Synthesis of the Perovskite Hosts

$RbLnNb_2O_7$ (Ln = La, Pr) were synthesized by grinding stoichiometric amounts of the corresponding oxides (La_2O_3 or Pr_6O_{11} and Nb_2O_5) and a 30% molar excess of Rb_2CO_3 similar to the previous reports.[78,79] The excess carbonate was used to compensate for the loss of alkali-metal oxides due to volatilization. The mixture was preheated at 850 °C overnight, ground, and

heated at 1050 °C (24 h and 6 h for Ln = La and Pr, respectively). After regrinding, the sample was heated at 1100 °C (24 h and 48 h for Ln = La and Pr, respectively).

$KCa_2Nb_3O_{10}$ was prepared based on a molten salt method:[80] Stoichiometric proportions of K_2CO_3, $CaCO_3$, and Nb_2O_5 were well ground with 15:1 molar excess of KCl. The mixture was heated for 24 h at 900 °C, 18 h at 950 °C, and 2 h at 1000 °C, without any intermediate grinding.

Inspired by the previous reports on the solid state synthesis of $RbCa_2Nb_2FeO_9$,[81,82] this host was synthesized by grinding 30% excess of Rb_2CO_3 with stoichiometric amounts of $CaCO_3$, Nb_2O_5, and Fe_2O_3, and then pre-heating the mixture (6 h at 550 °C, regrinding, and another preheating step at 850°C overnight). The final heating step was performed at 1150°C for 48 h with one intermediate grinding. Using Cs_2CO_3 rather than Rb_2CO_3, this exact regular method was also applicable for the synthesis of $CsCa_2Nb_2FeO_9$.

$RbLaCaNb_2MnO_{10}$, a novel triple-layered host recently made and characterized by one of our group members,[83] was also prepared via regular ceramic method: 25% excess of Rb_2CO_3 was added to stoichiometric proportions of La_2O_3, $CaCO_3$, Nb_2O_5 and MnO_2. The mixture was pre-heated (550 °C for 6 h, reground, and heated at 850 °C overnight), and then heated at 1150 °C for 30 h with one intermediate grinding.

The final perovskite hosts were washed with copious amount of water to remove the excess carbonate (as well as KCl in case of $KCa_2Nb_3O_{10}$), and dried at 100 °C for a few hours.

6.2.3 Microwave Assisted Reactions

Proton exchange, exfoliation, and post-exfoliation surface-modification reactions were carried out in a StartSYNTH Microwave Synthesis Labstation as demonstrated chapter 2.[84] For non-aqueous reaction mixtures, a Weflon button (graphite-doped Teflon) was maintained in the mixture during the reaction to aid the non-polar solvents absorbing the microwaves. The uniformity of each reaction was also ensured by using a Teflon stirring bar in all trials (transparent to microwaves). ***Caution:*** It is required to inspect the glass vessels for defects and cracks before each experiment; these defects can create hotspots and cause explosion.

6.2.3.1 Acid Exchange (Protonation)

$HLaNb_2O_7$, $HPrNb_2O_7$, $HCa_2Nb_3O_{10}$, $HCa_2Nb_2FeO_9$, and $HLaCaNb_2MnO_{10}$ were prepared by MA acid treatment of their hosts in a 6 M nitric acid solution at 60 °C for 3 h (with

continuous stirring and a maximum power of 300 W).[84] It is required to maintain a molar ratio of greater than 150:1 for the proton to interlayer cation (K, Rb, or Cs) in order to obtain above 95% yield in the proton exchange step. The protonated products were washed with copious amount of distilled water, and dried at 100 °C for a few hours.

6.2.3.2 Exfoliation of the Perovskite Hosts

The protonated perovskites were exfoliated in an aqueous solution of TBAOH with at least 10-fold molar excess of hydrated TBAOH. Typical microwave-assisted exfoliation reactions were carried out at 1 h at 60 °C (max 300 W), then ramped to 80 °C over a 10-minute period, before heating at 80 °C for another 1 h (max 350 W).[77] All products were washed with water and ethanol, and dried at 60 °C overnight.

6.2.3.3 Post-Exfoliation Surface-Exchange Reactions

Once exfoliated nanosheets were obtained (TBA-$PrNb_2O_7$, TBA-$Ca_2Nb_2FeO_9$, and TBA-$LaCaNb_2MnO_{10}$ NS), various surface groups with alcoxy or ammonium functional groups were successfully introduced by treating the NS containing TBA^+ surface groups in various solvents via MA exchange reactions:[77] $C_nH_{2n+1}OH$ (n = 3, 5, 10), benzyl alcohol (BA), benzylamine (BAm), and $C_nH_{2n+1}NH_2$ (n = 3, 6, 8) solvents. Typically, 20 mg of dried NS was reacted with 8 mL pure solvent containing a Weflon button: 1 h at 60 °C (max 300 W) in benzyl alcohol and benzylamine, 1 h at 100 °C (max 600 W) in n-propanol and 1-propylamine, 45 min at 120 °C (max 800 W) for n-pentanol and 1-hexylamine, and 30 min at 150 °C (max 1000 W) for n-decanol and 1-octylamine. The products were washed with acetone and dried at 70 °C for several hours.

6.2.4 Characterization

A Philips X'Pert system equipped with Cu Kα radiation (λ = 1.5418 Å) and a curved graphite monochromator was used in continuous mode with a scan rate of 0.02 °/s to collect the X-ray powder diffraction (XRD) data. Infrared spectroscopy was performed using a Perkin Elmer 2000 FT-IR spectrometer. Raman spectra were collected in a Thermo-Fisher DXR dispersive Raman spectrometer at a wavelength of 532 nm line with a spectral resolution of 3 cm^{-1}. The NS thicknesses were examined under an Asylum Research MFP-3D Atomic Force

Microscope (AFM) working in the dual amplitude resonance tracking (DART) mode; a very dilute suspension of each NS sample in ethanol was drop cast onto a mica sheet. Transmission electron microscopy (TEM) images and selected area electron diffraction (SAED) were taken at JEOL 2010 high-resolution microscope (200 keV) and FEI TECNAI G2 F30 FEG TEM (300 keV). For TEM measurements, a dilute dispersion of each NS in ethanol was drop cast onto a grid (carbon film coated fine mesh copper), and dried at room temperature for a few hours. Field emission SEM images of sample morphologies were obtained on a HITACHI S-4800 FEG CRYO-SEM. For the FESEM sample preparation, a dispersion of NS in ethanol was drop cast on small pieces of aluminum foil, lightly coated with gold, taped onto the FESEM stud using carbon tapes, and finally observed in 1-3 kV range.

Optical measurements were carried out using ultraviolet-visible (UV-Vis) and fluorescence (FL) spectroscopies, respectively collected on a Cary 500 UV-Vis/NIR spectrometer, and a Perkin Elmer LS 55 Luminescence Spectrometer. Each sample (TBA-$LaNb_2O_7$, TBA-$PrNb_2O_7$, TBA-$Ca_2Nb_3O_{10}$, TBA-$Ca_2Nb_2FeO_9$, and TBA-$LaCaNb_2MnO_{10}$ NS) was evaluated in two ways: either a very dilute suspension of the NS in ethanol was filled in quartz cuvettes, or a very concentrated suspension of NS in ethanol (more like a thick paste of NS) was coated on quartz slides to form an even thick film. The solid samples proved to show more variations rather than the dilute suspensions, and so all other hybrid nanosheets were only characterized as solid films on quartz slides. The UV-Vis and FL instruments are designed to carry both types of preparations; either solid or solution. However, the solution form in cuvettes is the default setup, which typically yields absorbance spectrum in case of UV-Vis or excitation/emission spectra for FL measurements. In order to study the solid films in UV-Vis, the *diffuse reflectance accessory* (DRA) was plugged to the instrument instead of the two front and back cuvette-holders. In case of FL spectroscopy, a *front surface accessory* was used in place of the cuvette holder which allowed for clipping the NS-coated quartz slide for excitation/emission measurements.

6.3– Results

6.3.1 Formation of Hybrid Oxide Nanosheets

As demonstrated in Chapter 4, MA exfoliation and following surface-modification reactions successfully lead into various hybrid nanosheets based on double-layered $LnNb_2O_7$ perovskites (Ln = La, Pr). Here, the same experimental methods[77] are applied for the production of novel oxide nanosheets and their various hybrid derivatives from two triple-layered DJ perovskites; $HCa_2Nb_2FeO_9$ and $HLaCaNb_2MnO_{10}$.

Focus of this chapter will be on the optical properties of the hybrid nanosheets that are obtained from $HPrNb_2O_7$, $HCa_2Nb_2FeO_9$, and $HLaCaNb_2MnO_{10}$ DJ perovskites, as it is expected to see interesting features due to the presence of Pr, Fe, and Mn elemenets, respectively. Novel TBA^+-$PrNb_2O_7$, TBA^+-$Ca_2Nb_2FeO_9$, and TBA^+-$LaCaNb_2MnO_{10}$ nanosheets are initially compared to well-known TBA^+-$LaNb_2O_7$, TBA^+-$Ca_2Nb_3O_{10}$ nanosheets, and then used as "hosts" for the preparation of other functionalized nanosheets using C_nH_{2n+1}-OH (n = 3, 5, and 10), C_nH_{2n+1}-NH_2 (n = 3, 6, and 8), C_7H_7-OH, and C_7H_7-NH_2. For the convenience, $LaNb_2O_7$-, $PrNb_2O_7$-, $Ca_2Nb_3O_{10}$-, $Ca_2Nb_2FeO_9$-, and $LaCaNb_2MnO_{10}$-based nanosheets are respectively abbreviated as LN, PN, CN, Fe, and Mn nanosheets throughout this chapter.

Figure 6-2 compares the XRD patterns of TBA-LN, TBA-PN, TBA-CN, TBA-Fe, and TBA-Mn to their protonated hosts, confirming the loss of crystallinity as the intercalation of TBA^+ delaminates the layered hosts into freestanding layers. In order to further approve of the formation of nanosheets in case of novel TBA-Fe and TBA-Mn NS, TEM was also tried, showing individual layers of nanosheets throughout the sample (Figure 6-3). SAED insets in Figure 6-3 confirms the maintained atomic order throughout each layer, prying apart the layered hosts only from their swollen and detached interlayers. The topology of individual nanosheets was further examined with AFM. The height contact-mode image and height profile from TBA-Fe and TBA-Mn nanosheet samples are provided in Figure 6-4. The average nanosheet thicknesses of TBA-Fe and TBA-Mn nanosheets, based on 45 values measured from different height profiles, were found to be 1.8(4) nm and 2.2(5) nm, respectively. A smaller average thickness for Fe NS compared to Mn NS seems to be reasonable considering the random oxygen vacancies of these nanosheets, as well as having only Ca^{2+} in the *A* site of the $A_{n-1}B_nO_{3n+1}$ slab

(rather than a combination of Ca^{2+} and larger La^{3+} in Mn NS). Estimating the thickness of each slab from the structure of $RbCa_2Nb_3O_{10}$,[85] any assembly of two nanosheets is expected to be greater than about 2.4 nm (two slabs as well as an interlayer spacing between adjacent organic layers). This implies the delamination of both of these hosts to *at most* two layers, similar to TBA-PN NS.[77] The morphology of TBA-Fe and TBA-Mn nanosheets was also examined by FESEM technique and presented in Figure 6-5, approving of assemblies of thin sheets, with TBA^+ aggregates appearing as surface dots similar to those observed for TBA-PN and TBA-LN nanosheets in chapter 4.[77]

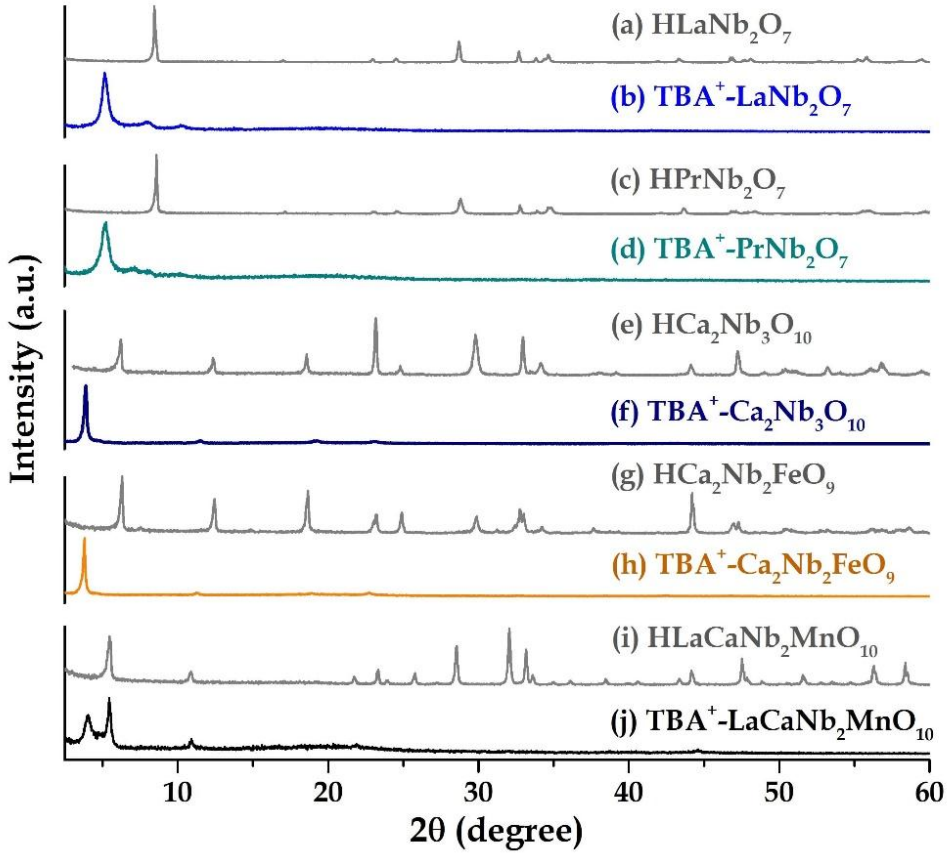

Figure 6- 2: XRD patterns of the as-synthesized nanosheets versus their protonated layered hosts; (a) HLN, (b) TBA^+-LN NS, (c) HPN, (d) TBA^+-PN NS, (e) HCN, (f) TBA^+-CN NS, (g) HFe, (h) TBA^+-Fe NS, (i) HMn and (j) TBA^+-Mn NS.

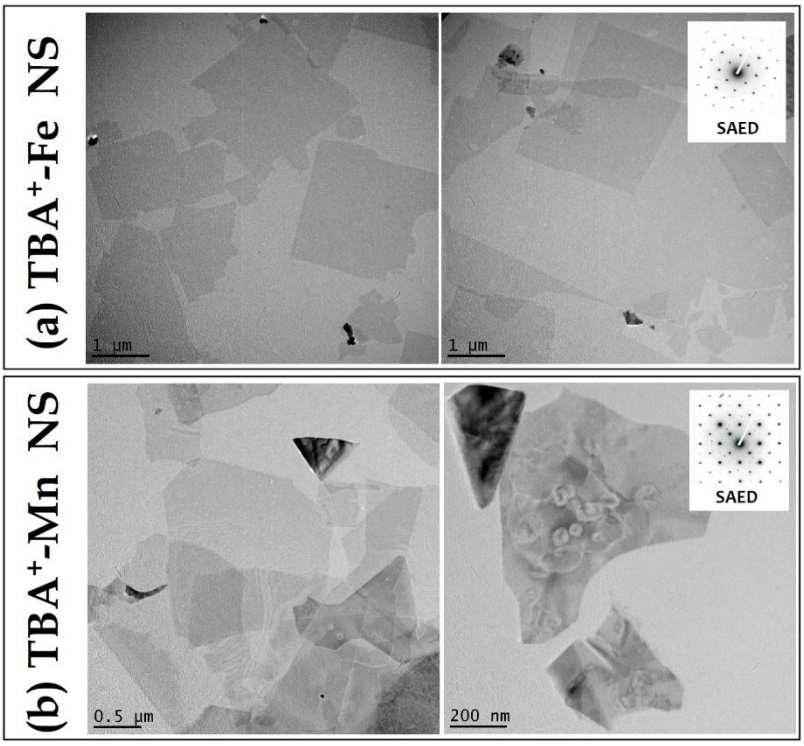

Figure 6- 3: TEM images and SAED patterns of (a) TBA-Fe NS and (b) TBA-Mn NS.

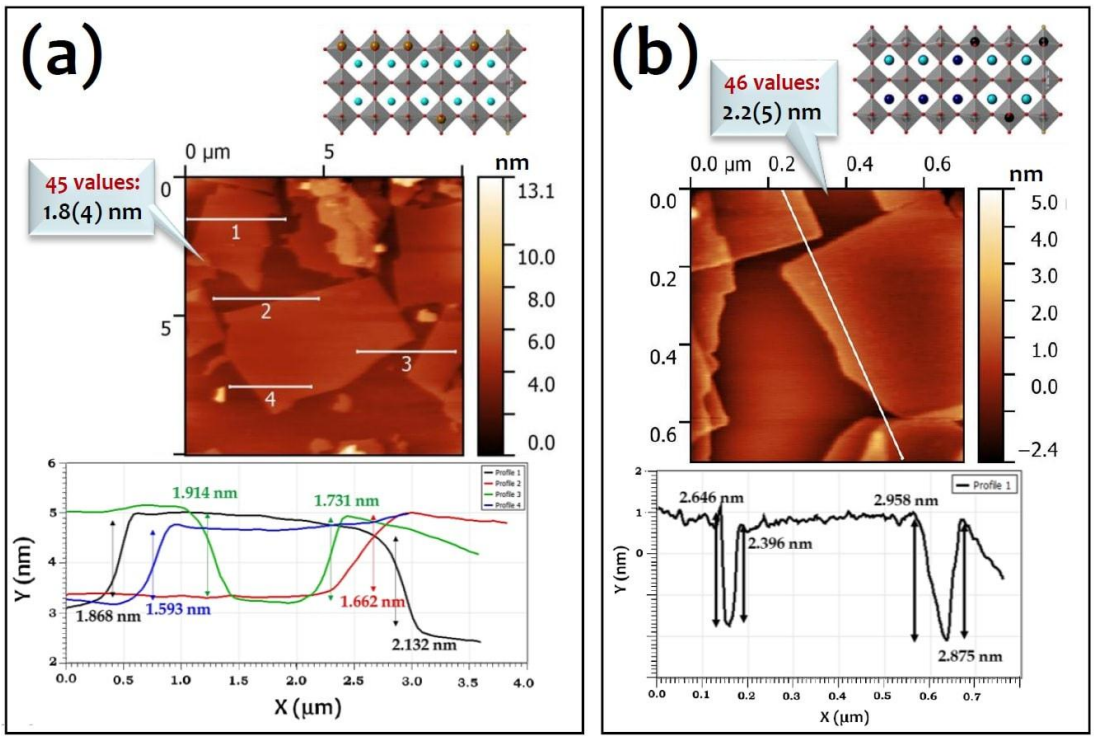

Figure 6- 4: Height contact-mode AFM images and height profiles for (a) TBA-Fe NS and (b) TBA-Mn NS samples.

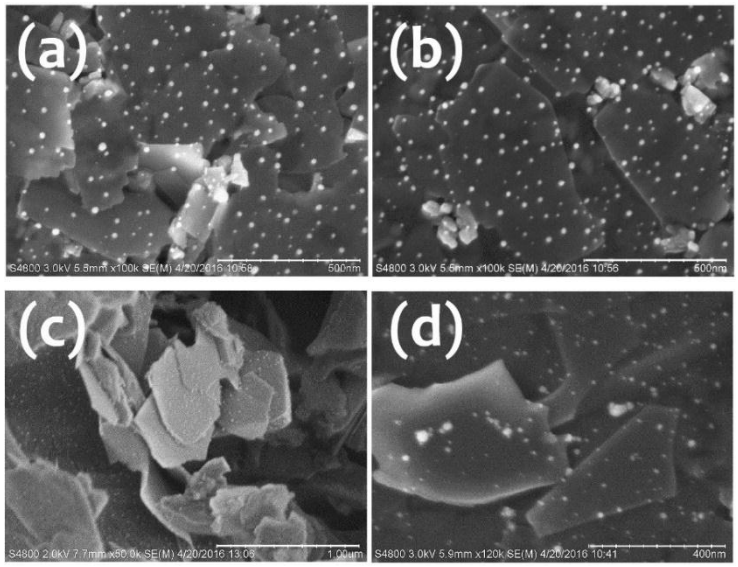

Figure 6- 5: FESEM images of (a,b) TBA-Fe NS and (c,d) TBA-Mn NS samples.

Post-exfoliation surface-modification of TBA-Fe and TBA-Mn nanosheets were perfomed using C_nH_{2n+1}-OH (n = 3, 5, and 10), C_nH_{2n+1}-NH_2 (n = 3, 6, and 8), C_7H_7-OH, and C_7H_7-NH_2 solvents, for introducing various linear/cyclic alcoxy and ammonium fanctionalities to these nanosheets. Figure 6-6 and 6-7 respectively present the XRD patterns of Fe NS and Mn NS hybrid nanosheets. In case of hybrid Fe NS, in some cases the first reflection is very weak (Figure 6-6 e and f) or even missing (Figure 6-6 b, h, and i), indicating a poorer reactivity for this type of metal oxide nanosheet as opposed to Mn NS (Figure 6-7) and PN NS (presented in chapter 4). Vibrational spectroscopy was carried out to evaluate the organic loading and the success of the surface-exchange reactions in case of these two classes of metal-oxide nanosheets. Figure 6-8 provides the Raman spectra of some of the hybrids obtained from Fe NS; the whole wavenumber range is presented in Figure 6-8a, and a smaller region was zoomed in b to highlight the bands pertinent to the organic groups. Two propoxy and propylammonium derivatives do not show alkane-related bands (marked with dashed square in Figure 6-8 b), which considering their previously presented XRD patterns (Figure 6-6 b and e) indicates a very low degree of organic loading, if any. However, the decent loading of the organic groups on the rest of the hybrids is supported via these Raman spectra—see the alkane-related bands in dashed square, as well as the peaks pertinent to the phenyl ring marked with solid traingles.[86] Raman spectroscopy was also investigated on hybrid Mn NSs. In this case, the laser beam in Raman seemed to interact unfavorably with this specific hosts and its derivatives, yielding a broad peak

that would shield all the important vibration bands. Therefore, IR spectroscopy was applied instead to study various vibrational modes expected for hybrid Mn NS (Figure 6-9). Despite better XRD patterns observed for hybrid Mn NS versus those of Fe NS, the quality of the IR spectra are in general poorer than the Raman, not indicative of better organic loading for the Mn derivatives as suggested by XRD (which is most likely instrumental). Based on the zoomed-in IR spectra presented in Figure 6-9b, the degree of organic loading in case of propylammonium, propoxy, and pentoxy derivatives is poor, while the other hybrids show the expected bands (the alkane-related peaks in dashed square, and the bands pertinent to the phenyl ring highlighted with solid traingles).[86]

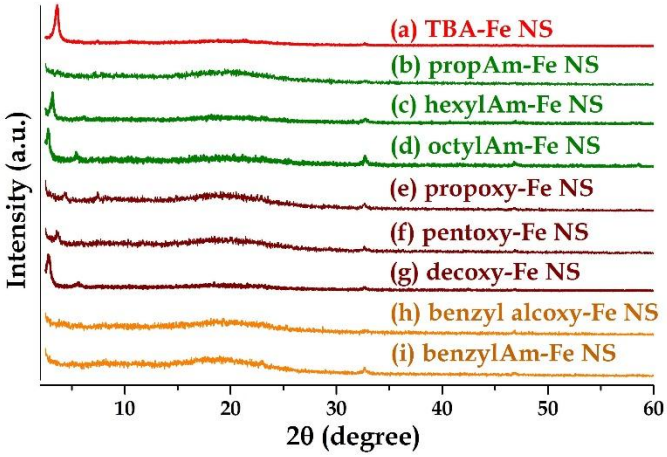

Figure 6- 6: XRD patterns of various hybrid Fe NS; (a) TBA-Fe, (b—d) C_nH_{2n+1}-Fe NS (n = 3, 5, and 10 in b, c, and d respectively), (e—g) C_nH_{2n+1}-NH_3^+-Fe NS (n = 3, 6, and 8 in e, f, and g respectively), (h) C_7H_7-Fe NS, and (i) C_7H_7-NH_3^+-Fe NS.

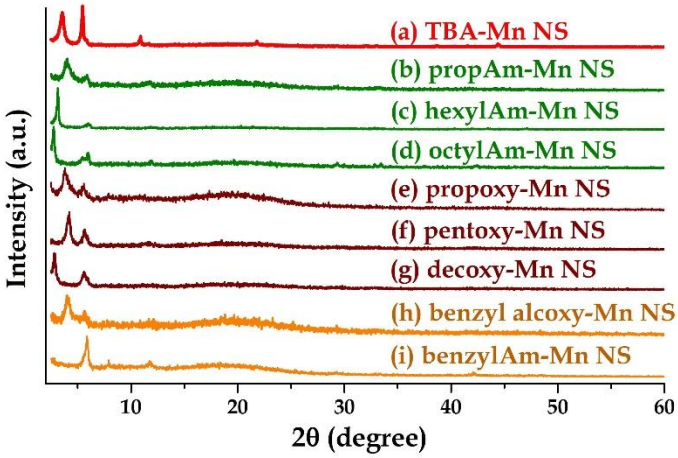

Figure 6- 7: XRD patterns of various hybrid Mn NS; (a) TBA-Mn, (b—d) C_nH_{2n+1}-Mn NS (n = 3, 5, and 10 in b, c, and d respectively), (e—g) C_nH_{2n+1}-NH_3^+-Mn NS (n = 3, 6, and 8 in e, f, and g respectively), (h) C_7H_7-Mn NS, and (i) C_7H_7-NH_3^+-Mn NS.

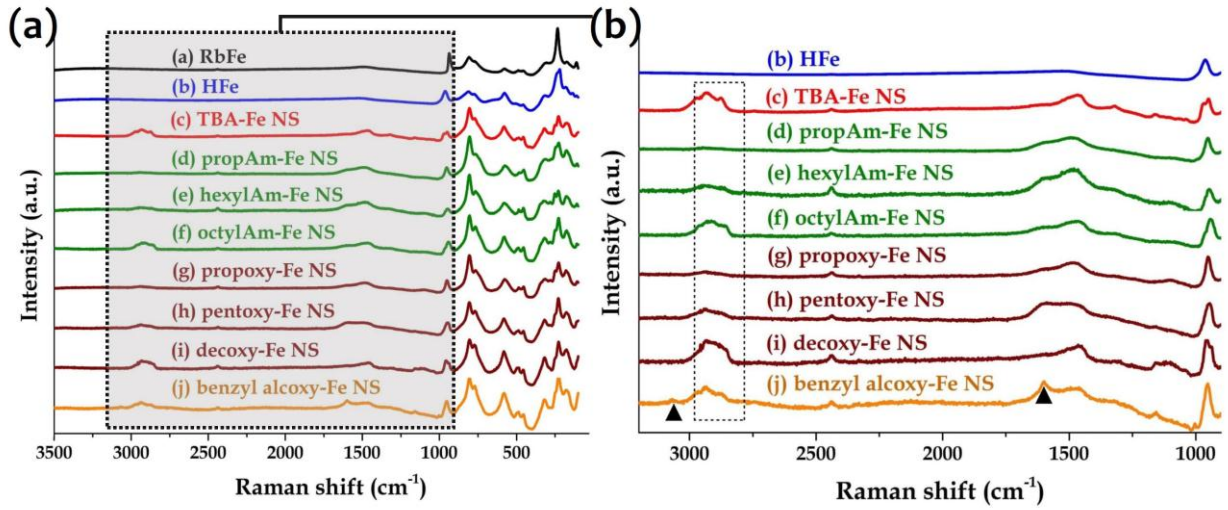

Figure 6- 8: Raman spectra of some hybrid Fe NS compared to their layered hosts; (a) layered $RbCa_2Nb_2FeO_9$, (b) layered $HCa_2Nb_2FeO_9$, and various hybrid Fe NS with TBA^+, $C_nH_{2n+1}NH_3^+$ (n = 3, 6, 8), C_nH_{2n+1}- (n = 3, 5, 10), and C_7H_7- surface groups respectively presented in (c—j). The spectra are provided in full range wavenumber in *a* and then zoomed in *b* (the peaks related to alkanes and phenyl groups are respectively highlighted with dashed square and solid traingles in *b*).

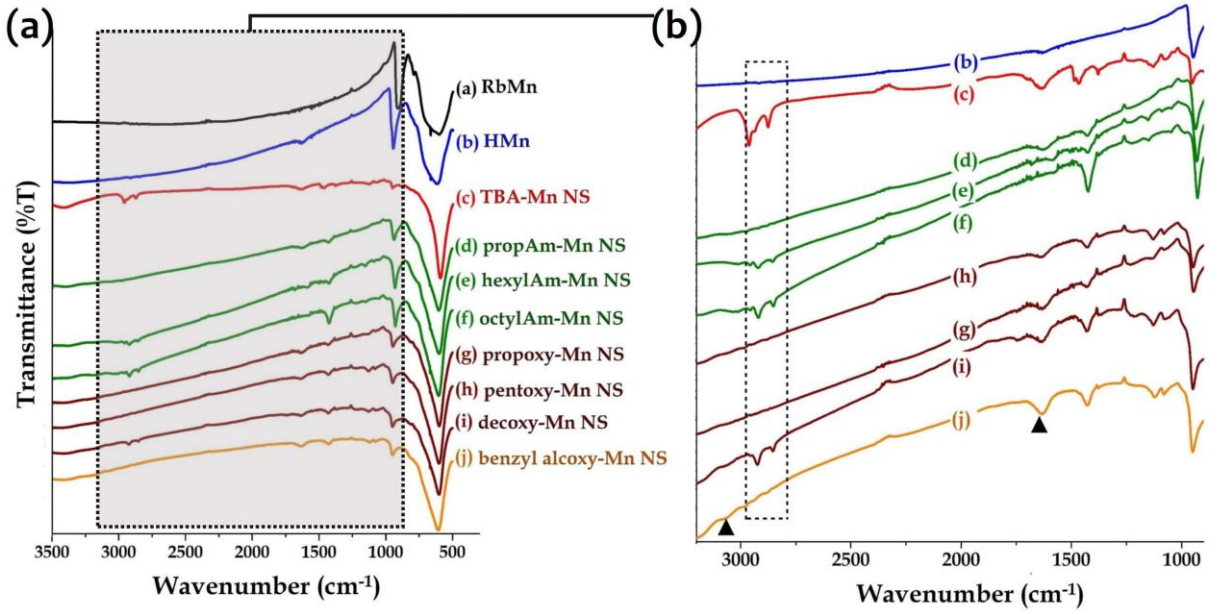

Figure 6- 9: IR transmittance spectra for various hybrid Mn NS versus their layered hosts provided in *a)* full-range wavenumber, as well as *b)* zoomed in region; (a) layered $RbLaCaNb_2MnO_{10}$, (b) layered $HLaCaNb_2MnO_{10}$, and various hybrid Mn NS with TBA^+, $C_nH_{2n+1}NH_3^+$ (n = 3, 6, 8), C_nH_{2n+1}- (n = 3, 5, 10), and C_7H_7- surface groups respectively presented in (c—j). The peaks related to alkanes and phenyl groups are respectively highlighted with dashed square and solid traingles in *b*.

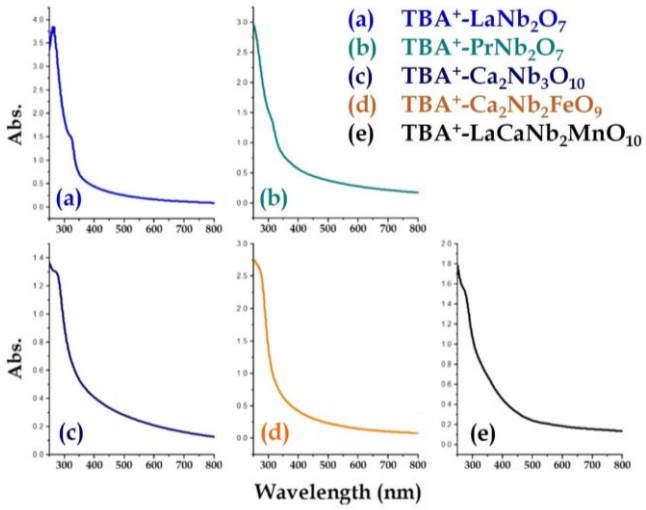

Figure 6- 10: Absorbance spectra of the dilute suspensions of the five NS; (a) TBA-LN, (b) TBA-PN, (c) TBA-CN, (d) TBA-Fe, and (e) TBA-Mn NS.

6.3.2 Optical Properties

6.3.2.1 TBA-Functionalized Nanosheets

The optical properties of TBA-PN, TBA-Fe, and TBA-Mn nanosheets were first evaluated in two different sets of experiments: 1) as-synthesized nanosheets were sonicated in a few drops of ethanol to form a very concentrated suspension. Then, using a very small portion of the concentrated batch, a very dilute suspension of each nanosheet was prepared for optical measurements by adding extra ethanol—*too dilute that the distinguished color of the nanosheets were no longer visible, and they all appeared transparent*, 2) thick films were prepared on quartz slides using the concentrated suspensions of the nanosheets (so-called "*reassembled nanocomposite thin films*"). The samples from these two preparation techniques are called "solution" and "solid" samples throughout the body and images presented later in. Absorbance, reflectance, and FL spectra are presented for solution and/or solid samples of these nanosheets, and compared to those of TBA-LN and TBA-CN nanosheets as known references. Figure 6-10 presents the absorbance spectra of the dilute suspensions of the five nanosheets, where very similar behavior is observed regardless of the elemental composition. However, the solid samples of the same nanosheets investigated via DRS show quite different responses as provided in Figure 6-11 (dashed patterns in case of b, d, and e show the spectra obtained for a replicate batch of each sample). To further clarify the impact of the elemental composition on the optical

properties exploiting the DRS results, the Tauc plot[87–90] was also obtained from the reflectance spectra. As proposed in the literature,[56] layered perovskites with indirect band gaps might change into direct band gaps after exfoliating into monolayers. However, sample preparation in form of thin film composites leads into restacked monolayers more likely to behave as indirect band gap materials again. Therefore, both direct and indirect band-gap estimations were taken into account providing the Tauc plots, respectively presented in Figures 6-12 and 6-13. In order to calculate the band-gap from the reflectance *(R)*, first *F(R)* is calculated based on the Kubelka–Munk function,[87,91] where $F(R) = \frac{(1-R)^2}{2R}$. The calculated *F(R)* can then replace α (absorption coefficient) in well-known Tauc-Davis-Mott formula; $(h\nu\alpha)^{1/n} = A\ (h\nu - Eg)$, where *h* is the Planck's constant, *v* is frequency, *Eg* is the band gap, *A* is the proportional constant, and *n* is 0.5 or 2 for direct and inderct band-gap materials, respectively.[87,91] The following Tauc plots, $(h\nu\alpha)^{1/n}$ for both n = 0.5 and 2, are provided versus *hv* (eV), calculated from hC/λ or simply $1239.7/\lambda$, where wavelength in nm is plugged in the equation. Using the Tauc plot, band gap can then be estimated similar to the literature.[9,28,92,93]

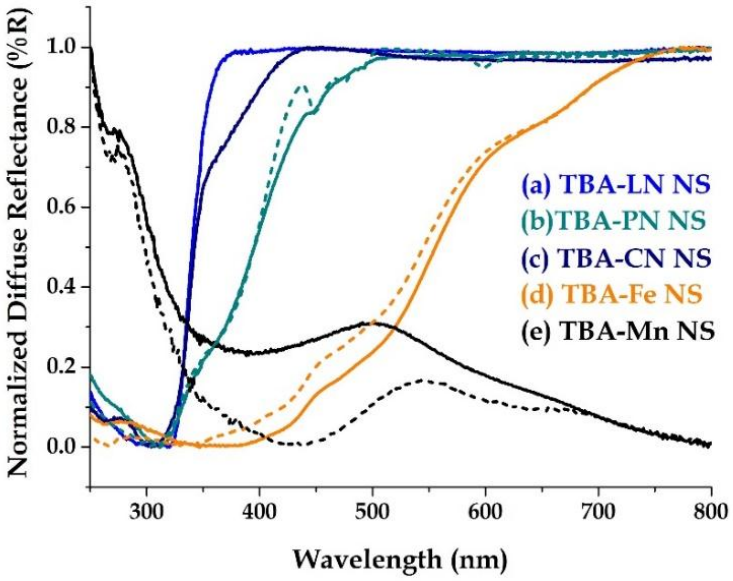

Figure 6- 11: Diffuse reflectance spectra of the five NS; (a) TBA-LN, (b) TBA-PN, (c) TBA-CN, (d) TBA-Fe, and (e) TBA-Mn NS. ***Dashed patterns in case of b, d, and e show the spectra obtained for a second batch of each sample.***

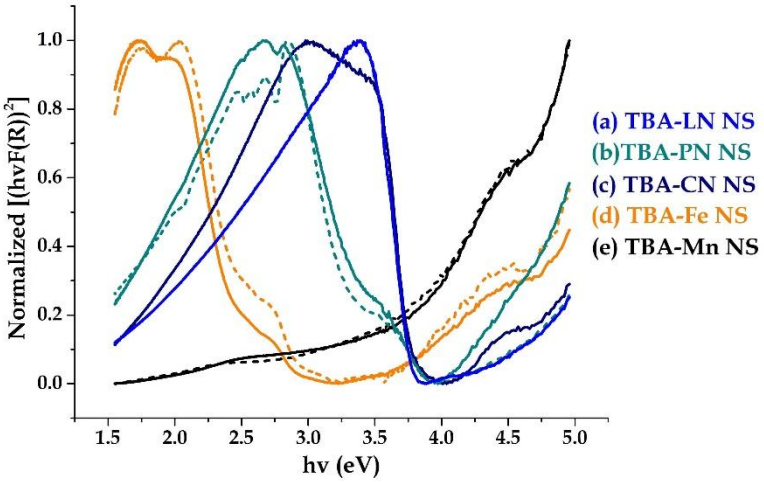

Figure 6- 12: Tauc plot considering a direct band gap; ($h\nu$F(R))^2 versus $h\nu$.

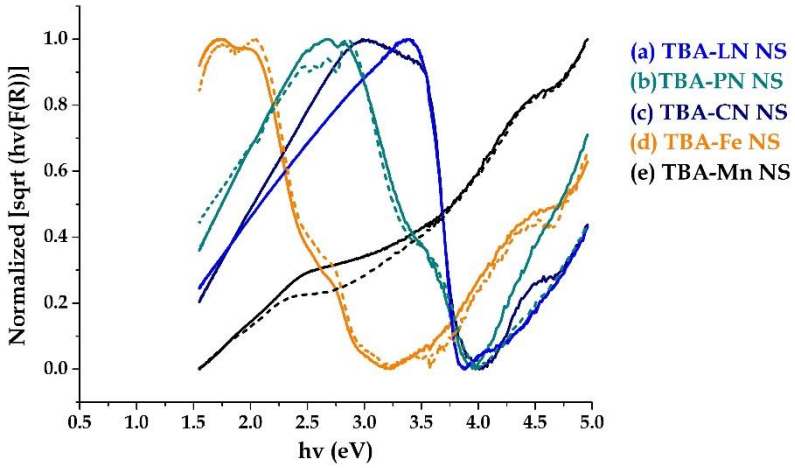

Figure 6- 13: Tauc plot considering an indirect band gap; ($h\nu$F(R))$^{1/2}$ versus $h\nu$.

The emission spectra of both solution and solid samples prepared from TBA-LN, TBA-PN, TBA-CN, TBA-Fe, and TBA-Mn NS were obtained via fluorescence spectroscopy with excitations at 250, 330, and 550 nm. The FL sectra obtained from dilute suspensions are presented in Figure 6-14, where the ones from the thin composite films are shown in Figure 6-15. *All the spectra are normalized in order to minimize the influence of the sample preparation on the optical responses.*

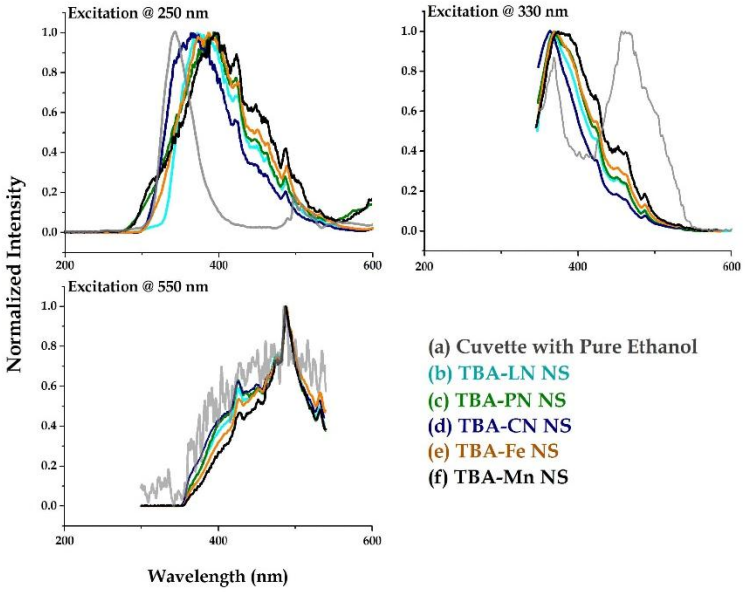

Figure 6- 14: Fluorescence spectra of solution samples prepared from TBA NS; emission spectra of (a) background—*cuvette filled with ethanol*, (b) TBA-LN, (c) TBA-PN, (d) TBA-CN, (e) TBA-Fe, and (f) TBA-Mn NS.

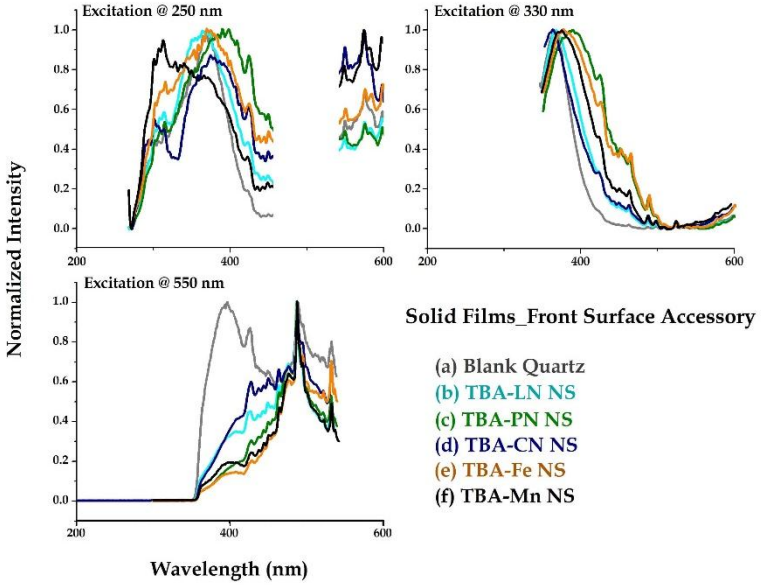

Figure 6- 15: Fluorescence spectra of solid films prepared from TBA NS; emission spectra of (a) background—*blank quartz slide*, (b) TBA-LN, (c) TBA-PN, (d) TBA-CN, (e) TBA-Fe, and (f) TBA-Mn NS.

Considering Figures 6-10, 6-11, 6-14, and 6-15, thin film composites better highlight the difference in the optical responses collected from TBA NS (as opposed to the dilute suspensions of the same samples). This observation was especially noticeable in case of DRS results. Thus, in

order to further investigate the impact of various organic functionalities on similar optical properties as those presented above, only solid samples were prepared and studied. In case of FL spectra, only excitation at 250 nm will be considered for various hybrid nanosheets to observe the influence of the organic functionalities on the emission response.

6.3.2.2 Various Hybrid $PrNb_2O_7$, $Ca_2Nb_2FeO_9$, and $LaCaNb_2MnO_{10}$ Nanosheets

Figures 6-16, 6-17, and 6-18 respectively provide the DRS results obtained for a number of hybrid PN, Fe, and Mn nanosheets. Hybrid Mn nanosheets show the highest dependance on the organic functionality, where the reflectance spectra obtained from various hybrid Fe nanosheets all superimpose, and in case of hybrid PN NS only one hybrid behaves differently from the others (benzyl alcoxy-PN NS).

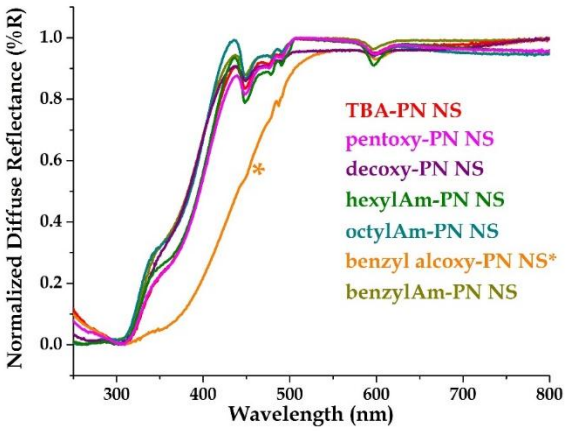

Figure 6- 16: DRS for various hybrid PN NS; TBA-PN, pentoxy-PN, decoxy-PN, hexylammonium-PN, octylammonium-PN, benzyl alcoxy-PN, and benzylammonium PN NS. Benzyl alcoxy-PN NS, marked with star, is the only hybrid responding different than the others.

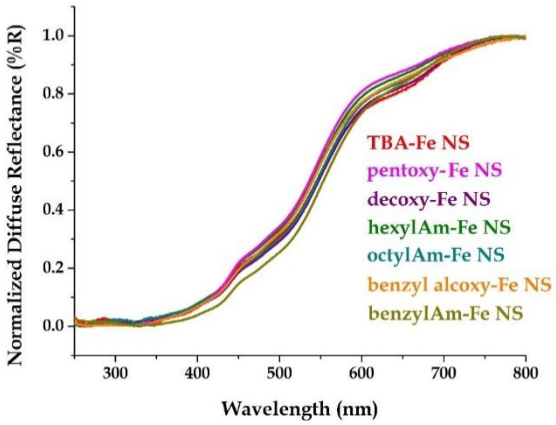

Figure 6- 17: DRS for various hybrid Fe NS; TBA-Fe, pentoxy-Fe, decoxy-Fe, hexylammonium-Fe, octylammonium-Fe, benzyl alcoxy-Fe, and benzylammonium-Fe NS, all superimposing.

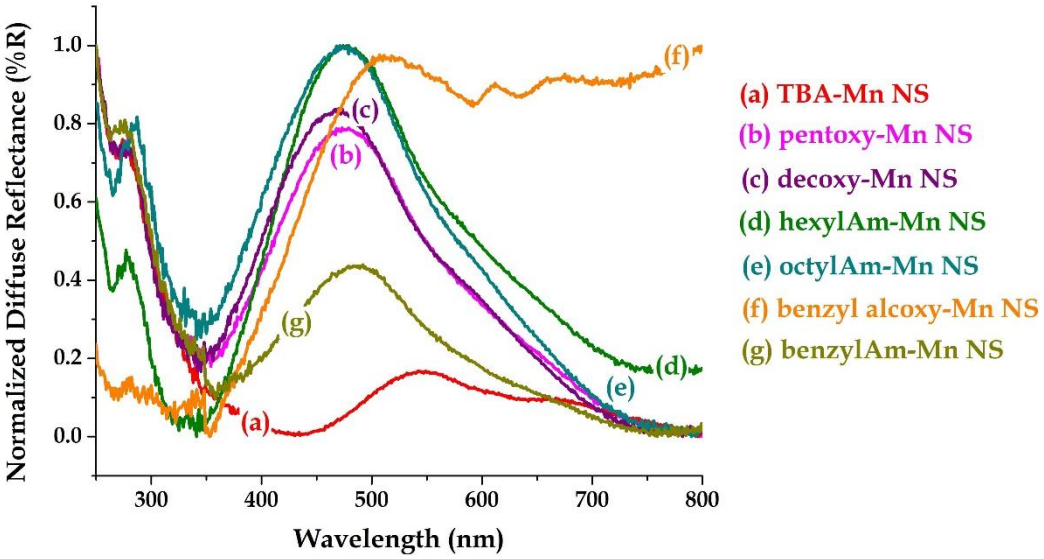

Figure 6- 18: DRS for various hybrid Mn NS; (a) TBA-Mn, (b) pentoxy-Mn, (c) decoxy-Mn, (d) hexylammonium-Mn, (e) octylammonium-Mn, (f) benzyl alcoxy-Mn, and (g) benzylammonium-Mn NS. Fine-tuning of the reflectance, and so the band gap, is possible by tailoring the surface groups.

Emission spectra at 250 nm-wavelength excitation were also collected for various hybrid PN, Fe, and Mn NS via fluorescence spectroscopy, and presented respectively in Figures 6-19, 6-20, and 6-21 below. The impact of the functionality in hybrid Mn nansheets is the most, and it mitigates as we go to Fe NS, and is the least in case of PN NS.

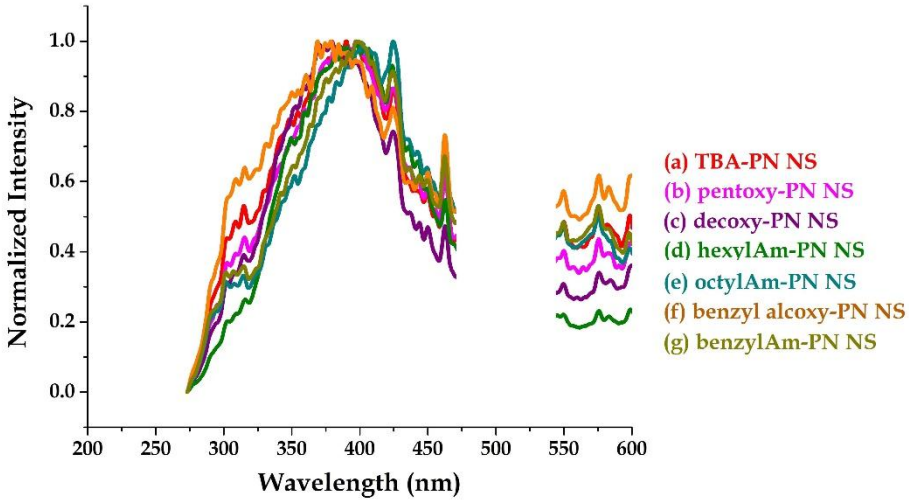

Figure 6- 19: FL spectra for various hybrid PN NS; (a) TBA-PN, (b) pentoxy-PN, (c) decoxy-PN, (d) hexylammonium-PN, (e) octylammonium-PN, (f) benzyl alcoxy-PN, and (g) benzylammonium-PN NS, showing the same emission at 250 nm excitation wavelength.

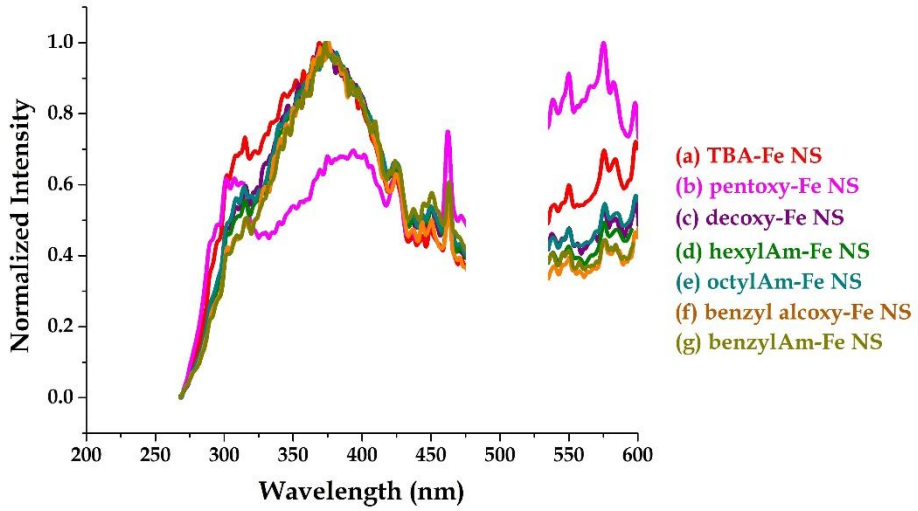

Figure 6- 20: FL spectra for various hybrid Fe NS; (a) TBA-Fe, (b) pentoxy-Fe, (c) decoxy-Fe, (d) hexylammonium-Fe, (e) octylammonium-Fe, (f) benzyl alcoxy-Fe, and (g) benzylammonium-Fe NS, showing the same emission at 250 nm excitation wavelength except for pentoxy hybrid (b).

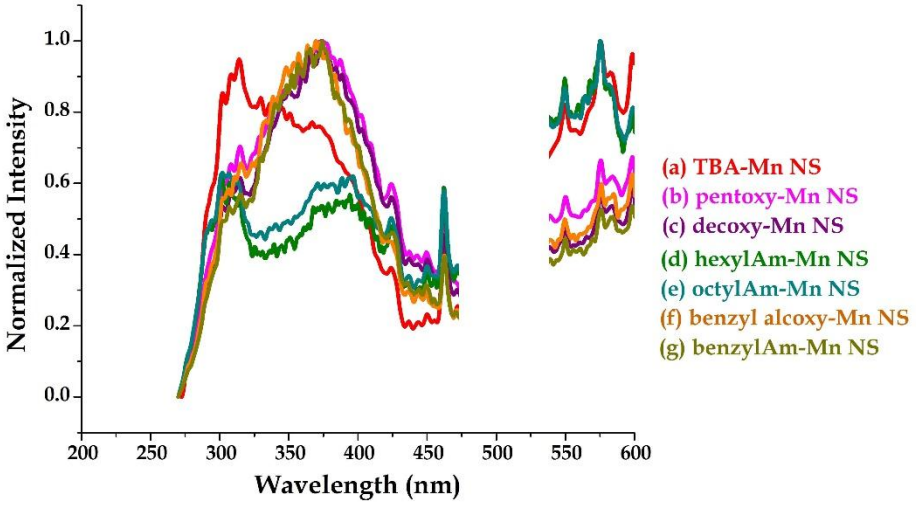

Figure 6- 21: FL spectra for various hybrid Mn NS, presenting the emission at 250 nm excitation wavelength; (a) TBA-Mn, (b) pentoxy-Mn, (c) decoxy-Mn, (d) hexylammonium-Mn, (e) octylammonium-Mn, (f) benzyl alcoxy-Mn, and (g) benzylammonium-Mn NS, the most-influenced emission spectra by the organic surface groups among the three classes of hybrid nanosheets.

6.4– Discussion

6.4.1 Formation of Hybrid Oxide Nanosheets

The main focus of this chapter was to investigate the impact of both elemental composition and the organic surface groups of hybrid metal-oxide nanosheets on their optical properties. In this regard, three DJ perovskites isostructural with well-known $HLaNb_2O_7$ and $HCa_2Nb_3O_{10}$ were selected, where the existance of an element with patially-filled *d/f* orbitals in *A* or *B* site of the $A_{n-1}B_nO_{3n+1}$ perovskite slab was ensured (n = 2 or 3 for double- and triple-layered hosts, respectively); Pr, Fe, and Mn in $HPrNb_2O_7$, $HCa_2Nb_2FeO_9$, and $HLaCaNb_2MnO_{10}$, respectively. Even though the impact of the elemental composition on photocatalytic activity, optical or electronic properties of some 2D materials has been studied before,[20,36,41,45,46,49–51] the influence of the functional groups on freestanding layers has not been investigated yet (possibly due to the limitation of the available experimental methods to freely tailor these surface groups as a post-exfoliation step).

The novel MA exfoliation and surface-modification techniques introduced in Chapter 4 for two double-layered DJ perovskites,[77] were successfully employed on triple-layered DJ hosts as well ($HCa_2Nb_2FeO_9$ and $HLaCaNb_2MnO_{10}$). Initially, the success of the MA exfoliation using TBAOH was confirmed for the new triple-layered hosts, using X-ray diffraction, as well as atomic force and electron microscopies (Figures 6-2, 6-3, 6-4, and 6-5). Intact exfoliation of the initial 3D-organization of the slabs into their freestanding 2D slabs is supported by the loss of crystalinity observed in the XRD patterns collected after delamination compared to those prior to the reaction (Figure 6-2), as well as the SAED patterns which approve of the maintained atomic order in each slab (Figure 6-3 inset). The formation of thin sheets is further confirmed by electron microscopy techniques (Figures 6-3 and 6-5), as well as observing at most twolayer-thick nanosheets in AFM profiles (Figure 6-4). Various organic derivatives of $Ca_2Nb_2FeO_9$ and $LaCaNb_2MnO_{10}$ nanosheets were then obtained similar to those of $PrNb_2O_7$ reported earlier.[77] In order to evaluate the organic loading in these post-exfoliation exchange reactions, XRD and vibrational spectroscopy were performed on the various nanosheet hybrids (provided in Figures 6-6, 6-7, 6-8, and 6-9). Despite high reactivity of the double-layered nanosheets with various organics observed for $LnNb_2O_7$ (Ln = La, Pr),[77] the reactivity of the triple-layereds are somewhat less. This is similar to the poorer reactivity of layered $HCa_2Nb_3O_{10}$ with alcohols observed in our

earlier work.[84] Even though the successful incorporation of n-propoxy and n-propylammonium surface groups remained questionable after XRD and vibrational spectroscopy, the rest of the hybrids were decent (n-pentoxy, n-decoxy, 1-hexylammonium, 1-octylammonium, benzyl alcoxy, and benzylammonium derivatives). In general, Mn NS showed better reactivty of the two triple-layereds studied here.

6.4.2 Optical Properties

6.4.2.1 TBA-Functionalized Nanosheets

The impact of the elemental composition of TBA-functionalized nanosheets on their reflectance and emission was studied by screening the five types of nanosheets in both solution and solid forms; TBA^+-$LaNb_2O_7$, TBA^+-$PrNb_2O_7$, TBA^+-$Ca_2Nb_3O_{10}$, TBA^+-$Ca_2Nb_2FeO_9$, and TBA^+-$LaCaNb_2MnO_{10}$. It is notable that PN, Fe and Mn NS all have different colors (green, orange, and black, respectively), as opposed to white LN and CN NS, which is a simple visual way to predict varying absorbance/reflectance behaviors for them. Dilute dispersions of these nanosheets in ethanol yielded very similar absorbance spectra (Figure 6-10), while the DRS performed on solid films showed quite different responses (Figure 6-11). It has been shown in the literature that the number of layers and their size quantization impact their band gap—band gap increasing as the number of monolayers decreases, for instance, bulk 3D hosts usually have a smaller band gap compared to their 2D exfoliated variations.[9,28,56,93] Other than the band gap energy, the type of the transmission also changes from indirect to direct when the dimensionality of a perovskite or layered material is decreased from three to two.[56] Based on these two general statements, we cannot confidently determine the type of the transition (direct or indirect) in restacked nanosheets; while being 2D strongly suggests a direct transition, formation of a restacked assembly might push it more towards an indirect type. Usually in case of absorbance studies, you can confidently take the exfoliated nanosheet as a direct-band gap, as you are studying a dispersion of monolayers. However, due to our focus on DRS of the thin composite films, we prefered to provide both forms of the Tauc-Davis-Mott formula; both $[h\nu(F(R))]^2$ and $[h\nu(F(R))]^{1/2}$ plotted versus $h\nu$, respectively, for direct and indirect-band gap materials, in Figures 6-12 and 6-13. The next important item to determine is "the point of inflection" – the maximum points of the first derivative of the Tauc plot.[87] Then, a line should be drawn tangent to the curve at the point of inflection, whose intersection with x axis ($h\nu$) will give the band gap

value (*Eg*). Band gap energy values for exfoliated $LaTa_2O_7$ and $Ca_2Nb_3O_{10}$ are respectively reported as 4.2 and 3.45 eV,[9,28] suggesting that the point of inflection should be on the linear portion of the $[hv(F(R))]^{1/n}$ plots for *hv* values greater than about 3 eV. However, the Eg of TBA-LN NS is estimated to be smaller than that of CN NS when the linear portion in 4-5 eV is considered (either with direct or indirect relationship), and almost equal when the linear portion in 3.5-4 eV is extended to the horizontal *hv* axis. In both cases, the triple-layered NSs do not yield a smaller Eg value as expected.[9,28,56,93] Despite this uncertainty on reporting definite Eg values for these nanosheets, their reflectance is obviously different due to their different elemental composition, most likely resulting from different band gaps.

The emission spectra of five TBA-functionalized nanosheets in solution are presented in Figure 6-14, compared with the blank run presented in light grey (quartz filled with pure ethanol). When excited at 250 nm (a), the maximum emission wavelength seems to slightly shift among the five samples; least for TBA-CN NS (370 nm) and highest for TBA-Mn NS (400 nm), with almost the same broadness of the emission peak. In case of excitation at 330 nm (b), the same order is observed, however, the range of shifting is narrower (about 390 to 400 nm). For 550 nm excitation (c), the maximum of all five nanosheets overlap, while their lower-wavelength tail shows various intensities for different types (most intense for TBA-CN and least for TBA-Mn NS, in other words, the emission peak at this wavelength is somewhat narrowest for TBA-Mn NS, and broadest for TBA-CN NS). The same examination was performed on the solid films prepared from the same samples (Figure 6-15). The shapes and maxima of the emission peaks for 250 nm excitation showed a wider variation among the solid samples (a). In case of excitations at 330 nm (b), a slight shift was again observed for the maxima of the emission peaks of the five samples (from 370 to 400 nm), where TBA-CN again had the lowest wavelength for its maximum, but this time TBA-PN showed the highest. The emission spectra for 550 nm excitation (c) showed overlapping broad peaks with a maximum similar to that of the solution samples. Again, the TBA-Mn sample yielded the narrowest peak, and TBA-CN the broadest (the difference in broadness was more significant in case of solid samples though). As most noticeable changes among different samples was observed in solid samples and at an excitation wavelength of 250 nm, different hybrid derivatives of PN, Fe, and Mn nanosheets were only plotted for this specific condition. Other than investigating the emission behavior using FL,

excitation spectra of various emission wavelengths were also studied for all the samples. However, due to very similar spectra obtained for these trials, they were not included in the results.

6.4.2.2 Various Hybrid $PrNb_2O_7$, $Ca_2Nb_2FeO_9$, and $LaCaNb_2MnO_{10}$ Nanosheets

DRS results for various PN, Fe, and Mn hybrids were presented on Figures 6-16, 6-17, and 6-18, respectively, showing the most significant impact of the functional groups among different derivatives of the Mn NS. According to Figure 6-18 (representing the DRS results for Mn NS hybrids), the reflectance at about 500 nm gradually increases in its relative intensity as TBA^+ is exchanged with benzylammonium, n-alkyl alcoxy, and n-alkylammonium groups. The benzyl alcoxy surface group also causes the most dramatic change in the absorbance behavior of Mn NS by changing the shape of the spectra (Figure 6-18f). Considering that benzyl alcoxy is the only organic that has an influence on the absorbance of hybrid PN NS (Figure 6-16), this surface group seems to have the most significant impact in cases that the absorbance is relatively dependant on the surface groups (here in case of Mn and PN NSs).

Considering the emission spectra of these three classes of hybrid nanosheets in Figures 6-19, 6-20, and 6-21, Mn NS again show the most dependance on the organic groups in their emission spectra collected at 250 nm excitation. Despite the strong emission of TBA-Mn NS at both 300 and 550 nm, the maximum emission of benzyl alcoxy-, benzylammonium-, pentoxy-, and decoxy-Mn NS is at about 380 nm, and for the two n-alkyl ammonium derivatives appears at about 550 nm (Figure 6-21).

Variations of organic surface groups seemed to have minimal impact on the optical properties of hybrid Fe and PN nanosheets. Conversely, fine tuning of the reflectance/emission spectra of Mn hybrids was possible by changing the surface groups.

6.5– Conclusions

A series of novel functionalized metal-oxide nanosheets were obtained from double- and triple-layered Dion-Jacobson perovskites; $HPrNb_2O_7$, $HCa_2Nb_2FeO_9$, and $HLaCaNb_2MnO_{10}$. Rapid microwave-assisted reactions were used to efficiently fabricate organic-inorganic nanostructures with controlled elemental composition, thickness, and surface groups. The optical properties, absorbance and emission behavior, of the various hybrid nanosheets were then

studied as a function of the elemental composition and the organic surface groups for both dispersed nanosheets and reassembled nanocomposite thin films. Studying the dispersed host nanosheets (TBA^+-$PrNb_2O_7$, TBA^+-$Ca_2Nb_2FeO_9$, and TBA^+-$LaCaNb_2MnO_{10}$) tended to exhibit similar optical properties, where nanocomposite films from the same samples showed a more noticeable variation versus the elemental composition of the nanosheets. The optical properties of various hybrid nanosheets were then investigated as a function of the organic surface groups for *nanocomposite films* prepared from n-pentoxy, n-decoxy, 1-hexylammonium, 1-octylammonium, benzyl alcoxy, and benzylammonium derivatives of all three types of $PrNb_2O_7$, $Ca_2Nb_2FeO_9$, and $LaCaNb_2MnO_{10}$ nanosheets. Diffuse reflectance and fluorescence spectra of the $LaCaNb_2MnO_{10}$ hybrid nanosheets changed the most under the impact of their organic surface groups, conversely, the emission of various $PrNb_2O_7$ hybrid nanosheets and the absorbance of $Ca_2Nb_2FeO_9$ hybrid nanosheets showed almost no dependance on their organic surface groups.

6.6– References

(1) Coleman, J. N.; Lotya, M.; O'Neill, A.; Bergin, S. D.; King, P. J.; Khan, U.; Young, K.; Gaucher, A.; De, S.; Smith, R. J.; et al. Two-Dimensional Nanosheets Produced by Liquid Exfoliation of Layered Materials. *Science* **2011**, *331* (6017), 568–571.

(2) Nicolosi, V.; Chhowalla, M.; Kanatzidis, M. G.; Strano, M. S.; Coleman, J. N. Liquid Exfoliation of Layered Materials. *Science* **2013**, *340* (6139), 1226419–1226419.

(3) Gupta, A.; Sakthivel, T.; Seal, S. Recent Development in 2D Materials beyond Graphene. *Prog. Mater. Sci.* **2015**, *73*, 44–126.

(4) Tahara, S.; Takeda, Y.; Sugahara, Y. Preparation of Organic−Inorganic Hybrids Possessing Nanosheets with Perovskite-Related Structures via Exfoliation during a Sol−Gel Process. *Chem. Mater.* **2005**, *17* (24), 6198–6204.

(5) Tahara, S.; Okamoto, T.; Sugahara, Y. Preparation of a Nanocomposite Consisting of a Siloxane Network and Perovskite-Related Nanosheets via a Sol–gel Process. *Sci. Technol. Adv. Mater.* **2006**, *7* (5), 446–450.

(6) Idota, N.; Fukuda, S.; Tsukahara, T.; Sugahara, Y. Preparation of Thermoresponsive Nanosheets Exhibiting Phase Transitions in Water via Surface Modification of Layered Perovskite Nanosheets with Poly(*N*-Isopropylacrylamide) (PNIPAAm). *Chem. Lett.* **2015**, *44* (2), 203–205.

(7) Geng, F.; Ma, R.; Ebina, Y.; Yamauchi, Y.; Miyamoto, N.; Sasaki, T. Gigantic Swelling of Inorganic Layered Materials: A Bridge to Molecularly Thin Two-Dimensional Nanosheets. *J. Am. Chem. Soc.* **2014**, *136* (14), 5491–5500.

(8) Maluangnont, T.; Matsuba, K.; Geng, F.; Ma, R.; Yamauchi, Y.; Sasaki, T. Osmotic Swelling of Layered Compounds as a Route to Producing High-Quality Two-

Dimensional Materials. A Comparative Study of Tetramethylammonium versus Tetrabutylammonium Cation in a Lepidocrocite-Type Titanate. *Chem. Mater.* **2013**, *25* (15), 3137–3146.

(9) Han, Y.-S.; Park, I.; Choy, J.-H. Exfoliation of Layered Perovskite, $KCa_2Nb_3O_{10}$,into Colloidal Nanosheets by a Novel Chemical Process. *J. Mater. Chem.* **2001**, *11* (4), 1277–1282.

(10) Schaak, R. E.; Mallouk, T. E. Prying Apart Ruddlesden−Popper Phases: Exfoliation into Sheets and Nanotubes for Assembly of Perovskite Thin Films. *Chem. Mater.* **2000**, *12* (11), 3427–3434.

(11) Ida, S.; Ogata, C.; Unal, U.; Izawa, K.; Inoue, T.; Altuntasoglu, O.; Matsumoto, Y. Preparation of a Blue Luminescent Nanosheet Derived from Layered Perovskite $Bi_2SrTa_2O_9$. *J. Am. Chem. Soc.* **2007**, *129* (29), 8956–8957.

(12) Osada, M.; Sasaki, T. Exfoliated Oxide Nanosheets: New Solution to Nanoelectronics. *J. Mater. Chem.* **2009**, *19* (17), 2503.

(13) Bizeto, M. A.; Shiguihara, A. L.; Constantino, V. R. L. Layered Niobate Nanosheets: Building Blocks for Advanced Materials Assembly. *J. Mater. Chem.* **2009**, *19* (17), 2512.

(14) Butler, S. Z.; Hollen, S. M.; Cao, L.; Cui, Y.; Gupta, J. A.; Gutiérrez, H. R.; Heinz, T. F.; Hong, S. S.; Huang, J.; Ismach, A. F.; et al. Progress, Challenges, and Opportunities in Two-Dimensional Materials Beyond Graphene. *ACS Nano* **2013**, *7* (4), 2898–2926.

(15) Ma, R.; Sasaki, T. Nanosheets of Oxides and Hydroxides: Ultimate 2D Charge-Bearing Functional Crystallites. *Adv. Mater.* **2010**, *22* (45), 5082–5104.

(16) Smith, R. J.; King, P. J.; Lotya, M.; Wirtz, C.; Khan, U.; De, S.; O'Neill, A.; Duesberg, G. S.; Grunlan, J. C.; Moriarty, G.; et al. Large-Scale Exfoliation of Inorganic Layered Compounds in Aqueous Surfactant Solutions. *Adv. Mater.* **2011**, *23* (34), 3944–3948.

(17) Takagaki, A.; Sugisawa, M.; Lu, D.; Kondo, J. N.; Hara, M.; Domen, K.; Hayashi, S. Exfoliated Nanosheets as a New Strong Solid Acid Catalyst. *J. Am. Chem. Soc.* **2003**, *125* (18), 5479–5485.

(18) Shibata, T.; Takano, H.; Ebina, Y.; Kim, D. S.; Ozawa, T. C.; Akatsuka, K.; Ohnishi, T.; Takada, K.; Kogure, T.; Sasaki, T. Versatile van Der Waals Epitaxy-like Growth of Crystal Films Using Two-Dimensional Nanosheets as a Seed Layer: Orientation Tuning of SrTiO3 Films along Three Important Axes on Glass Substrates. *J Mater Chem C* **2014**, *2* (3), 441–449.

(19) Chen, Y.; Zhao, X.; Ma, H.; Ma, S.; Huang, G.; Makita, Y.; Bai, X.; Yang, X. Structure and Dehydration of Layered Perovskite Niobate with Bilayer Hydrates Prepared by Exfoliation/self-Assembly Process. *J. Solid State Chem.* **2008**, *181* (7), 1684–1694.

(20) Ida, S.; Okamoto, Y.; Matsuka, M.; Hagiwara, H.; Ishihara, T. Preparation of Tantalum-Based Oxynitride Nanosheets by Exfoliation of a Layered Oxynitride, $CsCa_2Ta_3O_{10-x}N_y$, and Their Photocatalytic Activity. *J. Am. Chem. Soc.* **2012**, *134* (38), 15773–15782.

(21) Schaak, R. E.; Mallouk, T. E. Self-Assembly of Tiled Perovskite Monolayer and Multilayer Thin Films. *Chem. Mater.* **2000**, *12* (9), 2513–2516.

(22) Sasaki, T.; Watanabe, M.; Hashizume, H.; Yamada, H.; Nakazawa, H. Macromolecule-like Aspects for a Colloidal Suspension of an Exfoliated Titanate. Pairwise Association

of Nanosheets and Dynamic Reassembling Process Initiated from It. *J. Am. Chem. Soc.* **1996**, *118* (35), 8329–8335.

(23) Schaak, R. E.; Mallouk, T. E. Exfoliation of Layered Rutile and Perovskite Tungstates. *Chem. Commun.* **2002**, No. 7, 706–707.

(24) Allen, M. R.; Thibert, A.; Sabio, E. M.; Browning, N. D.; Larsen, D. S.; Osterloh, F. E. Evolution of Physical and Photocatalytic Properties in the Layered Titanates $A_2Ti_4O_9$ (A = K, H) and in Nanosheets Derived by Chemical Exfoliation †. *Chem. Mater.* **2010**, *22* (3), 1220–1228.

(25) Takagaki, A.; Tagusagawa, C.; Hayashi, S.; Hara, M.; Domen, K. Nanosheets as Highly Active Solid Acid Catalysts for Green Chemical Syntheses. *Energy Env. Sci* **2010**, *3* (1), 82–93.

(26) Wang, T.; Henderson, C. N.; Draskovic, T. I.; Mallouk, T. E. Synthesis, Exfoliation, and Electronic/Protonic Conductivity of the Dion–Jacobson Phase Layer Perovskite $HLa_2TiTa_2O_{10}$. *Chem. Mater.* **2014**, *26* (2), 898–906.

(27) Treacy, M. M. J.; Rice, S. B.; Jacobson, A. J.; Lewandowski, J. T. Electron Microscopy Study of Delamination in Dispersions of the Perovskite-Related Layered Phases K $[Ca_2Na_{n-3}Nb_nO_{3n-1}]$: Evidence for Single-Layer Formation. *Chem. Mater.* **1990**, *2* (3), 279–286.

(28) Lee, W.-J.; Yeo, H. J.; Kim, D.-Y.; Paek, S.-M.; Kim, Y.-I. Exfoliation of Dion-Jacobson Layered Perovskite into Macromolecular Nanoplatelet. *Bull. Korean Chem. Soc.* **2013**, *34* (7), 2041–2043.

(29) Li, B.-W.; Osada, M.; Ebina, Y.; Akatsuka, K.; Fukuda, K.; Sasaki, T. High Thermal Robustness of Molecularly Thin Perovskite Nanosheets and Implications for Superior Dielectric Properties. *ACS Nano* **2014**, *8* (6), 5449–5461.

(30) Compton, O. C.; Osterloh, F. E. Niobate Nanosheets as Catalysts for Photochemical Water Splitting into Hydrogen and Hydrogen Peroxide. *J. Phys. Chem. C* **2009**, *113* (1), 479–485.

(31) Kikuta, K.; Noda, K.; Okumura, S.; Yamaguchi, T.; Hirano, S. Orientation Control of Perovskite Thin Films on Glass Substrates by the Application of a Seed Layer Prepared from Oxide Nanosheets. *J. Sol-Gel Sci. Technol.* **2007**, *42* (3), 381–387.

(32) Zhao, J.; Osterloh, F. E. Photochemical Charge Separation in Nanocrystal Photocatalyst Films: Insights from Surface Photovoltage Spectroscopy. *J. Phys. Chem. Lett.* **2014**, *5* (5), 782–786.

(33) Ida, S.; Ishihara, T. Recent Progress in Two-Dimensional Oxide Photocatalysts for Water Splitting. *J. Phys. Chem. Lett.* **2014**, *5* (15), 2533–2542.

(34) Suzuki, H.; Tomita, O.; Higashi, M.; Abe, R. Two-Step Photocatalytic Water Splitting into H_2 and O_2 Using Layered Metal Oxide $KCa_2Nb_3O_{10}$ and Its Derivatives as O_2 Evolving Photocatalysts with IO_3^-/I^- or Fe^{3+}/Fe^{2+} Redox Mediator. *Catal Sci Technol* **2015**, *5* (5), 2640–2648.

(35) Maeda, K.; Sahara, G.; Eguchi, M.; Ishitani, O. Hybrids of a Ruthenium(II) Polypyridyl Complex and a Metal Oxide Nanosheet for Dye-Sensitized Hydrogen Evolution with Visible Light: Effects of the Energy Structure on Photocatalytic Activity. *ACS Catal.* **2015**, *5* (3), 1700–1707.

(36) Ida, S.; Ogata, C.; Eguchi, M.; Youngblood, W. J.; Mallouk, T. E.; Matsumoto, Y. Photoluminescence of Perovskite Nanosheets Prepared by Exfoliation of Layered Oxides, $K_2Ln_2Ti_3O_{10}$, $KLnNb_2O_7$, and $RbLnTa_2O_7$ (Ln: Lanthanide Ion). *J. Am. Chem. Soc.* **2008**, *130* (22), 7052–7059.

(37) Ebina, Y.; Akatsuka, K.; Fukuda, K.; Sasaki, T. Synthesis and In Situ X-Ray Diffraction Characterization of Two-Dimensional Perovskite-Type Oxide Colloids with a Controlled Molecular Thickness. *Chem. Mater.* **2012**, *24* (21), 4201–4208.

(38) Tanimaa, K.; Watanabeb, M.; Imanaria, Y.; Kameia, S.; Uematsub, K.; Ishigakic, T.; Todaa, K.; Satob, M.; Masakid, T.; Yoond, D. H. Research on New Precursor for Nanosheets Phosphors. *J. Ceram. Process. Res.* **2013**, *14*, S71–S73.

(39) Ebina, Y.; Sasaki, T.; Harada, M.; Watanabe, M. Restacked Perovskite Nanosheets and Their Pt-Loaded Materials as Photocatalysts. *Chem. Mater.* **2002**, *14* (10), 4390–4395.

(40) Wu, X.; Fei, F.; Chen, Z.; Su, W.; Cui, Z. A New Nanocomposite Dielectric Ink and Its Application in Printed Thin-Film Transistors. *Compos. Sci. Technol.* **2014**, *94*, 117–122.

(41) Takei, T.; Muraki, N.; Xu, N.; Miura, A.; Kumada, N. Anodic Hybridization of Fluorinated Layered Perovskite Nanosheet with Polyaniline for Electrochemical Capacitor. *Colloids Surf. Physicochem. Eng. Asp.* **2014**, *459*, 186–193.

(42) Asai, Y.; Ariake, Y.; Saito, H.; Idota, N.; Matsukawa, K.; Nishino, T.; Sugahara, Y. Layered Perovskite Nanosheets Bearing Fluoroalkoxy Groups: Their Preparation and Application in Epoxy-Based Hybrids. *RSC Adv.* **2014**, *4* (51), 26932.

(43) Ida, S. Development of Light Energy Conversion Materials Using Two-Dimensional Inorganic Nanosheets. *Bull. Chem. Soc. Jpn.* **2015**, *88* (12), 1619–1628.

(44) Li, B.-W.; Osada, M.; Ozawa, T. C.; Ebina, Y.; Akatsuka, K.; Ma, R.; Funakubo, H.; Sasaki, T. Engineered Interfaces of Artificial Perovskite Oxide Superlattices *via* Nanosheet Deposition Process. *ACS Nano* **2010**, *4* (11), 6673–6680.

(45) Kobayashi, Y.; Tian, M.; Eguchi, M.; Mallouk, T. E. Ion-Exchangeable, Electronically Conducting Layered Perovskite Oxyfluorides. *J. Am. Chem. Soc.* **2009**, *131* (28), 9849–9855.

(46) Ida, S.; Okamoto, Y.; Koga, S.; Hagiwara, H.; Ishihara, T. Black-Colored Nitrogen-Doped Calcium Niobium Oxide Nanosheets and Their Photocatalytic Properties under Visible Light Irradiation. *RSC Adv.* **2013**, *3* (29), 11521.

(47) Mitzi, D. B. Synthesis, Crystal Structure, and Optical and Thermal Properties of $(C_4H_9NH_3)_2MI_4$ (M = Ge, Sn, Pb). *Chem. Mater.* **1996**, *8* (3), 791–800.

(48) Mitzi, D. B.; Chondroudis, K.; Kagan, C. R. Organic-Inorganic Electronics. *IBM J. Res. Dev.* **2001**, *45* (1), 29–45.

(49) Nair, R. R.; Ren, W.; Jalil, R.; Riaz, I.; Kravets, V. G.; Britnell, L.; Blake, P.; Schedin, F.; Mayorov, A. S.; Yuan, S.; et al. Fluorographene: A Two-Dimensional Counterpart of Teflon. *Small* **2010**, *6* (24), 2877–2884.

(50) Wang, H.; Liu, F.; Fu, W.; Fang, Z.; Zhou, W.; Liu, Z. Two-Dimensional Heterostructures: Fabrication, Characterization, and Application. *Nanoscale* **2014**, *6* (21), 12250–12272.

(51) Liu, Z.; Ma, R.; Ebina, Y.; Iyi, N.; Takada, K.; Sasaki, T. General Synthesis and Delamination of Highly Crystalline Transition-Metal-Bearing Layered Double Hydroxides. *Langmuir* **2007**, *23* (2), 861–867.

(52) Ziegler, C.; Werner, S.; Bugnet, M.; Wörsching, M.; Duppel, V.; Botton, G. A.; Scheu, C.; Lotsch, B. V. Artificial Solids by Design: Assembly and Electron Microscopy Study of Nanosheet-Derived Heterostructures. *Chem. Mater.* **2013**, *25* (24), 4892–4900.

(53) Long, M.; Liu, E.; Wang, P.; Gao, A.; Xia, H.; Luo, W.; Wang, B.; Zeng, J.; Fu, Y.; Xu, K.; et al. Broadband Photovoltaic Detectors Based on an Atomically Thin Heterostructure. *Nano Lett.* **2016**, *16* (4), 2254–2259.

(54) Wang, H.; Liu, F.; Fu, W.; Fang, Z.; Zhou, W.; Liu, Z. Two-Dimensional Heterostructures: Fabrication, Characterization, and Application. *Nanoscale* **2014**, *6* (21), 12250–12272.

(55) Le, N. B.; Huan, T. D.; Woods, L. M. Interlayer Interactions in van Der Waals Heterostructures: Electron and Phonon Properties. *ACS Appl. Mater. Interfaces* **2016**, *8* (9), 6286–6292.

(56) Xia, F.; Wang, H.; Xiao, D.; Dubey, M.; Ramasubramaniam, A. Two-Dimensional Material Nanophotonics. *Nat. Photonics* **2014**, *8* (12), 899–907.

(57) Zhang, H. Ultrathin Two-Dimensional Nanomaterials. *ACS Nano* **2015**, *9* (10), 9451–9469.

(58) Geim, A. K.; Grigorieva, I. V. Van Der Waals Heterostructures. *Nature* **2013**, *499* (7459), 419–425.

(59) Lotsch, B. V. Vertical 2D Heterostructures. *Annu. Rev. Mater. Res.* **2015**, *45* (1), 85–109.

(60) Akatsuka, K.; Takanashi, G.; Ebina, Y.; Haga, M.; Sasaki, T. Electronic Band Structure of Exfoliated Titanium- And/or Niobium-Based Oxide Nanosheets Probed by Electrochemical and Photoelectrochemical Measurements. *J. Phys. Chem. C* **2012**, *116* (23), 12426–12433.

(61) Zhang, Y.; Ugeda, M. M.; Jin, C.; Shi, S.-F.; Bradley, A. J.; Martín-Recio, A.; Ryu, H.; Kim, J.; Tang, S.; Kim, Y.; et al. Electronic Structure, Surface Doping, and Optical Response in Epitaxial WSe_2 Thin Films. *Nano Lett.* **2016**, *16* (4), 2485–2491.

(62) Li, L.; Ma, R.; Ebina, Y.; Fukuda, K.; Takada, K.; Sasaki, T. Layer-by-Layer Assembly and Spontaneous Flocculation of Oppositely Charged Oxide and Hydroxide Nanosheets into Inorganic Sandwich Layered Materials. *J. Am. Chem. Soc.* **2007**, *129* (25), 8000–8007.

(63) Sasaki, T. Fabrication of Nanostructured Functional Materials Using Exfoliated Nanosheets as a Building Block. *J. Ceram. Soc. Jpn.* **2007**, *115* (1337), 9–16.

(64) Borges, J.; Mano, J. F. Molecular Interactions Driving the Layer-by-Layer Assembly of Multilayers. *Chem. Rev.* **2014**, *114* (18), 8883–8942.

(65) Ma, R.; Sasaki, T. Organization of Artificial Superlattices Utilizing Nanosheets as a Building Block and Exploration of Their Advanced Functions. *Annu. Rev. Mater. Res.* **2015**, *45* (1), 111–127.

(66) Osada, M.; Sasaki, T. Exfoliated Oxide Nanosheets: New Solution to Nanoelectronics. *J. Mater. Chem.* **2009**, *19* (17), 2503.

(67) Park, J. S.; Cho, S. M.; Kim, W.-J.; Park, J.; Yoo, P. J. Fabrication of Graphene Thin Films Based on Layer-by-Layer Self-Assembly of Functionalized Graphene Nanosheets. *ACS Appl. Mater. Interfaces* **2011**, *3* (2), 360–368.

(68) Wang, Y.; Tong, S. W.; Xu, X. F.; Özyilmaz, B.; Loh, K. P. Interface Engineering of Layer-by-Layer Stacked Graphene Anodes for High-Performance Organic Solar Cells. *Adv. Mater.* **2011**, *23* (13), 1514–1518.

(69) Gunjakar, J. L.; Kim, I. Y.; Lee, J. M.; Jo, Y. K.; Hwang, S.-J. Exploration of Nanostructured Functional Materials Based on Hybridization of Inorganic 2D Nanosheets. *J. Phys. Chem. C* **2014**, *118* (8), 3847–3863.

(70) Huang, S.; Cen, X.; Peng, H.; Guo, S.; Wang, W.; Liu, T. Heterogeneous Ultrathin Films of Poly(vinyl alcohol)/Layered Double Hydroxide and Montmorillonite Nanosheets via Layer-by-Layer Assembly. *J. Phys. Chem. B* **2009**, *113* (46), 15225–15230.

(71) Wang, L.; Sasaki, T. Titanium Oxide Nanosheets: Graphene Analogues with Versatile Functionalities. *Chem. Rev.* **2014**, *114* (19), 9455–9486.

(72) Wang, L.; Sasaki, T.; Ebina, Y.; Kurashima, K.; Watanabe, M. Fabrication of Controllable Ultrathin Hollow Shells by Layer-by-Layer Assembly of Exfoliated Titania Nanosheets on Polymer Templates. *Chem. Mater.* **2002**, *14* (11), 4827–4832.

(73) Kudo, A.; Sakata, T. Effect of Ion Exchange on Photoluminescence of Layered Niobates $K_4Nb_6O_{17}$ and KNb_3O_8. *J. Phys. Chem.* **1996**, *100* (43), 17323–17326.

(74) Yao, K.; Nishimura, S.; Imai, Y.; Wang, H.; Ma, T.; Abe, E.; Tateyama, H.; Yamagishi, A. Spectroscopic and Photoelectrochemical Study of Sensitized Layered Niobate K4Nb6O17. *Langmuir* **2003**, *19* (2), 321–325.

(75) Ida, S.; Ogata, C.; Matsumoto, Y. Synthesis and Photoluminescence Properties of Layered Oxides Intercalated with Eu^{3+} Ions by Electrostatic Self-Assembly Method Using Oxide Nanosheets. *IOP Conf. Ser. Mater. Sci. Eng.* **2009**, *1* (1), 012014.

(76) Matsumoto, Y.; Unal, U.; Kimura, Y.; Ohashi, S.; Izawa, K. Synthesis and Photoluminescent Properties of Titanate Layered Oxides Intercalated with Lanthanide Cations by Electrostatic Self-Assembly Methods. *J. Phys. Chem. B* **2005**, *109* (26), 12748–12754.

(77) Akbarian-Tefaghi, S.; Rostamzadeh, T.; Brown, T. T.; Davis-Wheeler, C.; Wiley, J. B. Manuscript Ready for Submission; "Rapid Exfoliation and Surface-Tailoring of Perovskite Nanosheets via Microwave-Assisted Reactions."

(78) Armstrong, A. R.; Anderson, P. A. Synthesis and Structure of a New Layered Niobium Blue Bronze: $Rb_2LaNb_2O_7$. *Inorg. Chem.* **1994**, *33* (19), 4366–4369.

(79) Montasserasadi, D.; Granier, M. W.; Spinu, L.; Rai, S. C.; Zhou, W.; Wiley, J. B. Synthesis and Characterization of the Rare-Earth Dion–Jacobson Layered Perovskites, $APrNb_2O_7$ (A = Rb, Cs and CuCl). *Dalton Trans* **2015**, *44* (23), 10654–10660.

(80) Geselbracht, M. J.; Scarola, R. J.; Ingram, D.; Green, C.; Caldwell, J. H. Early Transition Metal Oxides and a Pinch of Salt: New Synthetic Routes to Titanates and Niobates. *MRS Proc.* **1996**, *453*, 147–152.

(81) Uma, S.; Gopalakrishnan, J. Synthesis of Anion-Deficient Layered Perovskites, $ACa_2Nb_{3-x}M_xO_{10-X}$ (A = Rb, Cs; M = Al, Fe), Exhibiting Ion-Exchange and Intercalation. Evidence for the Formation of Layered Brownmillerites, $ACa_2Nb_2AlO_9$ (A = Cs, H). *Chem. Mater.* **1994**, *6* (7), 907–912.

(82) Hong, Y.-S. Reinvestigation of Dion-Jacobson Phases $CsCa_2Nb_2MO_9$ (M = Fe and Al). *Bull. Korean Chem. Soc.* **2006**, *27* (6), 853–856.

(83) Gustin, L. Synthesis and Topochemical Manipulation of New Layered Perovskites. *Univ. New Orleans Theses Diss.* **2016**.

(84) Akbarian-Tefaghi, S.; Teixeira Veiga, E.; Amand, G.; Wiley, J. B. Rapid Topochemical Modification of Layered Perovskites via Microwave Reactions. *Inorg. Chem.* **2016**, *55* (4), 1604–1612.

(85) Liang, Z.-H.; Tang, K.-B.; Chen, Q.-W.; Zheng, H.-G. $RbCa_2Nb_3O_{10}$ from X-Ray Powder Data. *Acta Crystallogr. Sect. E* **2009**, *E65*, i44.

(86) Mistry, B. D. *A Handbook of Spectroscopic Data Chemistry: (UV, IR, PMR, 13CNMR and Mass Spectroscopy)*; Oxford Book Company, 2009.

(87) *Shimadzu Application News, Spectrophotometric Analysis No.A428: "Measurements of Band Gap in Compound Semiconductors - Band Gap Determination from Diffuse Reflectance Spectra."*

(88) Tauc, J.; Grigorovici, R.; Vancu, A. Optical Properties and Electronic Structure of Amorphous Germanium. *Phys. Status Solidi B* **1966**, *15* (2), 627–637.

(89) Abelès, F. Optical Properties of Solids. **1972**.

(90) Davis, E. A.; Mott, N. F. Conduction in Non-Crystalline Systems V. Conductivity, Optical Absorption and Photoconductivity in Amorphous Semiconductors. *Philos. Mag.* **1970**, *22* (179), 0903–0922.

(91) Torrent, J.; Barron, V. Diffuse Reflectance Spectroscopy. *Methods Soil Anal. Part* **2008**, *5*, 367–387.

(92) Huang, T. J.; Thiang, Z. X.; Yin, X.; Tang, C.; Qi, G.; Gong, H. $(CH_3NH_3)_2PdCl_4$: A Compound with Two-Dimensional Organic–Inorganic Layered Perovskite Structure. *Chem. – Eur. J.* **2016**, *22* (6), 2146–2152.

(93) Woomer, A. H.; Farnsworth, T. W.; Hu, J.; Wells, R. A.; Donley, C. L.; Warren, S. C. Phosphorene: Synthesis, Scale-Up, and Quantitative Optical Spectroscopy. *ACS Nano* **2015**, *9* (9), 8869–8884.

Chapter 7. Concluding Remarks

The main goal of this work was to develop novel inorganic-organic hybrids based on layered oxide perovskites. This was fulfilled via topochemical manipulation of Dion-Jacobson (DJ) and Ruddlesden-Popper (RP) perovskite phases, with various alcohols and amines. These reactions typically start with an initial proton exchange step, followed by introducing short-chain n-alkyl alcohols and/or n-alkylamines. The short-chain organics are then exchangeable with longer ones, allowing for a variety of anchored organic groups, held in the interlayer via alcoxy covalent bonds or acid-base interactions (for alcohols and amines, respectively). Clearly, such topochemical modification reactions are naturally multi-step, and could take a very long time if each step requires a few days to yield a decent-quality product. Solvothermal approaches were the best option available for stepwise modification reactions at the time that we started this work in 2013. Despite being faster than traditional hot-plate stirring methods, such solvothermal modifications would still require over a week to efficiently yield a specific organic derivative of a layered perovskite (consider the steps for the solvothermal preparation of n-decoxy-$LaNb_2O_7$ from $RbLaNb_2O_7$). As demonstrated in *Chapter 2*, we were among the first groups exploiting microwave radiation in such topochemical modification reactions, introducing facile procedures for the production of a number of hybrid oxide perovskites. We specifically showed that proton exchange can also be performed in microwave apparatus, and combinations of proton exchange, grafting, and intercalation can decrease a multi-step modification procedure that is at least a week long to only a few hours. Various types of layered perovskites, double- and triple-layered DJ and RP, were investigated to evaluate the effectiveness of proposed microwave-assisted reactions. The results of this initial phase of our work were summarized in *Chapter 2*, presenting the great potential of this approach for rapid production of new and known organic-inorganic hybrids. It should be noted that despite high reactivity of double-layered DJ and RP hosts ($HLaNb_2O_7$, $HPrNb_2O_7$, and $H_2CaTa_2O_7$), the reactivity of the triple-layered hosts ($HCa_2Nb_3O_{10}$ and $H_2La_2Ti_3O_{10}$) were somewhat limited under our conditions.

Taking advantage of the efficiency of the microwave approaches demonstrated in *Chapter 2*, large amounts of organically modified $HLaNb_2O_7$ were readily obtained, allowing for the collection of decent-quality neutron diffraction patterns, and taking the very first step in refining the structure of a layered hybrid *oxide* perovskite. The results presented in *Chapter 3* are

very novel, and indeed the beginning of more research on locating the anchored organic chains in polycrystalline hybrid oxide perovskites.

Beyond three-dimensional (3D) hybrids presented in *Chapters 2 and 3*, exfoliation of DJ layered oxide perovskites and properties of various functionalized metal-oxide nanosheets were then fully discussed in *Chapters 4, 5, and 6*. The rapidity and effectiveness of microwaves were again employed in exfoliation reactions, leading to novel delamination processes as well as post-exfoliation surface-modification reactions to obtain a wide range of functionalized metal-oxide nanosheets within a few hours. *Chapter 4* specifically approves of the validity of these approaches looking at the simplest possible host ($HLnNb_2O_7$; Ln = La, Pr), showing how the surface of these oxide nanosheets can be tailored with various saturated and unsaturated linear or cyclic organics. Focusing more on unsaturated organic surface groups, so-called *monomer-grafted nanosheets* were obtained and their polymerization trials were reported in *Chapter 5*. In *Chapter 6*, microwave-assisted exfoliation and post-exfoliation surface-modification reactions were expanded to a few triple-layered DJ hosts as well; investigating $HCa_2Nb_3O_{10}$, $HCa_2Nb_2FeO_9$, and $HLaCaNb_2MnO_{10}$ perovskites, similar to $HLaNb_2O_7$ and $HPrNb_2O_7$. The impact that elements such as Pr^{3+}, Fe^{3+}, and Mn^{4+} would impose on the optical properties of such functionalized metal-oxide nanosheets was then presented, and the optical properties of $LaCaNb_2MnO_{10}$ nanosheets showed the highest dependence on their organic functional groups.

This work leads into novel microwave-assisted methods for the organic modification of layered oxide perovskites, as well as effective exfoliation and surface-modification of perovskite nanosheets. The ability to obtain functionalized metal-oxide nanosheets with engineered compositions and surfaces, is quite significant in developing new composites with potentially tunable properties (such as mechanical and optical).

Appendix A. Grafting Hydroxylated Fullerene in Layered Perovskites

A.1 Introduction

Interesting structure and properties of the C_{60} molecule have been studied extensively since its birth in 1980s.[1] C_{60} is a truncated icosehedron as shown in Figure A-1[2]; its nearly spherical structure is the main reason that C_{60} is mostly known as "*buckyball*". C_{60} or *buckminsterfullerene* was the firstly discovered member of *fullerene family* (closed-cage carbon-based spheroidal molecules such as C_{20}, C_{30}, C_{40}, C_{50}, C_{60}, C_{70}, C_{90}, C_{240}, and C_{720}[1,3] consisting of edge-sharing hexagons and pentagons).

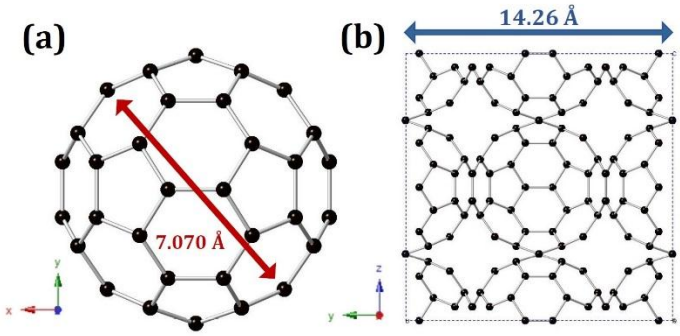

Figure A- 1: (a) Structure of a single C_{60} (buckminsterfullerene), and (b) *fcc* crystal structure of C_{60} at room temperature.

Buckminsterfullerene is famous because of its relatively high-temperature superconductivity when intercalated or doped with alkali metals.[4,5] Examples include, but are not limitted to, Cs_3C_{60}, Cs_2RbC_{60} and K_3C_{60} with *Tc*'s about 30 K.[6–14] Donation of the metal electrons to the fullerene is the reason why these alkali-doped fullerides (M_xC_{60}) can potentially show superconductivity.[15] *Endohedral fullerenes (endofullerenes)*,[16–20] where the dopant is inside of the C_{60} cage ($M@C_{60}$), may also be superconductors based on the same reasoning.[15] Another very important use of C_{60} is the incorporation of its derivatives in solar cells in order to enhance the performance and efficiency.[21–28] In this respect, functionalization and modification of buckminsterfullerene is vastly studied to provide different derivatives of C_{60} with various reactivities and properties.[29–38] Simplest C_{60} derivatives are amino fullerenes[21,39–42] and fullerenols (also know as fullerols)[25,43–56] with various applications in solar cells, electrochemistry, and biomedicine.

Modification of perovskites with fullerene derivatives has been limitted only to layered halide perovskites used in solar cells.[57,58] Incorporation of buckminsterfullerene in the interlayer of layered oxide perovskite was the main goal of the present work. Based on the very different properties of oxide perovskites compared to halides, such hybrids are expected to bring out interesting features once C_{60} is engaged in these novel hosts, even as interesting as superconductivity. Considering the efficient grafting of organics containing hydroxy groups in the interlayer of the Dion-Jacobson-type perovskites,[59,60] simple fullerene derivatives were made via hydroxylation of the pristine C_{60} based on the procedures[46–48,51,52,25] available in the literature. The simplest reactions to produce fullerol (also known as polyhydroxy fullerene as well as fullerenol) are based on vigorous stirring of C_{60} solution (usually in toluene or benzene) with an aqueous solution of NaOH or KOH, in the presence of a phase transfer catalyst such as with tetra(n-butyl)ammonium hydroxide (TBAOH).[25,46] Some reports suggest using polyethylene glycol-400 (PEG) as the phase transfer catalyst to increase the rate of the reaction.[48,51] Some other methods incorporate H_2O_2 in the following steps to increase the number of hydroxyl groups from about 12[44] to 30 or so.[52] Among all synthetic approaches for the production of fullerol, the solvent-free method proposed by *Wang et al.* seems to be the most straightforward, which only involves grinding the pristine C_{60} with solid NaOH and drops of H_2O_2.[49]

A.2 Experimental

A.2.1 Materials

Rb_2CO_3 (Alfa Aesar, 99.8%), C_{60} (Alfa Aesar, 99%), H_2O_2 (Alfa Aesar, 29-32% w/w aqueous solution), polyethylene glycol 400 (Alfa Aesar), and NaOH (BDH, 97%) were used as received. La_2O_3 (Alfa Aesar, 99.99%) and Nb_2O_5 (Alfa Aesar, 99.9985%) were heated at 1000˚C for 12 h in order to eliminate any impurities. Organic n-alkyl alcohols, 1-propanol (Alfa Aesar 99+%) and 1-decanol (Alfa Aesar 98+%), were used without any further distillation. For aqueous solutions (aq. soln.), milli-Q water (18.2 MV cm, Millipore) was used.

A.2.2 Synthesis of n-decoxy-$LaNb_2O_7$

$RbLaNb_2O_7$ was synthesized by grinding stoichiometric amounts of La_2O_3 and Nb_2O_5 oxides with a 30% molar excess of Rb_2CO_3 as previously reported.[61] The mixture was preheated at 850 °C overnight, reground, and heated at 1050 °C for 24 h. After regrinding, the sample was

finally heated at 1100 °C for 24 h. The product was washed with copious amount of water to remove the excess carbonate, and dried at 100 ˚C for a few hours. Acid treatment and alcoxy grafting reactions were performed in a StartSYNTH Microwave Synthesis Labstation as reported in earlier chapters.[60] Microwave protonation of the host was achieved by continuous stirring of ground $RbLaNb_2O_7$ in a 6M nitric acid solution for 3 h at 60˚C (max power of 300 W), maintaining the molar ratio of proton to Rb greater than 150:1 for an efficient exchange. The protonated product was washed with distilled water until pH 7 was obtained, and dried at 100 ˚C for 3 hours. C_3H_7-$LaNb_2O_7$ was synthesized by reacting 0.15 g of $HLaNb_2O_7$ with 14 mL of 80% v/v aq. soln. of 1-propanol for 1 h at 100 ˚C with the maximum power of 350 W. The 1-propoxy-$LaNb_2O_7$ intermediate was washed with distilled water and acetone and then dried at 70 ˚C for 1 h. Finally, the interlayer of C_3H_7-$LaNb_2O_7$ was successfully exchanged with longer chain n-decoxy substituent, yielding $C_{10}H_{21}$-$LaNb_2O_7$. The typical microwave procedure was carried out by reacting 0.1 g of n-propoxy-$LaNb_2O_7$ with 11 mL of 1-decanol for only 30 min at 150 ˚C with the maximum power of 1000 W. The n-decoxy-$LaNb_2O_7$ product was washed with acetone and dried at 70 ˚C for 1 h. This final hybrid was used in the following steps to easily replace the n-decoxy substituent with fullerol due to the large interlayer spacing that n-decoxy-$LaNb_2O_7$ has (about 17 Å).

A.2.3 Hydroxylation of Fullerene

Solution Method. Following the procedure reported by *Zhang et al.*,[48] hydroxylation was carried out using NaOH and PEG-400 (as the source of hydroxy groups and the phase transfer catalyst, respectively). Pure C_{60} was readily soluble in toluene (typically 25 mg C_{60} was dissolved in 15 mL of toluene). While vigorously stirring the C_{60} solution in ambient condition, 1 mL of 15 M NaOH was added dropwise (molar ratio of OH^- to C_{60} is about 400:1). Then, a few drops of an aqueous solution of PEG was added to the stirring mixture. For the preparation of aq. PEG, 0.111 g PEG-400 was dissolved in 5 mL water, and then 0.125, 0.375, 1 and 2 mL of this aqueous solution was used to yield various molar ratios of PEG to C_{60} for 4 different batches of C_{60}-$(OH)_n$ (0.20, 0.6, 1.6, and 3.2 to 1, respectively). Vigorous stirring of the mixture was continued for 10 mins, yielding C_{60}-$(OH)_n$ with various levels of solubility in toluene (more OH groups and less solubility in toluene with increasing the molar ratio of PEG, it should be noted that all batches above were still dispersible in toluene). The mixture of the product was washed a

few times with 30-50 mL of DI water in a separatory funnel, checking the pH every time, until the excess basic NaOH was thoroughly washed off from the product and pH 7 was obtained. Methanol was then added to the mixture of toluene and C_{60}-$(OH)_n$, aiding with the precipitation of the solid, and expediting the final step of solvent evaporation process which was carried out using a rotary evaporation apparatus for up to 15 minutes at 60 °C (Büchi Rotavapor R-200). This dark brown solid of C_{60}-$(OH)_n$ was dissolved and stored in 15 mL fresh toluene. C_{60}-$(OH)_n$ from this approach is named as *I*-C_{60}-$(OH)_n$.

Solvent-Free Approach. Based on the facile solvent-free hydroxylation method proposed by *Wang et al.*,[49] 0.36 g NaOH (9 mmole), 0.7 mL of 30% H_2O_2 (9 mmole), and 108 mg pure C_{60} (0.15 mmole) were added in a mortar, respectively. The reagents were well ground for 15 mins, yielding a brownish paste. The ground product was completely miscible with water, and was transferred to a centrifuge tube using less than 10 mL DI water. The mixture in the tube was topped with about 40mL methanol and centrifuged (when methanol is the dominant solvent, C_{60}-$(OH)_n$ readily precipitates). After a few centrifugation steps in methanol/water mixture, the precipitate was dried for a few hours at 70 °C. C_{60}-$(OH)_n$ from this approach is named as *II*-C_{60}-$(OH)_n$.

A.2.4 Grafting Fullerol in the Perovskite Interlayer

Based on C_{60}-$(OH)_n$ obtained above, two different procedures were planned to produce C_{60}-$LaNb_2O_7$ using the exchange of the two types of hydroxylate C_{60} with the interlayer of n-decoxy-$LaNb_2O_7$. In the first method, 3 mL of the toluene solution of *I*-C_{60}-$(OH)_n$, was mixed and stirred with 15 mg of n-decoxy-$LaNb_2O_7$ (roughly in a 0.25:1 molar ratio of the two solids, respectively). This mixture was then transferred to a Teflon-lined stainless steel autoclave, and heated at 100 °C for 15 h (200 °C for 6 h yielded some successful batches as well). In a second approach, 5 mg of water-miscible *II*-C_{60}-$(OH)_n$ was dissolved in 1 mL water, and mixed with 6 mL of 2-butanone solution containing 15 mg of n-decoxy-$LaNb_2O_7$. The mixture was sonicated for a few mins and then heated at 100-110 °C for 15 h in a Teflon-lined stainless steel autoclave.

A.2.5 Characterization

X-ray powder diffraction (XRD) data were collected on a Philips X'Pert system equipped with Cu Kα radiation (λ = 1.5418 Å) and a curved graphite monochromator. Typical scans were carried out in continuous mode with a scan rate of 0.02 °/s. Infrared spectroscopy was performed

using a Perkin Elmer 2000 FT-IR spectrometer. Thermogravimetric analysis (TGA) and differential scanning calorimetry (DSC) data were collected on a TA Instruments TGA-DSC SDT Q600 system in alumina pans under a dilute oxygen atmosphere (ca. 50% argon); samples were heated up to 1000 °C at a rate of 10 °C/min. *I*-C_{60}-$(OH)_n$ samples were run in a AB Sciex-3200 Q Trap mass spectrometer by direct injection in electrospray system with the temperature of 300 °C for the source. The curtain gas flow was maintained at 10 mL/min, and the ion source gas (nitrogen) was in the positive mode.

A.3 Results and Discussion

A.3.1 Grafting *I*-C_{60}-$(OH)_n$. Figure A-2 shows the C_{60} hydroxylation process by adding NaOH and PEG to the solution of C_{60}: (a) violet solution of pure C_{60} in toluene, and (b) Fullerol, *I*-C_{60}-$(OH)_n$, after the addition of 15 M NaOH and aq. PEG in molar ratios of 400 and 20 to 1 mole of C_{60}, respectively. Molar ratios of 5 or less for PEG:C_{60} yielded *I*-C_{60}-$(OH)_n$ that was completely miscible with toluene, reaction of which with n-decoxy-$LaNb_2O_7$ was studied under various conditions. Figure A-3 represents the schematic of the proposed exchange reaction of hydroxylated C_{60} with the interlayer of $C_{10}H_{21}$-$LaNb_2O_7$. The major issue with these reactions was poor reproducibility; despite using the same batch of fullerol and the exact same solvothermal condition, most of the reactions showed poor crystallinity for the C_{60}-$LaNb_2O_7$. The most successful reaction conditions with most consistent results turned out to be 15 h at 100 °C, or 3 h at 200 °C, using fullerols obtained at 0.6 for the molar ratio of PEG to C_{60}.

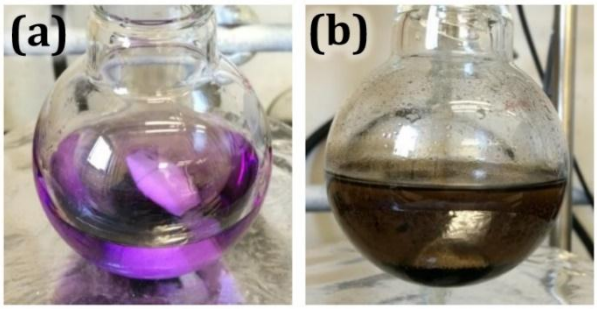

Figure A- 2: (a) Pure C_{60} dissolved in toluene, hydroxylation upon addition of NaOH and PEG to produce (b) *I*-C_{60}-$(OH)_n$.

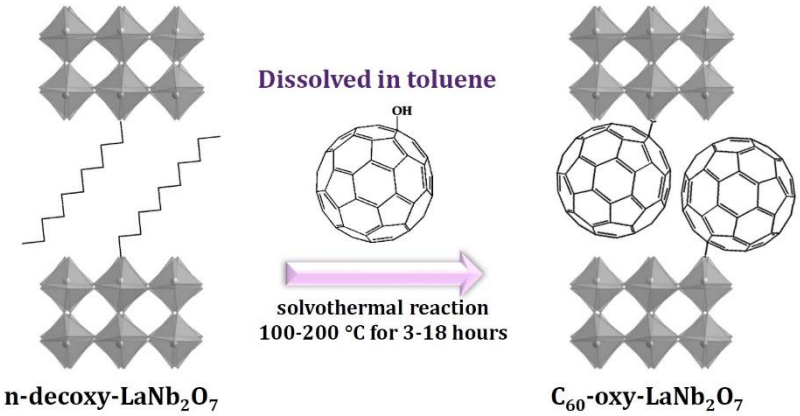

Figure A- 3: Grafting of hydroxylated fullerene in the perovskite interlayer

Figure A-4 shows the FTIR spectra for fullerene and fullerol, supporting the hydroxylation process due to the appearance of sharp alkoxy bands at 1260-1000 cm^{-1}. Observation of the OH bond with nuclear magnetic resonance (NMR) would work the best by dissolving the fullerol in D_2O which was not the case for hydrophobic *I*-C_{60}-$(OH)_n$. In order to further prove the successful formation of fullerol via an alternative analytical technique rather than FTIR and NMR, mass spectroscopy was done on *I*-C_{60}-$(OH)_n$. Figure A-5 shows the existance of molecular fragments with *m/Z* values higher than 720, which strongly suggests the formation of OH bonds on fullerene. It should be noted that the molar mass of fullerol can be estimated by adding OH (17 g/mole) to pure fullerene, yielding numbers such as 737, 754, 771, … , 720 + *n*(17) g/mole based on various *n* values in *I*-C_{60}-$(OH)_n$. The *m/Z* spacings between the fragments of hydroxylated C_{60} are consistently about either 44 or 58 Da for the two batches prepared with 0.6 and 1.6 molar ratio of PEG respectively, while the steps are about 35 in case of pure Fullerene. These spacings are differen from what reported in the litrature

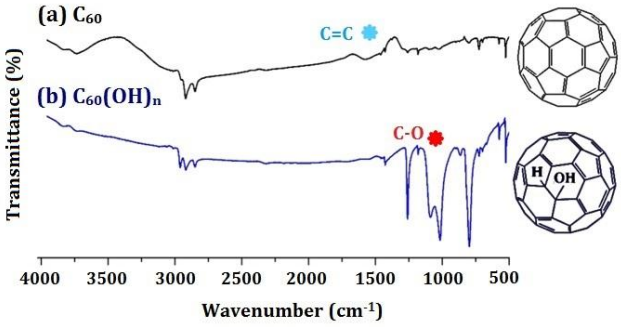

Figure A- 4: FTIR spectra of (a) pure C_{60} versus (b) the hydroxylated version

(respectively 74 and 24 Da for fullerol and fullerene),[62,63] but is related to losing hydrocarbon fragments regardless.

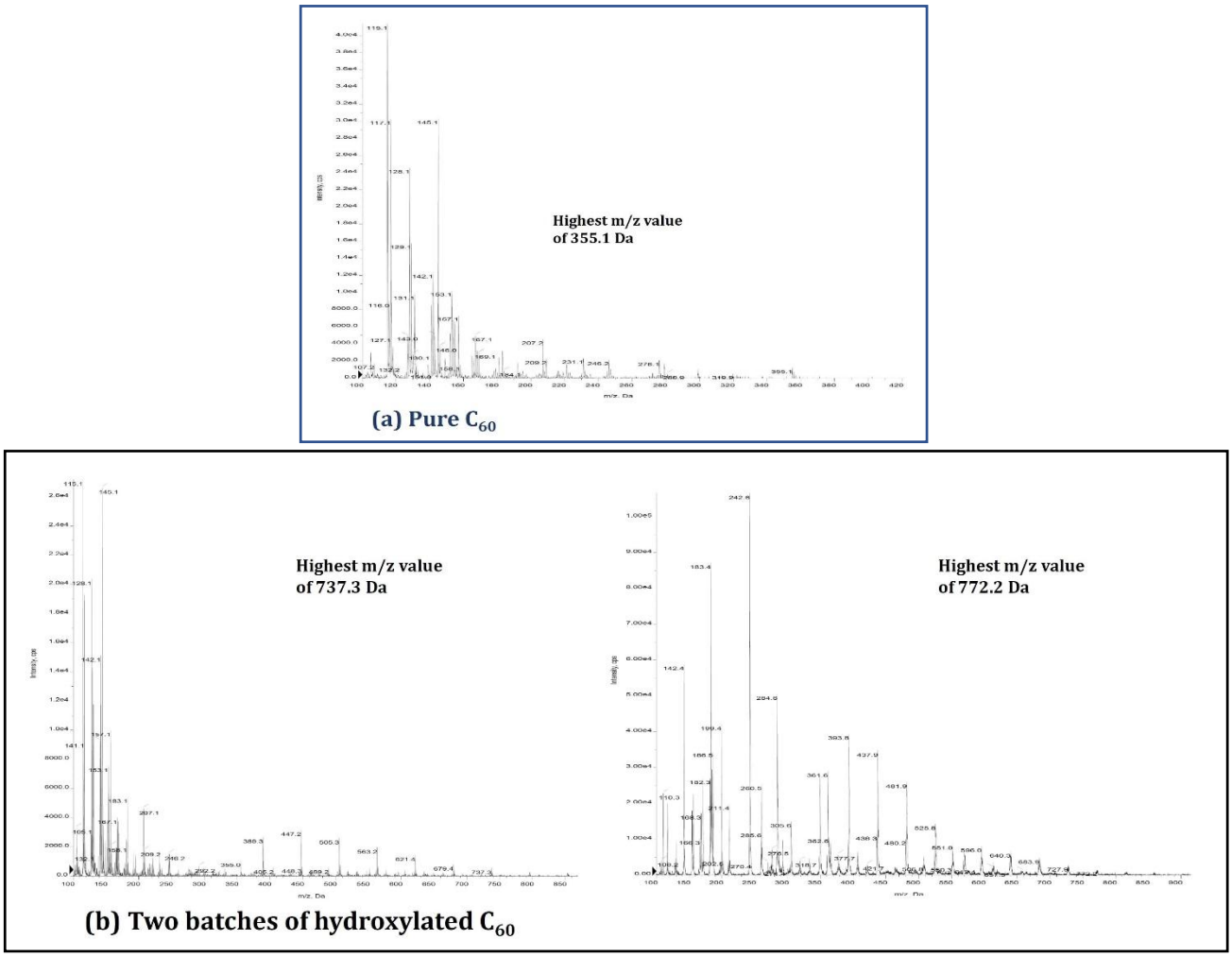

Figure A- 5: Mass spectra for (a) pure fullerene and (b) two batches of hydroxylated fullerene dissolved in pure toluene.

Thin layer chromatography (TLC) was performed on the hydoxylated fullerene using either dichloromethane (DCM) or toluene as the mobile phase and silica gel as the stationary phase. As presented in Figure A-6, DCM provided better separation due to its higher polarity index compared to toluene (2.4 and 3.1 respectively). The TLC test with DCM suggests the existance of both non-polar fullerene (marked with star) and polar fullerols with various *n* values (marked with square); the more polar the molecule, the more affinity with the stationary phase and less migration speed it will have. This incosistency in the hydroxylation products can be one

of the reasons that lead to poor reproducibility of the following grafting reactions with n-decoxy-$LaNb_2O_7$.

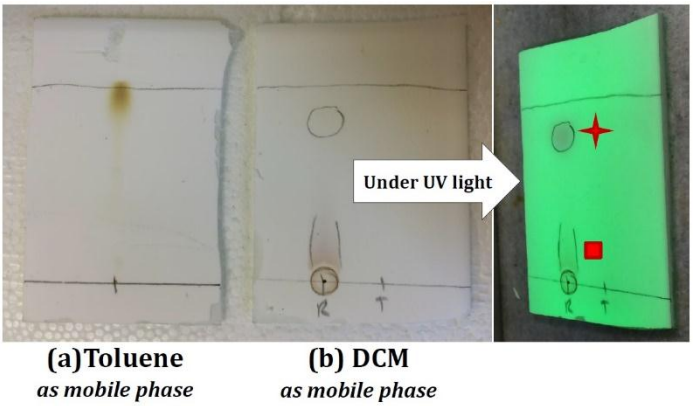

Figure A- 6: TLC test performed on hydroxylated fullerene using (a) toluene and (b) DCM as the mobile phase, as well as (b) under UV light showing both non-polar C_{60} (marked with star) and more polar fullerols (marked with square).

Figure A-7 compares the XRD patterns of n-decoxy-$LaNb_2O_7$ and C_{60}-$LaNb_2O_7$. XRD pattern of pure fullerene is presented to be able to trace unreacted fullerols that might be present outside of the perosvkite interlayer (XRD patterns of pure fullerene and *I*-C_{60}-$(OH)_n$ matched, confirmng the same crystalline structure after the hydroxylation method used here). Table A-1 shows the unit cell refinement results for $RbLaNb_2O_7$, $HLaNb_2O_7$, n-propoxy-$LaNb_2O_7$, n-decoxy-$LaNb_2O_7$ and C_{60}-$LaNb_2O_7$. The interlayer spacing of each hybrid should be about the dimensions of the organic present in the interlayer (this interlayer spacing is presented as Δc, calculated by subtracting the *c* parameter of $HLaNb_2O_7$ from the *c* parameter of the hybrid). Considering the diameter of a single fullerene (~7Å), a interlayer spacing of 10-11 Å seems to make perfect sense. Smilar XRD patterns with slight shifts in their first reflections were observed for 10-20% of the trials considered as successful batches, with the rest yielding noisy XRD patters suggesting either poor crystallinity or lack of organics due to high 2θ values for the first peak (Figure A-7 d). Figure A-8 shows the TGA curves for two successful reactions at 100 ºC. Based on the dimensions of C_{60} and the *a* and *b* parameters in the tetragonal cell of the host (Figure A-9), 8 fullerenes per 16 unit cell seems to be about the maximum possible C_{60} packing in the unit cell, yielding %45 weight loss in TGA. Based on this estimation, the loading of C_{60} in

the successful batches seems to be lower than what it can be. There is a chance that this loading can be enhanced via better hydroxylation of C_{60} and a more efficient exchange reaction. Despite this estimation, estereospecific limitations might also impact the maximum loading not ever getting to about %45. Once more reproducible exchange reactions are proposed for the production of C_{60}-$LaNb_2O_7$, hopefully these questions can be answered more definitely.

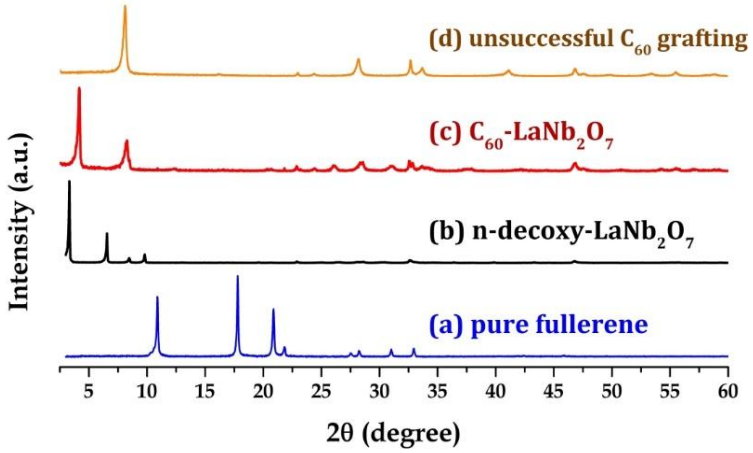

Figure A- 7: XRD patterns of (a) pure fullerene, (b) n-decoxy-$LaNb_2O_7$ used as the host, (c) C_{60}-$LaNb_2O_7$, typical product of successful C_{60} grafting, and (d) typical product of unsuccessful C_{60} grafting.

Table A- 1: Unit cell parameters of C_{60}-$LaNb_2O_7$ compared to three other similar compounds.

Compound	a (Å)	c (Å)	Δc (Å)	Chain length (Å)
$HLaNb_2O_7$	3.883(3)	10.4527(5)	-	-
n-propoxy-$LaNb_2O_7$	3.888(3)	15.4011(5)	4.9484	~ 5 (tilt angle of ~ 42° with the slab)
n-decoxy-$LaNb_2O_7$	3.876(5)	27.2380(6)	16.7853	~ 14 (tilt angle of ~ 42° with the slab)
C_{60}-$LaNb_2O_7$	3.882(7)	21.4953(9)	11.0426	~ 7.5

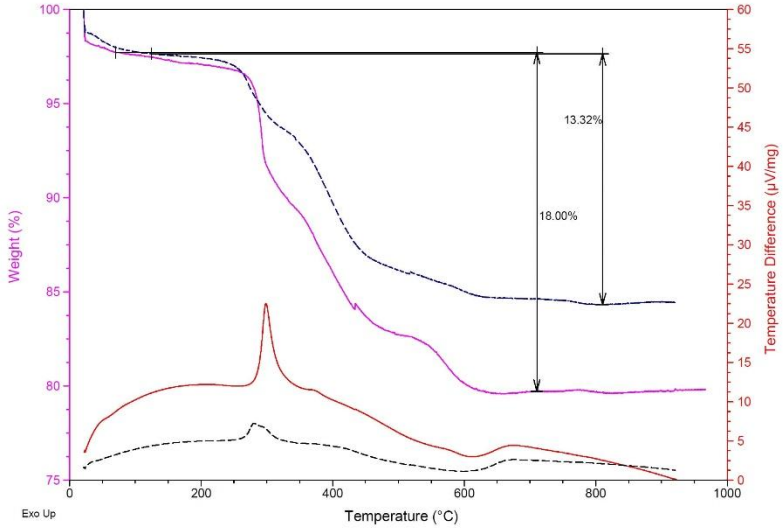

Figure A- 8: TGA-DSC results for two successful C_{60}-$LaNb_2O_7$ products

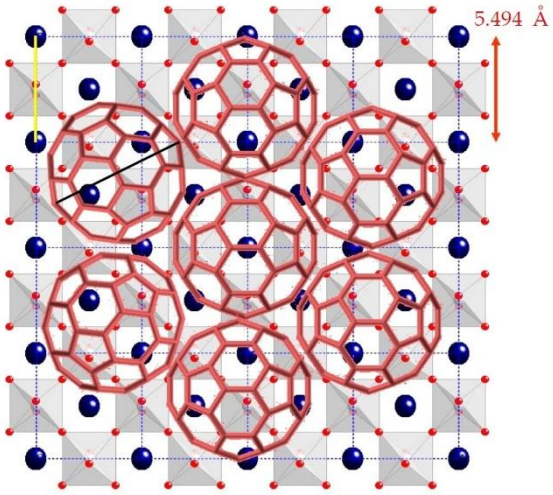

Figure A- 9: Estimation of the maximum loading of C_{60} per $LaNb_2O_7$ unit cell based on their sizes

As a complementary study, grafting *I*-C_{60}-$(OH)_n$ was also carried out in microwave: 3 mL of the toluene solution of *I*-C_{60}-$(OH)_n$ was mixed with the dispersion of 15 mg of n-decoxy-$LaNb_2O_7$ in 3 mL toluene. Three replicates of the same reaction was performed at 125 °C for 3 h with a maximum power of 1200 watts (using a Weflong button and a 30-min warmup time in all cases). These trials showed no trace of grafting; the XRD pattern of the product was exactly the

same as starting n-decoxy-$LaNb_2O_7$. As a final observation, 7 different batches of *I*-C_{60}-$(OH)_n$ with various PEG molar ratios and so various levels of hydroxylations (0.2, 0.6, 1.6, 3.2, 5.0, 10.0, and 20.0 to 1 mole of C_{60}), were produced based on the details provided in the experimental section. In order to keep the amount of the fullerol high with respect to n-decoxy-$LaNb_2O_7$ reagent, all the hydroxylation products (about 25 mg) were dissolved in 12 mL toluene and reacted with 15 mg of n-decoxy-$LaNb_2O_7$. These 7 trials were heated in microwave under conditions like the first three trials, only for shorter duration (15 minutes). Unfortunately, these trials yielded products with XRD patterns the same as the starting materials (n-decoxy-$LaNb_2O_7$), or as presented in Figure A-7 d with small *c* parameters which gives no evidence of C_{60} grafting in both cases.

A.3.2 Grafting *II*-C_{60}-$(OH)_n$. This version of hydroxylated C_{60} was absolutely miscible with water, which would not call for hydrophobic solvents such as toluene used in the previous section. Another complication that water-miscible C_{60}-OH imposes, is less compatibility with hydrophobic n-decoxy-$LaNb_2O_7$. To carry out reactions using *II*-C_{60}-$(OH)_n$, dry hydroxylated fullerene was well dispersed in either toluene or 2-butnone, which showed better miscibility with the latter. In other trials, the solution of hydroxylated fullerene in 1 mL water was mixed with 6 mL of either toluene or butanone. After the addition of n-decoxy-$LaNb_2O_7$ to the mixture, the autoclave was sealed and maintained at either 100 or 110 °C for 15 h. All of these trials turned out to be consistently unsuccesfful, showing the same XRD pattern as presented in Figure A-7 d, only with noisier and broader peaks.

Considering the results provided in Chapter four of this dissertation, grafting hydroxylated C_{60} would also be an option starting from the TBA-$LnNb_2O_7$ nanosheets (Ln = La, Pr). Since the groups are going to exchange in the surface of the nanosheets, there might be better chances for the C_{60}-OH bulky groups to react without having to penetrate the interlayer of n-decoxy-$LaNb_2O_7$. Two reactions were carried out where 15 mg of TBA-$LnNb_2O_7$ nanosheets were mixed with 10 mg of *II*-C_{60}-$(OH)_n$ and dispersed in 10 mL of pure water. It should be noted that both solids were completely miscible with water due to their hydrophilicity. The mixture was heated for 1 h at 80 ºC with a maximum power of 350 watts and a 20-min warmup. Unfortunately, unreacted fullerol was completely mixed with the product, and could not be

removed despite various washing methods. Even though the change in the XRD patterns presented in Figure A-10 might suggest that hydroxylated C_{60} is actually grafted on the nanosheets in the trials above, the success of these reactions cannot be further proved without complete removal of the unreacted fullerol. Considering that strating fullerol was absolutely soluble in water, the reason why there is this much difficulty in washing off the unreacted fullerol using water remained unknown. It is possible that the hydroxylated fullerene also undergoes changes during these reactions.

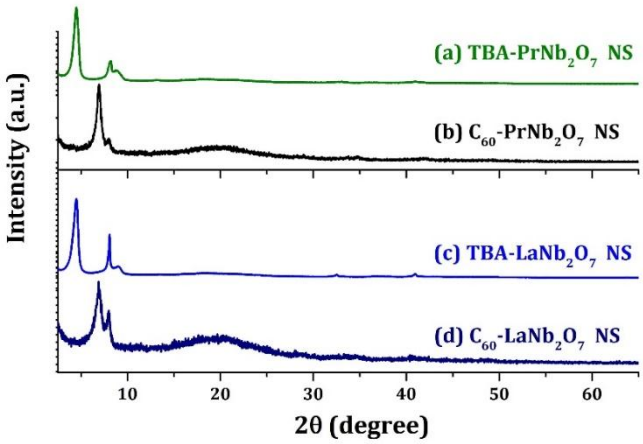

Figure A- 10: Grafting hydroxylated C_{60} on TBA-$LnNb_2O_7$ nanosheets.

In a few trials, n-pentoxy-$LaNb_2O_7$ was used instead of n-deoxy-$LaNb_2O_7$, and reacted with both *I*-C_{60}-$(OH)_n$ and *II*-C_{60}-$(OH)_n$. Especially in case of *II*-C_{60}-$(OH)_n$, n-pentoxy-$LaNb_2O_7$ was expected to perform better due to less hydrophobicity. However, no reaction or the unsuccessful XRD pattern in Figure A-7 d was again obtained despite this change.

A.4 Conclusions

Despite the low reproducibility in C_{60} grafting reactions, it was proved that it is possible to successfully graft C_{60} in the interlayer of the layered oxide perovskites. The chances of successfully grafting fullerene might be just intrinsically low due to the short length of the OH bond on these buckyballs. It is suggested that other functionalization reactions take place in order to introduce longer hydroxy groups to the surface. This can increase the facility of the following exchange reactions with the oxide perovskite. Another issue here could be low control in the

number of hydroxy bonds that get grafted to the fullerene, and so the large distribution in the fullerol products. Considering the price of pure fullerene, separation of the fullerols in a packed chromatography column was not tried in the current study. However, this is another suggestion which can enhance the reproducibility of the reactions in the following studies.

A.5 References

(1) Dresselhaus, M. S.; Dresselhaus, G.; Eklund, P. C. *Science of Fullerenes and Carbon Nanotubes*; Academic Press: San Diego, California, USA, 1996.

(2) Dorset, D. L.; McCourt, M. P. Disorder and the Molecular Packing of C_{60} Buckminsterfullerene: A Direct Electron-Crystallographic Analysis. *Acta Crystallogr. A* **1994**, *50* (3), 344–351.

(3) Weber, S. Crystallography Picture Book (Fullerenes) http://www.jcrystal.com/steffenweber/ (accessed Dec 2, 2016).

(4) Tanigaki, K. Present and Future of Fullerenes. In *Polymeric Materials for Microelectronic Applications*; ACS Symposium Series; American Chemical Society: Washington, D.C., 1995; Vol. 579, pp 343–356.

(5) Degiorgi, L. Fullerenes and Carbon Derivatives: From Insulators to Superconductors. *Adv. Phys.* **1998**, *47* (2), 207–316.

(6) Gunnarsson, O. Superconductivity in Fullerides. *Rev. Mod. Phys.* **1997**, *69* (2), 575–606.

(7) Schluter, M.; Lannoo, M.; Needels, M.; Baraff, G. A.; Tomanek, D. Superconductivity in Alkali Intercalated C_{60}. In *Physics and Chemistry of Finite Systems: From Clusters to Crystals*; Jena, P., Khanna, S. N., Rao, B. K., Eds.; NATO ASI Series; Springer Netherlands, 1992; pp 1371–1377.

(8) Zhou, O.; Cox, D. E. Structures of C_{60} Intercalation Compounds. *J. Phys. Chem. Solids* **1992**, *53* (11), 1373–1390.

(9) Stephens, P. W.; Mihaly, L.; Lee, P. L.; Whetteni, R. L.; Huangi, S.-M.; Kaneri, R.; Deiderfchi, F. Structure of Single-Phase Superconducting K_3C_{60} ". *Phys. Chem. Fuller. Repr. Collect.* **1993**, *1*, 134.

(10) Haddon, R. C.; Hebard, A. F.; Rosseinsky, M. J.; Murphy, D. W.; Duclos, S. J.; Lyons, K. B.; Miller, B.; Rosamilia, J. M.; Fleming, R. M.; Kortan, A. R.; et al. Conducting Films of C_{60} and C_{70} by Alkali-Metal Doping. *Nature* **1991**, *350* (6316), 320–322.

(11) Ganin, A. Y.; Takabayashi, Y.; Khimyak, Y. Z.; Margadonna, S.; Tamai, A.; Rosseinsky, M. J.; Prassides, K. Bulk Superconductivity at 38 K in a Molecular System. *Nat. Mater.* **2008**, *7* (5), 367–371.

(12) Tanigaki, K.; Ebbesen, T.; Kuroshima, S.; Mizuki, J. Superconducting Material Comprising Rb_x Cs_y C_{60}. US5294600 A, March 15, 1994.

(13) Rosseinsky, M. J.; Ramirez, A. P.; Glarum, S. H.; Murphy, D. W.; Haddon, R. C.; Hebard, A. F.; Palstra, T. T. M.; Kortan, A. R.; Zahurak, S. M.; Makhija, A. V. Superconductivity at 28 K in RbxC60. *Phys. Rev. Lett.* **1991**, *66* (21), 2830–2832.

(14) Morelli, D. T. Thermoelectric Power of Superconducting Fullerenes. *Phys. Rev. B* **1994**, *49* (1), 655–657.

(15) Bethune, D. S.; Johnson, R. D.; Salem, J. R.; de Vries, M. S.; Yannoni, C. S. Atoms in Carbon Cages: The Structure and Properties of Endohedral Fullerenes. *Nature* **1993**, *366* (6451), 123–128.

(16) A. Dolgonos, G.; H. Peslherbe, G. Encapsulation of Diatomic Molecules in Fullerene C_{60} : Implications for Their Main Properties. *Phys. Chem. Chem. Phys.* **2014**, *16* (47), 26294–26305.

(17) Cerón, M. R.; Li, F.-F.; Echegoyen, L. A. Endohedral Fullerenes: The Importance of Electronic, Size and Shape Complementarity between the Carbon Cages and the Corresponding Encapsulated Clusters. *J. Phys. Org. Chem.* **2014**, *27* (4), 258–264.

(18) Hermanns, C. F.; Bernien, M.; Krüger, A.; Schmidt, C.; Waßerroth, S. T.; Ahmadi, G.; Heinrich, B. W.; Schneider, M.; Brouwer, P. W.; Franke, K. J.; et al. Magnetic Coupling of $Gd_3N@C_{80}$ Endohedral Fullerenes to a Substrate. *Phys. Rev. Lett.* **2013**, *111* (16), 167203.

(19) Tománek, D.; Wang, Y.; Ruoff, R. S. Stability of Fullerene-Based Systems. *J. Phys. Chem. Solids* **1993**, *54* (12), 1679–1684.

(20) Yang, S.; Wang, C.-R. *Endohedral Fullerenes: From Fundamentals to Applications*; World Scientific: Singapore, 2014.

(21) Zhang, Z.-G.; Li, H.; Qi, B.; Chi, D.; Jin, Z.; Qi, Z.; Hou, J.; Li, Y.; Wang, J. Amine Group Functionalized Fullerene Derivatives as Cathode Buffer Layers for High Performance Polymer Solar Cells. *J. Mater. Chem. A* **2013**, *1* (34), 9624–9629.

(22) Lin, H.-K.; Su, Y.-W.; Chen, H.-C.; Huang, Y.-J.; Wei, K.-H. Block Copolymer-Tuned Fullerene Electron Transport Layer Enhances the Efficiency of Perovskite Photovoltaics. *ACS Appl. Mater. Interfaces* **2016**, *8* (37), 24603–24611.

(23) Wojciechowski, K.; Ramirez, I.; Gorisse, T.; Dautel, O.; Dasari, R.; Sakai, N.; Hardigree, J. M.; Song, S.; Marder, S.; Riede, M.; et al. Cross-Linkable Fullerene Derivatives for Solution-Processed N–i–p Perovskite Solar Cells. *ACS Energy Lett.* **2016**, *1* (4), 648–653.

(24) Watson, B. L.; Rolston, N.; Bush, K. A.; Leijtens, T.; McGehee, M. D.; Dauskardt, R. H. Cross-Linkable, Solvent-Resistant Fullerene Contacts for Robust and Efficient Perovskite Solar Cells with Increased JSC and VOC. *ACS Appl. Mater. Interfaces* **2016**, *8* (39), 25896–25904.

(25) Cao, T.; Wang, Z.; Xia, Y.; Song, B.; Zhou, Y.; Chen, N.; Li, Y. Facilitating Electron Transportation in Perovskite Solar Cells via Water-Soluble Fullerenol Interlayers. *ACS Appl. Mater. Interfaces* **2016**, *8* (28), 18284–18291.

(26) Dai, S.-M.; Tian, H.-R.; Zhang, M.-L.; Xing, Z.; Wang, L.-Y.; Wang, X.; Wang, T.; Deng, L.-L.; Xie, S.-Y.; Huang, R.-B.; et al. Pristine Fullerenes Mixed by Vacuum-Free Solution Process: Efficient Electron Transport Layer for Planar Perovskite Solar Cells. *J. Power Sources* **2017**, *339*, 27–32.

(27) Chang, C.-Y.; Tsai, B.-C.; Hsiao, Y.-C.; Huang, Y.-C.; Tsao, C.-S. High-Performance Printable Hybrid Perovskite Solar Cells with an Easily Accessible N-Doped Fullerene as a Cathode Interfacial Layer. *Phys. Chem. Chem. Phys.* **2016**, *18* (46), 31836–31844.

(28) Chen, S.; Du, X.; Ye, G.; Cao, J.; Sun, H.; Xiao, Z.; Ding, L. Thermo-Cleavable Fullerene Materials as Buffer Layers for Efficient Polymer Solar Cells. *J. Mater. Chem. A* **2013**, *1* (37), 11170–11176.

(29) Matsuo, Y. C60 Derivatives Having Self-Assembly Capabilities. *Fuller. Nanotub. Carbon Nanostructures* **2010**, *18* (4-6), 338–352.

(30) Hufnagel, M.; Fischer, M.; Thurn-Albrecht, T.; Thelakkat, M. Influence of Fullerene Grafting Density on Structure, Dynamics, and Charge Transport in P_3HT-B-$PPC_{61}BM$ Block Copolymers. *Macromolecules* **2016**, *49* (5), 1637–1647.

(31) López, A. M.; Mateo-Alonso, A.; Prato, M. Materials Chemistry of Fullerene C_{60} Derivatives. *J. Mater. Chem.* **2011**, *21* (5), 1305–1318.

(32) Badamshina, E.; Estrin, Y.; Gafurova, M. Nanocomposites Based on Polyurethanes and Carbon Nanoparticles : Preparation, Properties and Application. *J. Mater. Chem. A* **2013**, *1* (22), 6509–6529.

(33) Vougioukalakis, G. C.; Roubelakis, M. M.; Orfanopoulos, M. Open-Cage Fullerenes: Towards the Construction of Nanosized Molecular Containers. *Chem. Soc. Rev.* **2010**, *39* (2), 817–844.

(34) Murata, M.; Murata, Y.; Komatsu, K. Surgery of Fullerenes. *Chem. Commun.* **2008**, *0* (46), 6083–6094.

(35) *Fullerenes and Related Structures | Andreas Hirsch | Springer*.

(36) Hirsch, A.; Brettreich, M. *Fullerenes: Chemistry and Reactions*; Wiley-VCH Verlag GmbH & Co. KGaA: Weinheim, Germany, 2005.

(37) Shinar, J. *Optical and Electronic Properties of Fullerenes and Fullerene-Based Materials*; Marcel Dekker, Inc.: New York, NY, U.S.A., 2000.

(38) Tumanskii, B. L.; Kalina, O. *Radical Reactions of Fullerenes and Their Derivatives*; Kluwer Academic Publishers: US, 2001.

(39) Lim, S. H.; Yi, J.; Moon, G. M.; Ra, C. S.; Nahm, K.; Cho, D. W.; Kim, K.; Hyung, T. G.; Yoon, U. C.; Lee, G. Y.; et al. Method for the Synthesis of Amine-Functionalized Fullerenes Involving SET-Promoted Photoaddition Reactions of α-Silylamines. *J. Org. Chem.* **2014**, *79* (15), 6946–6958.

(40) Zhang, J.; Yang, W.; He, P.; Zhu, S.; Wang, S. Microwave- promoted One- Pot Three-Component Reaction to [60]Fulleropyrrolidine Derivatives. *Synth. Commun.* **2005**, *35* (1), 89–96.

(41) Isobe, H.; Tomita, N.; Nakamura, E. One-Step Multiple Addition of Amine to [60]Fullerene. Synthesis of Tetra(amino)fullerene Epoxide under Photochemical Aerobic Conditions. *Org. Lett.* **2000**, *2* (23), 3663–3665.

(42) Richardson, C. F.; Schuster, D. I.; Wilson, S. R. Synthesis and Characterization of Water-Soluble Amino Fullerene Derivatives. *Org. Lett.* **2000**, *2* (8), 1011–1014.

(43) Chiang, L. Y.; Upasani, R.; Swirczewski, J. W.; Creegan, K. Synthesis of Fullerols as Polyhydroxylated Fullerene Derivatives. *MRS Online Proc. Libr. Arch.* **1992**, *247*.

(44) Chiang, L. Y.; Wang, L.-Y.; Swirczewski, J. W.; Soled, S.; Cameron, S. Efficient Synthesis of Polyhydroxylated Fullerene Derivatives via Hydrolysis of Polycyclosulfated Precursors. *J. Org. Chem.* **1994**, *59* (14), 3960–3968.

(45) Arrais, A.; Diana, E. Highly Water Soluble C60 Derivatives: A New Synthesis. *Fuller. Nanotub. Carbon Nanostructures* **2003**, *11* (1), 35–46.

(46) Goswami, T. H.; Nandan, B.; Alam, S.; Mathur, G. N. A Selective Reaction of Polyhydroxy Fullerene with Cycloaliphatic Epoxy Resin in Designing Ether Connected Epoxy Star Utilizing Fullerene as a Molecular Core. *Polymer* **2003**, *44* (11), 3209–3214.

(47) Djordjevic, A.; Canadanovic-Brunet, J. M.; Vojinovic-Miloradov, M.; Bogdanovic, G. Antioxidant Properties and Hypothetic Radical Mechanism of Fullerenol $C_{60}(OH)_{24}$. *Oxid. Commun.* **2004**, *27* (4), 806–812.

(48) Zhang, J.-M.; Yang, W.; He, P.; Zhu, S.-Z. Efficient and Convenient Preparation of Water-Soluble Fullerenol. *Chin. J. Chem.* **2004**, *22* (9), 1008–1011.

(49) Wang, S.; He, P.; Zhang, J.-M.; Jiang, H.; Zhu, S.-Z. Novel and Efficient Synthesis of Water- Soluble [60]Fullerenol by Solvent- Free Reaction. *Synth. Commun.* **2005**, *35* (13), 1803–1808.

(50) Ratnikova, O. V.; Melenevskaya, E. Y.; Amsharov, K. Y.; Vlasova, E. N.; Volchek, B. Z.; Gribanov, A. V.; Shibaev, L. A.; Zgonnik, V. N. The New Method for the Synthesis of Fullerols Based on Radical Reaction. *Fuller. Nanotub. Carbon Nanostructures* **2005**, *12* (1-2), 155–158.

(51) Alves, G. C.; Ladeira, L. O.; Righi, A.; Krambrock, K.; Calado, H. D.; Gil, R. P. de F.; Pinheiro, M. V. B. Synthesis of $C_{60}(OH)_{18\text{-}20}$ in Aqueous Alkaline Solution under O^2-Atmosphere. *J. Braz. Chem. Soc.* **2006**, *17* (6), 1186–1190.

(52) Kokubo, K.; Matsubayashi, K.; Tategaki, H.; Takada, H.; Oshima, T. Facile Synthesis of Highly Water-Soluble Fullerenes More Than Half-Covered by Hydroxyl Groups. *ACS Nano* **2008**, *2* (2), 327–333.

(53) Wang, F. F.; Li, N.; Tian, D.; Xia, G. F.; Xiao, N. Efficient Synthesis of Fullerenol in Anion Form for the Preparation of Electrodeposited Films. *ACS Nano* **2010**, *4* (10), 5565–5572.

(54) Sardenberg, R. B.; Teixeira, C. E.; Pinheiro, M.; Figueiredo, J. M. A. Nonlinear Conductivity of Fullerenol Aqueous Solutions. *ACS Nano* **2011**, *5* (4), 2681–2686.

(55) Semenov, K. N.; Charykov, N. A.; Keskinov, V. N. Fullerenol Synthesis and Identification. Properties of the Fullerenol Water Solutions. *J. Chem. Eng. Data* **2011**, *56* (2), 230–239.

(56) Huang, H.; Zhang, G.; Liang, S.; Xin, N.; Gan, L. Selective Synthesis of Fullerenol Derivatives with Terminal Alkyne and Crown Ether Addends. *J. Org. Chem.* **2012**, *77* (5), 2456–2462.

(57) Tian, C.; Castro, E.; Wang, T.; Betancourt-Solis, G.; Rodriguez, G.; Echegoyen, L. Improved Performance and Stability of Inverted Planar Perovskite Solar Cells Using Fulleropyrrolidine Layers. *ACS Appl. Mater. Interfaces* **2016**, *8* (45), 31426–31432.

(58) Hamaguchi, A.; Yoshizawa-Fujita, M.; Takeoka, Y.; Rikukawa, M. Synthesis and Characterization of Organic-Inorganic Layered Perovskite Compounds Using Fullerene Derivatives. *Adv. Mater. Res.* **2012**, *409*, 492–496.

(59) Suzuki, H.; Notsu, K.; Takeda, Y.; Sugimoto, W.; Sugahara, Y. Reactions of Alkoxyl Derivatives of a Layered Perovskite with Alcohols: Substitution Reactions on the Interlayer Surface of a Layered Perovskite. *Chem. Mater.* **2003**, *15* (3), 636–641.

(60) Akbarian-Tefaghi, S.; Teixeira Veiga, E.; Amand, G.; Wiley, J. B. Rapid Topochemical Modification of Layered Perovskites via Microwave Reactions. *Inorg. Chem.* **2016**, *55* (4), 1604–1612.

(61) Armstrong, A. R.; Anderson, P. A. Synthesis and Structure of a New Layered Niobium Blue Bronze: Rb2LaNb2O7. *Inorg. Chem.* **1994**, *33* (19), 4366–4369.

(62) Chao, T.-C.; Song, G.; Hansmeier, N.; Westerhoff, P.; Herckes, P.; Halden, R. U. Characterization and Liquid Chromatography-MS/MS Based Quantification of Hydroxylated Fullerenes. *Anal. Chem.* **2011**, *83* (5), 1777–1783.

(63) Chiang, L. Y.; Bhonsle, J. B.; Wang, L.; Shu, S. F.; Chang, T. M.; Hwu, J. R. Efficient One-Flask Synthesis of Water-Soluble [60]fullerenols. *Tetrahedron* **1996**, *52* (14), 4963–4972.

Appendix B. Incorporating More Elaborate Structures in the Interlayer

B.1 Introduction

Other than grafting or intercalation of simple alkyl chains in the interlayer of the layered hosts, more compicated structures containing hydroxyl or amine functional groups are also prone to react with the terminal oxygens.[1–6] In this chapter the reactivity of $HLaNb_2O_7$ perovskite with a number of organics with more elaborate structures will be reviewed. Figure B-1 shows the structure of the organics that are mainly investigated in this chapter: 2-allylphenol, benzyl alcohol, and 4-amino-1,2,4-triazole.

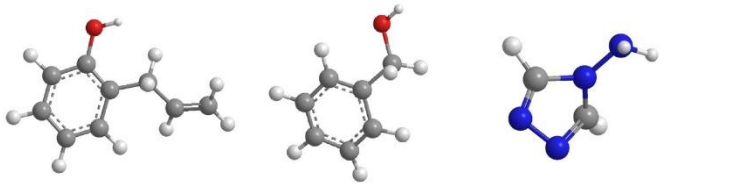

Figure B- 1: The structure of the organics incorporated in the interlayer.

The reactivity of hydroxymethylferrocene was also investigated in a few trials. Considering the structure of this compound presented in Figure B-2, it is highly expected that the ferrocene component grafts to the terminal oxygen via covalent bonds forming because of its hydroxymethyl functional groups.

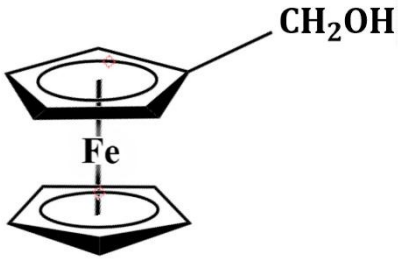

Figure B- 2: Structure of hydroxymethylferrocene.

The ability of organic-inorganic hybrids to pick up organic chains from an organic solvent is also briefly reviewed in the last part of this chapter. This so-called *adsorption* was done by studying the pickup of either n-octane chains by n-decoxy-$LaNb_2O_7$ hybrid, or toluene by benzyl alcoxy- $LaNb_2O_7$ (Figure B-3).

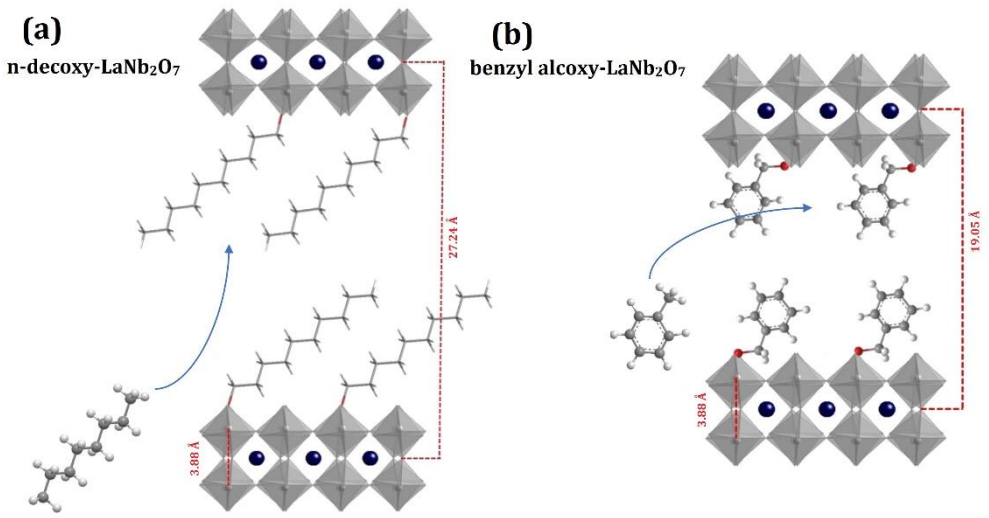

Figure B- 3: Adsorption of organic chains by the interlayer of the hybrid; (a) n-octane by n-decoxy-$LaNb_2O_7$, and (b) toluene by benzyl alcoxy-$LaNb_2O_7$.

B.2 Grafting 2-Allylphenol

As presented in Chapter 4 of this dissertation, both saturated and unsaturated cyclic and linear alcohols were grafted onto perovskite nanosheets via rapid microwave-assisted reactions. The reactivity of the terminal oxygens in the bulk perovskite is comparable to the surface oxygens, and so similar grafting reactions can be demonstrated for leyered perovskites as well as what was provided earlier for the nanosheets. Some of the results presented in this appendix were obtained prior to the microwave breakthrough, and so were carried out via conventional heating and longer reactions. However, conditions similar to those presented in the first chapters can be investigated for the bulk perovskites as well in the future, and are most likely to successfully work. The only difference between the reactivity of the layered perovskite and the nanosheets, is the limitation present for large organics permeating the interlayer as opposed to openly exposed oxygens on nanosheets. So, it is strongly recommended to prepare n-decoxy-$LaNb_2O_7$ (n-decoxy-LN) in order to successfully allow for the penetration of any organic in the interlayer, and the exchange of the n-decoxy group with the target organic. This intermediate hybrid has an interlayer spacing of about 16 Å which makes it a great starting material for almost any successful exchange with most of organics with amine or hydrxoyl functional groups, regardless of their sizes. In case of targeting unsaturated organics, reaction mixture can be sealed inside a

microwave vessel in an argon glovebox, and taken out to go through a microwave-assisted reaction while maintained under neutral atmosphere. The equivalent conventional approach presented in this section (emlpoyed a while before the microwave innovation), is a 7-d treatment in argon glovebox maintained at 80 ˚C. Typically 0.05 g of n-decoxy-LN was mixed with 3 mL of the pure solvent (target organic), and constantly stirred during the reaction. Unsaturated organics included: linear alcohols such as 3-buten-1-ol, 5-hexen-1-ol, 9-decen-1-ol, and cyclic alcohols such as 2-allylphenol. Figure B-4a presents the XRD pattern of 2-allylphenoxy-LN compared to that of n-decoxy-LN. A close-up of the first peaks of 5-hexen-1-oxy-, 9-decen-1-oxy-, and 2-allylphenoxy-LN is then provided in Figure B-4b versus their host.

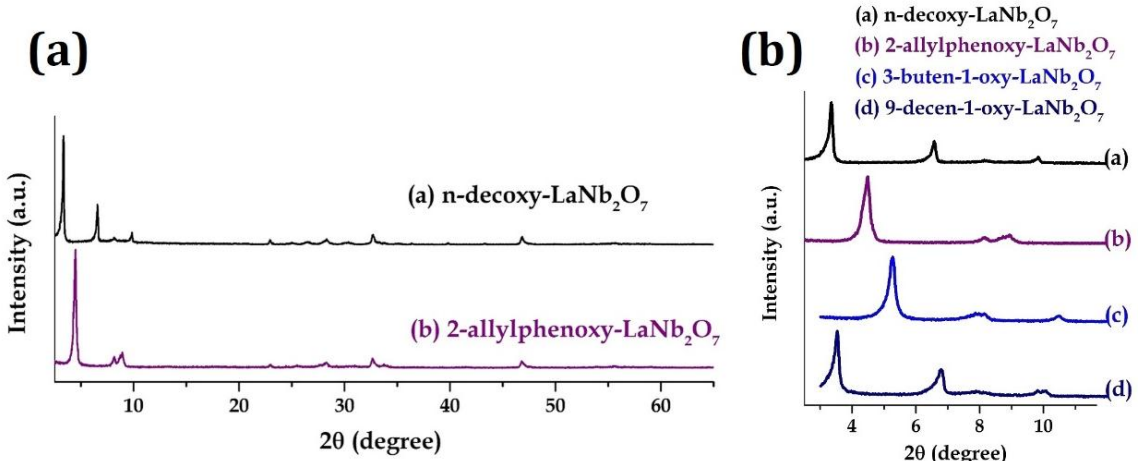

Figure B- 4: XRD pattern of n-decoxy-LN versus some of monomer-grafted perovskites.

Further reactions in the interlayer of the hybrid perovskites incorporating monomers are deemed pretty promising once microwave-assisted reactions are employed; this can be investigated in the future via a new approach towards new and known chemistries.[7–10]

B.3 Grafting Benzyl Alcohol

Successful grafting of benzyl alcohol does not call for any harsh conditions; leaving n-decoxy-LN in a few mL of benzyl alcohol at RT without any stirring, benzyl alcoxy-$LaNb_2O_7$ (BA-LN) can be prepared overnight. Various microwave heating conditions were explored to find out the shortest route to obtain BA-LN, and 1 h at 60 ˚C (maximum power of 300 W) appeared to be the best method. In case of applying higher temperatures for the synthesis of BA-LN, the sample comes out with an orange/brown color and less crystallinity. As n-decoxy-LN

compound (more a cotton shade of white) goes through an exchange reaction with benzyl alcohol, the color of the BA-LN product comes out as a sharp yellow color (Figure B-5). This change in the physical appearance suggests a different optical behavior in this product; absorbance in the visible range as opposed to the starting material (Figure B-6). The yellow color of as-synthesized BA-LN seems to change to orange upon exposure to sunlight (this change usually takes about a few months in ambient condition). Figure B-7 presents the XRD pattern of as-synthesized BA-LN and the same sample rescanned after 3 months exposure to sunlight, and it is clear that the interlayer spacing of BA-LN slightly shrinks upon this exposure (2θ shifting from 4.50˚ to 4.75˚). Interestingly, the orange aged BA-LN has a different absorbance when tested using diffuse-reflectance UV-Visible spectroscopy (Figure B-6 e versus d). This optical response strongly suggests a specific arrangement of phenyl rings grafted in the interlayer, possibly similar to π-π stacking.

Figure B- 5: Sharp yellow color of as-synthesized benzyl alcoxy-$LaNb_2O_7$.

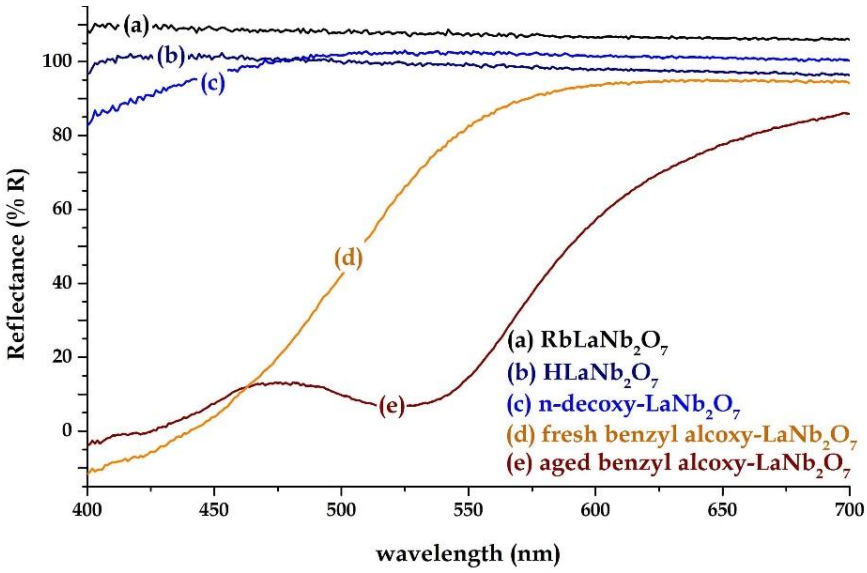

Figure B- 6: Diffuse-reflectance UV-Vis for (a) $RbLaNb_2O_7$, (b) $HLaNb_2O_7$, (c) n-decoxy-$LaNb_2O_7$, and benzyl alcoxy-$LaNb_2O_7$ (d) as-synthesized and (e) aged.

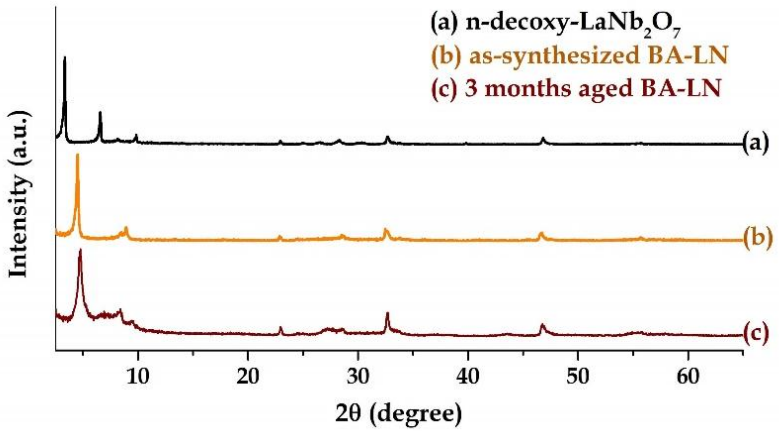

Figure B- 7: XRD patterns of BA-LN (b) as-synthesized and (c) aged, compared to (a) n-decoxy-$LaNb_2O_7$.

Another aspect investigated over BA-LN hybrid, was the intercalation of alkali metals in the interlayer. The idea was to incorporate electron-donating components into the stacked phenyl rings of the interlayer as illustrated in Figure B-8, producing A˚-BA-LN samples (where A was Li and K). Li˚ was introduced by reacting 2 mL of n-butyllithium solution (Sigma-Aldrich, 1.6 M in hexanes) with 10 mg BA-LN pressed as a pellet. While the pellet was submerged in the solution, gentle stirring was continued for 5 d at RT in an argon glovebox (without breaking the pellet). The yellow pellet turned into black in a few hours, and after the completion of the reaction was rinsed a few times with hexanes (every time pipetting out the solution to the waste and replacing it with fresh hexanes). After the final wash, the pellet was left for several hours with an open cap to fully dry out. The intercalation of K˚ was attempted by reacting 10 mg BA-LN pressed pellet with potassium vapor in evacuated and sealed 13-mm Pyrex tube for 6 d at 150 ˚C (6 mg of soft solid potassium element was placed in a smaller Pyrex tube trapped in the larger sealed tube, as presented in Figure B-9). The pellets of A˚-BA-LN were treated as air-sensitive samples: the black pellets were sealed using polymer film under argon prior to air exposure, and the XRD scans were run immediately after taking them out of the glovebox. Figure B-10 presents the XRD patterns of BA-LN, Li˚-BA-LN, and K˚-BA-LN samples (the peaks marked with star are due to the protective polymer film used for sealing the sample).

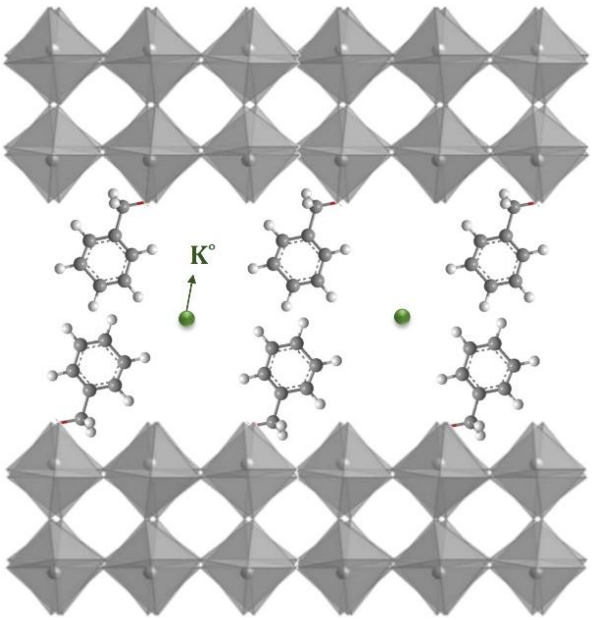

Figure B- 8: Illustration of alkali metal intercalation in benzyl alkocy-$LaNb_2O_7$ (here K° is presented as an example).

Figure B- 9: (a) sharp yellow BA-LN prior to intercalation, and (b) post-reaction picture of BA-LN pellet exposed to K° vapor under vacuum.

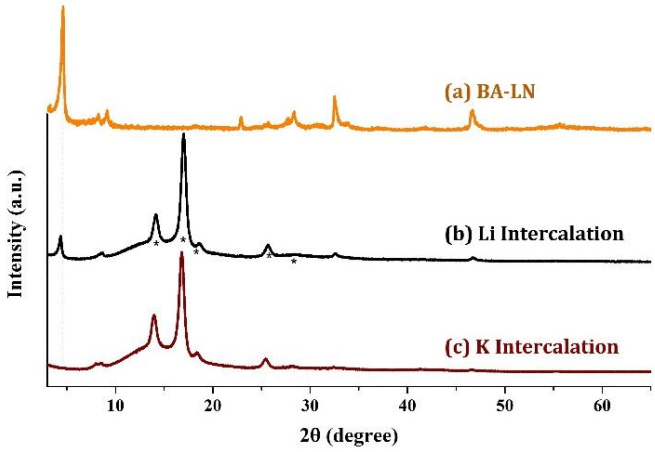

Figure B- 10: XRD pattern of (a) BA-LN compared to intercalation products using (b) Li° and (c) K°.

As presented in Figure B-10, the intercalation reaction with K˚ does not seem to be successful due to lacking a first peak. This is most likely due to the instability of BA-LN at 150 ˚C for a few days (even though 150 ˚C is still much lower than typical intercalation temperatures). This was further supported by running BA-LN in TGA-DSC under argon-oxygen atmosphere with an isotherm at 150 ˚C for a few hours: the sharp yellow sample already discolored to blackish brown indicating the initiation of decomposition for this sample. However, the intercalation of Li˚ turns out to be very promising comparing the two XRD patterns in Figure B-10 a and b. The first peak shifts to a lower angle after Li˚ intercalation, indicating a slight expansion in the interlayer spacing (which makes sense considering the addition of Li˚ component to benzyl alcoxy grafted groups). Li˚-BA-LN synthesis was replicated a few times, and tested using SQUID to investigate any interesting magnetic properties. Even though it showed an interesting magnetic behavior once as presented in Figure B-11, we were unable to replicate this result in the other batches. Considering the Zero Field Cooling (ZFC) and Field Cooling (FC) behavior of the sample measured at a 3500 Oe field as presented in Figure B-11 a, there is a magnetic event happening at 40 K (ignoring the noise at about 75 K). The magnetic hysteresis curve was then obtained at 5 K for this sample, showing a diamagnetic behavior mostly, with a different response in fields close to zero as provided in Figure B-11 b. (resembling either paramagnetic or antiferromagnetic behavior in this tiny portion of the field).

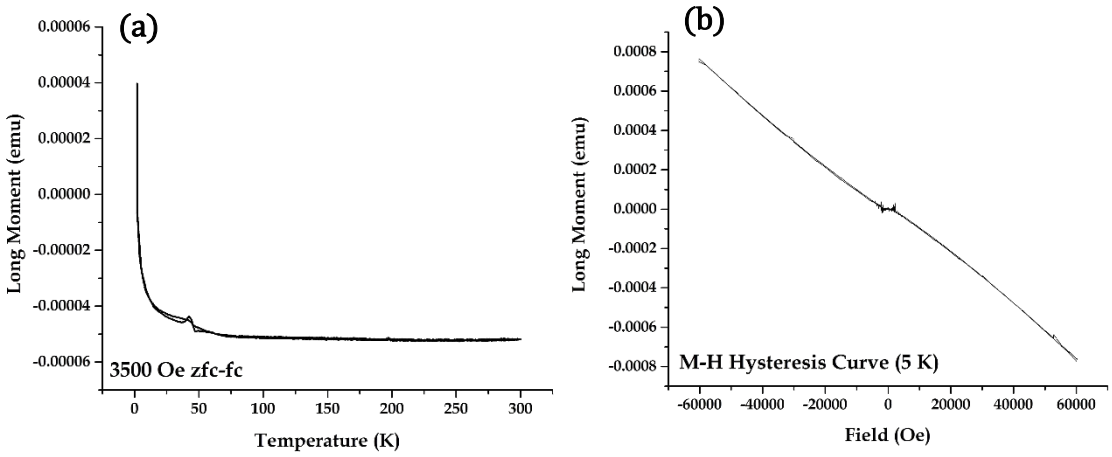

Figure B- 11: (a) ZFC-FC at 3500 Oe, and (b) hysteresis curve at 5 K for Li˚-BA-LN sample.

Even though we were unable to replicate the interesting result provided in Figure B-11, the sensitivity of the sample might be a factor contributing to this issue. Hopefully BA-LN

hybrid and metal intercalated variations of it can be further studied in the future, as they seem to offer interesting magnetic and optical properties that are yet to be explored.

B.4 Attempted Intercalation of 4-Amino-1,2,4-Triazole

Intercalation of 4-amino-1,2,4-triazole (AT) was carried out using different intermediates: n-propoxy-$LaNb_2O_7$, n-pentoxy-$LaNb_2O_7$, n-decoxy-$LaNb_2O_7$, 1-propylamine-$LaNb_2O_7$, and 1-hexylamine-$LaNb_2O_7$. All of these intermediates were dispersible in water except for n-decoxy-$LaNb_2O_7$. In case of these more hydrophilic intermediates, typically 0.1 g AT was dispersed in 10 mL of water, and reacted with 20 mg of the hybrid intermediate in the microwave- for1 h at 100 ˚C with the maximum power of 450 W in case of n-pentoxy-$LaNb_2O_7$ and 1-hexylamine-$LaNb_2O_7$, and 2 h at 80 ˚C with the maximum power of 300 W for n-propoxy-$LaNb_2O_7$ and 1-propylamine-$LaNb_2O_7$). Unfortunately, all the products obtained were identical to their starting materials, indicating no AT intercalation. Since n-decoxy-$LaNb_2O_7$ is very hydrophobic, AT intercalation trials using this intermediate was done in toluene as the solvent. In this case, typically 1 g AT was dissolved in 12 mL of toluene and reacted with 20 mg of the intermediate (either 1 h at 80 ˚C with the maximum power of 800 W, or 1 h at 100 ˚C with the maximum power of 1000 W, using a Weflon button in both cases). This reaction seemed to yield an acceptable XRD pattern as presented in Figure B-12. It is suggested to carry out more replicates similar to these successful conditions, and study the quality of intercalation via Raman spectroscopy and TGA analysis. Based on the successful surface-tailoring of the nanosheets with AT reported in Chapter 4, further tuning the reaction conditions is expected to yield AT-intercalated products with optimal loading.

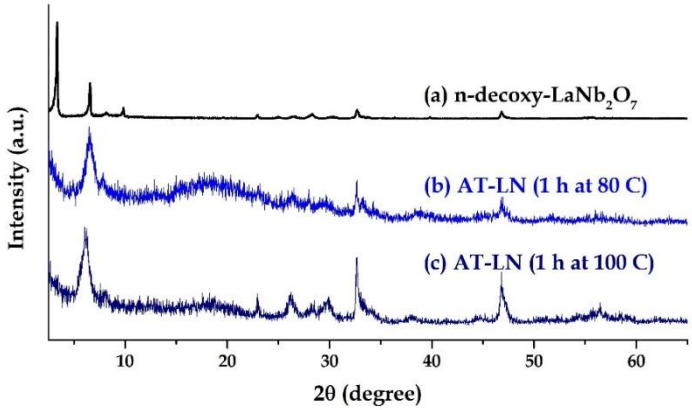

Figure B- 12: The most promising conditions obtained for the intercalation of 4-amino-1,2,4-triazole (AT).

B.5 Attempted Grafting of Hydroxymethylferrocene

Grafting of hydroxymethylferrocene (HMF) was performed using n-decoxy-LN and n-propoxy-LN intermediates. Typically, 20 mg of the intermediate hybrid was added to 100 mg HMF (Alfa Aesar, 97%) dissolved in 3 mL of toluene. Due to the sensitivity of HMF to moisture, the mixtures were maintained under argon in a glovebox, while constantly stirred for 7 d at 80 ˚C. The product was rinsed a few times with toluene, every time settling for a few hours to let the powder precipitate, and then pipetting out the solution to the waste and replacing it with fresh toluene. After the final wash, the wet powder was evacuated in the chamber of the glovebox, placed in a container filled with drierite desiccant and capped under argon. The sample was taken out while staying sealed, and was exposed to the ambient condition for less than 30 minutes for XRD and vibrational spectroscopy characterization.

Comparing the XRD pattern of the n-decoxy-LN sample after the experiment to that of the starting material (Figure B-13 b versus a), the same first reflections are observed, only broader and less intense. It is also notable that the crystallinity decreases based on the loss of the majority of the high angle peaks. Repeating the experiment with n-propoxy-LN also lead into similar results, only this time the loss of the high angle reflections was not as significant (Figure B-13 c and d). Further characterization with Raman and IR (Figures B-14 and B-15, respectively) suggests that HMF is actually present in the products (due to the existence of HMF characteristic peaks in the products). However, since the XRD patterns indicate no significant changes in the interlayer spacings, it is highly suggested that HMF only partially grafts to the surface rather than disturbing the interlayer and taking over the

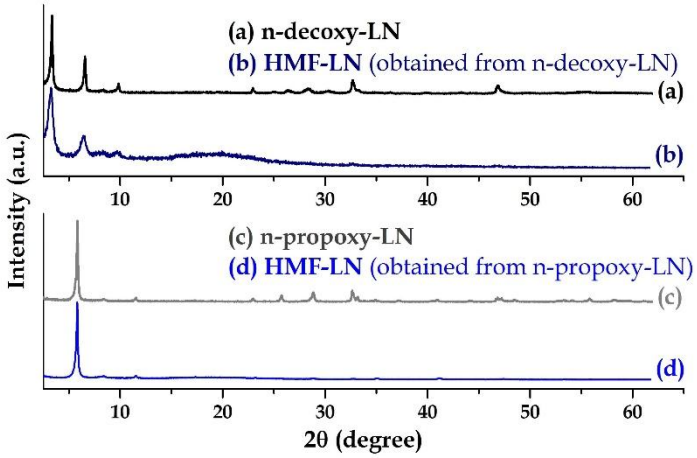

Figure B- 13: XRD patterns of HMF-LN samples obtained from (b) n-decoxy-LN and (d) n-propoxy-LN, compared to their hosts (respectively provided in a and c).

current organic. In case of n-decoxy-LN, it is also possible that HMF causes partial delamination of the layered hybrid, while the n-decoxy interlayer groups are mostly maintained.

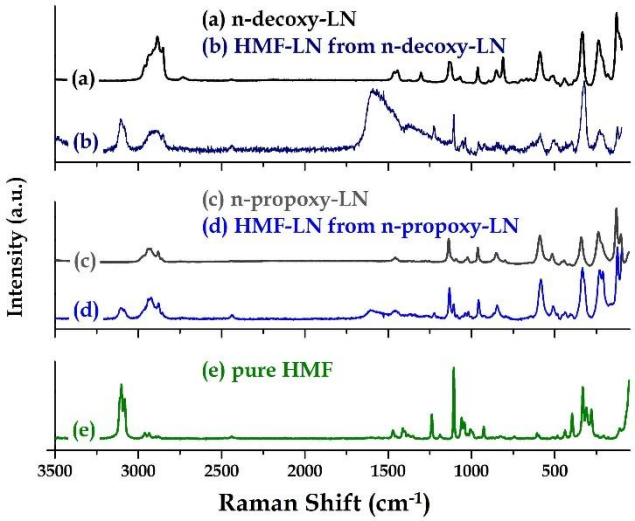

Figure B- 14: Raman spectra of (a) n-decoxy-LN and (c) n-propoxy-LN compared to (b, d) HMF-LN samples, as well as (e) pure HMF.

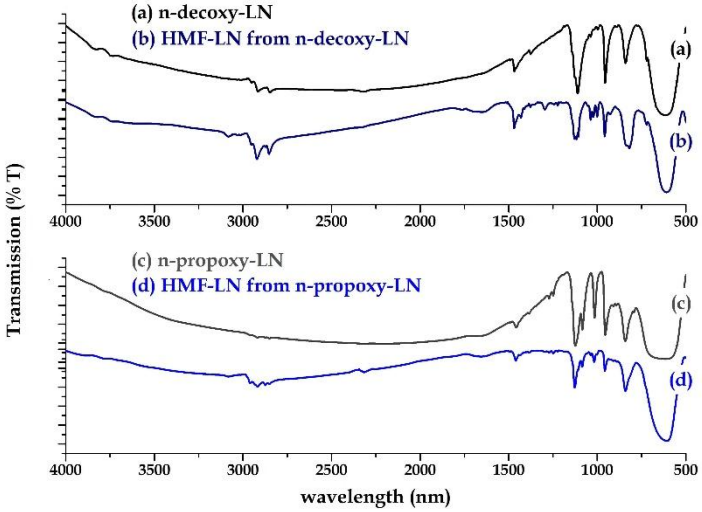

Figure B- 15: IR spectra of HMF-LN samples obtained from (b) n-decoxy-LN and (d) n-propoxy-LN, compared to their hosts (respectively provided in a and c).

B.6 Organic Adsorption to the Layered Hybrids

Three criteria were taken into account selecting the organic solvent and layered hybrid pairs: firstly, only organics similar to the interlayer groups are expected to have strong

interactions and possible adsorption (for instance a possible van der Waals interaction between n-octane target and n-decoxy groups, or possible π-π stacking as well as van der Waals interactions when toluene is targeted for the adsorption in benzyl alcoxy-grafted hybrids), secondly, the boiling point of the target organic should be high enough not to quickly escape the interlayer after adsorption (about 110 ˚C and 125 ˚C for toluene and n-octane, respectively), and lastly, not having any functional groups in the target organic which would interfere in an exchange reaction with the interlayer organic groups . To experimentally investigate the organic adsorption idea, 20 mg of the layered hybrid was dispersed in 6 mL of the pure target organic, and heated in microwave for 30 minutes at 80 ˚C (maximum power of 800 W). The products were not washed at all, not to intentionally extract the organics possibly trapped in the interlayer. After the reaction, the sample was centrifuged, and then RT dried after disposing of the supernatant.

The products were tested using XRD and TGA-DSC. Theoretically, XRD might stay the same after the experiment if the target organic is just entering the voids in between the interlayer organics, or might as well show a slight expansion in the interlayer spacing. However, a larger weight loss is expected in case of a successful organic adsorption. Adsorption of toluene in BA-LN consistently showed no change in the weight loss after the experiment, and the XRDs were also identical. Based on Figure B-16, some of the trials investigating n-octane adsorption yielded very interesting results: comparing the XRD pattern of (a) n-decoxy-LN with (b and c) two of the trials, broadening and shouldering of the 00ℓ peaks are clear after the experiment. Thermal analysis was then performed on the host versus these two trials (Figure B-17 a, b, and c), which further indicated successful adsorption of n-octane due to showing higher weight losses after the reaction: weight losses of 20%, 31%, and 39%, respectively, indicating a loading of 0.72 mole n-decoxy per 1 mole $LaNb_2O_7$ in the host, and addition of (b) 0.80 mole n-octane and (c) 1.46 mole n-octane per 1 mole n-decoxy-LN. However, a few exactly similar replicates yielded XRD patterns and TGA curves identical to the host, suggesting the poor reproducibility of the previous promising results. Running the experiment either for longer times (1 h at 80 ˚C), or at a lower temperature (12 h at RT, or 1 h at 60 ˚C), also lead into TGA-DSC curves indicating no trace of n-octane adsorption.

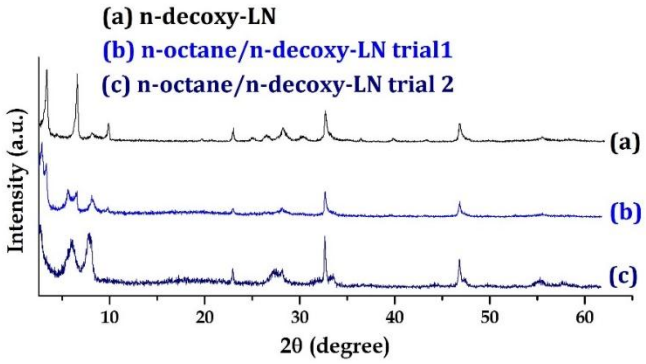

Figure B- 16: XRD patterns of (a) n-decoxy-LN, and (b, c) two promising trials inserting n-octane in n-decoxy-LN hybrid.

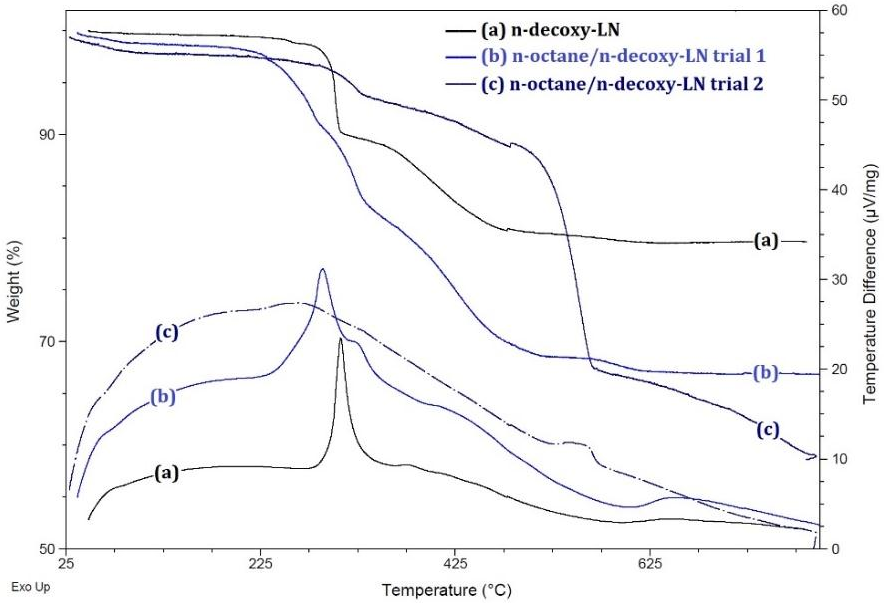

Figure B- 17: TGA-DSC curves showing an increase in the weight loss after two promising trials perfomed for the adsorption of n-octane to n-decoxy-LN hybrid.

The results obtained under the conditions studied here, seem to be inconclusive. In order to support the idea of organic adsorption to the interlayer of perovskite-based hybrids, more promising and reproducible results have to be attained.

B.7 Conclusions

As described throughout this chapter, some complementary experiments and tests have to be carried out in order to obtain more conclusive results in each case. The insertion of unsaturated organics has a simple and promising chemistry and only calls for more replicates and

following polymerization. Optical and magnetic properties of BA-LN and A˚-BA-LN products need to be more vastly studied, and already show interesting features as addressed above. More conditions are to be investigated for the successful intercalation of AT in layered perovskites, yielding more crystalline samples. Grafting of hydroxymethylferrocene in the interlayer of the perovskite seemed unsuccessful, only suggesting surface reactions or partial exfoliation of the layered habrid. In case of organic pickup by the interlayer of organic-inorganic hybrids, a couple of interesting results were obtained which appeared to be irreproducible; this idea also needs to be investigated more in order to draw any solid conclusions.

B.8 References

(1) Wang, Y.; Delahaye, E.; Leuvrey, C.; Leroux, F.; Rabu, P.; Rogez, G. Efficient Microwave-Assisted Functionalization of the Aurivillius-Phase Bi2SrTa2O9. Inorg. Chem. 2016, 55 (8), 4039–4046.

(2) Giannici, F.; Mossuto Marculescu, A.; Cattaneo, A. S.; Tealdi, C.; Mustarelli, P.; Longo, A.; Martorana, A. Covalent and Ionic Functionalization of HLN Layered Perovskite by Sonochemical Methods. Inorg. Chem. 2017, 56 (1), 645–653.

(3) Yoshioka, S.; Takeda, Y.; Uchimaru, Y.; Sugahara, Y. Hydrosilylation in the 2D Interlayer Space between Inorganic Layers: Reaction between Immobilized C=C Groups on the Interlayer Surface of Layered Perovskite HLaNb2O7·xH2O and Chlorohydrosilanes. J. Organomet. Chem. 2003, 686 (1–2), 145–150.

(4) Toihara, N.; Yoneyama, Y.; Shimada, A.; Tahara, S.; Sugahara, Y. Intercalation of Triethylphosphine Oxide Bearing a Phosphoryl Group into Dion–Jacobson-Type Ion-Exchangeable Layered Perovskites. Dalton Trans 2015, 44 (7), 3002–3008.

(5) Shimada, A.; Yoneyama, Y.; Tahara, S.; Mutin, P. H.; Sugahara, Y. Interlayer Surface Modification of the Protonated Ion-Exchangeable Layered Perovskite HLaNb2O7 • xH2O with Organophosphonic Acids. Chem. Mater. 2009, 21 (18), 4155–4162.

(6) Takeda, Y.; Suzuki, H.; Notsu, K.; Sugimoto, W.; Sugahara, Y. Preparation of a Novel Organic Derivative of the Layered Perovskite Bearing HLaNb2O7·nH2O Interlayer Surface Trifluoroacetate Groups. Mater. Res. Bull. 2006, 41 (4), 834–841.

(7) Uma, S.; Gopalakrishnan, J. Polymerization of Aniline in Layered Perovskites. Mater. Sci. Eng. B 1995, 34 (2–3), 175–179.

(8) Nam, H.-J.; Kim, H.; Chang, S. H.; Kang, S.-G.; Byeon, S.-H. Polymerization of Aniline in the Galleries of Layered HNbMoO6. Solid State Ion. 1999, 120 (1–4), 189–195.

(9) Moujahid, E. M.; Leroux, F.; Dubois, M.; Besse, J.-P. In Situ Polymerisation of Monomers in Layered Double Hydroxides. Comptes Rendus Chim. 2003, 6 (2), 259–264.

(10) Wang, Y.; Delahaye, E.; Leuvrey, C.; Leroux, F.; Rabu, P.; Rogez, G. Post-Synthesis Modification of the Aurivillius Phase Bi2SrTa2O9 via In Situ Microwave-Assisted "Click Reaction." Inorg. Chem. 2016, 55 (19), 9790–9797.

Appendix C. Bridging Layered Perovskites: $A_{2-x}La_2Ti_{3-x}Nb_xO_{10}$ and Ion Exchange Products

C.1 Introduction

Ion exchange (IE) is a very simple and effective topochemical manipulation technique for the modification of Dion-Jacobson (DJ) and Ruddlesden-Popper (RP) phases. IE is performed by replacing the interlayer cations with other cations or cationic structural units in solution, molten salt or under acidic conditions.[1–3] The interlayer ion can be simply exchanged with another ion with the same oxidation state,[4] or one of a different oxidation state (aliovalent exchange).[3,5] In cases an ionic array can also be formed (co-exchange).[6–8] Regardless, the specific stoichiometry of the replacing unit will keep the overall interlayer charge the same as the initial stage in the host. Considering the interlayer charge varying from +2 in the RP host to +1 in the DJ type, ion exchange products with simple metal halides (MX_2) will show distinct structures and properties. While $A_2La_2Ti_3O_{10}$ as a RP phase leads into aliovalent exchange with M^{2+} producing $MLa_2Ti_3O_{10}$,[3] co-exchange between DJ-type $ACa_2Nb_3O_{10}$ and MX_2 results in the formation of metal-halide arrays within perovskite slabs in $(MX)Ca_2Nb_3O_{10}$ product.[6,7] $A_{2-x}La_2Ti_{3-x}Nb_xO_{10}$ system ($0 \leq x \leq 1$) first reported by Uma et al.,[9] corresponds to a triple layered solid solution of $A_2[La_2Ti_3O_{10}]$ RP phase and $A[La_2Ti_2NbO_{10}]$ DJ phase. Therefore, $A_{2-x}La_2Ti_{3-x}Nb_xO_{10}$ (as demonstrated in Figure C-1) has a variable interlayer cation density and is bridging between the two end members.[9,10] Based on the literature, IE reactions with metal halides have never been studied for this bridging solid solution. Structure determination and topotactic manipulation of this intermediate bridging compound will be studied in this chapter. In order to meet this goal, $A_{2-x}La_2Ti_{3-x}Nb_xO_{10}$ system ($0 \leq x \leq 1$, A = Li, Na, K, and Rb) was prepared via ceramic method and IE reactions. IE with $CuCl_2$ as a metal halide was successfully done starting from the two end members (x = 0 and x = 1) and further efforts were done to perform the same manipulation on the intermediate hosts.

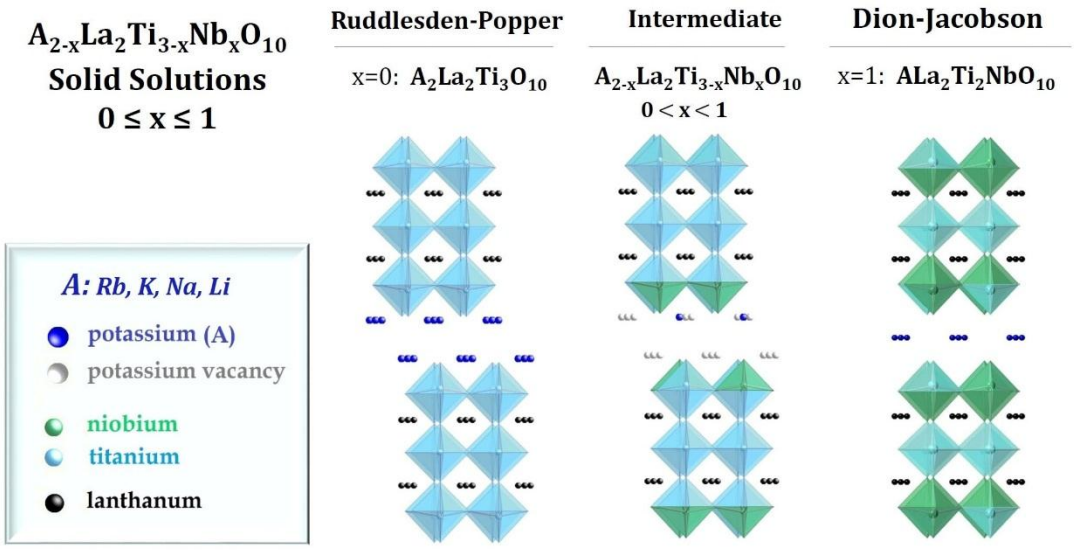

Figure C- 1: Structure of $A_{2-x}La_2Ti_{3-x}Nb_xO_{10}$ solid solutions where $0 \le x \le 1$.

C.2 Experimental

$A_{2-x}La_2Ti_{3-x}Nb_xO_{10}$. Members of $A_{2-x}La_2Ti_{3-x}Nb_xO_{10}$ (A = Rb, K, Na where x = 0, A = Rb where 0 < x < 1, and A= Rb, Cs where x = 1) were prepared through high temperature solid state reactions. Cs_2CO_3 (Alfa Aesar, 99.994%), Rb_2CO_3 (Alfa Aesar, 99.975%), K_2CO_3 (Alfa Aesar, 99.997%), Na_2CO_3 (Alfa Aesar, 99.997%), La_2O_3 (Alfa Aesar, 99.99%), TiO_2 (Alfa Aesar 99.995%) and Nb_2O_5 (Alfa Aesar, 99.9985%) were mixed in stoichiometric ratios according to the following equation (Eq. C-1) and in the presence of excess amount of carbonate (30%) to compensate for its volatilization. The mixture was pre-heated at 850 ˚C for 12 h, and heated at 1050 ˚C for 48 h in an alumina crucible in air, with at least three intermediate grindings.[9–11] (Note: La_2O_3 and Nb_2O_5 were preheated at 1000 ˚C for 12 h in order to eliminate any impurities). For the synthesis of the RP end members with Na or K as the interlayer cations ($A_{2-x}La_2Ti_{3-x}Nb_xO_{10}$ where x = 0 and A = Na, K), an extra pre-heating step at 550 ˚C prior to 850 ˚C found to be necessary. For the DJ end member ($A_{2-x}La_2Ti_{3-x}Nb_xO_{10}$ where x = 1 and A = Rb or Cs), it was best to do an extra heating step at 1150˚C for 12 h after the completion of heating at 1050˚C. In case of the solid solutions ($A_{2-x}La_2Ti_{3-x}Nb_xO_{10}$ where 0 < x < 1 and A = Rb), more intermediate grinding and less extreme heating had to be performed. Studying the structural evolution of $Rb_{2-x}La_2Ti_{3-x}Nb_xO_{10}$ (x = 0.15) using XRD revealed that more than 2 h heating at 1050 ˚C after the preheating step would yield a mixture of the end members rather than the

metastable solid solution. Note that the temperature has to be increased from 850 ˚C to 1050 ˚C in 50 ˚C increments with intermediate grindings in between. These extra grinding steps would compensate for the shorter reaction time and provide acceptable crystallinity. Direct synthesis of $Na_{1.65}La_2Ti_{2.65}Nb_{0.35}O_{10}$ from its oxide and carbonate reagents was also performed by heating the ground mixture at 550 ˚C (18 hr), 850 ˚C (24 hr), and finally 1050 ˚C (12 hr) with three intermediate grindings. After the reaction, the products were washed with copious amount of distilled water, rinsed with acetone and dried at 130˚C for several hours.

Equation C- 1:

$$(2-x)\,A_2CO_3 + 2\,La_2O_3 + (6-2x)\,TiO_2 + xNb_2O_5 \rightarrow 2\,A_{2-x}La_2Ti_{3-x}Nb_xO_{10} + (2-x)\,CO_2 \quad ;\ 0 \le x \le 1$$

Ion exchange was used as a topochemical method to obtain $A_{2-x}La_2Ti_{3-x}Nb_xO_{10}$ from corresponding nitrates (where A=Li and x=0, as well as cases where A=Li, Na, K and $0 < x \le 1$). $Rb_{2-x}La_2Ti_{3-x}Nb_xO_{10}$ was ground in a 1:10 molar ratio with $LiNO_3$ (Alfa Aesar, 99%), $NaNO_3$ (Alfa Aesar 99.999%) and KNO_3 (Alfa Aesar, 99.994%) and heated at 330, 400, and 400˚C for 2-3 days, respectively. After the ion exchange reaction, the products were washed with distilled water, rinsed with acetone and dried at 130˚C for an hour.

$(CuCl_x)La_2Ti_{3-x}Nb_xO_{10}$. $(CuCl_x)La_2Ti_{3-x}Nb_xO_{10}$ members ($0 \le x \le 1$) were prepared through a low temperature ion exchange reactions. Pressed pellets of $A_{2-x}La_2Ti_{3-x}Nb_xO_{10}$ and $CuCl_2$ (Alfa Aesar, 99.995%) in a 1:2 molar ratio were placed inside a 13-mm Pyrex tube, sealed under vacuum (<10-4 Torr), and heated at 350˚C for various durations based on the type of the A cation. IE reactions on $A_{2-x}La_2Ti_{3-x}Nb_xO_{10}$, where $0 \le x < 1$, worked best for A = Li and Na, for 7 days and 14 days, respectively. In case of $A_{2-x}La_2Ti_{3-x}Nb_xO_{10}$ where x = 1 (the DJ end member), the IE reaction completed regardless of the interlayer cation - performed for 7, 14, 16, 10, and 8 days where A was Li, Na, K, Rb, and Cs, respectively. After the ion exchange reaction, the product was washed with distilled water to remove unreacted $CuCl_2$ and any alkali halide byproduct (ACl), and dried at 130˚C for an hour.

Characterization. X-ray powder diffraction (XRD) data was collected on a Philips X'Pert system equipped with Cu Kα radiation (λ=1.5418 Å) and a curved graphite monochromator. Typical scans were collected in continuous mode with a scan rate of 0.02°/s. The peak positions

and lattice parameters were refined by a least-squares method with the ChekCell program. A JEOL (model JSM-5410) scanning electron microscope (SEM) equipped with the energy dispersive analysis (EDS), EDAX (DX-PRIME) microanalytical system, was used for elemental analysis. Raman spectra were obtained with a Thermo-Fisher DXR dispersive Raman spectrometer using the λ=532 nm line with a spectral resolution of 3 cm^{-1}.

C.3 Results and Discussion

C.3.1 $A_2La_2Ti_3O_{10}$. Figure C-2 shows the XRD patterns of the RP end members. First reflection (assigned to ℓ = 2 of the 00ℓ set of planes) shifts to lower angles as the interlayer cation becomes larger (from Li to Rb), indicating layer expansion as expected. IE with $CuCl_2$ was performed successfully starting from $Li_2La_2Ti_3O_{10}$ and $Na_2La_2Ti_3O_{10}$. XRD pattern of the $CuLa_2Ti_3O_{10}$ product is presented in Figure C-3 showing a good agreement with the reference pattern generated based on the crystal structure of $CuLa_2Ti_3O_{10}$.[3] Table C-1 summarizes the unit cell parameters of RP products ($A_2La_2Ti_3O_{10}$), which are all in good agreement with the literature values.[3,9,12,13]

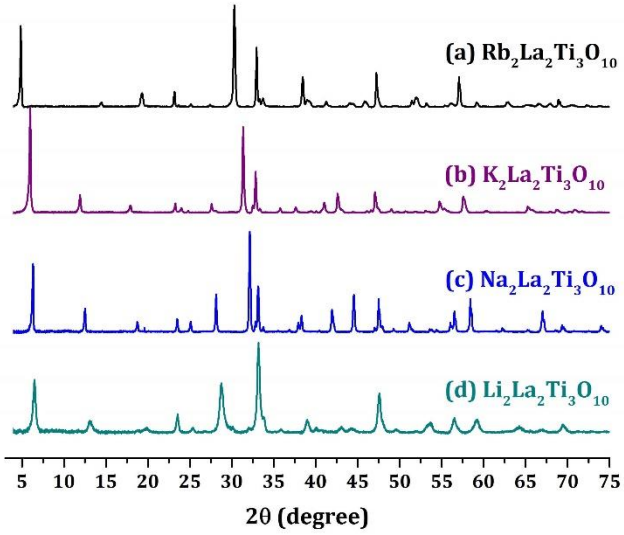

Figure C- 2: XRD patterns of the RP end members, $A_2La_2Ti_3O_{10}$, where A is (a) Rb, (b) K, (c) Na, and (d) Li.

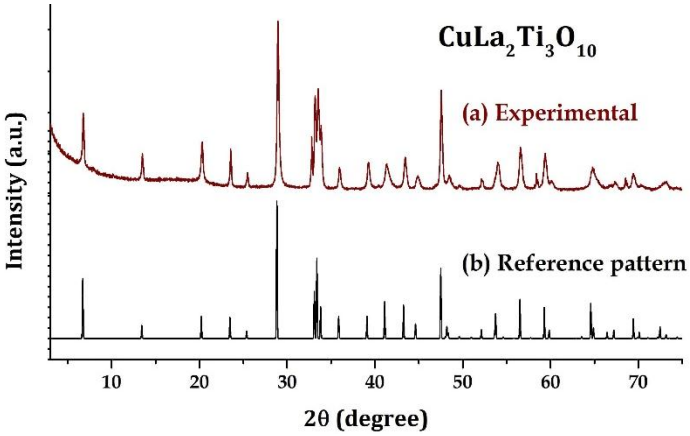

Figure C- 3: the XRD pattern of $CuLa_2Ti_3O_{10}$, (a) experimental trial versus (b) the reference pattern.

Table C- 1: Unit cell parameters of $A_2La_2Ti_3O_{10}$ (A = Li, Na, K, and Rb) and $CuLa_2Ti_3O_{10}$.

Unit Cell Parameters				
Compound	**Unit Cell (Å)**		**Literature Cell (Å)**	
	a	**c**	**a**	**c**
$Rb_2La_2Ti_3O_{10}$	3.882 (5)	30.2501(7)	3.898(3)	30.50(2)
$K_2La_2Ti_3O_{10}$	3.861(3)	29.6867(6)	3.8769(1)	29.824(1)
$Na_2La_2Ti_3O_{10}$	3.826(3)	28.4440(8)	3.83528(7)	28.5737(7)
$Li_2La_2Ti_3O_{10}$	3.824(3)	26.6197(8)	3.84116(1)	26.560(1)
$CuLa_2Ti_3O_{10}$	3.816(5)	26.124(1)	3.8248(2)	26.329(1)

C.3.2 $ALa_2Ti_2NbO_{10}$. Figure C-4 presents the XRD patterns of the DJ end members. As expected, the first reflection (typically $\ell = 1$ in 00ℓ) shifts to lower angles as the interlayer cation increases in size. In case of $NaLa_2Ti_2NbO_{10}$, existence of a hydrated form is obvious (the XRD pattern shown in light gray). The $(CuCl)La_2Ti_2NbO_{10}$ presented in Figure C-5 is the IE product of $CuCl_2$ and $LiLa_2Ti_2NbO_{10}$, however, the reaction was also successful from all the other members as presented in Figure C-6. The XRD pattern of the $(CuCl)La_2Ti_2NbO_{10}$ in Figure C-5 is compared to that of $LiLa_2Ti_2NbO_{10}$ as the starting material, as well as $(CuCl)Ca_2Nb_3O_{10}$ as the reference. $(CuCl)Ca_2Nb_3O_{10}$ pattern is generated based on its crystal structure,[7] and due to being isostructural with $(CuCl)La_2Ti_2NbO_{10}$, it can be used as a reasonable reference for this compound. Manipulating the crystal structure of $(CuCl)Ca_2Nb_3O_{10}$ was then done replacing two

third of the niobium elements with titanium, as well as exchanging the calcium element with lanthanum. Since the atomic number of the elements impact the intensity of the peaks, the XRD pattern generated after this structural manipulation is in better agreement with the experimental sample. Unit cell parameters of the DJ products ($ALa_2Ti_2NbO_{10}$) are presented in Table C-2, being in good agreement the values reported in the literature.[7,9]

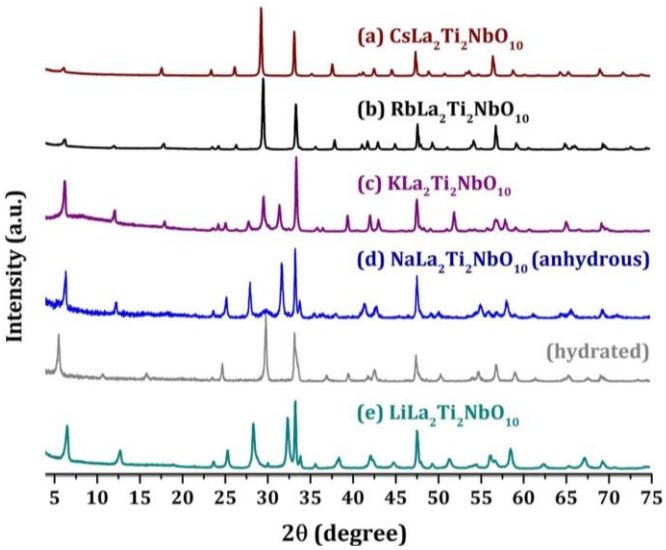

Figure C- 4: The DJ end member, $ALa_2Ti_2NbO_{10}$, where A is (a) Cs, (b) Rb, (c) K, (d) Na both anhydrous and hydrated, and (e) Li.

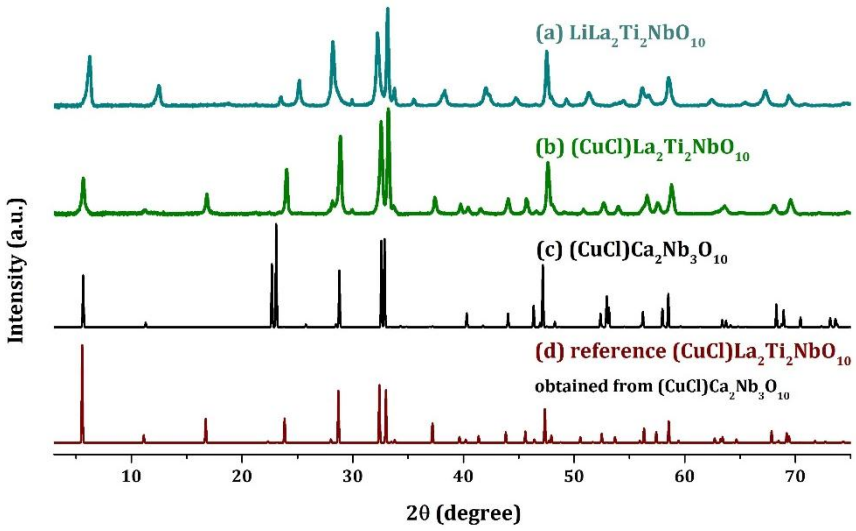

Figure C- 5: XRD pattern of experimental $(CuCl)La_2Ti_2NbO_{10}$ compared to (a) $LiLa_2Ti_2NbO_{10}$ starting material, and (c) $(CuCl)Ca_2Nb_3O_{10}$ and (d) $(CuCl)La_2Ti_2NbO_{10}$ references.

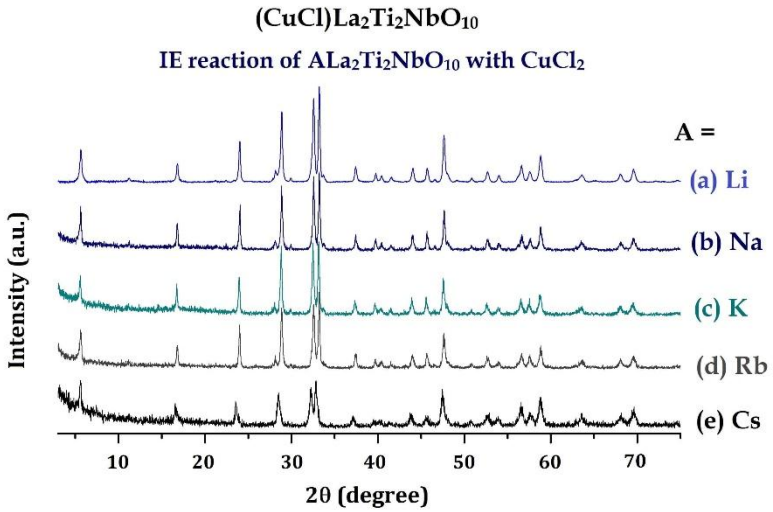

Figure C- 6: Successful synthesis of $(CuCl)La_2Ti_2NbO_{10}$ from all $ALa_2Ti_2NbO_{10}$ members .

Table C- 2: Unit cell parameters of $ALa_2Ti_2NbO_{10}$ (A = Li, Na, K, and Rb) and $(CuCl)La_2Ti_2NbO_{10}$.

	Unit Cell Parameters				
Compound	**Unit Cell (Å)**			**Literature Cell (Å)**	
	a	**c**	***Layer Spacing****	**a**	**c**
$RbLa_2Ti_2NbO_{10}$	3.818(2)	15.1910(3)	***15.1910(3)***	3.8383(9)	15.2189(9)
$KLa_2Ti_2NbO_{10}$	3.831(3)	30.1015(8)	***15.0508(4)***	3.853(7)	30.07(8)
$NaLa_2Ti_2NbO_{10}$	3.827(4)	29.656(4)	***14.828(2)***	This work	
$LiLa_2Ti_2NbO_{10}$	3.832(2)	28.3854(2)	***14.1927(1)***	This work	
$(CuCl)La_2Ti_2NbO_{10}$	3.824(2)	15.9037(2)	***15.9037(2)***	3.8356(9)	15.9010(4)

**calculated by halving the c parameter in case of K, Na, and Li members, to better highlight the dependence of layer spacing on the interlayer units.*

C.3.3 $A_{2-x}La_2Ti_{3-x}Nb_xO_{10}$. $Rb_{2-x}La_2Ti_{3-x}Nb_xO_{10}$ solid solutions were prepared by direct ceramic method for x = 0.05, 0.15, 0.25, 0.5, 0.75, and 0.85. The synthesis of the solid solutions via an indirect method (grinding and heating of the appropriate ratios of the two end members) turned out to be unsuccessful despite many different conditions attempted. The XRD patterns of Rb_{2-x} solid solutions are presented in Figure C-7. As the x value gets closer to the end-member values (0 for RP and 1 for DJ), the XRD patterns become more similar to the end members. This is highlighted by the slight shift in the peak at the 2θ range of 28 - 30 in Figure C-7. The XRD patterns of $A_{2-x}La_2Ti_{3-x}Nb_xO_{10}$ intermediate solid solutions are expected to more resemble that of $A_2La_2Ti_3O_{10}$ RP end member based on the structural evolution presented in Figure C-1.[9] Even though the XRD patterns do seem as expected in Figure C-7, there also seems to be a

competition between the structures of the two end members as the x value is increased to 0.5. The peak at 2θ=28-30 gets broad at x=0.5 and then exactly matches that of x=1 as x is increased. It should be noted that the synthesis of $Rb_{1.5}$ was the most challenging and could easily yield a mixture of the two end members if heated slightly more.

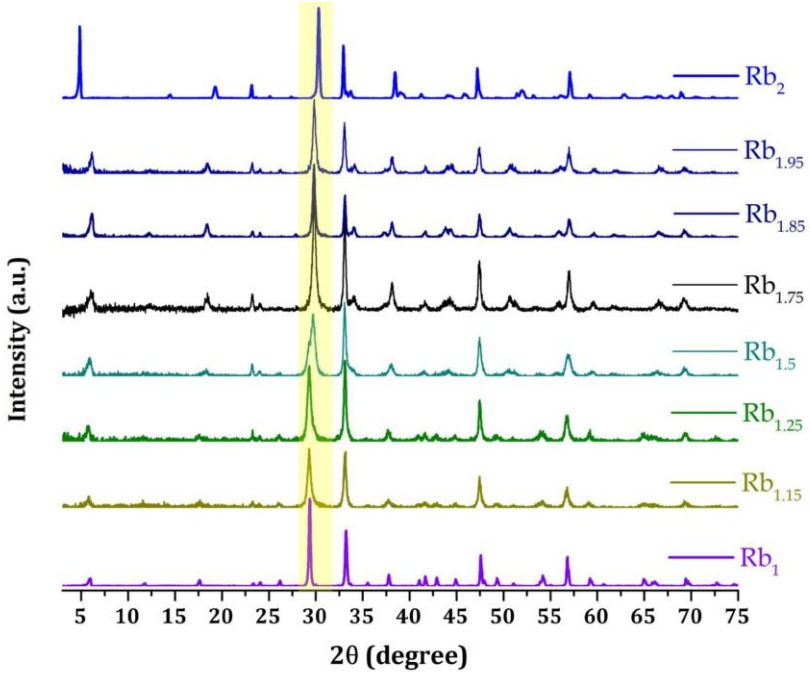

Figure C- 7: $Rb_{2-x}La_2Ti_{3-x}Nb_xO_{10}$ solid solutions for x = 0, 0.05, 0.15, 0.25, 0.5, 0.75, 0.85, and 1.

The XRD patterns by themselves, do not allow us to distinguish between the formation of a solid solution and an unsuccessful mixture of the two end members with certainty. Raman spectroscopy in Figure C-8 indicates a structural evolution as x is changed and more strongly supports the formation of a solid solution rather than a mixture of the two end members (though further studies are needed to verify this). Based on the vibrational study done on these solid solutions by Kim et al.,[10] appearance of a band at 1000-950 cm^{-1} by increasing the x value greater than zero, is indicative of NbO_6 octahedron formation. Considering the decrease of the band at 950-850 cm^{-1} and 580-510 cm^{-1}, which is assigned to the outer TiO_6 (not the central ones appearing at 720-670 cm^{-1}), the site preference of NbO_6 octahedra[10] was also confirmed. For any non-zero value of x, a sharp peak at 1000-950 cm^{-1} was observed and the extent of x value was reflected in the intensity of this peak.

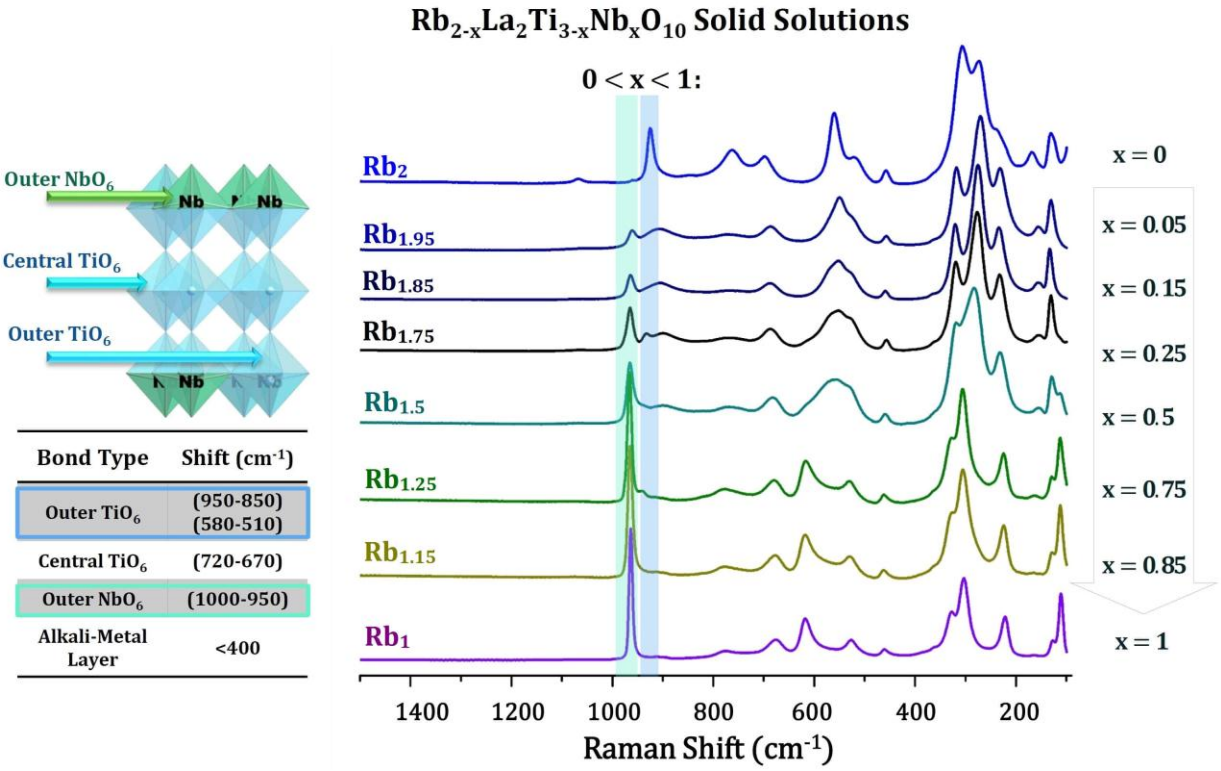

Figure C- 8: Raman spectra of $Rb_{2-x}La_2Ti_{3-x}Nb_xO_{10}$ solid solutions, confirming the strutural evolution.

Figure C-9 shows the XRD pattern of $Rb_{1.75}La_2Ti_{2.75}Nb_{0.25}O_{10}$ solid solution versus the two end members. It is clearly shown that the structure of this solid solution compound is distinct from the end members with decent similarities to both; which is exactly expected for a solid solution. Figure C-10 shows the XRD patterns of all $A_{1.75}La_2Ti_{2.75}Nb_{0.25}O_{10}$ solid solutions prepared via an IE reaction between $Rb_{1.75}La_2Ti_{2.75}Nb_{0.25}O_{10}$ and ANO_3 (A = Li, Na, and K). These patterns demonstrate the interlayer expansion as the interlayer cation grows larger (Li to Rb). Table C-3 shows the unit cell parameters of $A_{1.75}La_2Ti_{2.75}Nb_{0.25}O_{10}$ solid solutions. Since some of these products are not published before, in most cases there was not a reference pattern available from the literature. However, volume of one unit cell decreases for smaller cations as expected, as further confirmation to the success of the reactions.

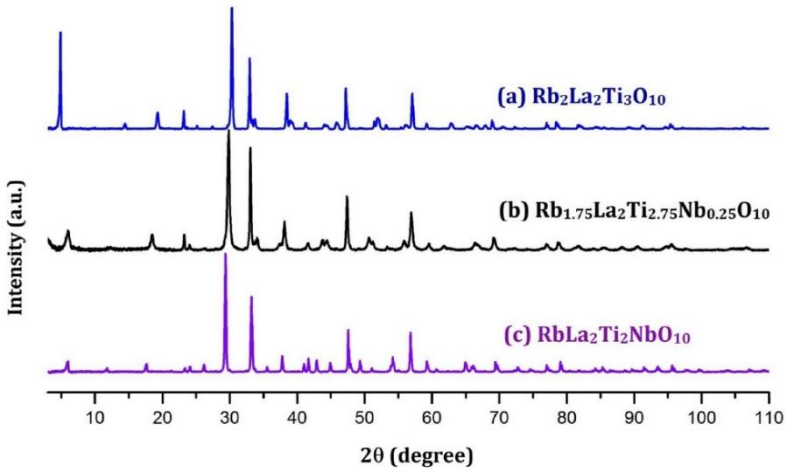

Figure C- 9: The XRD pattern of $Rb_{1.75}La_2Ti_{2.75}Nb_{0.25}O_{10}$ solid solution versus the two end members.

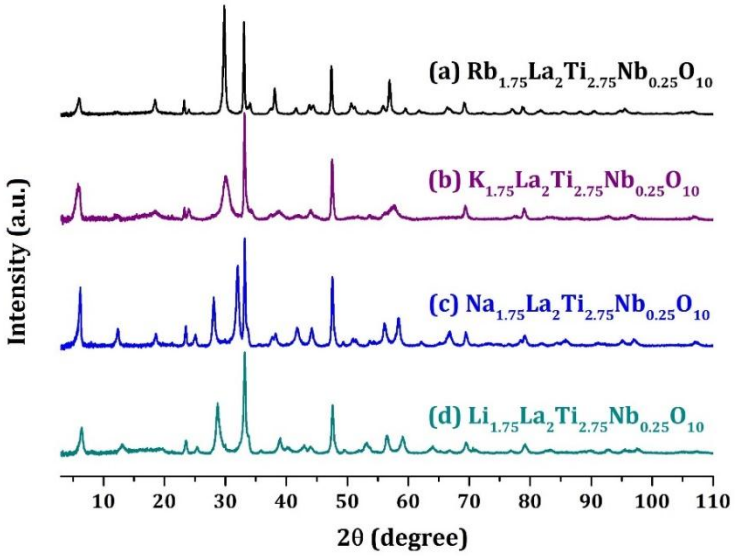

Figure C- 10: $A_{1.75}La_2Ti_{2.75}Nb_{0.25}O_{10}$ solid solutions where A is (a) Rb, (b) K, (c) Na, and (d) Li.

Table C- 3: Unit cell parameters of $A_{1.75}La_2Ti_{2.75}Nb_{0.25}O_{10}$ (A = Li, Na, K, and Rb).

	Unit Cell Parameters				
Compound	**Unit Cell (Å)**			**Literature Cell (Å)**	
	a	**c**	***Layer Spacing****	**a**	**c**
$Rb_{1.75}La_2Ti_{2.75}Nb_{0.25}O_{10}$	3.852(6)	18.6745(6)	***18.6745(6)***	This work	
$K_{1.75}La_2Ti_{2.75}Nb_{0.25}O_{10}$	3.833(3)	29.8751(3)	***14.9376(1)***	3.887(6)	29.75(5)
$Na_{1.75}La_2Ti_{2.75}Nb_{0.25}O_{10}$	3.831(3)	28.6508(6)	***14.3254(3)***	This work	
$Li_{1.75}La_2Ti_{2.75}Nb_{0.25}O_{10}$	3.827(3)	26.9181(9)	***13.4591(4)***	This work	

**calculated by halving the c parameter in case of K, Na, and Li members, to better highlight the dependence of layer spacing on the interlayer units.*

Table C-4 represents the results of elemental analysis for the end members ($A_2La_2Ti_3O_{10}$ and $ALa_2Ti_2NbO_{10}$, where A = Rb, K, Na, and Li), as well as their products of IE with $CuCl_2$. The elemental composition of $A_{1.75}La_2Ti_{2.75}Nb_{0.25}O_{10}$ solid solutions is included as well. Despite the error that is almost always reflected in such EDS results, the experimental compositions more highlight the difference between these three set of products, and appear to be promising.

Table C- 4: Elemental compositions of the end members and $A_{1.75}La_2Ti_{2.75}Nb_{0.25}O_{10}$ solid solution*

Elemental Analysis of the Experimental Samples		
$A_2La_2Ti_3O_{10}$	**$A_{1.75}La_2Ti_{2.75}Nb_{0.25}O_{10}$**	**$ALa_2Ti_2NbO_{10}$**
$Rb_{2.0(1)}La_{2.58(8)}Ti_{3.35(6)}$	$Rb_{1.11(4)}La_{2.00\ (6)}Ti_{2.36(6)}Nb_{0.27(4)}$	$Rb_{1.0(1)}La_{2.5\ (1)}Ti_{2.20(9)}Nb_{1.1(1)}$
$K_{2.00(7)}La_{2.71(5)}Ti_{3.61(4)}$	$K_{0.90(9)}La_{2.00(8)}Ti_{2.43(6)}Nb_{0.22(3)}$	$K_{0.89(4)}La_{2.16(6)}Ti_{1.93(8)}Nb_{1.00(9)}$
$Na_{2.0(2)}La_{2.13(4)}Ti_{2.9(1)}$	$Na_{1.1(4)}La_{2.00(1)}Ti_{2.43(4)}Nb_{0.24(2)}$	$Na_{0.96(4)}La_{2.17(6)}Ti_{2.00(5)}Nb_{1.00(7)}$
$Li_{1.82(4)}La_{2.00(4)}Ti_{2.54(3)}$	$Li_{0.96(3)}La_{2.00(3)}Ti_{2.45(6)}Nb_{0.22(2)}$	$Li_{0.91(3)}La_{2.00(5)}Ti_{1.84(4)}Nb_{0.97(7)}$
$Cu_{1.00(4)}La_{2.11(2)}Ti_{2.76(4)}O_{10}$		$(Cu_{0.94(8)}Cl_{0.79(6)})La_{2.16(6)}Ti_{1.98(9)}Nb_{1.00(8)}$

**Data from EDS analysis*

Based on the cartoon presented in Figure C-11, the ultimate goal of this research was to evaluate the structure of $(CuCl_x)La_2Ti_{3-x}Nb_xO_{10}$ solid solutions. One approach to this is the direct method which demonstrates the IE reaction of $A_{2-x}La_2Ti_{3-x}Nb_xO_{10}$ solid solutions with $CuCl_2$. The direct approach was carried out in various trials using the successful $A_{2-x}La_2Ti_{3-x}Nb_xO_{10}$ products. Equation C-2 provides the equation of the proposed ion exchange reaction based on the $A_{1.75}La_2Ti_{2.75}Nb_{0.25}O_{10}$ as an example among these solid solutions. Considering the structural similarity between the solid solutions and the RP end member, it is expected that these IE reactions yield the best results where A = Na and Li. Some of these results are provided in Figure C-12 based on $A_{1.65}La_2Ti_{2.65}Nb_{0.35}O_{10}$. Unfortunately, despite so many trials attempted, all the products of IE with $CuCl_2$ seemed to be very similar to that of starting material, not approving of the success of the IE reaction. Instead of using $Na_{2-x}La_2Ti_{3-x}Nb_xO_{10}$ as a product of the IE reaction of $Rb_{2-x}La_2Ti_{3-x}Nb_xO_{10}$ and $NaNO_3$, the synthesis of $Na_{1.65}La_2Ti_{2.65}Nb_{0.35}O_{10}$ was also carried out directly using the oxide and carbonate reagents. As presented in Figure C-13, the direct $Na_{1.65}La_2Ti_{2.65}Nb_{0.35}O_{10}$ does show sharper peaks and better crystallinity rather than the IE $Na_{1.65}La_2Ti_{2.65}Nb_{0.35}O_{10}$. Interestingly, they also share similar peaks which provides further confirmation that they both resemble the same structure (only with different crystallinities). It is expected to obtain better results from the IE reaction of the direct $Na_{1.65}La_2Ti_{2.65}Nb_{0.35}O_{10}$ with

$CuCl_2$ due to its better crystallinity. Comparing patterns **c** and **d** in Figure C-13, this trial does seem to be the best attempt so far; it is different from the starting material and also shows multiple overlapping peaks at 2θ = 33-34 º similar to that of $CuLa_2Ti_3O_{10}$ provided earlier in Figure C-3. However, this compound lacks a defined first peak which can be hopefully fixed in the following works continuing this research.

Equation C- 2:

$$A_{1.75}La_2Ti_{2.75}Nb_{0.25}O_{10} + CuCl_2 \rightarrow CuCl_{0.25}La_2Ti_{2.75}Nb_{0.25}O_{10} + 1.75\ ACl$$

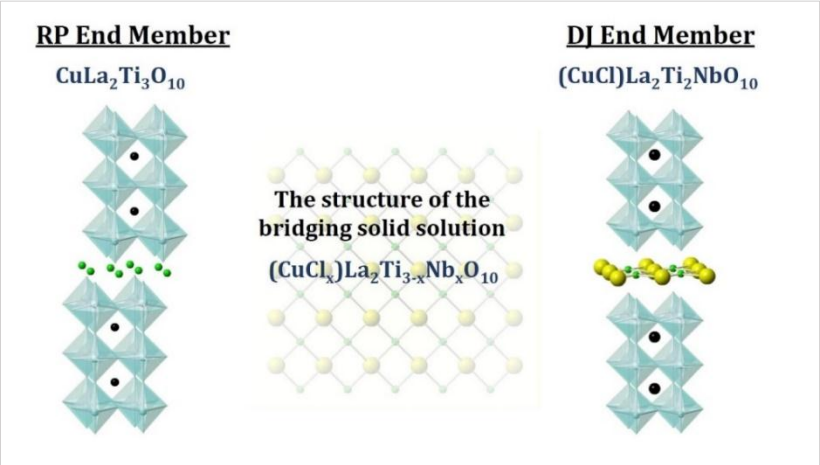

Figure C- 11: Demonstrating the main goal of this chapter.

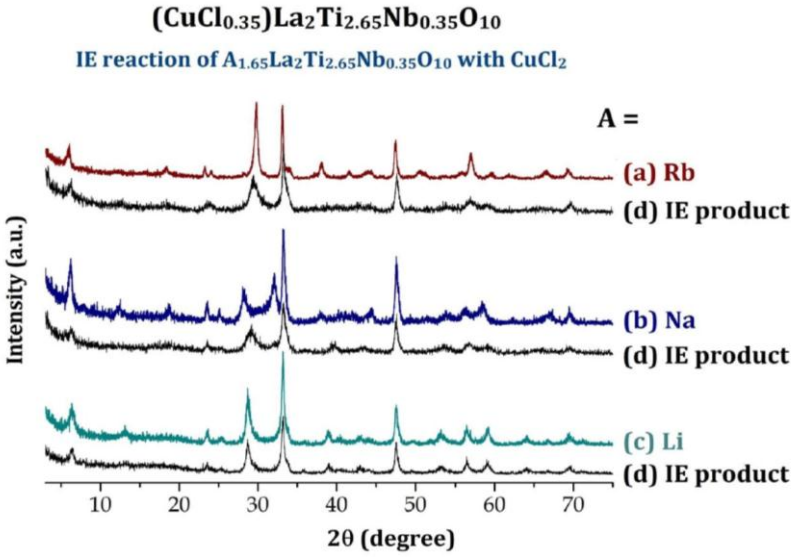

Figure C- 12: IE reaction between $A_{1.65}La_2Ti_{2.65}Nb_{0.35}O_{10}$ and

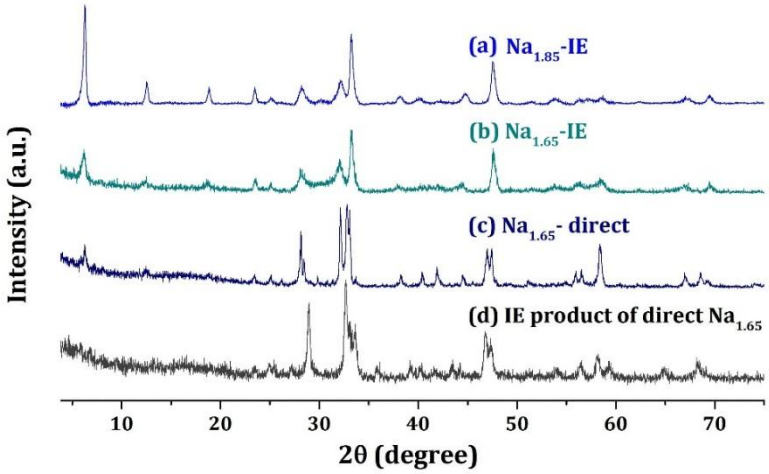

Figure C- 13: Direct synthesis of $Na_{1.65}La_2Ti_{2.65}Nb_{0.35}O_{10}$, and its IE product with $CuCl_2$.

Other than the direct method for the synthesis of $(CuCl_x)La_2Ti_{3-x}Nb_xO_{10}$, an indirect approach was also attempted based on equation C-3 by mixing appropriate ratios of the two end members $CuLa_2Ti_3O_{10}$ and $(CuCl)La_2Ti_2NbO_{10}$. The end members were ground together, pressed as a pellet, and reacted for either 10 days at 350 ºC, or 3 days at 400 ºC. The few trials were consistently yielding a mixture of the end members rather than a solid solution. One example is provided in Figure C-14.

Equation C- 3:

$$0.35\ (CuCl)La_2Ti_2NbO_{10} + 0.65\ CuLa_2Ti_3O_{10} \rightarrow CuCl_{0.35}\ La_2Ti_{2.65}Nb_{0.35}O_{10}$$

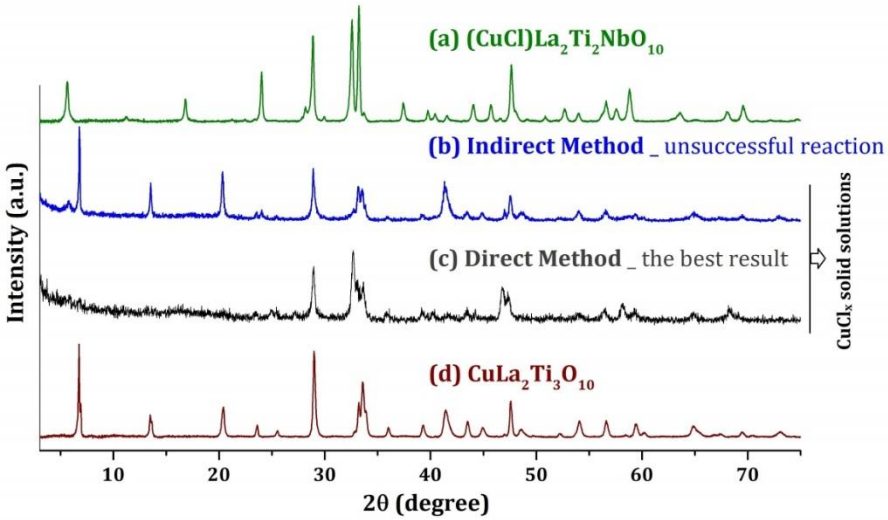

Figure C- 14: Comparison of the end members, $CuLa_2Ti_3O_{10}$ and $(CuCl)La_2Ti_2NbO_{10}$, to the $(CuCl_{0.35})La_2Ti_{2.65}Nb_{0.35}O_{10}$ solid solutions synthesized from both direct and indirect methods.

C.4 Conclusions

$A_{2-x}La_2Ti_{3-x}Nb_xO_{10}$ was successfully prepared for x = 0, 0.05, 0.15, 0.25, 0.5, 0.75, 0.85, and 1 where A = Li, Na, K, and Rb. Some of the solid solutions produced in this work, are reported here for the very first time: $A_{1.75}La_2Ti_{2.75}Nb_{0.25}O_{10}$ (A: Rb, Na, and Li). $(CuCl_x)La_2Ti_{3-x}Nb_xO_{10}$ members (x = 0 and 1) were successfully synthesized via an IE reaction between $CuCl_2$ and each end member. Indirect preparation of $(CuCl_x)La_2Ti_{3-x}Nb_xO_{10}$ bridging members from the end members was not successful. Direct synthesis of $Na_{1.65}La_2Ti_{2.65}Nb_{0.35}O_{10}$ from its oxide and carbonate reagents yielded a product with better crystallinity, and so better reactivity with $CuCl_2$. The most promising trial was the synthesis of solid solution $(CuCl_{0.35})La_2Ti_{2.65}Nb_{0.35}O_{10}$ from this direct Na-based host reacted with $CuCl_2$. It is strongly recommended that the research following this work focuses on this aspect and obtains better quality $(CuCl_{0.35})La_2Ti_{2.65}Nb_{0.35}O_{10}$ for structure refinement.

C.5 References

(1) Sanjaya Ranmohotti, K. G.; Josepha, E.; Choi, J.; Zhang, J.; Wiley, J. B. Topochemical Manipulation of Perovskites: Low-Temperature Reaction Strategies for Directing Structure and Properties. *Adv. Mater.* **2011**, *23* (4), 442–460.

(2) Schaak, R. E.; Mallouk, T. E. Perovskites by Design: A Toolbox of Solid-State Reactions. *Chem. Mater.* **2002**, *14* (4), 1455–1471.

(3) Hyeon, K.-A.; Byeon, S.-H. Synthesis and Structure of New Layered Oxides, $M^{II}La_2Ti_3O_{10}$ (M = Co, Cu, and Zn). *Chem. Mater.* **1999**, *11* (2), 352–357.

(4) Gopalakrishnan, J.; Bhat, V.; Raveau, B. AILaNb$_2$O$_7$: A New Series of Layered Perovskites Exhibiting Ion Exchange and Intercalation Behaviour. *Mater. Res. Bull.* **1987**, *22* (3), 413–417.

(5) Viciu, L.; Liziard, N.; Golub, V.; Kodenkandath, T. A.; Wiley, J. B. Transition-Metal Dion-Jacobson Layered Perovskites, M0.5LaNb2O7. *Mater. Res. Bull.* **2004**, *39* (14–15), 2147–2154.

(6) Kodenkandath, T. A.; Lalena, J. N.; Zhou, W. L.; Carpenter, E. E.; Sangregorio, C.; Falster, A. U.; Simmons, W. B.; O'Connor, C. J.; Wiley, J. B. Assembly of Metal−Anion Arrays within a Perovskite Host. Low-Temperature Synthesis of New Layered Copper−Oxyhalides, $(Cu_X)LaNb_2O_7$, X = Cl, Br. *J. Am. Chem. Soc.* **1999**, *121* (46), 10743–10746.

(7) Kodenkandath, T. A.; Kumbhar, A. S.; Zhou, W. L.; Wiley, J. B. Construction of Copper Halide Networks within Layered Perovskites. Syntheses and Characterization of New Low-Temperature Copper Oxyhalides. *Inorg. Chem.* **2001**, *40* (4), 710–714.

(8) Kageyama, H.; Viciu, L.; Caruntu, G.; Ueda, Y.; Wiley, J. B. New Magnetic Materials Obtained by Ion-Exchange Reactions from Non-Magnetic Layered Perovskites. *J. Phys. Condens. Matter* **2004**, *16* (11), S585.

(9) Uma, S.; Raju, A. R.; Gopalakrishnan, J. Bridging the Ruddlesden–Popper and the Dion–Jacobson Series of Layered Perovskites: Synthesis of Layered Oxides, $A_{2-x}La_2Ti_{3-x}Nb_xO_{10}$(A = K, Rb), Exhibiting Ion Exchange. *J. Mater. Chem.* **1993**, *3* (7), 709–713.

(10) Kim, H. J.; Byeon, S. H.; Yun, H. S. Raman Spectra of the Solid-Solution between $Rb_2La_2Ti_3O_{10}$ and $RbCa_2Nb_3O_{10}$. *Bull. Korean Chem. Soc.* **2001**, *22* (3), 298–302.

(11) Huang, Y.; Wu, J.; Wei, Y.; Hao, S.; Huang, M.; Lin, J. Synthesis and Photocatalytic Activity of Hydrated Layered Perovskite $K_{2-x}La_2Ti_{3-x}Nb_xO_{10}$ ($0 \leqslant X \leqslant 1$) and Protonated Derivatives. *Scr. Mater.* **2007**, *57* (5), 437–440.

(12) Toda, K.; Watanabe, J.; Sato, M. Crystal Structure Determination of Ion-Exchangeable Layered Perovskite Compounds, $K_2La_2Ti_3O_{10}$ and $Li_2La_2Ti_3O_{10}$. *Mater. Res. Bull.* **1996**, *31* (11), 1427–1435.

(13) Toda, K.; Kameo, Y.; Kurita, S.; Sato, M. Crystal Structure Determination and Ionic Conductivity of Layered Perovskite Compounds $NaLnTiO_4$ (Ln = Rare Earth). *J. Alloys Compd.* **1996**, *234* (1), 19–25.

Appendix D. $A_{1-x}A'_xLaNb_2O_7$ (A/A′ = Li, Na, K, Rb, Cs) Perovskite Solid Solutions*

D.1 Introduction

Various *M*$LaNb_2O_7$ perovskites,[1–5] and more specifically the *A*$LaNb_2O_7$ alkali series (*A* = Li, Na, K, Rb, Cs),[6–12] have been studied vastly. $KLaNb_2O_7$, $RbLaNb_2O_7$, and $CsLaNb_2O_7$ are members of this series that are stable at high temperatures (>1000 °C),[6,7,10,11] and so attainable via direct solid state reaction of their oxide and carbonate reagents. Conversely, $NaLaNb_2O_7$ and $LiLaNb_2O_7$ members are metastable and should be prepared at lower temperatures that do not intrigue any decomposition.[5,8,9,11] Simple ion exchange reactions are employed in the preparation of metastable *A*$LaNb_2O_7$ members, where the interlayer ion of an existing stable host (*A* = Cs, Rb, or K) is substitutes by another ion (such as Li and Na) supplied by a molten salt at low temperatures (<600 °C).[5,8,9,11]

The *A*$LaNb_2O_7$ family of compounds is illustrated in Figure D-1, presenting how the atomic radii of the interlayer cations make the perovskite slabs arranging in specific relative orientations.[21–26] The goal of this research was to establish a continuous solid solution series based on this family, $A_{1-x}A'_xLaNb_2O_7$ (A/A′ = Li, Na, K, Rb, Cs where $0 \leq x \leq 1.0$), and further investigate the variations in the structure as a function of the solid solution composition. These solid solutions were prepared via low-temperature reactions (< 600 °C) between the two end-members (x = 0, 1) as illustrated in Figure D-2. The structures of $A_{1-x}A'_xLaNb_2O_7$ solid solutions vary as differences in A/A′ cation atomic radii allow the perovskite slabs to adopt different relative orientations.

Thermodynamically stable and metastable compounds readily formed solutions upon appropriate heating conditions from all adjacent end members, however, the metastable compounds forming from nonadjacent end members were found to decompose into $LaNbO_4$ and $ANbO_3$ before any effective interlayer mixing occurred (with the exception of $K_{1-x}Cs_xLaNb_2O_7$ solid solutions). X-ray powder diffraction was used to determine the lattice parameters of the $A_{1-x}A'_xLaNb_2O_7$ series (x = 0, 0.25, 0.5, 0.75, 1) and to discern structural variations as a function of

* *Manuscript in preparation*

composition. These solid solutions can potentially target partial ion exchange reactions favoring one of the interlayer ions over the other one.

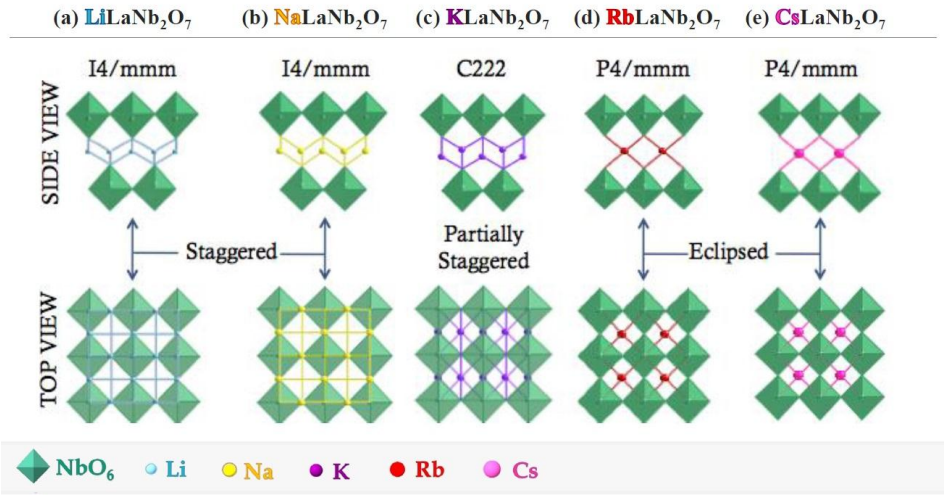

Figure D- 1: Schematic structures of $ALaNb_2O_7$ perovskites, where A is: (a) Li, (b) Na, (c) K, (d) Rb, and (e) Cs, highlighting different orientations of the perovskite slab based on the interlayer cation; (a, b) staggered, (c) partially staggered, and (d, e) eclipsed.

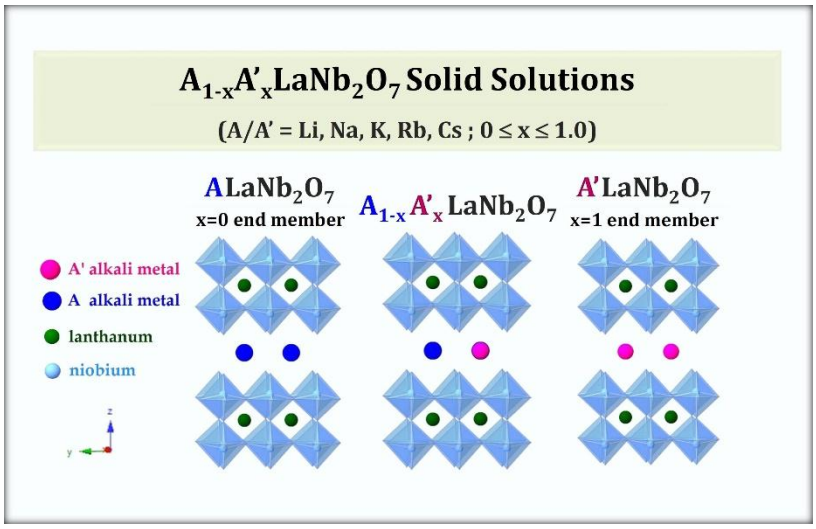

Figure D- 2: Illustrating the overal synthetic approach of this chapter; indirect synthesis of the solid solutions by reacting appropriate ratios of the two end members.

D.2 Experimental

Synthesis. *A*$LaNb_2O_7$ (*A* = Cs and Rb)[6,7,12] were prepared via high-temperature solid-state reactions from the corresponding oxides and carbonates: Cs_2CO_3 (Alfa Aesar, 99.994%), Rb_2CO_3 (Alfa Aesar, 99.975%), La_2O_3 (Alfa Aesar, 99.99%), and Nb_2O_5 (Alfa Aesar, 99.9985%) were mixed in stoichiometric ratios and in the presence of excess amount of carbonate (30%) to compensate for its volatilization. ***Note:*** Prior to use, La_2O_3 and Nb_2O_5 were treated at 1000 °C for 12-24 h to remove any impurities or non-stoichiometries. The mixture of the reagents was thoroughly ground and preheated in an alumina crucible in air at 850 °C for 12 hours. The preheated mixture was reground and then heated for 48 h at 1050 °C with one intermediate grinding. The product was rinsed with copious amount of distilled water to remove unreacted carbonates, and dried at 130 °C for several hours.

Metastable *A*$LaNb_2O_7$ members (A = Li and Na) as well as $KLaNb_2O_7$ were prepared by grinding $RbLaNb_2O_7$ with the corresponding nitrate in a 1:10 molar ratio, and heating the mixture for 3 days at temperatures about 50 °C higher than the melting point of *A*NO_3:[8–10,13] $LiNO_3$ (Alfa Aesar, 99%), $NaNO_3$ (Alfa Aesar 99.999%) and KNO_3 (Alfa Aesar, 99.994%), respectively heated at 300, 360, and 380 °C. After the ion exchange reaction, the products were washed with distilled water, rinsed with acetone and dried at 130 °C for an hour. Due to the hygroscopic nature of $NaLaNb_2O_7$, this sample was dehydrated at 250 °C for 6 h, transferred to a desiccator right after removing from the furnace, and rapidly moved inside an argon glovebox. The XRD sample of $NaLaNb_2O_7$ was also prepared under polymer film inside the glovebox (sealed on all the sides to stay anhydrous), and taken out for quick characterization.

Appropriate molar ratios of A/A′$LaNb_2O_7$ end members were ground for the preparation of $A_{1-x}A'_xLaNb_2O_7$ solid solutions (x = 0.25, 0.5, and 0.75), pressed as pellets, and heated for 2-3 days at 325-600 °C (temperatures and durations varying based on the A/A′ elements). Figure D-3 provides a summary of the successful reactions conducted for the preparation of $A_{1-x}A'_xLaNb_2O_7$ solid solutions: $Li_{1-x}Na_xLaNb_2O_7$ and $Na_{1-x}K_xLaNb_2O_7$ were respectively obtained at 325 °C and 350 °C in 2 days, $K_{1-x}Rb_xLaNb_2O_7$ and $Rb_{1-x}Cs_xLaNb_2O_7$ were attainable at 400 °C in 3 days, and $K_{1-x}Cs_xLaNb_2O_7$ was made at 600 °C in 3 days (the only solid solution that could be obtained from non-adjacent end members). Interestingly, solid

solutions rich in $NaLaNb_2O_7$ member also turned out to be hygroscopic, and were treated and scanned in the same manner as $NaLaNb_2O_7$ explained above: $Li_{0.25}Na_{0.75}LaNb_2O_7$, $Na_{0.5}K_{0.5}LaNb_2O_7$ and $Na_{0.75}K_{0.25}LaNb_2O_7$. Attempts to make $A_{0.5}A'_{0.5}LaNb_2O_7$ solid solutions from non-adjacent end members (Li solutions with K, Rb and Cs, as well as Na with Rb and Cs), were not successful: reactions were carried out over several days at various temperatures up to 600 ºC, and in cases exceeding that, yielding either a mixture of the end members rather than a solid solution, or the $LaNbO_4$ decomposition product.[5]

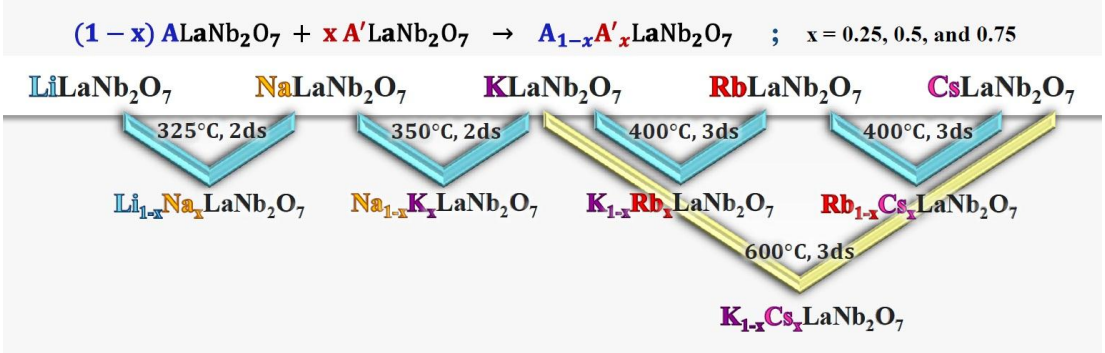

Figure D- 3: Diagram of the successful reactions for the preparation of $A_{1-x}A'_xLaNb_2O_7$ solid solutions from the end members.

Characterization. X-ray powder diffraction (XRD) data were collected on a Philips X'Pert system equipped with Cu Kα radiation (λ = 1.5418 Å) and a curved graphite monochromator. Scans were conducted in continuous mode with a rate of 0.02 °/s. The peak positions and lattice parameters were refined using Fullprof[14] and a least-squares method with the ChekCell program.[15] Raman spectra were collected on a Thermo-Fisher DXR dispersive Raman spectrometer with a wavelength of 532 nm line and a spectral resolution of 3 cm^{-1}. A JEOL (model JSM-5410) scanning electron microscope (SEM), equipped with the energy dispersive analysis (EDS), EDAX (DX-PRIME) microanalytical system, was used for elemental analysis. Thermogravimetric analysis (TGA) and differential scanning calorimetry (DSC) data were obtained using a TA Instruments TGA-DSC SDT Q600 system in alumina pans under pure argon, where samples were heated up to 1000 °C with a rate of 20 °C/min.

D.3 Results

$ALaNb_2O_7$ end members were successfully prepared and compared to the references reported in the literature: direct ceramic method was employed for the synthesis of $CsLaNb_2O_7$ and $RbLaNb_2O_7$, and low-temperature ion exchange reactions were conducted for the preparation of $KLaNb_2O_7$, $NaLaNb_2O_7$ and $LiLaNb_2O_7$ by reacting $RbLaNb_2O_7$ with the corresponding nitrate under specific conditions reported above. Figure D-4 presents the XRD patterns of the $ALaNb_2O_7$ end members, with their calculated unit cell parameters reported in Table D-1 along with the literature values. The unit cell parameters are in great agreement with the reported ones, providing proof of the great quality of the end members.[7–10,12] As an extra visual confirmation, the XRD patterns of all the end members are lined up with their simulated references in Figure D-5.

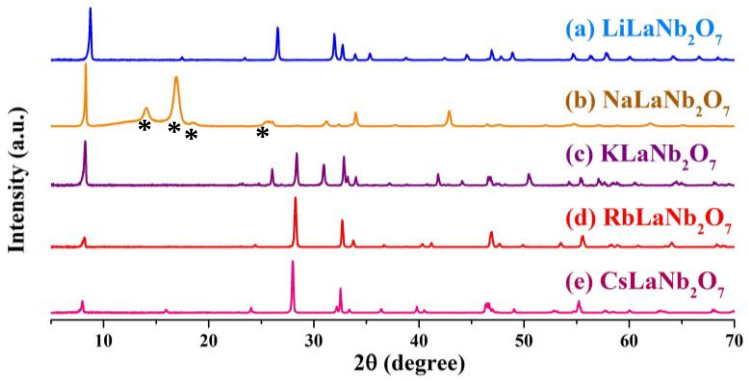

Figure D- 4: XRD patterns of $ALaNb_2O_7$ end members where A is: (a) Li, (b) Na, (c) K, (d) Rb, and (e) Cs. *Peaks pertinent to the polymer film are marked with *.*

Table D- 1: Unit cell parameters of the $ALaNb_2O_7$ end members compared to the literature values.

Unit Cell Parameters for $ALaNb_2O_7$ End Members						
A	**Experimental Values (Å)**			**Literature Values (Å)**		
	a	**b**	**c**	**a**	**b**	**c**
Li[a]	3.874(3)	-	20.3000(4)	3.8799(1)	-	20.3606(5)
Na[a]	3.903(3)	-	21.0654(3)	3.9022(1)	-	21.1826(8)
K[b]	3.895(2)	21.602(7)	3.879(2)	3.9060(1)	21.6030(7)	3.8879(1)
Rb[a]	3.874(2)	-	10.9815(2)	3.885(2)	-	10.989(3)
Cs[a]	3.898(4)	-	11.1386(3)	3.908(1)	-	11.160(4)

***a**: tetragonal cell, and **b**: orthorhombic cell*

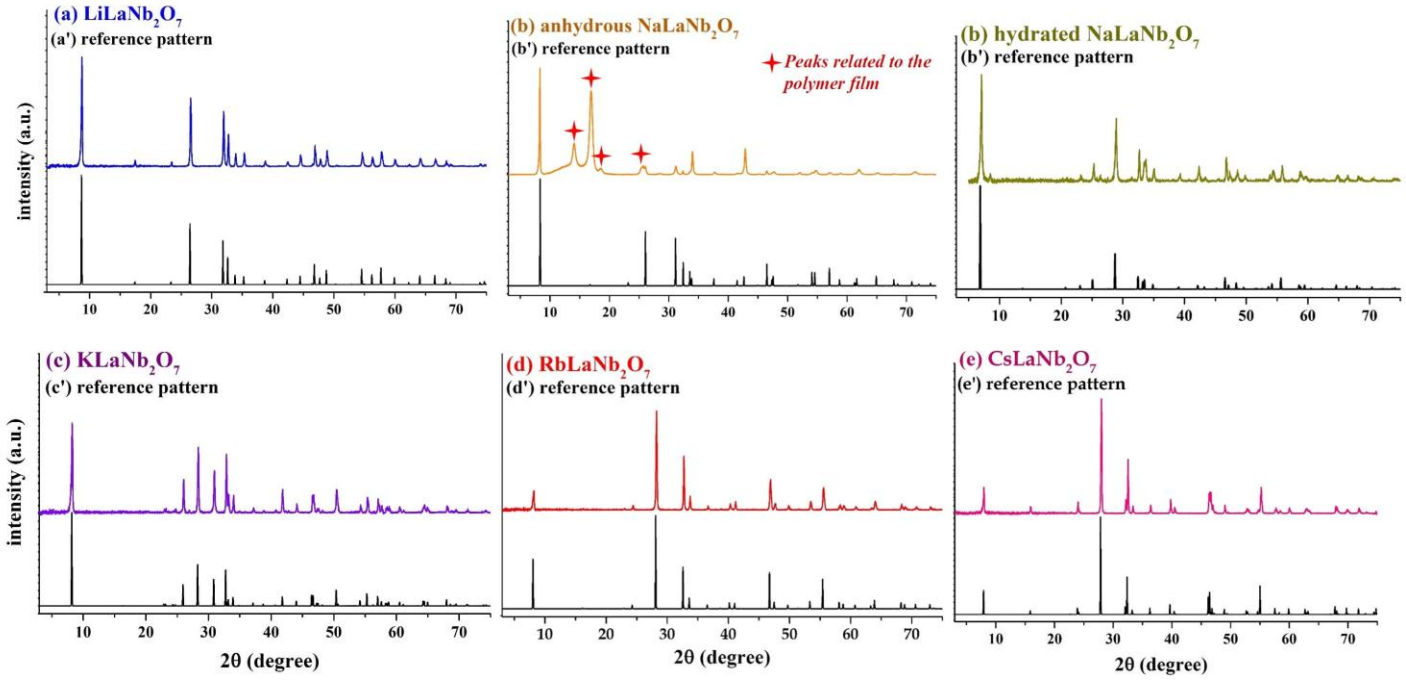

Figure D- 5: XRD patterns of $ALaNb_2O_7$ end members, where A is: (a) Li, (b) Na -both anhydrous and hydrated, (c) K, (d) Rb, and (e) Cs, with the corresponding reference patterns presented respectively in a′- e′.

$A_{1-x}A'_xLaNb_2O_7$ solid solutions were obtained by an indirect method consisting of mixing, grinding and heating appropriate ratios of the two corresponding end members: A/A′ = Li, Na, K, Rb, Cs, for x = 0.25, 0.5, and 0.75, with the two end members falling on the two extremes for x = 0 and 1. Formation of a solid solution rather than a mixture was fulfilled from all of the adjacent end members only, with the successful synthesis of $K_{1-x}Cs_xLaNb_2O_7$ as an exception in case of non-adjacent end members. In case of $K_{1-x}Cs_xLaNb_2O_7$, a solid solution was not formed within the 325-400 °C range. $KLaNb_2O_7$ is thermally stable at high temperatures (~1250°C),[5,10] as so more extreme reaction conditions could be applied until a solution was formed. Reacting the mixture at 600 °C for two days was realized as the best procedure. As mentioned earlier, the reaction temperatures at which the solid solutions are formed, cannot exceed the stability window of the end members themselves ($LiLaNb_2O_7$ and $NaLaNb_2O_7$ are stable only up to about 730 and 820 °C respectively, while the three other end members are synthesized at temperatures above 1000 °C and are thermodynamically stable).[5]

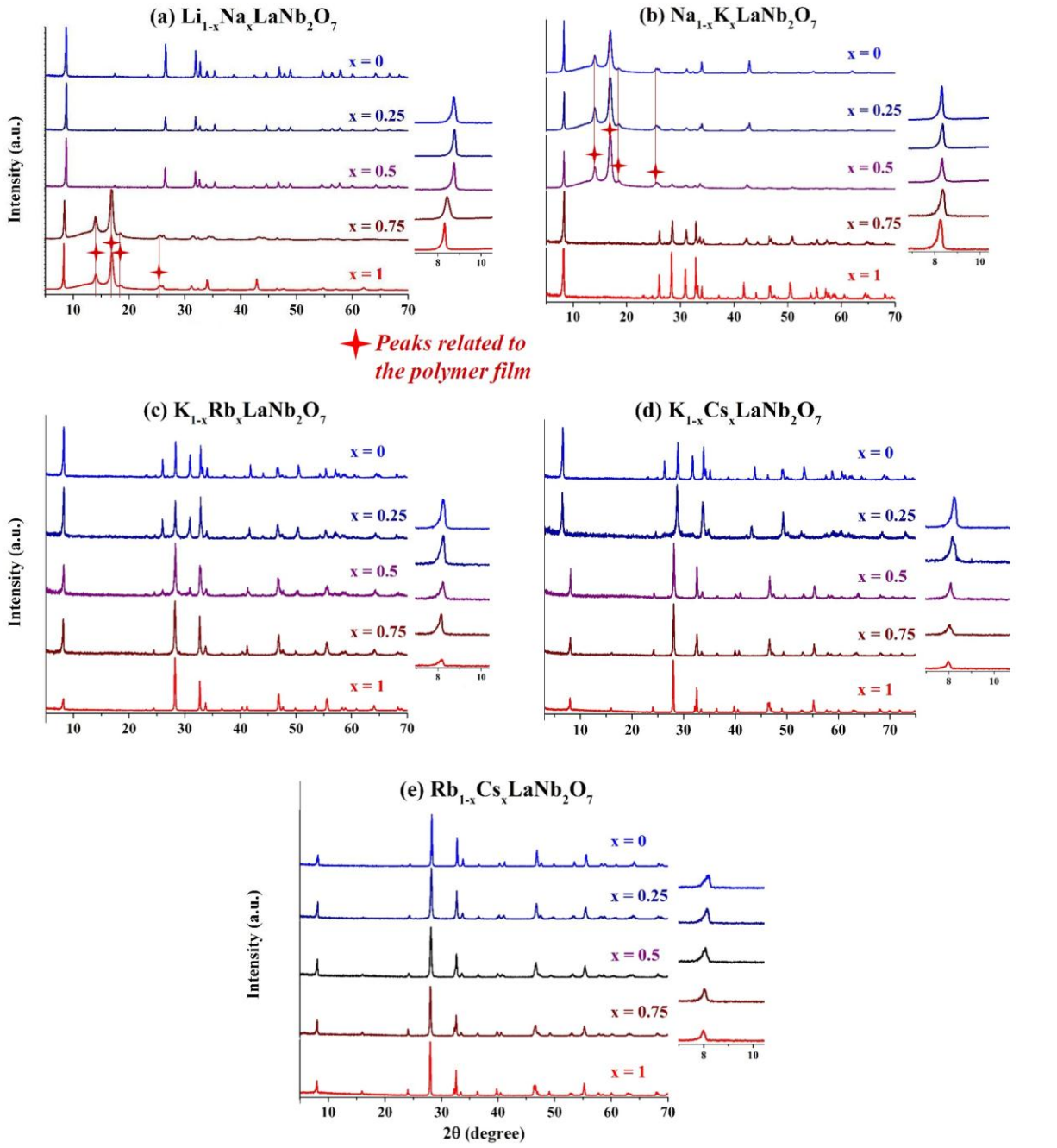

Figure D- 6: XRD patterns of 5 series of solid solutions: (a) $Li_{1-x}Na_xLaNb_2O_7$, (b) $Na_{1-x}K_xLaNb_2O_7$, (c) $K_{1-x}Rb_xLaNb_2O_7$, (d) $K_{1-x}Cs_xLaNb_2O_7$, and (e) $Rb_{1-x}Cs_xLaNb_2O_7$. A close-up of the first reflection is presented on the right of each series

Figures D-6 a—e provide the XRD patterns of all 5 series of the solid solutions: (a) $Li_{1-x}Na_xLaNb_2O_7$, (b) $Na_{1-x}K_xLaNb_2O_7$, (c) $K_{1-x}Rb_xLaNb_2O_7$, (d) $K_{1-x}Cs_xLaNb_2O_7$, and (e) $Rb_{1-x}Cs_xLaNb_2O_7$. There seems to be an acceptable trend among all the patterns; as one solid solution is richer in one end member, the XRD pattern also resembles that end member more.

Interestingly, the middle solid solutions ($A_{0.5}A'_{0.5}LaNb_2O_7$) which are equally rich in both end members, appear to stand on their own rather than a mixture of the end members: $Li_{0.5}Na_{0.5}LaNb_2O_7$, $Na_{0.5}K_{0.5}LaNb_2O_7$, and $K_{0.5}Rb_{0.5}LaNb_2O_7$ matching the XRD pattern of the end member with the smaller cation (Li-, Na-, and K-$LaNb_2O_7$, respectively), while $K_{0.5}Cs_{0.5}LaNb_2O_7$ has a structure very similar to the Cs end member. Also, the solid solutions that were rich in $NaLaNb_2O_7$, appeared to present the hygroscopic nature of this end member as well ($Li_{0.25}Na_{0.75}LaNb_2O_7$, $Na_{0.5}K_{0.5}LaNb_2O_7$ and $Na_{0.75}K_{0.25}LaNb_2O_7$). Figure D-7 provides the XRD patterns for three 1:1 solid solutions ($A_{0.5}A'_{0.5}LaNb_2O_7$ where A/A′ is K/Rb, K/Cs, and Rb/Cs), and compares each pattern to a sample prepared just by grinding a 1:1 mixture of the end members without any heat treatment. Clearly, the first peak of a solid solution is particularly distinguished; not a shouldered peak that indicates a mixture of the end members gone through an incomplete reaction. This is most notable in case of the $K_{0.5}Cs_{0.5}LaNb_2O_7$ solid solution with the largest difference in the atomic radii of the two end members.

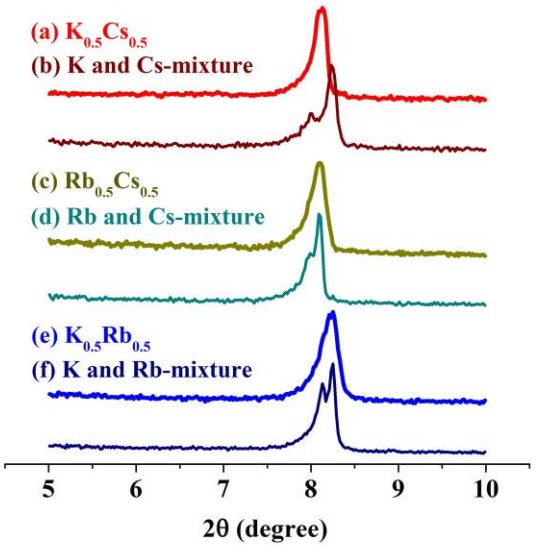

Figure D- 7: The first peaks of three 1:1 solid solutions with (a) K/Cs, (c) Rb/Cs, and (e) K/Rb, compared to the corresponding 1:1 mixtures of the end members.

Unit cell refinement was attempted for all the solid solutions, and the unit cell parameters are provided in Table D-2. In cases, there were more than one acceptable set of unit cell parameters for a $A_{1-x}A'_xLaNb_2O_7$ solid solution with specific x, A and A′. The structural evolution among these solid solution series is expected to impact the largest unit cell parameter as well as the cell volume as the ratio of the larger interlayer ions changes.

Table D- 2: Unit cell parameters of all $A_{1-x}A'_xLaNb_2O_7$ solid solutions.

Unit Cell Parameters (Å) for $A_{1-x}A'_xLaNb_2O_7$ (A/A′ = Li, Na, K, Rb, Cs) Solid Solutions			
	a	**b**	**c**
$LiLaNb_2O_7$[a]	3.874(3)	-	20.3000(4)
$Li_{0.75}Na_{0.25}Nb_2O_7$[a]	3.876(2)	-	20.2989(4)
$Li_{0.5}Na_{0.5}Nb_2O_7$[a]	3.883(2)	-	20.2917(2)
	3.880(3)	-	20.2489(4)
$Li_{0.25}Na_{0.75}Nb_2O_7$[a]	3.899(5)	-	20.9117(5)
$NaLaNb_2O_7$[a]	3.903(3)	-	21.0654(3)
$Na_{0.75}K_{0.25}Nb_2O_7$[a]	3.897(4)	-	21.0885(4)
$Na_{0.5}Ka_{0.5}Nb_2O_7$[b]	3.905(1)	21.284(7)	3.882(2)
$Na_{0.25}K_{0.75}Nb_2O_7$[b]	3.897(2)	21.309(7)	3.869(2)
	3.896(2)	21.55(1)	3.884(3)
$KLaNb_2O_7$[b]	3.895(2)	21.602(7)	3.879(2)
$K_{0.75}Rb_{0.25}Nb_2O_7$[b]	3.896(2)	21.655(9)	3.884(2)
$K_{0.5}Rb_{0.5}Nb_2O_7$[b]	3.875(3)	21.966(9)	3.853(2)
	3.884(3)	21.80(1)	3.872(3)
	3.900(3)	21.74(2)	3.882(1)
$K_{0.25}Rb_{0.75}Nb_2O_7$[a]	3.880(2)	-	10.9451(2)
$RbLaNb_2O_7$[a]	3.874(2)	-	10.9815(2)
$Rb_{0.75}Cs_{0.25}Nb_2O_7$[a]	3.875(3)	-	11.0137(5)
$Rb_{0.5}Cs_{0.5}Nb_2O_7$[a]	3.883(4)	-	11.0440(3)
	3.887(4)	-	11.0684(5)
$Rb_{0.25}Cs_{0.75}Nb_2O_7$[a]	3.892(3)	-	11.1079(4)
$CsLaNb_2O_7$[a]	3.898(4)	-	11.1386(3)

$KLaNb_2O_7$[b]		
a	**b**	**c**
$K_{0.75}Cs_{0.25}Nb_2O_7$[a]		
3.884(3)	-	10.9277(3)
$K_{0.5}Cs_{0.5}Nb_2O_7$[a]		
3.887(3)	-	11.0076(3)
3.882(5)	-	10.9995(2)
$K_{0.25}Cs_{0.75}Nb_2O_7$[a]		
3.890(2)	-	11.0753(3)
$CsLaNb_2O_7$[a]		

***a**: tetragonal cell, and **b**: orthorhombic cell*

In order to visually present the unit cell parameters as a function of the solid solution composition, the evolution of the largest unit cell parameter is provided in Figure D-8a versus the ionic radius of each composition. The largest unit cell parameter is named as *c* in this plot, which is the *c* parameter for a tetragonal cell, and *b* parameter in an orthorhombic structure. Another consideration was halving this value as needed in order to present them within a comparable range (10-11.5 Å). Ionic radius of each composition was also calculated based on the weighted average of the interlayer cation(s) for a specific point, using the literature values for the radii of the interlayer ions of the end members[16]; $[(1-x)\times r_A + (x)\times r_{A'}]$ for the $A_{1-x}A'_xLaNb_2O_7$ solid solution. The coordination number of the A/A′ cation in the $A/A'LaNb_2O_7$ end members was considered 4 in case of Li or Na, 6 for partially staggered K, and 8 for Rb or Cs,[7–10,12,17] and

then the radii were found to be 0.730, 1.13, 1.52, 1.75, and 1.88 Å where the interlayer cation was Li^+, Na^+, K^+, Rb^+ and Cs^+, respectively. Figure D-8b illustrates the evolution of the cell volumes among these solid solutions versus their ionic radii. Similar to Figure D-8a, the cell volumes were halved as needed to fall within a comparable range (140-180 $Å^3$).

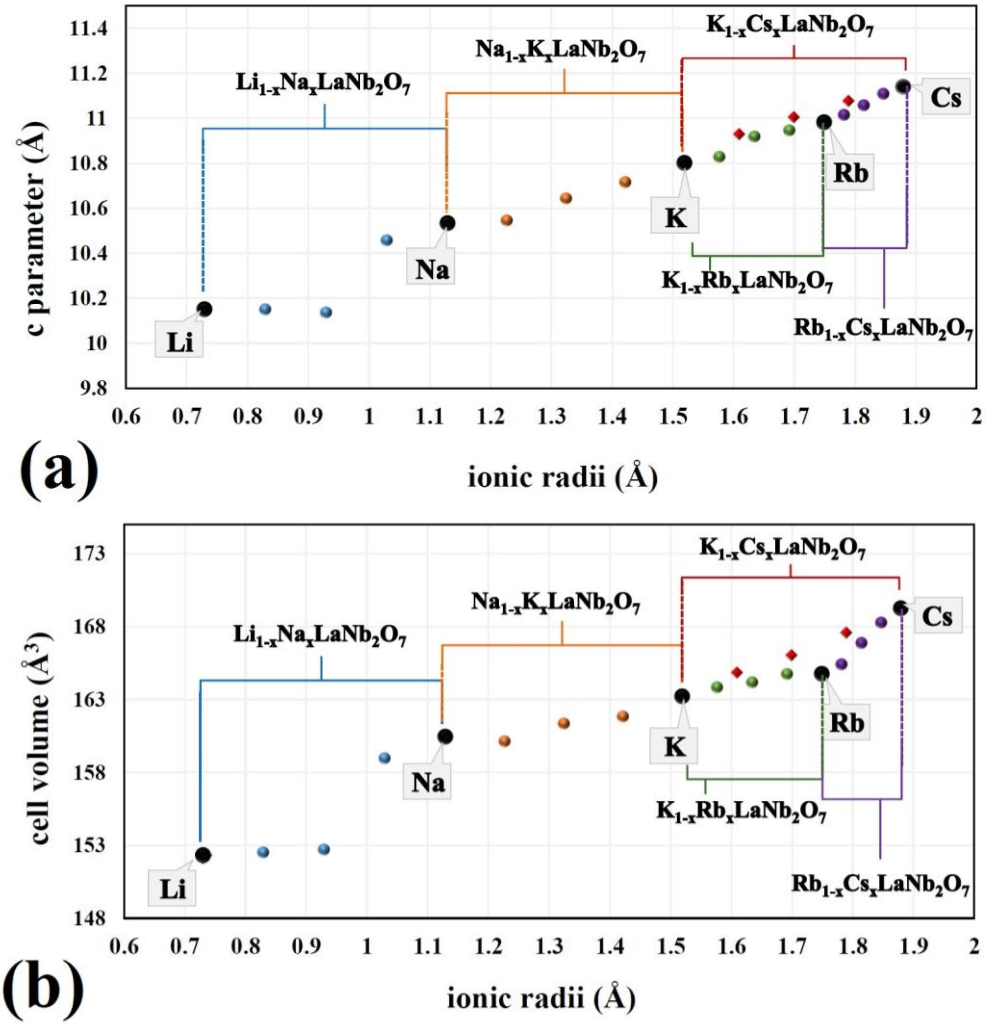

Figure D- 8: Plotting (a) the c parameters, and (b) the cell volumes of the solid solutions versus the ionic radii in each case.

As presented in Figures D-8 a and b, the changes in the unit cell parameters and cell volumes are generally consistent with the perovskite structure adopting a more favorable configuration to accommodate a larger cation while moving towards the Cs end member. $K_{1-x}Rb_xLaNb_2O_7$, $Rb_{1-x}Cs_xLaNb_2O_7$, and $K_{1-x}Cs_xLaNb_2O_7$ solid solutions well follow the Vegard's

law; where the unit cell parameters are expected to *linearly* change with the solid solution composition.[18] The R-squared values for these three series are all higher than 0.94 which translates to a good linear fit plotting either the c parameters, or the cell volumes versus the ionic radii in each group (Figures D-9 a—c). However, $Li_{1-x}Na_xLaNb_2O_7$ and $Na_{1-x}K_xLaNb_2O_7$ seem to offer negative departures from Vegard's law (Figures D-10 a and b). It should be noted that Vegard's law is more of a generalization than a law,[18] and this does not disapprove of the successful formation of solid solutions in the last two cases.

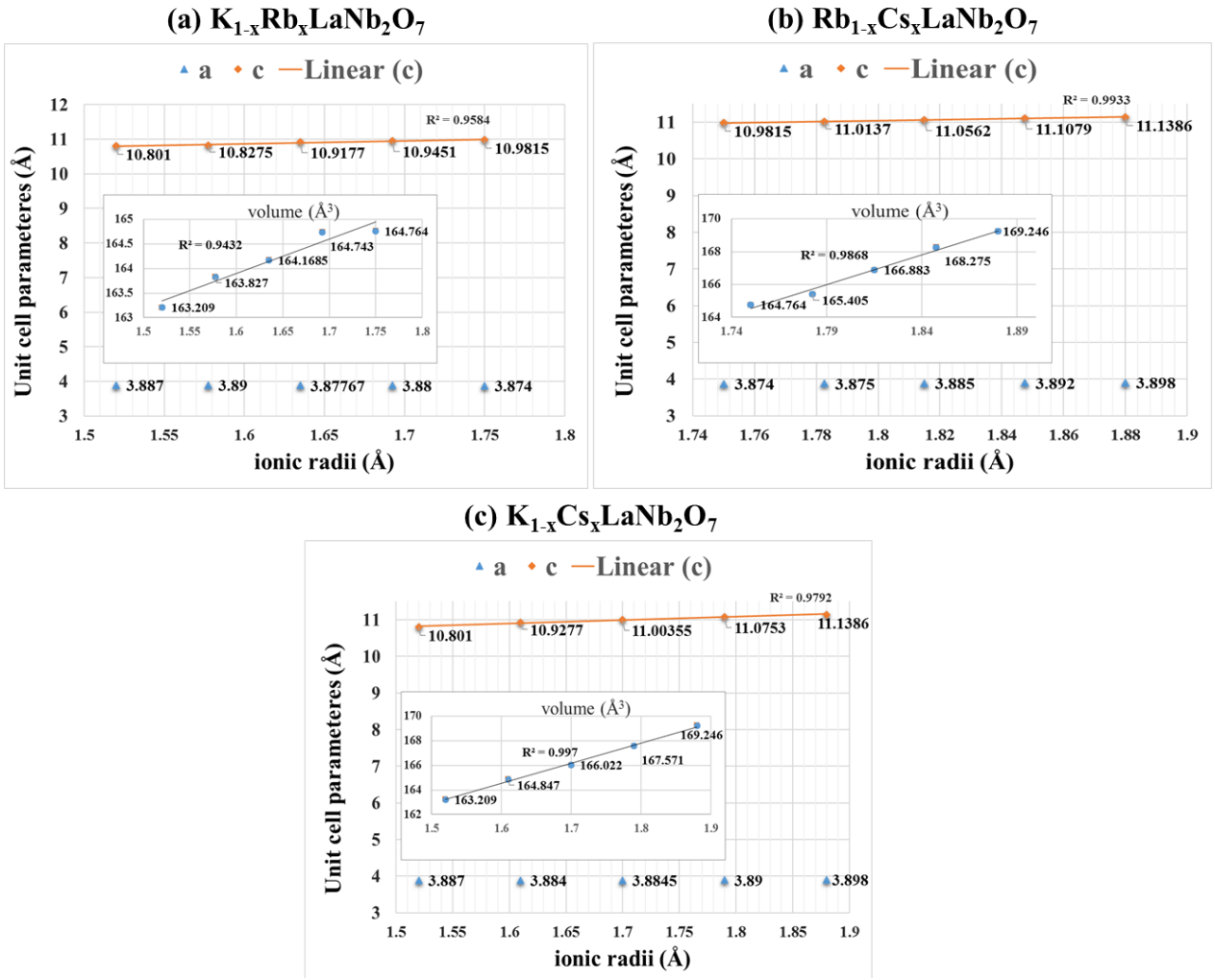

Figure D- 9: Unit cell parameters and the cell volumes of (a) $K_{1-x}Rb_xLaNb_2O_7$, (b) $Rb_{1-x}Cs_xLaNb_2O_7$, and (c) $K_{1-x}Cs_xLaNb_2O_7$ solid solutions plotted versus the ionic radius of the interlayer cation(s).

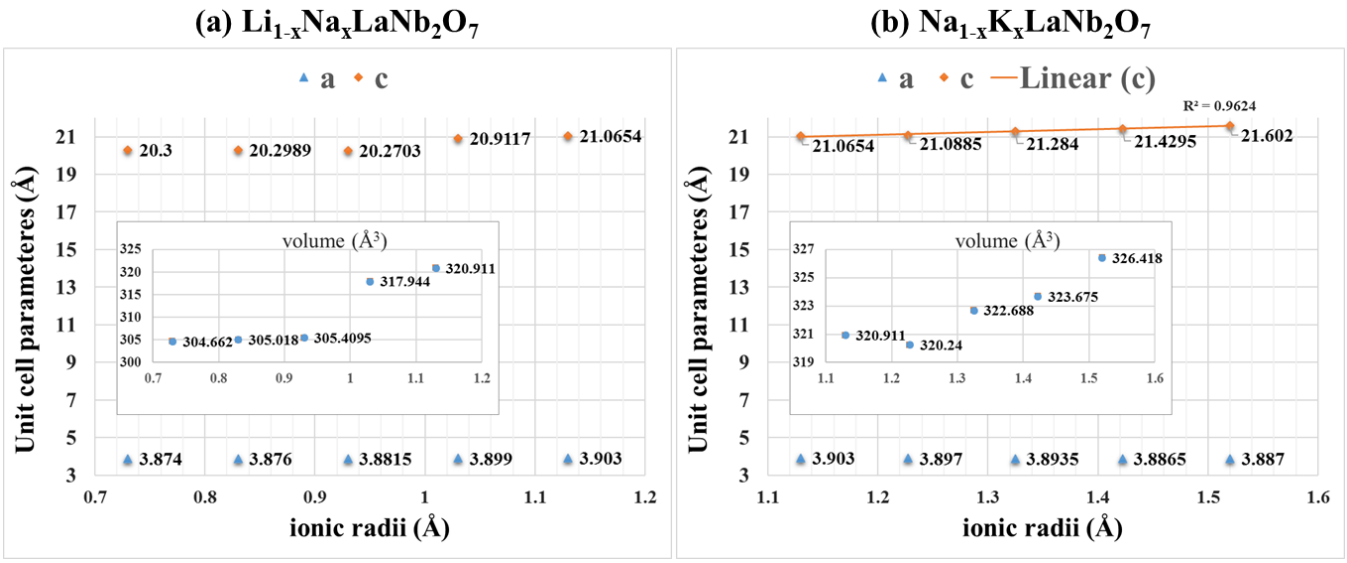

Figure D- 10: Unit cell parameters and the cell volumes of (a) $Li_{1-x}Na_xLaNb_2O_7$ and (b) $Na_{1-x}K_xLaNb_2O_7$ solid solutions plotted versus the ionic radius of the interlayer cation(s).

$Li_{1-x}Na_xLaNb_2O_7$ solid solutions were selected as the only group with metastable products through the whole range of x values, and further thermal analysis was conducted on them. As presented in Figure D-11, the exothermic DSC peak in the range of 740-830 ºC shows a sensible transition as one moves from x = 0 to x = 1 across this series. In Figure D-12, the DSC transitions of the $Li_{0.5}Na_{0.5}LaNb_2O_7$ solid solution is compared to that of a 1:1 rough mixture of the two end members. It is clear that the solid solution has a more distinguished exotherm peak as opposed to the 1:1 mixture which shows a shouldered peak in a slightly wider range. However, it should be noted that the partial formation of a solid solution in case of the 1:1 mixture is also intrigued under these heating conditions; only a poor structure is formed due to the shorter time available for the two end members to fully react. Even though Raman spectroscopy is known as a strong tool for the determination of the successful formation of solid solutions,[17,19] no conclusive patterns were found in the spectra collected on four $A_{1-x}A'_xLaNb_2O_7$ solid solution series (Figure D-13).

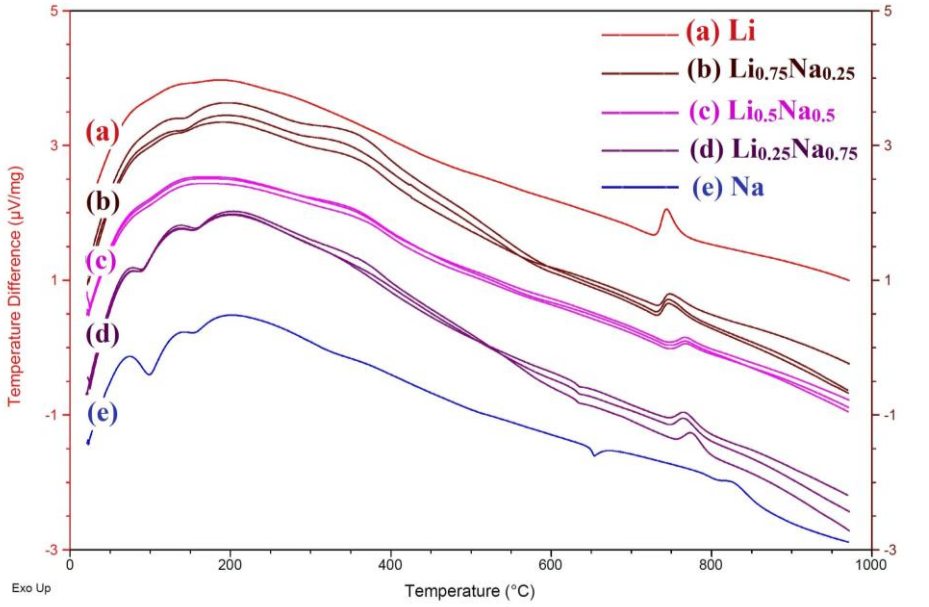

Figure D- 11: DSC analysis performed on the metastable solid solution seris ($Li_{1-x}Na_xLaNb_2O_7$), where: (a) x = 0, (b) x = 0.25, (c) x = 0.5, (d) x = 0.75, and (e) x = 1.

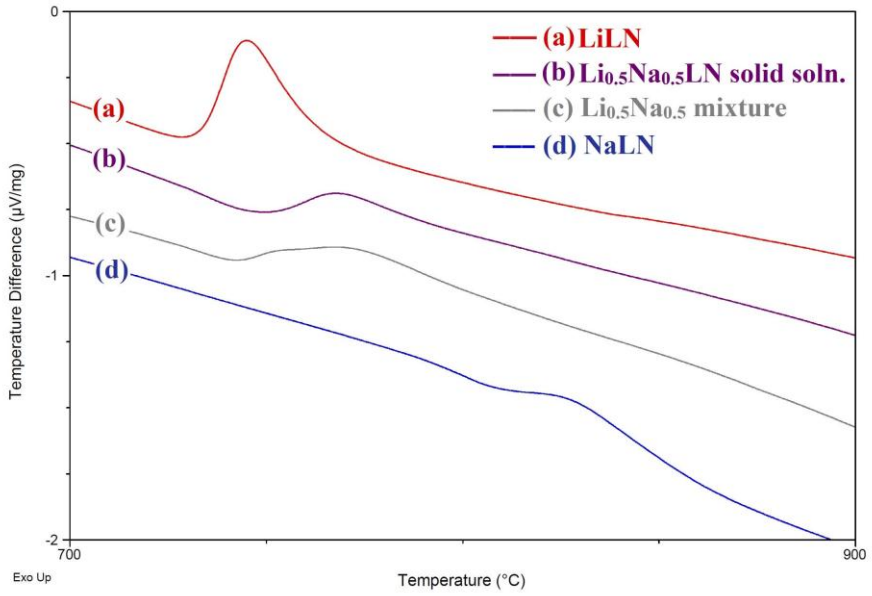

Figure D- 12: DSC analysis performed on (b) a 1:1 solid solution of Li/Na and compared to (c) a 1:1 rough mixture, with the end members presented in (a, d).

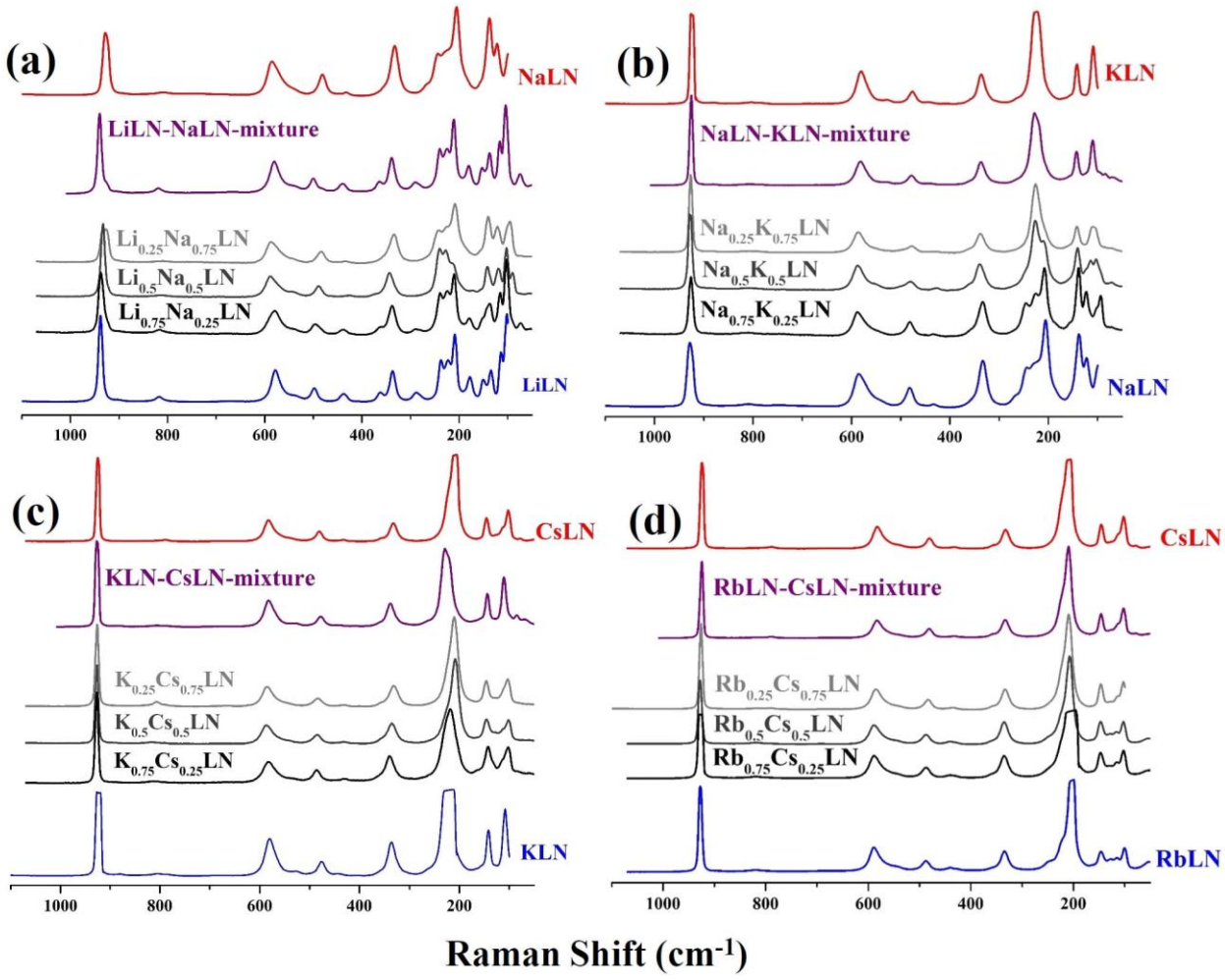

Figure D- 13: Raman spectra presented for (a) Li/Na, (b) Na/K, (c) K/Cs, and (d) Rb/Cs solid solutions.

D.4 Discussion

The structures of the five end members are compared in Figure D-1, highlighting the impact of the interlayer ionic radii on the relative orientation of the perovskite slabs.[6–12,17] $LiLaNb_2O_7$ and $NaLaNb_2O_7$ phases have a partially staggered conformation where the perovskite layers are shifted by ½ in two directions (compared to the Cs or Rb members). Conversely, the perovskite layers of $RbLaNb_2O_7$ and $CsLaNb_2O_7$ are eclipsed and so the NbO_6 octahedra in both layers are well aligned. The orientation of the slabs in $KLaNb_2O_7$ is intermediate to these two types and adopts a partially staggered configuration where the layers are shifted by ½ in a single direction compared to that of the eclipsed members.[6–12] The small size of Li^+ (0.73 Å) and Na^+

(1.13 Å) cations results in low coordination of these cations, and is related to the inherently low thermal stability of $LiLaNb_2O_7$ and $NaLaNb_2O_7$ compounds.[5] The ionic radii of the six-coordinate K^+ (1.52 Å) conveys greater stability to the overall crystal structure than the four coordinate Li^+ and Na^+. As a result, this stability permits $KLaNb_2O_7$ to form a solid solution with the nonadjacent parent compound $CsLaNb_2O_7$.

Once the quality of the five end members are confirmed comparing the XRD patterns and the resulted unit cell parameters with their references (Figures D-4 and D-5, as well as Table D-1), various series of $A_{1-x}A'_xLaNb_2O_7$ solid solution can be formed using an indirect reaction between appropriate ratios of two specific end members (illustrated in Figures D-2 and D-3). Figure D-6 shows the XRD patterns of all successful solid solutions: (a) $Li_{1-x}Na_xLaNb_2O_7$, (b) $Na_{1-x}K_xLaNb_2O_7$, (c) $K_{1-x}Rb_xLaNb_2O_7$, (d) $K_{1-x}Cs_xLaNb_2O_7$, and (e) $Rb_{1-x}Cs_xLaNb_2O_7$. The XRD patterns well prove the formation of particular solid solutions rather than mixtures of the end members which would show peaks related to both starting materials. A close-up of the first peak in the XRD patterns of three 1:1 solid solutions ($K_{0.5}Rb_{0.5}LaNb_2O_7$, $K_{0.5}Cs_{0.5}LaNb_2O_7$, and $Rb_{0.5}Cs_{0.5}LaNb_2O_7$) compared to a 1:1 mixture of the end members further highlights the shouldered peaks expected in case of incomplete formation of the solid solutions (Figure D-7). In order to better study the evolution of the structure as a function of the composition, unit cell refinement was first realized for all the systems (Table D-2), and then plotted versus the weighted average ionic radii of the interlayer cations (Figure D-8, D-9, and D-10). Except for Figures D-6a and e which consist of isostructural end members, solid solutions in all other cases adopted a new configuration moving from one end member to the other; both tetragonal and orthorhombic cells were to be used to perform unit cell refinement across one group of solid solutions in Figures D-6b—d and Table D-2. Figure D-8 illustrates the continuous evolution across the entire series of the solid solutions, while Figures D-9 and D-10 present them group by group. The *c* parameters and unit cell volumes show a gradual increase across the whole series as the ionic radii increase (from Li to Cs), however, there are a few inconsistencies happening in $Li_{1-x}Na_xLaNb_2O_7$ and $Na_{1-x}K_xLaNb_2O_7$ series. $LiLaNb_2O_7$, $Li_{0.75}Na_{0.25}LaNb_2O_7$ and $Li_{0.5}Na_{0.5}LaNb_2O_7$ have very similar *c* parameters and cell volumes, quite different from those of $Li_{0.25}Na_{0.75}LaNb_2O_7$ and $NaLaNb_2O_7$, which causes a sharp departure from Vegard's law (as if there are two separate lines for the beginning solutions and the later ones with higher x values).

The $Na_{1-x}K_xLaNb_2O_7$ solid solutions ($0.25 \leq x \leq 0.75$) seem to fit to a line once two end members are excluded from the series, again causing a negative departure from Vegard's law. This observation seems to be the characteristic of these two solid solution series, without any indication of the incomplete solution formation. Thermal analysis of $Li_{1-x}Na_xLaNb_2O_7$ metastable series also showed a transition in the DSC peak moving from one end member to the other (Figure D-11). The sensible transition observed via thermal analysis, as well as the increasing trend of the *c* parameter/cell volume versus the ionic radii, strongly support the successful formation of $A_{1-x}A'_xLaNb_2O_7$ solid solutions.

D.5 Conclusions

Low temperature topochemical reactions were proved to be effective pathways for the synthesis of alkali metal solid solutions ($A_{1-x}A'_xLaNb_2O_7$) from adjacent $ALaNb_2O_7$ and $A'LaNb_2O_7$ end members (A/A′ = Li, Na, K, Rb, Cs). Decomposition occurred with attempted solid solutions comprised of $LiLaNb_2O_7$ or $NaLaNb_2O_7$ with a nonadjacent end member. $K_{1-x}Cs_xLaNb_2O_7$ was the only instance where nonadjacent cation mixing led into the successful formation of solid solutions. The unit cell parameters of these solid solutions were found to vary with the solid solution composition for each series in which the cations were randomly distributed in the interlayer. Layer expansion and translation occurred with increasing ionic radii across the entire $A_{1-x}A'_xLaNb_2O_7$ family corresponding to the accommodation of larger cations within the perovskite layers. For the $K_{1-x}Rb_xLaNb_2O_7$, $Rb_{1-x}Cs_xLaNb_2O_7$, and $K_{1-x}Cs_xLaNb_2O_7$ solid solutions, the Vegard's law was well realized, while the two other groups showed negative departures from this generalization. These solid solutions can be further used to direct partial ion exchange reactions favoring one of the interlayer ions more than the other.

D.6 References

(1) Sato, M.; Watanabe, J.; Uematsu, K. Crystal Structure and Ionic Conductivity of a Layered Perovskite, AgLaNb2O7. J. Solid State Chem. 1993, 107 (2), 460–470.

(2) Viciu, L.; Caruntu, G.; Royant, N.; Koenig, J.; Zhou, W. L.; Kodenkandath, T. A.; Wiley, J. B. Formation of Metal−Anion Arrays within Layered Perovskite Hosts. Preparation of a Series of New Metastable Transition-Metal Oxyhalides, (MCl)LaNb2O7 (M = Cr, Mn, Fe, Co). Inorg. Chem. 2002, 41 (13), 3385–3388.

(3) Viciu, L.; Liziard, N.; Golub, V.; Kodenkandath, T. A.; Wiley, J. B. Transition-Metal Dion-Jacobson Layered Perovskites, M0.5LaNb2O7. Mater. Res. Bull. 2004, 39 (14–15), 2147–2154.

(4) Kodenkandath, T. A.; Kumbhar, A. S.; Zhou, W. L.; Wiley, J. B. Construction of Copper Halide Networks within Layered Perovskites. Syntheses and Characterization of New Low-Temperature Copper Oxyhalides. Inorg. Chem. 2001, 40 (4), 710–714.

(5) Hermann, A. T.; Wiley, J. B. Thermal Stability of Dion–Jacobson Mixed-Metal-Niobate Double-Layered Perovskites. Mater. Res. Bull. 2009, 44 (5), 1046–1050.

(6) Armstrong, A. R.; Anderson, P. A. Synthesis and Structure of a New Layered Niobium Blue Bronze: Rb2LaNb2O7. Inorg. Chem. 1994, 33 (19), 4366–4369.

(7) Kumada, N.; Kinomura, N.; Sleight, A. W. CsLaNb2O7. Acta Crystallogr. C 1996, 52 (5), 1063–1065.

(8) Sato, M.; Jin, T.; Ueda, H. Structural Change in Lithium Intercalation of Layered Perovskite LiLaNb2O7. Chem. Lett. 1994, 23 (1), 161–164.

(9) Sato, M.; Abo, J.; Jin, T. Structure Examination of NaLaNb2O7 Synthesized by Soft Chemistry. Solid State Ion. 1992, 57 (3), 285–293.

(10) Sato, M.; Abo, J.; Jin, T.; Ohta, M. Structure Determination of KLaNb2O7 Exhibiting Ion Exchange Ability by X-Ray Powder Diffraction. Solid State Ion. 1992, 51 (1–2), 85–89.

(11) Sato, M.; Jin, T.; Uematsu, K. Proton Conduction of MLaNb2O7 (M = K, Na, H) with a Layered Perovskite Structure. J. Solid State Chem. 1993, 102 (2), 557–561.

(12) Gopalakrishnan, J.; Bhat, V.; Raveau, B. AILaNb2O7: A New Series of Layered Perovskites Exhibiting Ion Exchange and Intercalation Behaviour. Mater. Res. Bull. 1987, 22 (3), 413–417.

(13) Josepha, E. A.; Farooq, S.; Mitchell, C. M.; Wiley, J. B. Synthesis and Thermal Stability Studies of a Series of Metastable Dion–Jacobson Double-Layered Neodymium-Niobate Perovskites. J. Solid State Chem. 2014, 216, 85–90.

(14) Carvajal, R. Comm Powder Diffr IUCr 2001, 26, 12.

(15) Laugier, J.; Bochu, B. LMGP-Suite Suite of Programs for the Interpretation of X-Ray Experiments, by Jean Laugier and Bernard Bochu, ENSP/Laboratoire Des Matériaux et Du Génie Physique, BP 46. 38042 Saint Martin d'Hères, France. WWW: http://www.inpg.fr/LMGP and http://www.ccp14.ac.uk/tutorial/lmgp/.

(16) Shannon, R. D. Revised Effective Ionic Radii and Systematic Studies of Interatomic Distances in Halides and Chalcogenides. Acta Crystallogr. A 1976, 32 (5), 751–767.

(17) Byeon, S.-H.; Nam, H.-J. Neutron Diffraction and FT-Raman Study of Ion-Exchangeable Layered Titanates and Niobates. Chem. Mater. 2000, 12 (6), 1771–1778.

(18) West, A. R. Chapter 2: Crystal Defects, Non-Stoichiometry and Solid Solutions. In Solid State Chemistry and its Applications; John Wiley & Sons, Ltd: United Kingdom, 2014; pp 83–123.

(19) Kim, H. J.; Byeon, S. H.; Yun, H. S. Raman Spectra of the Solid-Solution between Rb2La2Ti3O10 and RbCa2Nb3O10. Bull. Korean Chem. Soc. 2001, 22 (3), 298–302.

Appendix E. Inelastic Neutron Scattering Performed on Inorganic-Organic $LaNb_2O_7$ Hybrid Perovskites

E.1 Introduction

Inelastic neutron scattering (INS) measurements were carried out to collect information about molecular vibrations of C_nH_{2n+1}-$LaNb_2O_7$ (n = 3, 5, and 10), $C_nH_{2n+1}NH_3$-$LaNb_2O_7$ (n = 3 and 6), C_7H_7-$LaNb_2O_7$ and $C_{13}H_{11}$-$LaNb_2O_7$ hybrids, synthesis of which was explained in details in Chapter 3. Contrary to IR and Raman, INS is not limited with any optical selection rules.[1] In order to extract more information from the INS spectra, advanced molecular models have to be demonstrated for these hybrid systems.

E.2 Experimental

Characterization. High-resolution inelastic neutron scattering (INS) measurements were carried out on the vibrational spectrometer VISION (BL-16B)[2] at the Spallation Neutron Source (SNS) of the Oak Ridge National Laboratory (ORNL). Unlike POWGEN which suffers from incoherent and inelastic scattering of hydrogen-rich samples, VISION is especially sensitive to hydrogen due to its large incoherent scattering cross section. Therefore, INS was used as a powerful tool to evaluate the organic substituents of all the hybrids regardless of the level of hydrogen; C_nH_{2n+1}-$LaNb_2O_7$ (n = 3, 5, and 10), $C_nH_{2n+1}NH_3$-$LaNb_2O_7$ (n = 3 and 6), C_7H_7-$LaNb_2O_7$ and $C_{13}H_{11}$-$LaNb_2O_7$. 0.3—0.35 g of each sample was loaded in cylindrical vanadium sample holder 6 or 8 mm in diameter. Data were collected at 5 K for a duration of typically 4 to 6 hours. Instrument related background (vacuum shroud, heat shield, sample holder) was subtracted from the measured spectra. The TOF spectra were converted to energy transfer with the MantidPlot software, covering energy transfers from zero up to 496 meV (16-4000 cm^{-1}). Other than standard rebinning and smoothing, the displayed spectra have not undergone any alterations.

E.3 Results

Inelastic neutron scattering (INS) spectra are presented in Figure E-1 where the molecular vibrations are detected using netrons, without any optical selection rules.[1] Other than relying on similar methods[1,3–6] to generally confirm the expected organic groups in each structure (like in

Figure 3-2), advanced molecular models have to be demonstrated to extract more information from this data.[1,5,7,8]

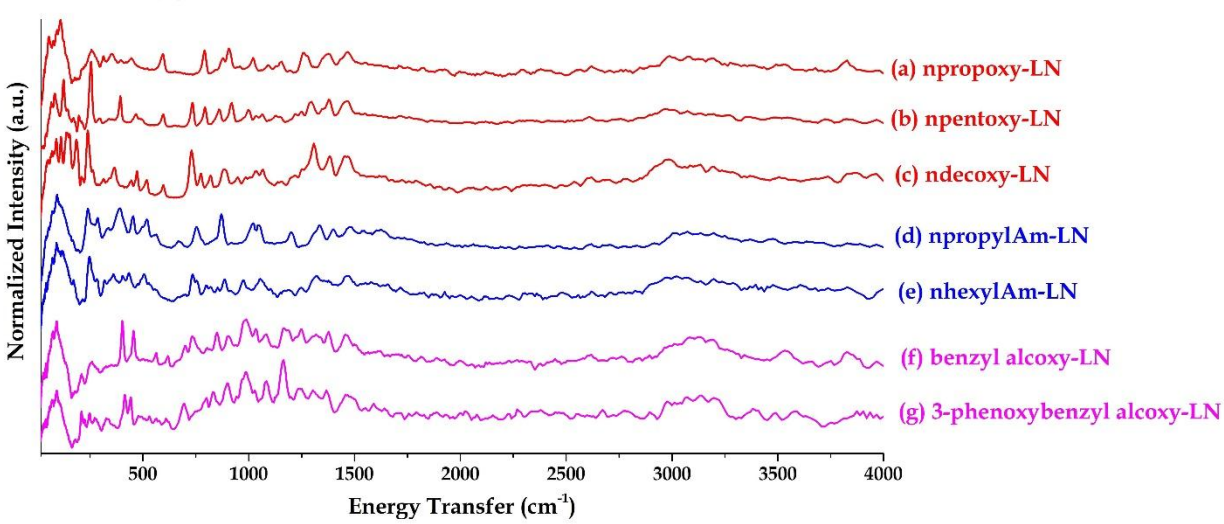

Figure E- 1: INS spectra of the hybrids; (a) n-propoxy-$LaNb_2O_7$, (b) n-pentoxy-$LaNb_2O_7$, (c) n-decoxy-$LaNb_2O_7$, (d) n-propylammonium-$LaNb_2O_7$, (e) n-hexylammonium-$LaNb_2O_7$, (f) benzyl alcoxy-$LaNb_2O_7$, and (g) 3-phenoxybenzyl alcoxy-$LaNb_2O_7$.

E.4 References

(1) Mitchell, P. C. H.; Parker, S. F.; Ramirez-Cuesta, A. J.; Tomkinson, J. Vibrational Spectroscopy with Neutrons: With Applications in Chemistry, Biology, Materials Science and Catalysis (Vol.3 from Series on "NeutronTechniques and Applications"; Finney, J. L., Worcester, D. L., Series Eds.; World Scientific: MA, USA, 2005.

(2) Seeger, P. A.; Daemen, L. L.; Larese, J. Z. Resolution of VISION, a Crystal-Analyzer Spectrometer. Nucl. Instrum. Methods Phys. Res. Sect. Accel. Spectrometers Detect. Assoc. Equip. 2009, 604 (3), 719–728.

(3) Mistry, B. D. A Handbook of Spectroscopic Data Chemistry: (UV, IR, PMR, 13CNMR and Mass Spectroscopy); Oxford Book Company, 2009.

(4) Lehn, J.-M.; Alberti, G.; Bein, T. Chapter 2: Vibrational Spectroscopy (By J. Eric D. Davies and Horst Forster). In Comprehensive supramolecular chemistry volume 8, Physical Methods in Supramolecular Chemistry.; Pergamon: Oxford; New York; Tokyo, 1996; pp 1–23.

(5) E. Casco, M.; Q. Cheng, Y.; L. Daemen, L.; Fairen-Jimenez, D.; Ramos-Fernández, E. V.; J. Ramirez-Cuesta, A.; Silvestre-Albero, J. Gate-Opening Effect in ZIF-8: The First Experimental Proof Using Inelastic Neutron Scattering. Chem. Commun. 2016, 52 (18), 3639–3642.

(6) Hartl, M.; Gillis, R. C.; Daemen, L.; Olds, D. P.; Page, K.; Carlson, S.; Cheng, Y.; Hügle, T.; Iverson, E. B.; Ramirez-Cuesta, A. J.; et al. Hydrogen Adsorption on Two

Catalysts for the Ortho- to Parahydrogen Conversion: Cr-Doped Silica and Ferric Oxide Gel. Phys. Chem. Chem. Phys. 2016, 18 (26), 17281–17293.

(7) Sato, T.; Ramirez-Cuesta, A. J.; Daemen, L.; Cheng, Y.-Q.; Tomiyasu, K.; Takagi, S.; Orimo, S. Hydrogen Release Reactions of Al-Based Complex Hydrides Enhanced by Vibrational Dynamics and Valences of Metal Cations. Chem. Commun. 2016, 52 (79), 11807–11810.

(8) Dyatkin, B.; Zhang, Y.; Mamontov, E.; Kolesnikov, A. I.; Cheng, Y.; Meyer, H. M.; Cummings, P. T.; Gogotsi, Y. Influence of Surface Oxidation on Ion Dynamics and Capacitance in Porous and Nonporous Carbon Electrodes. J. Phys. Chem. C 2016, 120 (16), 8730–8741.

Vita

The author of this work was born in 1988 in Tehran, Iran. In 2006 she entered the Amirkabir University of Technology (Tehran Polytechnic) which was known as the best school for studying Polymer Engineering in Iran. After completing her Bachelor's in 2010, she was exempted from the entrance exam for the Master's degree due to ranking 8th in her class. She finished her Master's in Polymer Engineering in 2012 and decided to continue her higher education studies in the United States. She joined the chemistry graduate program at the University of New Orleans in August 2012 in order to obtain a Ph.D. in Materials Chemistry. Later that year she joined Professor John B. Wiley's research group where she carried out various inorganic and nanomaterials studies. She earned a second Master's degree in Fall 2016 prior to finishing her Ph.D. degree in Spring 2017.